Max-Planck-Institut für Plasmaphysik
Garching bei München

Interface development for a EUROFER steel matrix composite with SiC-fibre reinforcement

Svetlana Levchuk

Vollständiger Abdruck der von der Fakultät für Maschinenwesen der Technischen Universität München zur Erlangung des akademischen Grades eines

Doktor-Ingenieurs

genehmigten Dissertation.

Vorsitzender:	Univ.-Prof. Dr.-Ing. H. Baier
Prüfer der Dissertation:	1. Hon.-Prof. Dr.-Ing., Dr.-Eng.(Japan) H. H. Bolt
	2. Univ.-Prof. Dr. mont. habil. E. Werner

Die Dissertation wurde am 19.09.2005 bei der Technischen Universität München eingereicht und durch die Fakultät für Maschinenwesen am 05.12.2005 angenommen.

To my family

Abstract

The reduced activation ferritic martensitic steel EUROFER 97 is currently considered as a reference material for the first wall and structural components of future fusion reactors. These wall materials should be compatible with high neutron fluences to minimise the necessary replacement of the in-vessel components and should be of a "low-activation" type. The only drawback of this steel is that its use would limit the maximum operating temperature to 550 °C due to the loss of creep strength at higher temperatures. A possible approach to solving this problem is the reinforcement of EUROFER 97 with long SiC fibres. This novel composite may allow an increase of the operating temperature up to 750 °C, which is essential for efficient energy production.

To obtain a matrix material, the fibres have to be coated with a thick EUROFER layer. In addition, to provide acceptable mechanical properties of the composite, a good adhesion between matrix and reinforcement is required. Therefore, a magnetron sputter device was used to deposit a fine structured EUROFER coating as an interface layer. Subsequently, a plasma arc with a high deposition rate was utilisied to produce a thick steel layer. To form the final composite material the so prepared fibres will have to be consolidated by using hot isostatic pressing.

The aim of this work was to develop a thermally stable interface between the SiC fibre and the EUROFER matrix. Diffusion in metal matrix composites can lead to the formation of undesirable compounds in the interface region between fibres and matrix, therefore an appropriate diffusion barrier between the fibres and the steel is necessary. In the case of SiC - EUROFER 97 the main problem was found to be C diffusion into the steel from the outer fibre coating. Different metallic and ceramic interlayers were selected as a diffusion barrier to suppress C diffusion into the matrix. To make an examination of the coatings with a number of different analysis methods, planar samples instead of fibres were coated and then annealed at different temperatures. Among the metallic interlayers tested in this work were Ti, Cr, Re, W and a combination of Re and W interlayers. The best results on the suppression of C diffusion were achieved through the application of a W interlayer and Re / W multilayer. As for the ceramic interlayers, before the annealing tests the different deposition parameters were varied to achieve the required stoichiometry and structure of the coating. The following ceramic layers were investigated as diffusion barriers: TiC, TiN and Er_2O_3. The application of an Er_2O_3 barrier showed the most promising result. The Er_2O_3 layer was not only stable with respect to interaction with EUROFER but it also effectively suppressed any C diffusion.

Finally, one of the interlayers, namely W, was tested with fibres. No interdiffusion between the fibre and W-EUROFER coatings was observed at the assumed working temperature of the new composite material, 750 °C.

Kurzfassung

Der niedrigaktivierende ferritisch-martensitische Stahl EUROFER 97 wird gegenwärtig als Strukturmaterial für die erste Wand zukünftiger Fusionsreaktoren in Erwägung gezogen. Dieser Stahl ist unter Neutronenbeschuss beständig, jedoch stellt die geringe Kriechfestigkeit bei höheren Temperaturen und damit die Begrenzung der maximalen Einsatztemperatur auf 550 °C einen wesentlichen Nachteil dieses Stahls dar. Eine mögliche Lösung für dieses Problem ist die Verstärkung von EUROFER 97 mit SiC Langfasern. Dieser neuartige Verbundwerkstoff könnte eine Erhöhung der Einsatztemperatur bis auf 750 °C, einer Temperatur für effizientere Stromerzeugung, erlauben.

Für den Verbundwerkstoff müssen die Fasern mit einer dicken Schicht EUROFER 97 als spätere Matrix beschichtet werden. Außerdem ist eine gute Haftung zwischen Matrix und Fasern erforderlich, um die gewünschten mechanischen Eigenschaften des Komposits zu erreichen. Deshalb wurde mit Hilfe einer Magnetron-Sputteranlage in einem ersten Schritt eine fein strukturierte EUROFER 97 Schicht als Zwischenschicht auf den Fasern abgeschieden. In einem zweiten Schritt wurde durch Plasma-Lichtbogenverdampfung mit hoher Abscheiderate eine dicke Stahlschicht als Matrix aufgebracht. Als letzter Schritt zur Synthese eines Verbundwerkstoffs folgt das heiß-isostatische Verpressen der beschichteten Einzelfasern.

Ziel dieser Arbeit ist die Entwicklung einer thermisch stabilen Grenzfläche zwischen SiC Fasern und EUROFER 97 Matrix. Diffusion in einem Metallmatrix Verbundwerkstoff kann zur Bildung unerwünschter Verbindungen an der Faser-Matrix Grenzfläche führen. Deshalb muss eine geeignete Diffusionsbarriere zwischen Faser und Stahl gefunden werden. Das Hauptproblem im Verbundwerkstoff SiC-EUROFER 97 ist die C Diffusion von der äußeren Faserschicht in die Stahlmatrix. Es wurden verschiedene metallische und keramische Zwischenschichten als Diffusionsbarriere ausgewählt, um die C Diffusion in die Matrix zu unterdrücken. Eine Vielzahl zur Verfügung stehender Analysemethoden zur Charakterisierung der Zwischenschichten erforderte ebene Substrate, die anstatt der Fasern beschichtet und bei verschiedenen Temperaturen wärmebehandelt wurden. Die besten Ergebnisse zur Unterdrückung der C Diffusion bei den metallischen Zwischenschichten, die in dieser Arbeit getestet wurden (Ti, Cr, Re, W), erreichten die W Schichten und die Re / W-Mehrschichtsysteme. Bei den keramischen Zwischenschichten wurden die verschiedenen Abscheideparameter variiert, um die geforderte Stöchiometrie und Struktur der Schichten zu erreichen. Folgende keramische Schichten wurden als Diffusionsbarriere untersucht: TiC, TiN und Er_2O_3. Die Verwendung von Er_2O_3 zeigte nach der Wärmebehandlung viel versprechende Ergebnisse. Die Er_2O_3 Schicht ist nicht nur chemisch stabil im Hinblick auf mögliche Reaktionen mit EUROFER 97, sondern sie unterdrückt auch jegliche C Diffusion.

Abschließend wurde eine W Zwischenschicht auf SiC Fasern getestet. Bei der für das neue Kompositmaterial angestrebten Einsatztemperatur von 750 °C wurde keine Diffusion zwischen Faser und W-EUROFER 97 beobachtet.

Contents

List of Symbols

n: plasma density
τ_E: energy confinement time
J: mass flux
D: diffusion coefficient
C: concentration
T: temperature
D_0: pre-exponential factor
k: Boltzmann constant
E_d: activation energy of diffusion
E_f: energy for defect formation
E_m: migration energy
S_0: instantaneous source
p: diffusion depth
B: mobility
μ: chemical potential
K: reaction rate constant
x_{C}: solubility of carbon
σ: ultimate tensile strength
E: Young's modulus
ν: Poisson's ratio
ρ: density
α: coefficient of thermal expansion
V_{Bias}: substrate bias voltage
Z: atomic number
λ: wavelength
θ_d diffraction angle
a: lattice parameter
n_i: integer value
E_1: ion energy after collision
E_0: primary ion energy
M_0: ion mass
M: atom mass
θ_s: scattering angle
R_a: surface roughness
q: applied power density
Q: gas flow
R: ratio of the partial pressures of Ar and N_2
P: pressure in the chamber during deposition

r:	deposition rate
d:	layer thickness

Abbreviations

bcc:	body-centered cubic
bct:	body-centered tetragonal
BSE:	backscattered electrons
CFC:	carbon-fibre reinforced carbon
CMF:	carbon monofilament
cph:	close-packed hexagonal
CVD:	chemical vapour deposition
DBTT:	ductile to brittle transition temperature
DC:	direct current
DEMO:	demonstration fusion power plant
EDX:	x-ray energy dispersive analysis
fcc:	face-centered cubic
HIP:	hot isostatic pressing
IBA:	ion beam analysis
ITER:	international tokamak experimental reactor
Me:	metal
MMC:	metal matrix composite
ODS:	oxide dispersion strengthened
OES:	optical emission spectroscopy
PFC:	plasma facing component
PVD:	physical vapour deposition
RAFM:	reduced activation ferritic martensitic
RF:	radio frequency
sccm:	standard cubic centimeters per minute
SE:	secondary electrons
SEM:	scanning electron microscopy
TEM:	transmission electron microscopy
XRD:	x-ray diffraction analysis

1 Introduction

Energy generating systems based on nuclear fusion have the potential to provide a CO_2 emission-free, sustainable, safe and clean energy option for the future. Considerable effort is being expended worldwide to develop fusion as a long-term energy source. The most favourable fusion reaction occurs between the hydrogen isotopes D and T:

$$^{2}\mathrm{D}_{1} + {}^{3}\mathrm{T}_{1} \longrightarrow {}^{4}\mathrm{He}_{2}\,(3.5\,\mathrm{MeV}) + {}^{1}\mathrm{n}_{0}\,(14.1\,\mathrm{MeV})$$

and releases 17.6 MeV of energy. The fuel changes from a gas to plasma at the temperatures, as high as 100 million °C required for the D-T fusion reaction to occur. The hot plasma has to be magnetically confined within a vacuum vessel to isolate it from the vessel walls. Very promising magnetic confinement systems are of a toroidal type, and the most advanced of these systems is a tokamak reactor [1,2]. The deuterium fuel is abundant and can be readily extracted from seawater. T does not occur naturally but sufficient quantities to fuel a fusion reactor may be bred from Li in a blanket surrounding the vacuum vessel via the following reactions [3]:

$$^{6}\mathrm{Li}_{3} + {}^{1}\mathrm{n}_{0} \longrightarrow {}^{3}\mathrm{T}_{1} + {}^{4}\mathrm{He}_{2} + 4.8\,\mathrm{MeV}$$
$$^{7}\mathrm{Li}_{3} + {}^{1}\mathrm{n}_{0} \longrightarrow {}^{3}\mathrm{T}_{1} + {}^{4}\mathrm{He}_{2} + {}^{1}\mathrm{n}_{0} - 2.5\,\mathrm{MeV}$$

A schematic view of a fusion power station based on the tokamak configuration is given in Fig. 1.1 [4].

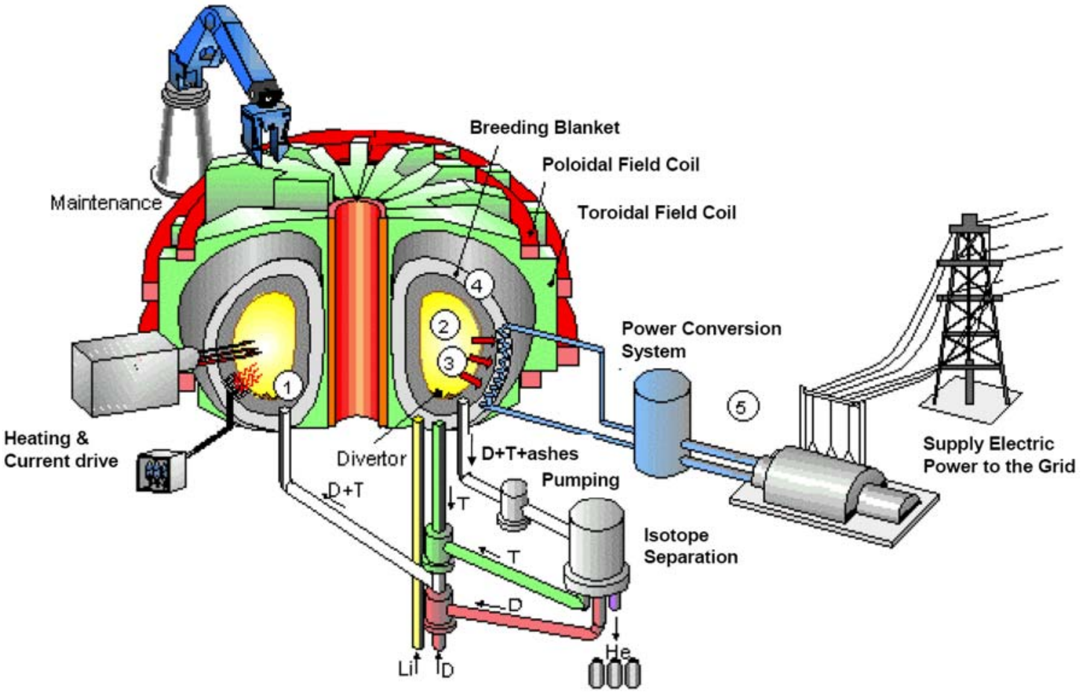

Figure 1.1: Schematic diagram of a tokamak fusion power station [4]

In the plasma, 80% of the energy produced by the D-T reactions is in the form of energetic neutrons, which escape the plasma across the magnetic field and are then trapped in a surrounding blanket that contains Li. Plasma in the reactor core is self-heated by α-

particles ($^4He_2$), which possess the remaining 20% of the energy produced. In the blanket, neutrons react with Li to produce T and He, and, as they slow down, their kinetic energy is converted into heat. Heat is extracted to raise steam to drive conventional turbines for electricity generation.

The long-term development towards a demonstration fusion power plant (*DEMO*) aims for structural materials which can withstand high heat fluxes and coolant pressure conditions at temperatures attractive for efficient thermodynamic energy production [5]. In addition, these materials have to be compatible with high neutron fluences ($10 - 15\,\mathrm{MW\,y\,m^{-2}}$ in a power reactor) to minimise the necessary replacement of the in-vessel components and be of a "low-activation" type. It is assumed that the main specifications of *DEMO* will be as follows: fusion power of $2.5 - 5.0\,\mathrm{GW}$ with a net electrical output of $1.5\,\mathrm{GW}$; neutron wall loading of $2.0 - 2.4\,\mathrm{MW\,m^{-2}}$; surface heat flux on the first wall up to $0.5\,\mathrm{MW\,m^{-2}}$; Plasma Facing Component (*PFC*) operational temperature in the range of $550 - 700\,^{\circ}\mathrm{C}$ [6, 7].

1.1 Structural materials for a fusion reactor

Materials in the first wall and blanket regions of a fusion reactor are in contact through the coolant, the breeding media and the mechanical structure. The blanket communicates with other parts of the plant through the coolant and the T recovery systems. Thus, it is not reasonable to select a breeder, coolant or structural material without consideration of the entire system. Numerous factors have to be taken into account when selecting the structural materials [8, 9], including:

- material availability, cost, fabricability, joining technology
- mechanical and thermo-physical properties
- radiation effects (degradation of properties)
- chemical compatibility and corrosion issues
- safety and waste disposal aspects (decay heat, etc.)
- nuclear properties (impact on tritium breeding ratio, solute burn-up, etc.)

Neutrons produce two forms of damage which can significantly alter the properties of structural materials: (1) kinetic energy is transferred from the neutrons to the atomic lattice and leads to displacement damage in the form of vacant lattice sites (vacancies) and atoms in interstitial positions (interstitials); (2) nuclear reactions result in transmutations that alter the composition. When subjected to neutron irradiation, materials tend to change their mechanical properties thus revealing hardening, loss of ductility, loss of fracture toughness, and loss of creep strength. The microstructure of irradiated materials results from interactions between the various irradiation-induced defects: small defect clusters, dislocation loops, precipitates, voids, and He bubbles. Additionally, the materials become radioactive. Due to the important requirement that the long-term induced radioactivity of fusion reactor components be of a low level, strong emphasis has been placed within the past $10-15$ years on the development of candidate materials which have a chemical composition based on low activation chemical elements: Fe, Cr, V, Ti, Si, C, W, and Ta. The main candidate structural materials are Reduced Activation Ferritic Martensitic (*RAFM*) steels, Oxide Dispersion Strengthened (*ODS*) *RAFM* steels, V based alloys, and SiC / SiC-composites [7]. They all reveal reasonably good thermo-physical and mechanical properties, low sensitivity to radiation-induced swelling and helium embrittlement under fission neutron irradiation together with good compatibility with the majority of cooling and breeding materials [10, 11].

V alloys based on V-Cr-Ti possess a favourable combination of thermo-physical properties, high creep strength and the lowest long-term activation. A major drawback of V alloys however is their high solubility and permeability of T and the high solubility of the interstitial elements O, N and C in V, which can lead to catastrophic embrittlement. SiC / SiC composite materials have potentially high pay-offs in terms of very low radioactivity and short to intermediate heat decay times as well as offering high operation temperatures in breeding blanket components due to high temperature strength. However, the very limited technology base for production, joining and insufficient hermetic sealing capacity is a serious disadvantage of SiC / SiC composites.

Martensitic steels containing $9-12$ wt.% of Cr with about 1 wt.% of Mo, $0.1-0.2$ wt.% of C and combinations of small amounts of V, W, Nb, etc. (MANET1, MANET2, HT9) have the strength, including elevated temperature strength, and thermal properties (conductivity and expansion coefficient) that result in excellent resistance to thermal stresses [12]. They have successfully been used at temperatures up to 600 °C in the power-generation and chemical industries [1]. It is recalled that *RAFM* steels are alloys whose main compositions are derived from the conventionally modified 9Cr - 1Mo steel where the high activation elements, such as Mo and Nb, are replaced by their equivalent low activation elements (e.g. W, V and Ta) [13]. The presence of high activation residual elements is also kept as low as possible. The selection and development of ferritic martensitic $9-12$ wt.% Cr steels with reduced activation for nuclear fusion is based on the excellent experience collected on commercial $9-12$ wt.% Cr steels. *RAFM* steels are planned to be used in the EU Test Blanket Modules and be tested in International Tokamak Experimental Reactor (*ITER*) for validation of the *DEMO* blanket concept.

1.1.1 EUROFER 97

EUROFER 97 is an industrial batch of 9% CrWVTa reduced activation ferritic martensitic steel specified in 1997 and produced by Böhler, Austria, with the presently available steel manufacturing technology developed in 1999. In Table 1.1 the composition of EUROFER 97 is presented together with Japanese *RAFM* steel F82H [14].

For EUROFER 97 the contents of Cr, Ta, W were specified carefully based on experience with precursor *RAFM*-alloys of OPTIFER type. A minimum of the ductile to brittle tran-

Elements	EUROFER 97 steel [wt.%]	F82H steel [wt.%]
C	0.09 – 0.12 [0.11]	0.09
Cr	8.5 – 9.5 [9.0]	7.7
W	1.0 – 1.2 [1.1]	1.94
V	0.15 – 0.25	0.16
Ta	0.06 – 0.09	0.02
Mn	0.20 – 0.60 [0.40]	0.16
Si	$<$ 500 ppm	1100 ppm
Ni	$<$ 50 ppm	200 ppm
Cu	$<$ 50 ppm	100 ppm
Co	$<$ 50 ppm	50 ppm
Mo	$<$ 50 ppm	30 ppm
Al	$<$ 100 ppm	30 ppm
Nb	$<$ 10 ppm	1 ppm

Table 1.1: Specified chemical compositions of EUROFER 97 and F82H steels

sition temperature (*DBTT*) corresponds to a Cr content of 9 wt.%, and in order to achieve a better corrosion resistance 9 wt.% Cr has been chosen [14]. Ta stabilises the grain size by carbide formation and improves *DBTT* and strength. About 1 wt.% of W represents a good compromise regarding low activation, *DBTT*, tensile strength, ductility and creep strength. The effect of undesired impurities is shown in Fig. 1.2, where the surface gamma dose rate is the ordinate and the time after irradiation is the abscissa. Steels like EUROFER 97 and F82H reach the remote recycling level in about 100 y and can be stored as low level waste.

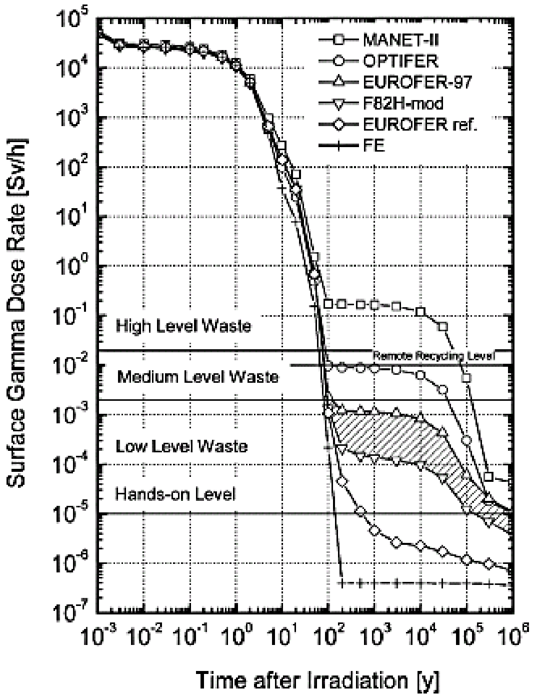

Figure 1.2: Calculated γ-surface dose rate of pure Fe and *RAFM* steels after irradiation in a first wall *DEMO* spectrum ($12.5\,\mathrm{MW\,y\,m^{-2}}$) [14].

The difference between these two alloys (hatched area) is due to lower Nb content in F82H (1 ppm) compared with 10 ppm for EUROFER 97.

EUROFER 97 possesses a martensite structure, which is a supersaturated solid solution of C trapped in a body-centered tetragonal (*bct*) structure. The displacive transformation from face-centered cubic (*fcc*) lattice is initiated by quenching from austenitizing temperature to ambient temperature. The steel is then subsequently tempered to obtain a good combination of strength, ductility, and toughness. The axial ratio of lattice constants c/a increases with C content to a maximum of 1.08, thus for a steel containing 0.1 wt.% of C, the lattice constants are a $= 0.286\,\mathrm{nm}$ and c $= 0.287\,\mathrm{nm}$ and the ratio is 1.003 [15]. The undesirable formation of δ-ferrite in martensite can be avoided by addition of the austenite-forming elements, such as C, V, Nb, Ta, Ti or Al, to a steel composition [1]. In the case of EUROFER 97 Ta and V have been used. The initial treatment of EUROFER produces a fully martensitic structure without δ-ferrite with lath-shaped martensite subgrains [16]. It reveals a fine structure with a prior austenite grain size in the range of $10 - 11.5\,\mu$m (see Fig. 1.3a). Treatment of the steel in the normalized (980 °C / 27 min) plus tempered (760 °C / 90 min / air cooled) conditions is made to produce a more uniform prior austenite grain size and martensite lath structure and homogeneity in properties after tempering. The tempering treatment produces large amounts of carbide precipitation, distributed preferentially along grain and lath boundaries but precipitates appear also in the bulk of the martensite lathes (see Fig. 1.3b). Two types of carbides have been observed in EUROFER 97, namely Cr rich precipitates and Ta / V rich precipitates, identified as $M_{23}C_6$ type and (Ta,V)C type, respectively [16].

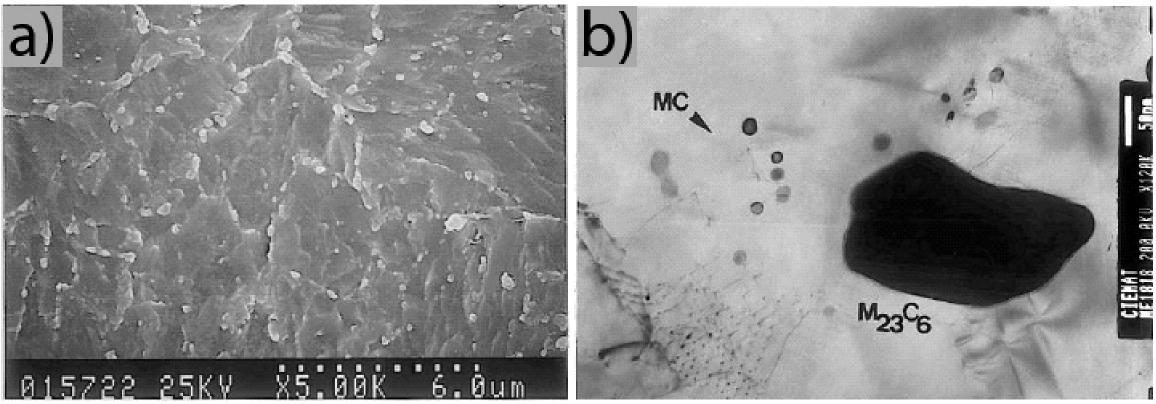

Figure 1.3: a) *SEM* micrograph of EUROFER 97 as-received state, b) *TEM* micrographs of an $M_{23}C_6$ precipitate [16]

The metallurgical properties (microstructural and mechanical) and the microchemistry at grain boundaries of the EUROFER 97 steel after simulated service conditions by aging treatment in the range of temperatures from 400 to 600 °C up to $10,000\,\mathrm{h}$ were thoroughly investigated [17]. It was found that after the aging treatments at 500 and 600 °C for $10,000\,\mathrm{h}$ the equiaxed grains and subgrain structure had replaced the martensite laths. The grain boundary microchemistry observed in the steel in the as-received condition and after the aging consisted of Cr enrichment and Fe depletion. The values of ultimate tensile strength and 0.2% proof stress revealed similar values for each temperature regardless of aging condition.

1.1.2 ODS-steel

A serious disadvantage of *RAFM* alloys is the reduction of creep strength at temperatures above 550 °C and this has been overcome by the development of *ODS* variants of these steels. These *ODS* materials allow an increase in the operating temperature by about 100 °C [18]. As the first step in the *RAFM ODS* steel development, EUROFER 97 has been chosen as a base material and Y_2O_3 particles as dispersed particles because the addition of yttria does not impair the long-term activation property. Two variants with Y_2O_3 contents of 0.3 and 0.5 wt.% have been produced by experienced industrial manufacturers. The Hot Isostatic Pressing (*HIP*) process has been applied at 1050 °C as an appropriate consolidation process for the *ODS* steel production. *HIP* process (or hipping) is regarded to as the most promising production route for nearly end-shaped structures for future fusion reactors.

The grain size of the hipped material lies in the range of 2 to 8 μm. The boundaries of these grains are decorated with Cr-rich precipitates of $M_{23}C_6$ type, while the matrix structure is ferritic in contrast to the basic EUROFER 97 steel [18]. In the case of 0.5 wt.% of Y_2O_3, the carbides at the grain boundaries with sizes up to about 1 μm are larger than in the case of 0.3 wt.% of Y_2O_3, where they attain about 0.2 μm maximum. The Y_2O_3 particles are heterogeneously distributed with regions free of them and appear in the material in either groups of about $20 - 40$ nm round particles or groups of $1 - 5$ nm round particles [19]. The crystallographic lattice of the metal matrix corresponds to α-Fe with a body-centered cubic (*bcc)* structure and a lattice constant $a_0 = 0.287$ nm, while the Y_2O_3 particles embedded in the alloy have a crystalline *bcc* structure with a 1.06 nm lattice constant [20]. Additionally, there is a strong orientation correlation observed between the structure of the particles and the FeCr matrix. The microstructure of *ODS* steel is described as an alloy with a spatially homogeneous distribution of the particles as well as the composition. Different microstructures can in principle appear due to the applied *HIP* process.

The first results on hipped EUROFER *ODS* variants are quite encouraging with respect to tension and creep [7]. The creep tests have been conducted at temperatures between 600 and 700 °C in air reaching rupture times up to 5000 h. The results are given in the form of a Larson–Miller plot in Fig. 1.4 and are comparing to those of EUROFER 97 and F82H mod. *ODS* EUROFER steels containing 0.3 and 0.5 wt.% of Y_2O_3 show a substantially higher creep strength than the two non-reinforced *RAFM* steels [18]. Thus, an applied stress of 100 MPa would lead at 650 °C to a rupture time of $50,000$ h compared to 500 h for EUROFER (see Fig. 1.4).

The *ODS* steel containing 0.3 wt.% of Y_2O_3 has superior tensile resistance and similar, if not better, uniform elongation behaviour than the base material, while in the case of 0.5 wt.% of Y_2O_3 the material shows weak mechanical properties. The microstructure of the latter cannot sustain stresses even to the level of the base material.

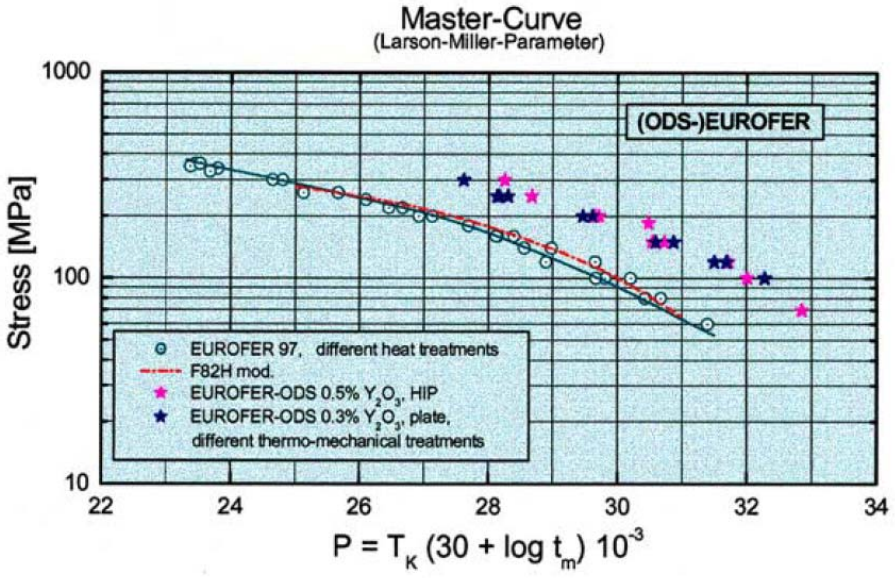

Figure 1.4: Creep properties of EUROFER compared to *ODS* EUROFER [7]

This fact is related to the presence of porosity and large carbides [19].

1.2 Objectives

An alternative approach to using *ODS* EUROFER to solve the problem of the limited operating temperature is material reinforcement with SiC fibres, resulting in a new composite material SiC - EUROFER 97. Firstly, silicon carbide fibres do not worsen the radiological behaviour of EUROFER 97 since SiC itself is a low activation material. Secondly, this reinforcement can significantly improve the mechanical properties over a wide temperature range. This approach is supported by the results of [21] where the thermo-mechanical properties of this composite material have been calculated for the case of an unidirectional fibre array assuming a perfect interface. The results of the calculations indicate that yield stress, ultimate tensile strength and creep resistance can be effectively increased by reinforcement of EUROFER with long SiC fibres. Therefore the reinforcement of the steel with the long SiC fibres should allow an increase in the operation temperature of the composite to about 750 °C.

The composite material SiC - EUROFER 97 is proposed to be manufactured in three steps. During the initial stage of composite processing the SiC fibres are coated by magnetron sputtering resulting in a fine-structured steel interface layer on the fibre's surface. Subsequently, a thick EUROFER matrix layer is formed by arc deposition. To form the final composite material the so prepared fibres will have to be consolidated by using *HIP* at 1000 °C and 100 MPa.

However, interface reactions between the EUROFER 97 matrix and reinforcing SiC fibres can lead to structural instability and thereby degradation of the mechanical properties of the composite. To prevent, or at least reduce, undesirable interactions, it is necessary to apply an effective diffusion barrier in the form of a fibre coating which has to be uniform in thickness and free of pores. Therefore, an interlayer is proposed to be deposited between the fibre and matrix material utilizing the magnetron sputtering technique, since this provides a fine layer structure without porosity.

The selection of an appropriate diffusion barrier relies on the detailed knowledge of the reactions taking place at the interface region EUROFER 97 / SiC. In particular, the interdiffusion and phase formation between elements in the SiC fibres and in the EUROFER 97 are the most important processes to consider in the choice of a diffusion barrier.

In the present research, the interactions at three different interfaces are investigated:

- Interaction between C and the interlayer at the interface between the outer coating of the SiC fibre and the interlayer. The SiC fibres are of the SCS6 type produced by Specialty Materials.
- Interaction between SiC and the interlayer at the interface between the outer coating of the SiC fibre and the interlayer.
- Interaction between EUROFER (mainly Fe) and the interlayer at the interface between the interlayer and EUROFER matrix.

A schematic view of these systems is shown in Fig. 1.5. The outer coating of SiC fibres is SiC doped C (see more details on fibre structure in subsection 3.1.1).

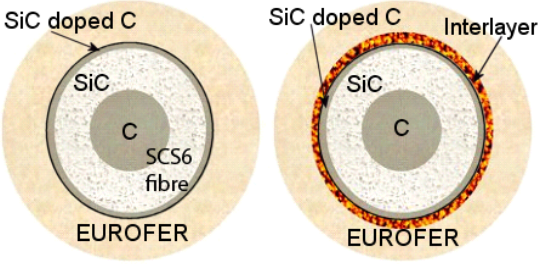

Figure 1.5: Schematic view of system SiC / EUROFER 97 with and without interlayer

To investigate the diffusion processes between the fibre and matrix as well as the effectiveness of the application of an interlayer as a diffusion barrier, the samples are annealed at temperatures $400 - 1000\,^{\circ}$C and compared with the pristine ones using a number of analysis techniques. The temperature range is selected based on the suggested operating temperature of the composite to be of $750\,^{\circ}$C and the *HIP* temperature of $1000\,^{\circ}$C. To get the complete picture about the processes which take place at the interface between the fibre and matrix caused by the annealing, the surface structure, crystalline structure and the composition of the interface layer have to be investigated. For this purpose the following techniques are used:

- Scanning Electron Microscopy (*SEM*) and X-ray Energy Dispersive analysis (*EDX*) allow the analysing of the condition of the interface layer surface and its composition, as well as the composition of the individual formations

- X-Ray Diffraction analysis (*XRD*) gives an indication about the crystalline structure of the interface layer

- Optical Emission Spectroscopy (*OES*) gives the composition of the investigated layer with the exception of gas elements

- Ion Beam Analysis (*IBA*) allows the investigation of the concentration depth profile of the layer for all elements and, by using a diffusion code, an estimation of the rate of the diffusion processes.

The collection of the data obtained by these analyses makes it possible to estimate the condition of the interface layer before and after annealing. For *OES*, *XRD*, and *IBA* it is necessary to use planar samples. Therefore, to simplify examination of the coatings using the available analysis methods, planar samples of pyrolytic graphite, SiC, and glass are investigated.

Different materials are chosen as diffusion barriers for suppressing the C diffusion which can be divided in two groups: Metal (*Me*) interlayers (Ti, Cr, W, Re, and Re / W multilayer system) and ceramic interlayers (TiC, TiN, ZrO_2, and Er_2O_3). In Tables 1.2 and 1.3, a brief description of the reasons for each selection is given.

Me interlayers	
Ti	SiC fibres initially specified for application with Ti
Cr	Medium diffusivity of Fe and low diffusivity of C
W	Low diffusivities of C and Fe and low self-diffusion
Re	Low solubility of C
Re / W	Suppression of C diffusion at $T \leq 1600\,^{\circ}$C

Table 1.2: Reasons for selection of metal interlayers as a diffusion barreir

Ceramic interlayers	
TiC	Low diffusivity of C and stable with respect to Fe
TiN	Suppression of C diffusion at $T \leq 950\,^{\circ}$C
ZrO_2	α-ZrO_2 stable up to 1200 °C
Er_2O_3	stable up to 2000 °C

Table 1.3: Reasons for selection of ceramic interlayers as a diffusion barreir

Based on the results of analyses, the performance of each interlayer and, hence, their applicability as a diffusion barrier is valued according to the following criteria:

- how strong the interlayer components interdiffuse with the EUROFER layer

- how effectively the interlayer suppresses the C diffusion into EUROFER

- does the decomposition of SiC occur with the application of the interlayer

- whether delamination of the layers is observed after annealing.

2 Literature Review

Fibre composite technology is based on taking advantages of high strength and high stiffness of fibres, which are combined with matrix materials [22]. In composites, both the fibres and the matrix retain their original physical and chemical identities yet together they produce a combination of mechanical properties that cannot be achieved with either of the constituents alone due to the presence of an interface between these two constituents. The chemical, physical and mechanical properties of the interface are different from those of both the bulk fibre and the matrix, and since the interface is responsible for the load transfer between them it plays a substantial role. A thorough knowledge of the microstructure of the interface region, or rather understanding the mechanisms of adhesion, is an essential key to the successful design and proper use of composite materials. However, one of the mechanisms of adhesion, namely diffusion in Metal Matrix Composite (*MMC),* may not always be beneficial because of the formation of undesirable compounds which degrade the desired properties [22]. For this reason, a detailed understanding of these processes is also desirable. New phases in the form of precipitates, layered compounds, or even voids may arise from subsequent reactions and alter the initial film integrity through the generation of stress or reduction of adhesion. A balance is thus always required between the reaction necessary for efficient interfacial bonding and fibre degradation caused by excessive reaction. Therefore, a diffusion barrier in the form of a fibre coating is necessary to prevent interdiffusion between fibres and matrix.

To analyse the problem of interdiffusion between the EUROFER matrix and the SiC fibre with and without an interlayer, diffusion coefficients for SiC - *Me* and C - *Me* couples are needed. Since the interlayer has to provide not only the suppression of diffusion but also a good bonding between fibre and matrix, the interaction between the EUROFER and the interlayer EUROFER - *Me* also has to be known.

2.1 Basics of diffusion

There are two mechanisms of diffusion in the bulk of a crystal: interstitial diffusion and vacancy diffusion. In the first case small atoms dissolved in the crystal diffuse around by squeezing between atoms, jumping - when they have enough energy - from one interstice to another [23]. Carbon, a small atom, diffuses through steel in this way; in fact, C, O, N and H diffuse interstitially in most crystals. These small atoms diffuse very quickly. The second mechanism is that by which most diffusion in crystals takes place. Atoms have to wait until a vacancy, or missing atom, appears next to them before they can move further. Diffusion in the bulk crystals may be short circuited by diffusion down grain boundaries or dislocation cores. Rapid diffusion within individual grain boundaries, coupled with their great profusion due to small grain size, make them pathways through which the majority of mass is transported. The boundary acts as a planar channel, about two atoms wide, with a local diffusion rate which can be as much as 10^6 times greater than in the bulk [23]. The dislocation core, too, can act as a high conductivity “wire” of cross-section about $(2b)^2$, where b is the atom size. These effects become important when grains are small or dislocations numerous and so a diffusion barrier has to possess the crystalline structure without numerous defects.

Diffusion in solids can be defined as the migration of atomic or molecular species within a given matrix under the influence of a concentration gradient [24]. The relation between concentration gradients and the resultant diffusional transport is known as Fick’s first law given here for one dimensional case for simplicity:

$$J = -D\frac{dC}{dx},$$

where J is the mass flux in the x direction, D is the diffusion coefficient, and C is the concentration. The diffusion coefficient depends on both the diffusing species and the matrix and determines the amount of observable mass transport. In addition, D increases in exponential fashion with temperature T according to a Maxwell-Boltzmann relation:

$$D = D_0 \exp\left(-\frac{E_\mathrm{d}}{kT}\right),$$

where D_0 is the pre-exponential factor, k is the Boltzmann constant, and E_d is the activation energy of diffusion. The activation energy is the sum of the energy for defect formation E_f (in most cases about 1 eV per atom) and the migration energy E_m. The high density of defects, grain boundaries and vacancies in deposited films cause them to behave differently from bulk material.

Since solid-state diffusion is generally a slow process with compositional change occurring over a long time, it is necessary to solve Fick’s second law that in its simplest form is given as:

$$\frac{\partial C\left(x,t\right)}{\partial t} = D\frac{\partial^2 C\left(x,t\right)}{\partial x^2}, \tag{2.1}$$

where a concentration varies with position and time and the diffusion coefficient is independent on them. If the film thickness is very large or effectively infinite compared to the extent of diffusion, a simple solution can be received with the following boundary condition:

$$\int_0^\infty C(x,t)\,dx = S_0.$$

It means that a very thin layer of diffusant provides an instantaneous source S_0 of surface atoms per unit area. In this connection the surface concentration decreases with time as atoms diffuse into the underlying substrate:

$$C\left(x,t\right) = \frac{S_0}{\sqrt{\pi D t}} \exp\left(-\frac{x^2}{4Dt}\right).$$

To calculate the diffusion depth p, often the random walk expression is used:

$$p = 2\sqrt{Dt}. \tag{2.2}$$

When $\sqrt{Dt}$ becomes large compared to the film dimensions, the assumption of an infinite matrix is not valid and this solution does not hold. In this case D depends on the concentration and, therefore, appears to be a function of x and t (2.1) and has a more complicated form [25, 26]:

$$\frac{\partial C\left(x,t\right)}{\partial t} = \frac{\partial C\left(x,t\right)}{\partial x}\frac{\partial D\left(x,t\right)}{\partial x} + D\left(x,t\right)\frac{\partial^2 C\left(x,t\right)}{\partial x^2}, \text{ with } D\left(x,t\right) \equiv D\left(C\left(x,t\right)\right). \tag{2.3}$$

The numerically calculated diffusion depth profile can be fitted to the experimental depth profile, for instance, by the program DIFFUSEDC [26,27] to find the concentration dependent diffusion coefficient $D(C)$. This particular code uses the following boundary condition:

$$\left.\frac{dC\left(x,t\right)}{dx}\right|_{\text{boundary}} = 0.$$

This means that the flux through the surface is absent, that is the concentration of the diffusion species is not zero at the surface. More details concerning these calculations are given in Appendix B.

In [28] the diffusion coefficient D_1 of component 1 for a binary alloy is described as:

$$D_1 = B_1 \frac{d\mu_1}{d\ln C_1}, \tag{2.4}$$

where B_1 is the mobility of component 1, μ_1 is the chemical potential of component 1, and C is the concentration of component 1. The same relation holds for component 2. Therefore, diffusion of component 1 depends not only on the concentration (as in equation (2.3)) but also on the mobility and chemical potential. It becomes particularly important for the case of phase formation during diffusion, since the chemical potential of a component will be different in each phase.

As described above, a small atom like C, diffuses very quickly. Therefore, to suppress diffusion, a material in which C has a low diffusion coefficient should be selected as a diffusion barrier. How to select a proper material and which types of barriers exist?

In an ideal case, a barrier layer X placed between materials A and B should [24]:

- have low diffusivity of A and B in it
- be thermodynamically stable with respect to A and B within the temperature range of interest and have low solubility in A and B
- be easy to deposit, adhere well to A and B, possess low stress, and be compatible with a variety of processing procedures.

Some of these requirements are difficult to comply with; moreover, they are sometimes even mutually exclusive. Therefore, some compromises are necessary. Another requirement to the barrier is its thickness. If the kinetic reaction rates of compounds AX and BX are known, then either the effective lifetime or the minimum thickness of a barrier can be predicted.

There are basically three types of diffusion barriers:

- Packed barriers. These barriers rely on the segregation of impurities along rapid diffusion paths such as grain boundaries to block further two-way atomic transport. A marked improvement is found for sputtered Ti, Mo, and Ti - W alloys as diffusion barriers when they contain small quantities of intentionally added nitrogen or oxygen. Typically, concentrations of $\sim 10^{-1}$ to 10^{-3} at.% of such interstitial impurities are required to decorate grain boundaries and induce the packed barrier protection.

- Passive compound barriers. An ideal barrier that exhibits chemical inertness and negligible mutual solubility and diffusivity. Although there are numerous variations among the carbides, nitrides and borides, only the transition-metal nitrides have been widely used.

- Sacrificial barriers. A sacrificial barrier maintains separation of A and B but only for a limited duration. It exploits the fact that reactions between adjacent materials produce uniform layered compounds AX and BX, which appear to be separated by the narrow X barrier film. Protection in this case is afforded as long as X is not consumed.

For a composite material it is important to not only suppress the material intermixing but also to provide a good adhesion between the components of a composite. Therefore, different types of diffusion barriers are investigated in this work: a sacrificial barrier (Ti, Cr), a passive compound barrier (TiC, TiN, Er_2O_3), and a hybrid of the sacrificial-passive barriers (W, Re, Re / W). The latter means that a passive compound barrier is formed during diffusion, for example WC in the case of W - graphite interaction. On the one hand, C and W interact with each other and form a carbide, therefore, the W layer in this case is the sacrificial barrier. On the other hand, C has a lower diffusivity in WC than in pure W and hence WC acts as a passive compound barrier revealing long term stability.

2.2 Literature data on diffusion interaction

In systems like SiC / EUROFER and C / EUROFER a diffusion barrier coating must be applied to prevent the formation of deleterious carbides and silicides, so interactions between SiC / *Me* and C / *Me* have to be known. All binary and ternary phase diagrams for these systems are shown in Appendix C.

2.2.1 SiC / Me

SiC is a ceramic material that is widely used in high temperature structural applications and is utilized as reinforcement in composite materials to improve their mechanical properties.

A lot of investigations have dealt with the analysis of different phases within the reaction zone of SiC with metals [29–38].

The Si-C-X ternary systems can be divided into type I and type II groups based on the shape of the isothermal phase diagram [29]. The main features of type I and type II are as follows:

Type I: Fe, Re

- there is no compound formation in equilibrium *Me*-C binary system
- three phase region (SiC-C-Silicide) exists on the ternary isothermal phase diagram

$$Me + \text{SiC} \longrightarrow \text{silicides} + \text{C (graphite)}$$

Type II: Cr, Ti, W

- at least one compound exists in *Me*-C binary system
- if the ternary phase exists, it is in equilibrium with silicide and carbide (no ternary phase in Si-C-W)

$$Me + \text{SiC} \longrightarrow \text{silicides} + \text{carbides} + (\text{M}_\text{X}\text{Si}_\text{Y}\text{C}_\text{Z})$$

SiC is stable up to approx. 2500 °C and the decomposition of SiC is related to the thermodynamics of the reaction between SiC and a metal, where the latter can play the role of a catalyst. From the thermodynamical point of view the SiC phase is not stable in combination with many metals and tends to form other compounds at temperatures below 1000 °C.

SiC / Fe

The solid state reaction between SiC and Fe in the temperature range from 800 to 1100 °C and the duration $0.5-40\,\text{h}$ was investigated in [30] with a heating rate of $0.5\,\text{K}\,\text{s}^{-1}$. The tube furnace was flushed during annealing with a gas mixture of Ar - 20 vol.% H_2. The reaction zone had a band structure: modulated C precipitation zone / random C precipitation zone / C precipitation free zone. The reaction products were Fe_3Si, Fe(Si), and the graphitic C precipitates. Only the metal richest silicide, Fe_3Si, was detected in the reactive zone, since only its formation was thermodynamically favoured:

$$3\text{Fe} + \text{SiC} \longrightarrow \text{Fe}_3\text{Si} + \text{C}_\text{Gr}.$$

The existence of the carbon precipitation free zone indicated that Si diffused faster than C. A cluster of voids in the zone adjacent to the random C precipitation zone was found. The formation of voids was attributed to the non-equilibrium diffusion of Fe and Si during the reaction process. The thermal expansion property of the random C precipitation zone and the C precipitation free zone was different because of their different composition. Hence, a crack was formed along voids of the couple. From the measured reaction zone thickness for different annealing temperatures from 800 to 1100 °C, the reaction rate constant, K, was calculated:

$$K = 4.9 \cdot 10^{-4} \exp\left(-\frac{180 \cdot 10^3}{RT}\right) \; \left[\mathrm{m^2\,s^{-1}}\right].$$

Thus, after annealing at 1000 °C over 2 h the reaction zone thickness appeared to be about 300 μm. The value of K was of the same order of magnitude as the diffusion coefficient of Fe in Fe_3Si, whereas it was nearly 10^3 times larger than the diffusion coefficient of Si in Fe_3Si. Consequently, the Fe atoms in Fe_3Si were found to be the dominating diffusion species of the reaction.

SiC / Fe-20 Cr

Similar investigations were performed for the system SiC / Fe - 20Cr in [31]. Analysis was performed with the samples annealed at temperatures from 900 to 1200 °C with duration up to 20 h and a heating rate of 0.5 K s^{-1}. The tube furnace was flushed during annealing with a gas mixture of Ar - 20 vol.% H_2. The reaction zone was mainly composed of Fe_3Si, Cr_3Si, M_7C_3-type carbide (M = Cr, Fe) and graphitic C precipitates. This zone had two sections which were different in their microstructure and element distribution. The first one, adjacent to the SiC site, had high Si, Fe and low Cr concentrations with randomly distributed C precipitates. The particle size of the C precipitates increased with increasing distance from the SiC side. The second zone, adjacent to the Fe - 20Cr side, was uniform and free from C precipitates. This zone had extremely high Cr content, low Fe content, and no Si content. The selectivity of the interface reaction between SiC and the Fe - 20Cr alloy was detected. Hence, Si atoms, decomposed from SiC, selectively reacted with Fe atoms to form Fe_3Si. C atoms selectively reacted with Cr atoms from the Fe - 20Cr alloy to form the M_7C_3-type of carbide. This reaction was partially attributed to the high formation enthalpies of these compounds. The reaction rate constant, K, was found to be:

$$K = 1.9 \cdot 10^{-4} \exp\left(-\frac{235 \cdot 10^3}{RT}\right) \; \left[\mathrm{m^2\,s^{-1}}\right].$$

Consequently, the reaction zone thickness after annealing at 1000 °C over 2 h was 20 μm, which is 15 times smaller than that for the SiC / Fe system [30] due to the interface reaction control of the Cr element in the Fe matrix.

SiC / Ti

For SiC / Ti, the composition in the reaction zone was investigated for both SCS6 fibre / Ti and SiC / Ti plane interface at 950 °C over 100 – 300 h and at 1200 °C over 1 – 100 h, respectively [32]. The reaction zone was found to be a two-phase zone that consisted of TiC_X crystals within a matrix of $Ti_5Si_3C_X$. The product phases were:

SCS6 / Ti	SiC / Ti_3SiC_2 / $Ti_5Si_3C_X$ + TiC_X / TiC_X / Ti
SiC / Ti	SiC / $Ti_5Si_3C_X$ + TiC_X / Ti,

with the highest x value of about 11 at.%. The ternary phase diagram was investigated in [33] (see Fig. C.1 in Appendix C). The reaction rate constants, K, determined at 900 °C were:

SCS6 / Ti $3.4 \cdot 10^{-16}\,\mathrm{m^2\,s^{-1}}$
SiC / Ti $5.3 \cdot 10^{-16}\,\mathrm{m^2\,s^{-1}}$.

Therefore, after around 2 h at 900 °C, the reaction zone thicknesses were:

SCS6 / Ti $1.6\,\mu\mathrm{m}$
SiC / Ti $2.0\,\mu\mathrm{m}$.

SiC / Cr

For SiC / Cr with a plane interface the product phase was found to be SiC / Cr_5Si_3C / Cr_7C_3 + Cr_3Si / Cr_7C_3 / $Cr_{23}C_6$ / Cr [34] after annealing at 1000 °C over 40 h. *SEM* images of the cross-section of the sample showed a good contact between SiC and the diffusion zone. However, there was a gap ($5\,\mu\mathrm{m}$) appeared at the diffusion zone / Cr interface due to a large difference in the thermal expansion coefficients. In [35] the isothermal phase diagram was determined (see Fig. C.2 in Appendix C). The SiC / Cr diffusion couple showed a layered structure. Carbide layers were produced next to the Cr side indicating that the diffusion distance of C from SiC was larger than that of Si from SiC. A parabolic growth law was assumed for the reaction zone thickness, from which the reaction rate constant, K, was determined as:

$$K = 2.6 \cdot 10^{-8} \exp\left(-\frac{176.8 \cdot 10^3}{RT}\right) \ \left[\mathrm{m^2\,s^{-1}}\right].$$

After less than 2 h 1000 °C the reaction zone thickness appeared to be $3.9\,\mu\mathrm{m}$.

SiC / W

Studying the interaction of SiC with W in the temperature range 1600 – 1800 °C revealed the formation of W_5Si_3 and W_2C, i.e. a layered structure was formed consisting of SiC / W_5Si_3 / W_2C / W [36].

Interfacial reactions between a thin W film and single-crystal (001) β-SiC substrate during annealing at 600 to 1100 °C for 60 s were reported in [37]. It was found that the film began to react with SiC at 950 °C and had completely transformed to W_5Si_3 and W_2C at 1100 °C. These reaction products are known to be unstable phases on silicon carbide, therefore at longer annealing times WSi_2 or WC should be formed. The calculated isothermal section of the W-Si-C ternary phase diagram at 1100 °C [37] is presented in Fig. C.3 Appendix C.

SiC / Re

The interaction of thin Re films being in contact with a single-crystal (001) of β-SiC at temperatures from 700 to 1100 °C for durations of 30 min was reported in [38]. The authors found that Re grains did not grow notably under post-deposition annealing at 1100 °C but a strong columnar texture parallel to the substrate surface appeared upon annealing. Both experiments and a thermodynamic theory described in the article proved that Re did not react with SiC. This work is applicable at annealing temperatures up to 1100 °C and the results and conclusions can be applied strictly only to a single-crystal β-SiC substrate. For a polycrystalline SiC substrate the presence of grain boundaries affects the internal energy of SiC and might also alter the interdiffusion behaviour between SiC and Re. The isothermal section of the Re-Si-C phase diagram for 1100 °C calculated in [38] is shown in Fig. C.4 Appendix C.

As a short summary of the available experimental data, the reaction constants of interaction SiC-*Me* are presented in Fig. 2.1. The fastest diffusion process occurs in the diffusion couple SiC-Fe. The addition of 20 wt.% of Cr results in a significant diminution of the reaction rate. Cr and Ti do not react with SiC as intensively as pure Fe. All of the described metals, with the exception of Re, react with SiC at the assumed hipping temperature of 1000 °C. Therefore, it is necessary to prevent dissolution of the outer fibre coating (SiC doped carbon) in the interlayers and matrix to protect the SiC coating from decomposing. For this purpose, estimation of the diffusion rate of C in different metals is necessary.

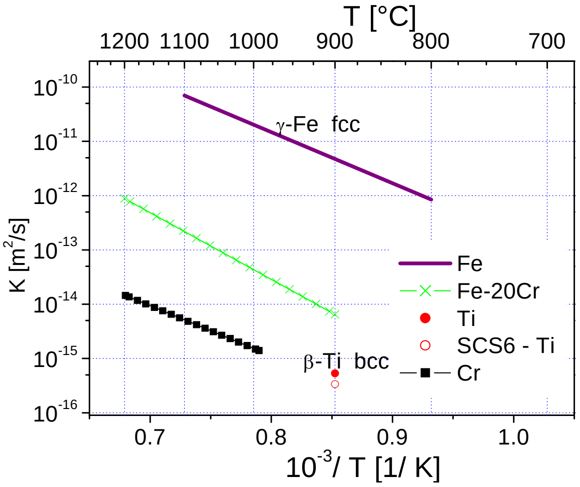

Figure 2.1: Reaction rate constants for SiC - *Me* interaction [30, 31, 33, 35]

2.2.2 C / Me

In many applications it is necessary to control the C diffusion in materials and a lot of studies have dealt with this task [26, 39–50]. Literature data on diffusion coefficients are often based on experimental results which have been obtained in the 1960's [51–53]. An Arrhenius plot that relies upon the known diffusion coefficients for C in different metals is presented in Fig. 2.2 [39, 51–54].

One can see in Fig. 2.2 that the highest diffusion coefficient of C appears to be in α-Fe. The plot then has a step at 914 °C corresponded to the phase transformation from α-Fe with more open *bcc* lattice with a packing density of 68% to γ-Fe with the *fcc* lattice, which has a higher packing density of 74%. The diffusion coefficient of C in Ti has the same step at 882 °C, but in the reverse direction, where Ti changes its structure from close-packed hexagonal (*cph*) lattice of α-Ti to *bcc* of β-Ti. This polymorphism can, however, be brought about at room temperature by alloying.

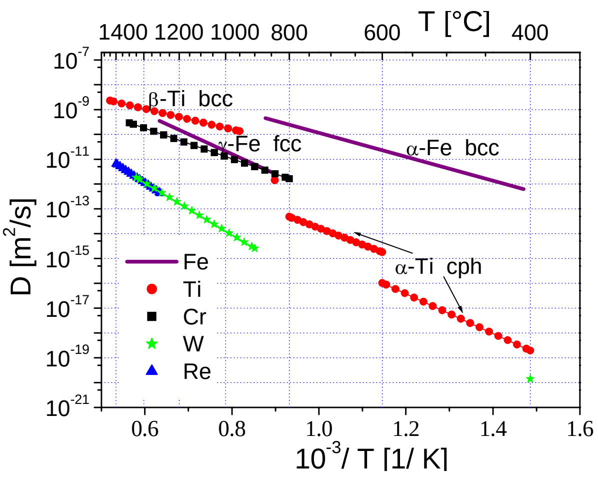

Figure 2.2: Arrhenius plot for C diffusion in different *Me* [39, 51–54]

The picture is not complete due to absence of data over the whole temperature range; it is therefore only possible to extrapolate the available data to predict the behavior of different metals. In comparison with Fe, all metals presented in Fig. 2.2 have a lower diffusion coefficient of C, especially W and Re. This is also confirmed by the wide use of these W and Re as diffusion barriers with respect to C in different applications.

C / Fe

The C - Fe phase diagram (see Fig. C.5 [55] in Appendix C) is non-equilibrium, since cementite Fe_3C is presented. The decomposition of the cementite into Fe and graphite is a very slow process, therefore virtually all C in steel will appear in the form of Fe_3C instead of graphite [56]. This compound is formed when the solubility limit of C in α-ferrite exceeds 0.102 at.% at temperatures as high as 727 °C. Mechanically, cementite is brittle which could dramatically degrade the adhesion between the matrix and fibres in *MMC*. The addition of *S*i to cast Fe greatly accelerates the cementite decomposition reaction to form graphite, that is why no Fe_3C is presented as a product of the reaction between SiC and Fe as described in subsection 2.2.1. The diffusion coefficient of C in α- and γ-Fe is described by the following expression in the temperature range 410 to 1300 °C [51]:

$$\text{for } \alpha\text{-Fe} \qquad D \text{ varies from } 6.25 \cdot 10^{-13} \text{ to } 4.54 \cdot 10^{-10} \ [\mathrm{m^2\,s^{-1}}]$$

$$\text{for } \gamma\text{-Fe} \qquad D = 4.5 \cdot 10^{-5} \exp\left(-\frac{154.1 \cdot 10^3}{RT}\right) \ [\mathrm{m^2\,s^{-1}}] \,.$$

Thus, the diffusion depth of C in Fe after annealing even at such low temperatures as 400 °C over 2 h is 130 μm, which is larger than the thickness of the suggested matrix layer of EUROFER (80 μm) on the SiC fibre. The diffusion of C in Fe is so fast since it diffuses by the interstitial diffusion mechanism (see subsection 2.1).

C / Ti

In contrast to Fe, Ti builds stable carbides and TiC already appears at 500 °C (see Fig. C.6 [57] in Appendix C). The model of Ti - C interaction for the case of a Ti layer on graphite substrate is described in [39]. During the initial interaction, C diffuses preferably along Ti grain boundaries. A C net is forming in the vicinity of the Ti - C interface within a Ti layer of about 10 nm in thickness. Then, as the C concentration increases at Ti grain boundaries, TiC crystallites grow into the intergranular spaces at the expense of the adjacent Ti grains. The transfer of C from the graphite substrate towards the Ti layer occurs preferably at the TiC crystallite - Ti grain boundaries and in Ti adjacent to the C - Ti interface, rather than through the TiC crystallites. After that, the TiC crystallites are able to grow in directions parallel to the C - Ti interface up to the formation of a continuous TiC interphase. Finally, C diffuses from the substrate through the TiC interphase towards the residual Ti film. At the same time, after formation of TiC the diffusion coefficient of C is significantly lower in the TiC than in the pure Ti. To prevent undesirable TiC crystallites forming at the interface zone, it was suggested to deposit a thin TiC layer [39].

The diffusion coefficient of C in α-Ti has been derived in [39] and [52] for the different temperatures:

$$\text{from 400 to 600}\,^\circ\text{C} \qquad D = 1.5 \cdot 10^{-7} \exp\left(-\tfrac{153\cdot 10^3}{RT}\right) \ [\mathrm{m^2\,s^{-1}}]$$

$$\text{from 600 to 800}\,^\circ\text{C} \qquad D = 7.9 \cdot 10^{-8} \exp\left(-\tfrac{127.7\cdot 10^3}{RT}\right) \ [\mathrm{m^2\,s^{-1}}]\,.$$

The diffusion depth of C in α-Ti after annealing at 400 °C over 2 h is 75 μm, which is almost 2 times lower than that in α-Fe.

C / Cr

The main features of the equilibrium Cr - C phase diagram (see Fig. C.7 [57] in Appendix C) are the occurrence of three intermediate phases in the solid state: $Cr_{23}C_6$, Cr_7C_3, and Cr_3C_2. These three phases have a narrow homogeneity range. Two of these carbides, namely $Cr_{23}C_6$ and Cr_7C_3, can also be formed by interaction with SiC, as has been shown above in subsection 2.2.1. The linear correlation of the experimental results of the C diffusion coefficient in Cr corresponds to the parabolic relation (2.2). The diffusion coefficient of C in Cr in the temperature range of 800 to 1500 °C is [52]:

$$D = 8.3 \cdot 10^{-7} \exp\left(-\frac{117.2 \cdot 10^3}{RT}\right) \ \left[\mathrm{m^2\,s^{-1}}\right].$$

After 2 h at 1000 °C the diffusion depth appears to be about 600 μm.

C / W

W forms carbides at temperatures above 700 °C. At the beginning, only subcarbide α-W_2C is formed but at temperatures above 1000 °C it transforms into WC [42]. The formation of these two phases was detected after heating to 800 °C where subcarbides comprised only a minor part ($\sim$ 10%) of the entire carbide layer [43]. A $4 - 5\,\mu$m thick WC layer was found to be formed after 2 h of annealing at 800 °C. A rough estimation of the diffusion coefficient of C gives a value of $10^{-15}\,\mathrm{m^2\,s^{-1}}$ which is four orders of magnitude higher than that reported in [26]. This difference can be explained by the presence of defects in the W layer produced during deposition in [43]. The W - C binary phase diagram is shown in Fig C.8 [45], Appendix C. For high temperatures, from $900 - 1450\,^\circ$C, the diffusion coefficient of C in W is described by the relation [54]:

$$D = 2.2 \cdot 10^{-6} \exp\left(-\frac{200.8 \cdot 10^3}{RT}\right) \;\left[\mathrm{m}^2\,\mathrm{s}^{-1}\right].$$

The diffusion depth of C in W after 2 h of annealing at 1000 °C is about 20 μm that is 30 times lower than that in Cr at the same temperature. Diffusion decreases with the formation of WC compared to pure W because of the higher activation energy of diffusion in carbide. Thus, diffusion coefficient of C in W at 1530 °C is $2.8 \cdot 10^{-12}\,\mathrm{m}^2\,\mathrm{s}^{-1}$ [52], while in W_2C at the same temperature it is $8.1 \cdot 10^{-14}\,\mathrm{m}^2\,\mathrm{s}^{-1}$ [48]. The slow diffusion of C in W and its carbides is caused by the fact that it proceeds via a vacancy mechanism rather than via the grain boundaries.

C / Re

In the presence of C, many metals form carbides when heated to elevated temperatures, while Re does not. However, the solubility of C in solid Re increases with temperature resulting in a good bonding between graphite and Re. Solubility $x_{\mathrm{C,max}}$ is defined as the atom ratio of C to Re and is described by the formula in a temperature range of 820 – 1250 °C [46]:

$$\log x_{\mathrm{C,max}} = 1.68 - \frac{5270}{T},$$

where T is the temperature in K. Thus, at 820 °C about 0.1 at.% of C is dissolved in Re.

In the experiments [47] with a Re layer as a diffusion barrier between C and *Me*, C was found to diffuse through the Re coating and to cause embrittlement of the *Me*. The reaction rate of carbide formation decreased exponentially with increasing barrier thickness. In addition, the carbide layer increased in thickness with decreasing grain size of the Re layer because columnar grain boundaries in the latter acted as fast diffusion paths for carbides providing the layer growth. The C - Re binary phase diagram is shown in Fig. C.9 [58], Appendix C.

C / Re/W multilayer

A Re / W multilayer with a total thickness of 25 μm was investigated as a diffusion barrier for C in [59, 60] and the multilayer was found to suppress WC formation in the W coating on carbon-fibre reinforced carbon (*CFC*) at temperatures above 1300 °C over a time of 20 s. In these experiments the specimens were heated with a uniform electron beam. The multilayer consisted of two W and three Re layers and the system looked as follow: *CFC* / Re / W / Re / W / Re / coating. After heat treatment the first W interlayer (nearest to *CFC*) was found to contain 40 at.% of C, i.e. C had diffused through the first Re layer. This diffusion led to the formation of WC and therefore C diffusion diminution due to an increase of the activation energy of diffusion. WC is itself brittle, but in the case of a 4 μm thick layer the strength and ductility of the layer were high [59]. Finally, a new multilayer structure of Re and WC had appeared to behave as a diffusion barrier at temperatures below 1600 °C. At these temperatures the terminal solid solubility of W in Re was 11 at.% and Re in W was

27.5 at.% [45]. Therefore, the layers of Re and W started to mix and lose their original multilayer structure [60]. With a longer duration time, the intermixing of Re and W layers took place at lower temperatures.

2.2.3 Fe / Me

Pure Fe / Me

If the diffusion coefficients of C and Fe in a *Me* are close to each other then diffusion in both directions occurs at the same time. Thus, both diffusion paths have to be taken into consideration during calculations of barrier thickness. The diffusion coefficients of Fe, the main constituent of EUROFER, in different *Me* and *Me* in pure Fe are listed in Table 2.1. This comparison is useful for the analysis of the consequence of possible reactions which could happen. Fe has a low diffusivity in Cr, Ta, and W; medium in Cu, Au, and Ag; and high in Ti [52, 53]. The diffusion coefficients of Cr and W in Fe are significantly higher than for Fe in Cr and W. Therefore, interdiffusion proceeds mainly in the direction of EUROFER instead of metallic interlayer.

		Temperature [°C]	Diffusion coefficient [$m^2\,s^{-1}$]
Fe ⟶	β-Ti	900	$3.05 \cdot 10^{-8}$
	Cr	980	$6.93 \cdot 10^{-19}$
	W	980	$4.31 \cdot 10^{-18}$
Cr ⟶	α-Fe	900	$1.58 \cdot 10^{-15}$
W ⟶	α-Fe	900	$1.02 \cdot 10^{-14}$

Table 2.1: Diffusion coefficient of Fe in Cr, Ti, and W and diffusion coefficients of Cr and W in Fe

It is of special concern for Ti because it forms the compounds of TiFe and $TiFe_2$ already at 400 °C (see Fig. C.10 [57] in Appendix C). The addition of Fe to α-Ti influences the temperature of the crystalline transformation from α-Ti to β-Ti. This transformation takes place at 882 °C in the absence of Fe, while the Fe concentration of 15 at.% decreases the temperature to 595 °C (see Fig. C.10 [57] in Appendix C).

The phase diagram of Cr - Fe is given in Fig. C.11 [57] in Appendix C. The alloys containing $\geq$ 13 wt.% Cr have a bcc structure all the way to the melting point. They do not enter the fcc phase field and cannot be quenched to form martensite.

Fe and W form two stable intermediate phases, Fe_7W_6 (μ) (42.1 at.% of W) and FeW (δ) (50 at.% of W), as well as a metastable transition phase, Fe_2W (λ) (33.3 at.% of W) [48] (see the Fe - W binary phase diagram in Fig. C.12 [48], Appendix C). The phase of Fe_7W_6 exists only at temperatures above 1200 °C, which is higher than the assumed hipping temperature, while the other two phases, FeW and Fe_2W, can already be formed at 400 °C. When α-Fe is cooled down from the high temperature single-phase region the system moves towards equilibrium by precipitating the second phase containing a large amount of solute. The maximum solubility of W in α-Fe at 700 °C is 1.72 at.%. The diffusion coefficient of W in α-Fe at 750 °C is about $1.9 \cdot 10^{-16}\,m^2\,s^{-1}$.

Fe and Re also form stable compounds like Fe and W. But in contrast to W, data on Re is limited. In Fig. C.13 [49], Appendix C the Fe - Re binary phase diagram is presented. Three compounds, $Fe_{20}Re_9$, Fe_3Re_2, and Fe_2Re_3, exist at temperatures as low as 500 °C, and differ in Re and Fe concentrations.

Fe-12Cr / Cr

If diffusion in an alloy is studied, the effect of self-diffusion must be taken into consideration. For example, the diffusion coefficient of Cr in the binary alloy of Fe and Cr (12 wt.%) for a temperature range of 900 to 1400 °C is [52]:

$$D = 1.29 \cdot 10^{-4} \exp\left(-\frac{230.5 \cdot 10^3}{RT}\right), \quad \left[\mathrm{m^2\,s^{-1}}\right].$$

The diffusion coefficient of Cr in alloy at 980 °C, about $3.2 \cdot 10^{-14}\,\mathrm{m^2\,s^{-1}}$, is significantly higher than the diffusivity of Cr in pure Fe, $2.2 \cdot 10^{-17}\,\mathrm{m^2\,s^{-1}}$, and Fe in Cr, $6.9 \cdot 10^{-19}\,\mathrm{m^2\,s^{-1}}$, at the same temperature. This fact is of great importance regarding EUROFER 97 because the steel contains 9 wt.% of Cr. Therefore, the interdiffusion between EUROFER and Cr layers proceeds faster in the direction of the steel than in Cr interlayer and self-diffusion of Cr can influence significantly on the rate of the process.

2.2.4 C / interlayer / steel

Experiments on diffusion reactions between Ti and stainless steel [61] indicated the formation of Fe, Cr and Ni formed intermetallic compounds. The Transmission Electron Microscopy (*TEM*) / *SEM* investigation performed in interdiffusion studies of stainless steel (AISI 316) and commercially pure Ti showed the formation of TiFe, $TiFe_2$ and σ-Fe-Cr, where the σ-phase had the average composition as follow: Fe ($59.8 - 61.8$ at.%), Cr ($29.2 - 31.8$ at.%), Ni ($4.7 - 5.8$ at.%) and Ti (balance). The phases appeared during annealing at 950 °C and were found to be: stainless steel / Fe_2Ti(Cr, Ni) / Fe_2Ti(Cr, Ni) + Cr_2Ti(Fe) / FeTi(Cr, Ni) / σ-Ti(Fe, Cr, Ni) / Ti.

The investigation of a steel substrate and C layer couple with Ti and Cr interlayers [41] showed that the Cr interlayer was insufficient to stop the Fe diffusion into the C.

TiN layers were tested as a diffusion barrier in [44]. The system C / TiN / steel was found to withstand temperatures up to 950 °C. With further temperature increased, TiN reacted to form titanium carbonitride and delamination occurred.

W as a diffusion barrier for C - steel system was investigated in [43]. A good bonding of the C layer to the buffer layer, as well as of W to the steel substrate, was observed.

Interactions between Fe, W, and C in W-containing steels (up to 2.5 wt.% of W and 0.85 wt.% of C) were studied at 700 °C over times up to 500 h [50]. Depending on the tempering time, three different carbides were observed, namely Fe_3C, M_6C (Fe_4W_2C - Fe_2W_4C), and (Fe, W)$_{23}C_6$. After short tempering times, cementite and M_6C carbide precipitates appeared. The rate of cementite dissolution and the amount of W-based carbides such as $M_{23}C_6$

(4 – 7 at.% of W) and M_6C (41 – 48 at.% of W) increased with increasing concentration of W. After annealing for longer times, only the formation of $M_{23}C_6$ precipitates were observed. Thus, it was concluded that the sequence of carbide precipitation in W steels was $Fe_3C \longrightarrow M_6C \longrightarrow M_{23}C_6$. Diffusion controlled transformations were characterised by a large difference in mobility of C and substitutional elements, which could be explained by the difference in the diffusion mechanisms: interstitial diffusion for C, while for W it was vacancy diffusion (see more details in subsection 2.1).

3 Materials and Experimental Procedures

3.1 Materials

As was mentioned in subsection 1.2, the composite material being investigated in this work is the system of EUROFER 97 as a matrix and SiC fibres as reinforcement. To prevent the degradation of mechanical properties of the composite, a diffusion barrier has to be formed between the matrix and the fibre.

3.1.1 Fibre

In this work, SCS6 Speciality Materials fibres have been used. Their structure is shown in Fig. 3.1.

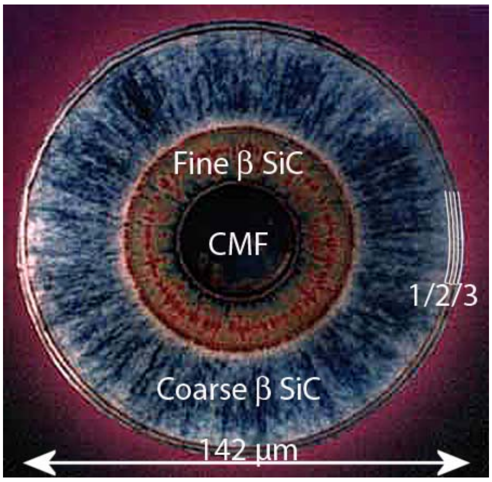

Figure 3.1: SCS6 fibre: *CMF*, 1 - amorphous carbon ($0.5\,\mu$m), 2 - SiC doped C ($1\,\mu$m), 3 - SiC doped C ($1.5\,\mu$m)

This type of fibre with a diameter of $142\,\mu$m is produced by a Chemical Vapour Deposition (*CVD*) process. The fibre core consists of a $33\,\mu$m diameter carbon monofilament (*CMF*) originally spun from a pitch-based material, which is then sealed by a $1.5\,\mu$m thick overcoat of pyrolytic C [62, 63]. There are two β-SiC zones grown with the columnar structure; they consist of subgrains of β-SiC with close-packed $\{111\}$ planes. The first zone is slightly C rich with a fine grain size of about $10 - 60\,$nm and extension to about $15\,\mu$m. The second one has coarse grains with dimensions of $70 - 140\,$nm, extension about $35\,\mu$m and stoichiometric composition. C and SiC are in chemical equilibrium; therefore, no reaction occurs between them. The fibre has as an outer coating consisted of three layers with a total thickness of about $3\,\mu$m. This coating is used for reducing the surface sensitivity to damage during handling. Additionally, C heals the defects at the SiC surface and enhances the strength of the fibre.

SCS6 has the following thermo-mechanical properties given in Table 3.1 [64].

σ [MPa]	3450
E [GPa]	380
ν	0.17
ρ [g cm^{-3}]	3.0
α [10^{-6} K^{-1}]	4.1

Table 3.1: Thermo-mechanical properties of SCS6 fibre

Here σ is the ultimate tensile strength, E - Young's modulus, ν - Poisson's ratio, ρ - density, α - coefficient of thermal expansion.

3.1.2 Planar substrates

Planar substrates have been utilized in the work because some of the analyses, namely *OES*, *XRD*, and *IBA*, are only applicable to flat surfaces. Three types of material have been chosen: pyrolytic graphite (HPG), silicon carbide (SiC) and glass.

Pyrolytic graphite produced by Union Carbide (UC, USA) has a polycrystalline structure with a mosaic spread of ±11 ° cut parallel to the main graphitic basal plane [65]. It reveals nearly no porosity and its density of 2.20 g cm^{-3} is very close to that of an ideal graphite. The size of its crystallites can reach several microns. Thermo-mechanical properties of this pyrolytic graphite at room temperature are shown in Table 3.2 [66, 67]. Here "a" and "c" mean the direction parallel and perpendicular to the graphite basal planes. In the basal planes, the a dimension has been found to contract slightly up to 400 °C and then expand at higher temperatures [67]:

$$\begin{aligned} 0\,^\circ\mathrm{C} \leq T \leq 150\,^\circ\mathrm{C} \qquad & \alpha_\mathrm{a} = -1.5 \cdot 10^{-6}\,\mathrm{K}^{-1} \\ T = 400\,^\circ\mathrm{C} \qquad & \alpha_\mathrm{a} = 0 \\ 600\,^\circ\mathrm{C} \leq T \leq 800\,^\circ\mathrm{C} \qquad & \alpha_\mathrm{a} = +0.9 \cdot 10^{-6}\,\mathrm{K}^{-1}. \end{aligned}$$

This material appears to be rather suitable for diffusion investigations using *IBA*, *SEM*, and *XRD* techniques, since SiC fibres, which are planned to be used as reinforcement in EUROFER 97 matrix composite, have a SiC doped pyrolytic graphite as the outer layer. However, this material is not suitable for the layer thickness measurements because of its relatively high surface roughness (R_a = 60 nm after polishing (see subsection 3.2.2)), which is comparable with the depositing layer thickness.

SiC planar substrate produced by Wacker Ceramics has no orientation in a wafer. This is a hexagonal SiC with a density of 3.16 g cm^{-3} and polycrystalline structure with a mean grain size less than 5 μm [68]. SiC substrate was included in the investigation for the same reason as pyrolytic graphite. In spite of its low roughness $R_\mathrm{a} = 1 - 5$ nm is considerably less than that of pyrolytic graphite, pores can hinder the estimation of the layer thickness (porosity of 0.6 − 0.8%). As it has been shown in subsection 2.2.1, a SiC - *Me* couple reveals no interdiffusion at temperatures below 900 °C. Therefore, the SiC substrate does not influence on the interaction between *Me* - EUROFER in the system SiC - *Me* - EUROFER caused by annealing at temperatures below 900 °C. The diffusion code DIFFUSEDC used in this work for calculation of the concentration dependent diffusion coefficient $D(C)$ treats diffusion only in a binary system. The SiC substrate, therefore, appears to be a convenient choice for this investigation of interdiffusion between the EUROFER and *Me* layer since diffusion between only two components *Me* and EUROFER can be considered. The thermo-mechanical properties of SiC at room temperature are shown in Table 3.2 [68].

Amorphous glass substrate produced by Carl Roth is a soda-lime glass ISO Norm 8037/1 (typical composition in wt.%: 70 SiO_2, 10 CaO, 15 Na_2O [69]). It has been used for the thickness measurements, which were carried out with the help of a profilometer, as well as for two other types of analysis, *OES* and *XRD*. The material is suitable for *OES* analysis due to its large deposited area: analysis appears to be more precise owing to the fact that more material in the deposited layer is investigated. As to the second, i.e. *XRD*, the analysis is possible to perform because of the amorphous structure of the glass and hence no peaks from the substrate should be observed in *XRD* spectra. The softening point of soda-lime glass is 700 °C and so this substrate has not been used for annealing experiments. The thermo-mechanical properties of soda-lime glass at room temperature are shown in Table 3.2 [69].

Material	Pyrolytic graphite	SiC	Soda-lime glass
E [G Pa]	28	420	60 – 70
ν	"a" direction −0.1 to −0.2 "c" direction 0.9 to 0.95	0.17	0.23
ρ [g cm^{-3}]	2.20	3.16	2.4
α [10^{-6} K^{-1}]	"a" direction −1.5 "c" direction 28.6	4.0	8.9

Table 3.2: Thermo-mechanical properties of SiC and soda-lime glass at room temperature

In this table E is Young's modulus, ν - Poisson's ratio, ρ - density, α - coefficient of thermal expansion.

3.1.3 Interlayers

Two types of material have been used in the form of an interlayer: metals and ceramics. The bulk material properties of Ti, Cr, W, and Re as a metal interlayer material are presented in Table 3.3 [23, 48, 70]. The bulk material properties of TiC, TiN, ZrO_2, and Er_2O_3 as a ceramic interlayer material are presented in Table 3.4 [23, 71–75].

Material	Ti	Cr	W	Re
σ [MPa]	300 – 400	216 – 448	411 – 1776	1135 – 2223
E [G Pa]	120	279	390 – 410	466
ν	0.36	0.21	0.28 – 0.30	0.26
ρ [g cm^{-3}]	4.5	7.1	19.3	21.0
α [10^{-6} K^{-1}]	8.9	6.5	4.5	6.6

Table 3.3: Thermo-mechanical properties of selected metals

Material	TiC	TiN	ZrO_2	Er_2O_3
E [GPa]	$370 - 380$	$460 - 600$	$160 - 241$	186.3
ν	0.19	0.25	0.3	
ρ [g cm^{-3}]	4.92	5.24	5.7	8.65
α [10^{-6} K^{-1}]	6.5	8.9	10	

Table 3.4: Thermo-mechanical properties of selected ceramics

In these tables, σ is the ultimate tensile strength, E - Young's modulus, ν - Poisson's ratio, ρ - density, α - coefficient of thermal expansion.

3.1.4 Matrix

The *RAFM* steel EUROFER 97 is manufactured by Böhler Edelstahl GmbH in Austria. To distinguish the properties of this steel, a number of experiments have been carried out in different laboratories. The composition, microstructure, and some other properties of EUROFER 97 are given in subsection 1.1.1. The thermo-mechanical properties of the steel at room temperature are presented in Table 3.5 [14, 21, 76].

σ [MPa]	690
E [GPa]	206
ν	0.3
ρ [g cm^{-3}]	7.8
α [10^{-6} K^{-1}]	10

Table 3.5: Thermo-mechanical properties of EUROFER 97 at room temperature

Here σ is the ultimate tensile strength, E - Young's modulus, ν - Poisson's ratio, ρ - density, α - coefficient of thermal expansion.

3.1.5 Denotation of samples

The layers have been deposited using a magnetron sputtering device, as well as a plasma arc filtered device and plasma arc device. A schematic view of the samples with different interlayers is shown in Fig. 3.2.

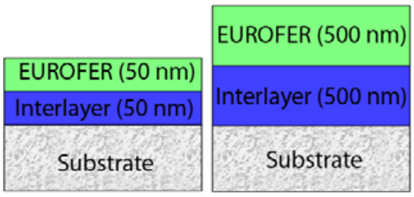

Figure 3.2: Schematic view of the thin (50 nm / 50 nm) and thick (500 nm / 500 nm) samples

In the following tables, only the names of the samples described below in section 4 are shown. The description of the samples with *Me* interlayers deposited by magnetron sputtering is given in Table 3.6. In Table 3.7 the denotation of the samples with a ceramic interlayer is presented. Before deposition and following investigation of the annealed samples with ceramic and EUROFER layers, the samples with only ceramic layers have been investigated to find appropriate deposition parameters. Some of these samples are listed in Table 3.8. Finally, the samples with plasma arc deposited layers and coated fibres are presented in Tables 3.9 and 3.10, correspondingly.

Sample name	Substrate	Layer 1 (interlayer)	Layer 2
Thin layers			
SiCE41	SiC	EUROFER (50 nm)	-
CWE41	C		
SiCE_Ti2	SiC	Ti (45 nm)	EUROFER (50 nm)
CWE_Ti2	C		
SiCE_Cr1	SiC	Cr (50 nm)	
CWE_Cr1	C		
SiCE_W1	SiC	W (50 nm)	
CWE_W1	C		
SiCE_Re1	SiC	Re (50 nm)	
CWE_Re1	C		
Thick layers			
SiCE43	SiC	EUROFER (400 nm)	-
CWE43	C		
SiCE_Ti3	SiC	Ti (500 nm)	EUROFER (500 nm)
CWE_Ti3	C		
SiCE_Cr4	SiC	Cr (500 nm)	
CWE_Cr4	C		
SiCE_W2	SiC	W (500 nm)	
CWE_W2	C		
SiCE_Re2	SiC	Re (500 nm)	
CWE_Re2	C		
CWE_Re_W1	C	W / Re / W (500 nm)	
CWE_Re_W2	C	Re / W / Re / W (500 nm)	EUROFER (500 nm)

Table 3.6: List of investigated planar samples with metal layers deposited by magnetron sputtering technique

Sample name	Substrate	Layer 1 (interlayer)	Layer 2
SiCE_TiC1	SiC	TiC (50 nm)	EUROFER (50 nm)
CWE_TiC1	C		
SiCE_TiN2	SiC	TiN (50 nm)	
CWE_TiN2	C		
CWE_Erbia1	C	Er_2O_3 (500 nm)	EUROFER (500 nm)

Table 3.7: List of investigated planar samples with ceramic layers deposited by magnetron sputtering and plasma arc filter techniques

Sample name	Substrate	Target / Deposition technique
TiC layer (45 - 125 nm)		
SiCTiC4, SiCTiC6	SiC	Ti and C / magnetron
CWTiC1, CWTiC4, CWTiC6	C	
glassTiC4, glassTiC6	glass	
SiCTiC10	SiC	TiC / magnetron
CWTiC10	C	
glassTiC10	glass	
CWTiC15	C	Ti and C / magnetron
TiN layer (60 - 350 nm)		
SiCTiN1, SiCTiN6 SiCTiN7, SiCTiN8	SiC	Ti / magnetron
CWTiN1, CWTiN6 CWTiN7, CWTiN8	C	
glassTiN1, glassTiN6	glass	
ZrO$_2$ layer (30 - 60 nm)		
SiCZrO$_2$5, SiCZrO$_2$6	SiC	Zr / magnetron
CWZrO$_2$5, CWZrO$_2$6	C	
Er$_2$O$_3$ layer (160 - 500 nm)		
CWEr$_2$O$_3$2, CWEr$_2$O$_3$3	C	Er / magnetron
CWErbia1	C	Er / filtered arc

Table 3.8: List of deposited planar samples with ceramic layers

Sample name	Magnetron deposition	Arc deposition
CWE33A3	EUROFER (108 nm)	EUROFER ($\sim 10\,\mu$m)
CSE33A3		
CW_W1A5	W (50 nm)	EUROFER ($\sim 30\,\mu$m)
CS_TiN9A5	TiN (50 nm)	

Table 3.9: List of planar samples with layers deposited by both PVD techniques

Sample name	Magnetron deposition	Arc deposition
SCS6E3A6	EUROFER ($\sim$ 180 nm)	EUROFER ($\sim 6\,\mu$m)
SCS6E_W3	W ($\sim$ 500 nm) / EUROFER ($\sim$ 500 nm)	-

Table 3.10: Coatings deposited on the SiC fibres

In these tables, SiC, graphite (C) and glass substrates denoted by the abbreviations "SiC", "CW", and "glass", have been coated simultaneously. For instance, according to Table 3.6, samples SiCE_Ti2 and CWE_Ti2 have the same EUROFER and Ti coatings, i.e. produced during the same deposition run. In Table 3.8, the sample names SiCTiC4, CWTiC4, and glassTiC4 denote SiC, graphite (CW), and glass substrates coated with a TiC layer during the 4th run. The names of the samples in Table 3.9, for example, CWE33A3 and SiCE33A3 denote graphite CW and SiC substrates coated by magnetron sputtering with EUROFER coating during the 33rd run and then during the 3rd run of the arc deposition.

3.2 Experimental procedures

3.2.1 PVD techniques and layer deposition procedures

Using Physical Vapour Deposition (*PVD*) techniques with plasma assistance (for example, sputter deposition or ion plating), thin films of pure metals, compounds such as carbides, nitrides or oxides and even alloys can be formed on substrates [77].

Magnetron sputtering technique

Sputter deposition utilizes the physical sputtering effects caused by ion bombardment of a target material. The sputtering yield changes according to the energy of the impinging ion and has a maximum at $1-10$ keV. The ion energy is determined by the electric field strength in the region close to the target.

If a magnetic field is applied perpendicular to the electric field, electrons are trapped near the surface of the electrode and trace cycloidal orbits. Such devices using crossed electric and magnetic fields are called magnetrons [77]. There are several types of magnetrons for practical application: cylindrical, circular or planar magnetrons. The magnetron can operate in either Direct Current (*DC*) or Radio Frequency (*RF*) mode.

Permanent magnets are arranged to form a toroidal-type tunnel of the magnetic field. The electron motion in the case of a planar magnetron electrode is shown in Fig. 3.3 [24, 77]. Electrons are trapped in this tunnel and continue their motion in a cycloidal trajectory. The plasma density increases in this magnetically confined region. The high current densities obtained make it possible to increase the sputter rate and thus the deposition rate of films. The sputtered area of a target defines the effectiveness of its usage because the material is sputtered preferentially from this zone.

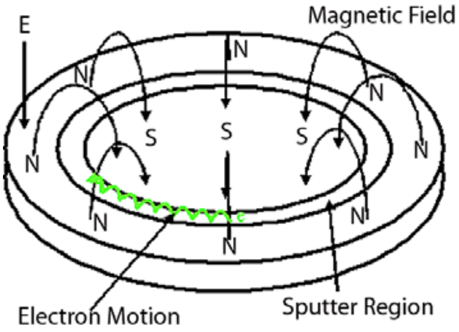

Figure 3.3: Electric and magnetic fields and a trace of electron motion in a planar magnetron electrode

In this work, a commercial magnetron sputter device “Discovery 18DC/RF Research Magnetron Sputter Deposition System” has been used. It has three planar magnetron electrodes operated in *DC* or *RF* mode, where *DC* or *RF* power up to 700 W or 600 W, correspondingly, can be applied. Three gases, namely Ar, N_2 and O_2, can be used both separately and mixed (reactive sputtering) with a maximum gas flow of up to 50 sccm. Gas flow is given in

[sccm] units (standard cubic centimeters per minute). The *RF* electric field can be applied to bias the substrate in order to vary the flux and energy of depositing charged species. The maximum bias power is 600 W, whereas in the regime named "voltage control" the maximum voltage is 1000 V. Samples can be heated before or during deposition at temperatures in the range from 0 to 600 °C.

A schematic view of the magnetron device with only one electrode for simplicity is presented in Fig. 3.4.

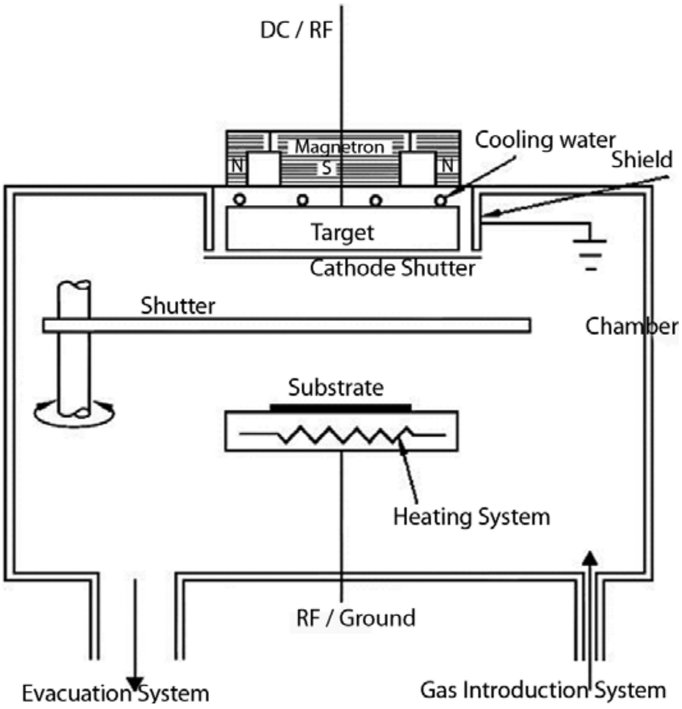

Figure 3.4: Schematic view of the magnetron

The target is cooled with water to prevent overheating. It is surrounded by the shield to avoid any discharge at undesirable regions of the electrode surface and to localise sputtering to the target surface only. The shutters are aimed for protection of the target and samples: the target shutter is used during sputtering of another target while the substrate shutters are used during heating and for protection of the samples from dust during target discharge cleaning. A homogeneous distribution of a deposited layer can be achieved by rotating the substrate.

During sputter deposition, the energy of sputtered atoms impinging on the substrate is large. Inter-mixing and mutual diffusion between incoming atoms and the substrate material tends to occur easily. Therefore, adhesion of the film to the substrate obtained by sputter deposition is stronger than that by, for example, evaporation or plasma assisted *CVD*. By variation of the working gas (Ar) pressure the stress in the film changes from compressive to tensile. A compressive stress is observed at low Ar pressures and changes to a tensile stress as the pressure increases [77]. Investigations on how to affect the stress in a deposited layer is important for the formation of an appropriate interface in a future composite.

The density of both metal and dielectric films increases with thickness and reaches a plateau value which asymptotically approaches that of the bulk material [24]. The gradient in film density is thought to be due to several reasons: higher crystalline disorder, formation of oxides, greater trapping of vacancies and holes, and pores produced by gas incorporation.

The technique of bias application can be utilised in the present sputter device at a maximum voltage of 1000 V. Bias affects a broad range of properties in deposited films [24]:

- improves film adhesion during the initial stage of film formation
- increases film density
- significantly reduces the resistance of metal films
- changes film hardness and residual stress (either increasing or decreasing it)
- modifies the film morphology (for example, columnar microstructure of Cr is replaced by a compact fine grain structure).

In addition, the energetic particle bombardment prior to and during film formation and growth promotes numerous changes and processes at a microscopic level. These changes include removal of contaminations, alteration of surface chemistry, enhancement of nucleation and re-nucleation at elevated film temperatures which are followed by an acceleration of atomic reaction and interdiffusion rates.

Deposition of Me layers by magnetron sputtering

EUROFER 97 consists of several chemical elements (see Table 1.1 in subsection 1.1.1) and, therefore, a appropriate deposition technique should be chosen to keep the stoichiometry of a deposited layer close to that of the steel. Neither *CVD*, nor evaporation techniques are suitable for this purpose: the former method makes deposition of a multi-component material very complicated or even impossible, while the latter one does not ensure the right stoichiometry due to the difference in vapour pressures of the elements of EUROFER 97. In contrast, *PVD* techniques such as arc and magnetron depositions are both able to provide the required composition of a deposited coating. Another requirement is that the steel coating should have a good adhesion to the fibres to provide the required mechanical properties of the composite. In addition, the coating must be thick enough to serve as a matrix material if the composite is to be produced by hipping of bundles of coated fibres. For this reason a two-step deposition process is chosen: (i) magnetron sputtering deposition of a thin initial steel layer which forms a well defined interface to the surface of the SiC fibre followed by (ii) arc deposition over the sputtered layer to form a thick coarse layer, since the arc deposition rate is one order of magnitude higher than that of magnetron sputtering. To date, several deposition experiments of stainless steels have been performed by use of magnetron [78–80] and arc [81] facilities but sputtering a ferromagnetic target requires additional effort to be applied to create an appropriate magnetic field near the target since otherwise the deposition rate is unacceptable low.

The base pressure in the deposition chamber was better than $3.0 \cdot 10^{-5}$ Pa for all depositions. Homogeneous distribution of a deposited layer was obtained by rotation of the substrates and a confocal arrangement of the target. In the experiments, metallic discs (EUROFER 97, Ti, Cr, W, and Re) 75 mm in diameter were used as the target. During all depositions, the substrate holder was placed at a distance of 12 cm from the target and was not intentionally heated. For all targets, a standard magnetron cathode unit was utilized in *DC* mode except for the EUROFER target that required the *RF* mode to be used. Thicknesses of the targets also varied: the discharge on the EUROFER target was found to be stable at thicknesses as high as 1 mm, while for others, depositions were possible at thicknesses up to a recommended value of 6 mm.

To optimise the sputtering process of the EUROFER target, a specially designed cathode "Angstrom Science ONYX-3^{TM}" which produced a stronger magnetic field that penetrated through the target was installed. With utilization of the stronger magnets, the deposition of EUROFER in *DC* mode also became possible. A stable discharge in *DC* mode was able to be obtained with a target thickness less than 1.8 mm. This feature of the EUROFER deposition arose from the ferromagnetic properties of the material itself. With the standard magnetron cathode unit, only a cathode sputtering regime of the EUROFER target took place. By increasing the magnetic field in the target region with the enhanced magnetron cathode unit, the regime of sputtering changed to the magnetron sputtering regime resulting in a much higher deposition rate owing to the effective electron confinement.

All deposition parameters for all targets are presented in Table 3.11. To produce a 500 nm thick EUROFER coating, higher power density (and therefore higher deposition rate) was applied compared to that used for the thin EUROFER coating.

Deposition run	EUROFER		Ti	Cr	W	Re
	Standard	Enhanced				
q [W cm^{-2}]	*RF* 11.3	*DC* 1.1, 2.3	*DC* 6.8	*DC* 4.5	*DC* 2.3	*DC* 4.5
Q_{Ar} [sccm]	50	20	25	20	20	20
P [Pa]	0.75	0.45	0.54	0.45	0.37	0.37
r [nm min^{-1}]	0.5	4.7, 10	15.6	17.5	6.5	15.7
d [nm]	max180	50, 500	40, 500	50, 500	50, 500	50, 500

Table 3.11: Parameters of the magnetron deposition of Me layers

In this table q is applied power density, Q - gas flow, P - pressure in the chamber during deposition, r - deposition rate and d - layer thickness. Three cathodes installed in the magnetron device were used one after another for deposition of the multilayer samples (CWE_Re_W1 and CWE_Re_W2): cathode 1 - W, cathode 2 - Re, and cathode 3 - EUROFER 97. This allowed avoiding the ingress of contaminants to the interface region since all layers were deposited without breaking the vacuum.

Deposition of TiC by dual magnetron sputtering

With the Magnetron Sputter System, film production with material mixtures and graded compositions is possible by simultaneous and independent power application to two targets of different compositions, in other words dual magnetrons. The device does not allow the identical power regime (*DC* or *RF*) application simultaneously to both the targets, i.e. one target has to work in *DC* mode while the second is in *RF* mode. In spite of this fact, layers with different concentrations of doped materials can be formed, for example, TiC film from dual magnetron sputtering of pure C and Ti targets.

Both the dual magnetron sputtering and standard one were utilized for TiC deposition: Ti and C targets were used simultaneously for the dual magnetron deposition, while for the standard deposition TiC was sputtered. To form a compound and produce a dense coating, a bias was applied to the substrate in both cases. As it was mentioned in subsection 3.1.5, samples with the "TiCn" notation, where n is a number of the run, were coated at the same time. Therefore, in Table 3.12 parameters for the different deposition processes with two targets of Ti and C are given with the names of "TiCn". All samples coated with TiC had the following common parameters: deposition time 30 min, Ar gas flow 20 sccm.

Deposition run	TiC4	TiC6	TiC10	TiC15
q_{Ti} $[\mathrm{W\,cm^{-2}}]$	1.4	1.4	–	1.4
q_{C} $[\mathrm{W\,cm^{-2}}]$	6.3	4.5	–	4.5
q_{TiC} $[\mathrm{W\,cm^{-2}}]$	–	–	2.3	–
V_{Bias} $[\mathrm{V}]$	119 – 129	124 – 134	69 – 81	$*$
P $[\mathrm{Pa}]$	0.45	0.49	0.47	0.41
r $[\mathrm{nm\,min^{-1}}]$	4.2	3.7	1.5	3.3
d $[\mathrm{nm}]$	125	110	45	100

Table 3.12: Parameters of the magnetron deposition of TiC layers. * Bias voltage was switched every 5 min from 54 to 176 V

In this table q_{Ti} is applied power density to Ti target, q_{C} - applied power density to C target, q_{TiC} - applied power density to TiC target, V_{Bias} - the substrate bias voltage, P - pressure in the chamber during deposition, r - deposition rate and d - the layer thickness. During deposition of TiC15 V_{Bias} switched between 54 and 176 V every 5 min. The made possible an improvement of the coating bonding to the substrate and the formation of a dense layer with lower stress than would have been created by only applying a high bias voltage of 176 V.

Before the application of a TiC layer as a barrier, all the samples with this coating had been examined regarding their crystalline and surface structures and stoichiometry. The deposition parameters of the coating with appropriate properties were later used for the deposition of the interlayer as a diffusion barrier. The deposition of the TiC layer was done directly before the EUROFER deposition (samples SiCE_TiC1 and CWE_TiC1) without breaking the vacuum to avoid the ingress of contaminants at the interfaces.

Deposition of compounds by reactive sputtering

Reactive sputtering is used for the fabrication of thin compound coatings on different types of substrates. The deposition rate is known to be extremely sensitive to the supply of the reactive gas [82]. Without the introduction of a reactive gas, films deposited by the sputtering process appear to be metallic. Upon introduction of a reactive gas species, the gas atoms combine with the atoms sputtered from the target to form a compound thin film [83]. A too low supply of the reactive gas causes high deposition rate metallic sputtering but can result in an understoiciometric composition of the deposited film. Too high a supply of the reactive gas leads to compound formation not only on the substrate as a deposited film but also on the surface of the sputtering target. At the same time, the sputtering yield of the compound material is substantially lower than the sputtering yield of the elemental target material that causes the deposition rate to decrease as the supply of the reactive gas increases [82]. This compound formation on the target surface persists as the flow of reactive gas is reduced, until at a significantly low flow level the metal target is eroded by physical sputtering [83]. This process is known as a hysteresis effect.

As it was already mentioned above, three gases are available for use in the deposition process by "Discovery 18DC/RF Research Magnetron Sputter Deposition System" where only two of them can be used simultaneously. For instance, a mixture of Ar (working gas) and N_2 (reactive gas) was used for reactive sputtering of a pure Ti target to produce TiN. Metallic targets were used for reactive deposition of ceramic layers. All parameters for the TiN, ZrO_2, and Er_2O_3 deposition runs are presented along with process names in Tables 3.13 and 3.14, correspondingly.

Deposition run	TiN1	TiN6	TiN7	TiN8
q $[\mathrm{W\,cm^{-2}}]$	2.3	2.3	2.3	6.8
V_{Bias} [V]	$43-62$	$65-81$	$53-70$	$44-62$
Q_{Ar} [sccm]	18	30	30	30
$Q_{\mathrm{N_2}}$ [sccm]	3	10	2	10
P [Pa]	0.42	0.81	0.66	0.8
r $[\mathrm{nm\,min^{-1}}]$	0.5	0.5	0.7	2.9
d [nm]	60	65	80	350

Table 3.13: Parameters of the magnetron deposition of TiN layers.

In these tables q is applied power density, V_{Bias} - the substrate bias voltage, Q_{Ar} - Ar gas flow, $Q_{\mathrm{N_2}}$ - N_2 gas flow, P - pressure in the chamber during deposition, r - deposition rate and d - the layer thickness. The same procedures of layer investigation were carried out with TiN, ZrO_2, and Er_2O_3, as were for TiC. Samples with the TiN interlayer deposited for investigation of the diffusion of substrate elements into the EUROFER layer were coated with both the TiN and EUROFER layers without vacuum breaking. Parameters for this process were chosen from among the settings used prior in the experiments on TiN deposition. For the case of oxide layers, optimal parameters had not been found. Therefore, the filtered arc device was used for the Er_2O_3 coating production as an alternative coating technique.

Deposition run	ZrO_2		Er_2O_3	
	ZrO_25	ZrO_26	Er_2O_32	Er_2O_33
$q\ [\mathrm{W\,cm^{-2}}]$	4.5	4.5	11.3	11.3
V_{Bias} [V]	*	*	$36-43$	$32-39$
Q_{Ar} [sccm]	40	20	20	20
$Q_{\mathrm{O_2}}$ [sccm]	15	10	10	10
P [Pa]	1.1	0.6	0.5	0.5
$r\ \left[\mathrm{nm\,min^{-1}}\right]$	1.0	1.2	5.4	5.1
d [nm]	30	60	160	455

Table 3.14: Parameters of the magnetron deposition of oxide layers. * Bias voltage was switched every 5 min from 60 to 155 V

Plasma arc deposition technique

The use of plasma arc deposition results in a much higher rate of coating deposition in comparison to that by magnetron sputtering which is of importance in the processing of composite matrix coatings.

The arc is a high current (tens to hundreds of Amps) low DC voltage (tens of Volts) gas discharge [24]. A very small luminous cathode spot (10^{-8} to 10^{-4} m in diameter) forms extremely high current densities ($\sim 10^8$ to $10^{12}\,\mathrm{A/m^2}$). This causes erosion of the cathode by melting and vaporisation as well as ejection of solid and molten particles. Furthermore, the spot rapidly jumps around the surface of the cathode in a manner dependent on the cathode composition, gas species and pressure, presence of magnetic fields etc. The arc spot is active for a short period of time, then extinguishes, and then re-forms in a new location adjacent to the previous arc crater [83]. This gives rise to the appearance of motion of the arc. The motion rate is a function of the cathode material, temperature, magnetic field, and the presence of gas molecules. Electrons, ions, macroparticles and neutral vapor species are emitted from the cathode spot. The greatest drawback of the cathodic arc is that the process involves the emission of macroparticles. These are thought to be the result of sputtering of molten material from the edges of the arc crater. The vast majority of these macroparticles with μm size is emitted at an angle of roughly $10-20\,^\circ$ from the cathode plane [83]. Magnetic fields affect the arcing voltage as well as the rate and direction of motion of the arc spot.

In the present work, two plasma arc devices have been used: a vacuum arc for deposition of a matrix layer and a vacuum filtered arc for deposition of an interlayer, where the filter of the second arc is aimed to suppress the transfer of macroparticles from cathode to substrate. Both these have the same arc source with a plane evaporated surface shown in Fig. 3.5 [84]. The arc source includes the following main design elements: cathode unit, ignition device, arc magnetic control system and anode unit. Magnetic confinement of the arc to the top surface of the cathode is carried out by means of the magnetic field of a stabilising coil, which is arranged on the anode unit of the arc source [85,86]. Magnetic focusing of the plasma stream is carried out by the focusing coil which is also arranged on the anode unit of the source. In this case, cathodic spots are pushed out to the top surface of the cathode.

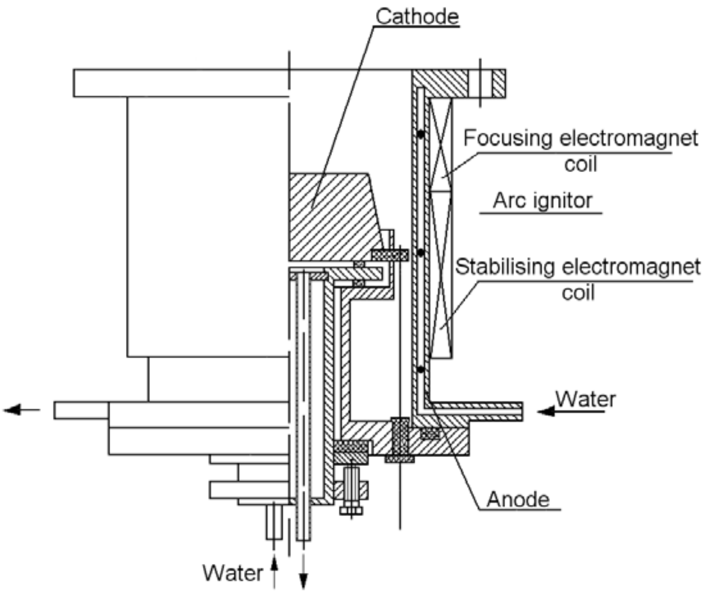

Figure 3.5: Schematic view of the arc source [84]

The cathodic spots move quasi-randomly eroding the cathode surface in such a way that it forms a surface normal to magnetic field lines.

Different methods exist to reduce the droplet contamination of substrates by separating the plasma stream and particle trajectories. Among them, a toroidal separator where plasma is magnetically guided through a toroidal segment is frequently used [87]. This segment is covered inside with a ribbed structure to catch the droplets on the walls of the toroid. A schematic view of a vacuum arc setup with toroidal filter system is presented in Fig. 3.6 [88].

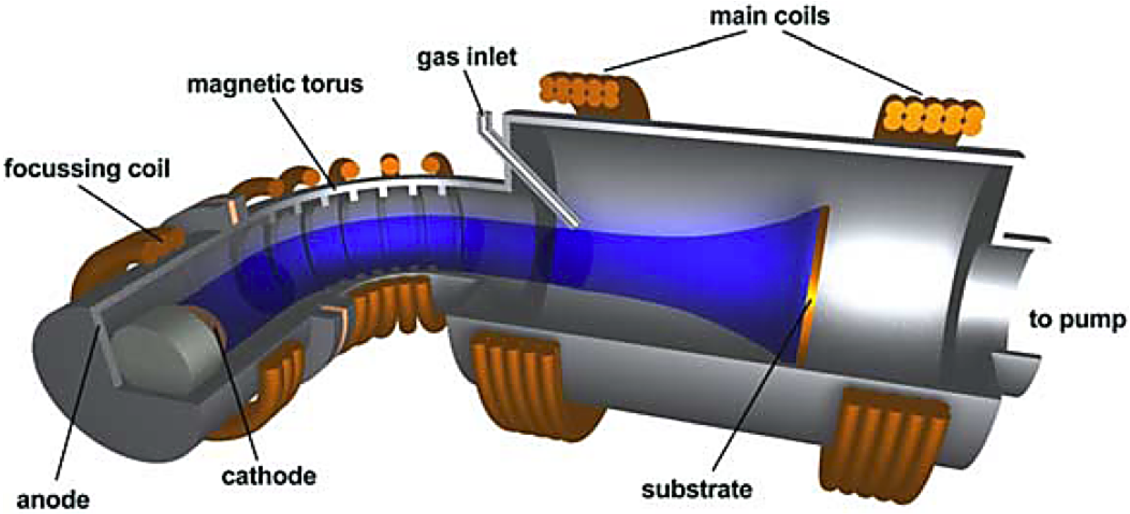

Figure 3.6: Vacuum arc setup with toroidal filter system [88]

The vacuum arc device used for deposition of the matrix coatings does not allow the application of a substrate bias. The substrate holder as well as samples are heated due to the plasma stream during deposition up to $\sim 400\,^{\circ}\mathrm{C}$. No additional heating of the substrate is possible. Therefore, this device was utilized only for the deposition of metallic coatings where it was not necessary to apply additional substrate heating and substrate bias. For the reactive deposition, the filtered arc setup was used to avoid the presence of droplets and to produce a crystalline structure of the compound coating by simultaneously applying bias and heating the substrate. *RF* induced bias voltages up to $-300\,\mathrm{V}$ were used and heating of the samples up to 800 °C was possible by means of an infrared heater installed behind the sample [88].

Deposition of Me layers by the plasma arc technique

Only EUROFER coatings were produced by plasma arc deposition. The diameter of the EUROFER 97 cathode was 70 mm, the distance between the substrate holder and the cathode was 24 cm. The deposition chamber was evacuated to a pressure of $5.8 \cdot 10^{-5}\,\mathrm{Pa}$ by a turbomolecular pump prior to deposition. The coatings were deposited on both the planar samples and fibres at a working pressure of 0.2 Pa in an Ar atmosphere without applying a substrate bias. The deposition rate and the maximum thickness were estimated to be $320\,\mathrm{nm\,min^{-1}}$ and $10\,\mu\mathrm{m}$, respectively.

During initial depositions the arc was found to be unstable, moving onto a side surface of the cathode; even standstill of the cathode spot was observed resulting in strong local melting. This problem also appeared during magnetron sputtering due to ferromagnetic properties of the cathode which strongly influenced the magnetic field distribution. Therefore, the arc plasma source was redesigned with the aim of optimising the magnetic field and the electrode system for arc focusing. It was done in collaboration with Efremov Institute (St.-Petersburg, Russia). After that, deposition was successfully performed and a maximum coating thickness of $30\,\mu\mathrm{m}$ was measured. A specially designed fibre holder was also developed for the arc facilities to provide a uniform deposition of the coatings on the fibres.

Deposition of Er_2O_3 layer by the plasma arc technique

Samples with the name of "CWErbia1" were coated using the plasma filtered arc device with the following parameters: discharge current 80 A, Q_{O_2} 25 sccm, *RF* induced V_{Bias} $-100\,\mathrm{V}$ and substrate temperature 600 °C. The deposition rate and the layer thickness d were $100\,\mathrm{nm\,min^{-1}}$ and $\sim 500\,\mathrm{nm}$, respectively.

For the deposition of the samples with Er_2O_3 / EUROFER layers vacuum breaking was the only option, since deposition of the oxide layer for the annealing experiments was performed using the plasma filtered arc device while EUROFER was deposited using magnetron sputtering. Before deposition of the EUROFER layer, the samples were analysed through a number of investigation techniques. They were then etched in an Ar plasma for 1 min under a power density of $0.28\,\mathrm{W\,cm^{-2}}$ ($390-400\,\mathrm{V}$) and were subsequently coated with an EUROFER layer ($\sim 500\,\mathrm{nm}$). All the etching parameters for the Erbia1 samples were lower than those for the other samples to avoid degradation of the oxide coating under ion bombardment but at the same time still be able to remove surface contaminants.

3.2.2 Substrate preparation

For the correct interpretation of the analysis of a thin layer of $\sim 50\,\mathrm{nm}$ in thickness, it is necessary to use a substrate with roughness less than the layer's thickness, i.e. a very smooth substrate. The graphite substrate used in this work initially had a roughness $R_\mathrm{a} = 400\,\mathrm{nm}$ that was assumed to be much higher than acceptable. Therefore the substrates were mechanically polished prior to deposition with a final achieved value of $R_\mathrm{a} = 60\,\mathrm{nm}$. The polishing consisted of three steps:

- primary polishing using hard chemical fibre cloth with $6\,\mu\mathrm{m}$ diamond paste for 2 min
- intermediate polishing using natural fibre cloth with $1\,\mu\mathrm{m}$ diamond paste for 1 min
- fine polishing using soft synthetic cloth with fine polishing suspension for 10 s.

The substrates were rinsed ultrasonically in isopropanol prior to loading into the deposition chamber. They were then etched with an Ar plasma with a power density of $0.57\,\mathrm{W\,cm^{-2}}$ $(560-600\,\mathrm{V})$ for 2 min. This cleaning treatment was performed to avoid contamination of the layer - substrate interface zone. The target was also cleaned in an Ar plasma for $2-10\,\mathrm{min}$ depending on the oxidation level of the target material.

3.2.3 Annealing

To investigate the behaviour of the deposited samples under heat load during operation and fabrication, annealing in the temperature range of 400 to 1000 °C was performed in a high vacuum annealing apparatus. The upper limit was chosen according to the fact that the hipping temperature during composite fabrication would be 1000 °C. Thin coatings with a 50 nm interlayer and 50 nm EUROFER layer were annealed at these temperatures, while the thick coatings with 500 nm of each layer were annealed at only 750 °C which corresponds to the maximum operating temperature of the composite.

The heating rate of $20\,\mathrm{K\,min^{-1}}$ remained unchanged. The total working pressure during heating and annealing was controlled to be $(2-9)\cdot 10^{-4}\,\mathrm{Pa}$. Only during annealing at 1000 °C the pressure increased to about $2.2\cdot 10^{-3}\,\mathrm{Pa}$. The duration was 2 h for all the samples except the samples consisting of thick W or Re / W layers. To investigate the behaviour of the latter samples under long-term heat load they were heated for 2 and then 16 h.

3.2.4 Layer characterisation techniques

In this work, different techniques for the characterisation of the interface were used: *SEM*, *EDX*, *OES*, *XRD*, and *IBA* (while utilizing $^4\mathrm{He}^+$ ions with an energy of 2 MeV, this analysis is called Rutherford BackScattering spectroscopy).

The comparative strengths and weaknesses for particular analytical applications are as follow [24, 89]:

- *EDX* and *IBA* generally analyse the total thickness of a thin film ($\sim 1\,\mu$m) and often some portion of a substrate as well. Unlike *IBA* with its depth resolution of ~ 20 nm, *EDX* has low depth resolution capability. *EDX* ordinarily detects elements with atomic number $Z > 11$ and IBA is restricted only to selected combinations of elements whose spectra do not overlap.

- The detection limits for *EDX* and *IBA* are similar ranging from about ~ 0.1 to 1 at.%.

- Only *IBA* is quantitatively precise to within an atomic percent. It is the only non-destructive technique that provides simultaneous depth and composition information.

SEM / EDX

SEM is one of the most widely employed film and coating characterization instruments. In *SEM* analysis, only a small portion of the total image is probed at any moment and the image is built up serially by scanning the probe. The most common imaging mode relies on detection of secondary electrons (*SE*) possessing the lowest portion of the emitted energy distribution [89]. Their very low energy means they originate from a subsurface depth no larger than several angstroms. Resolution specifications based on research quality *SEM*s are less than 2 nm.

Additionally, backscattered electrons (*BSE*) are high energy electrons which are elastically scattered and essentially possess the same energy as the incident electrons. The probability of backscattering increases with the atomic number Z of the sample material. Useful image contrast can occur between specimen regions which differ widely in Z. Since the escape depth for high energy backscattered electrons is much greater than for low energy secondary electrons there is much less topological contrast in the image.

In *EDX* the electron beam serves to excite characteristic X-rays from the probed area of a specimen.

In this work, a “Philips XL 30 ESEM” was used to acquire images from the samples in *SE* or *BSE* modes and to investigate the layer composition with help of an interfaced *EDX*. The beam energy used varied from 1 to 30 kV with a spot size of 1.0 to 10.0 and magnification in the range from ×30 to ×40000. The resolution for gold in carbon was 6 nm, for lighter elements it was worse at only $10 - 20$ nm.

OES

The method of *OES* is based on measurements of the radiation line and band intensity of primarily excited particles, atoms and molecules. Excitation means the transfer of the particles to their higher energetic states - electronic, oscillating or rotational, in which they live for a short time. De-excitation leads to radiation with a certain wavelength to occur. A certain emission spectrum corresponds to given excited atoms and molecules, and from this fact a substance can be identified.

With the help of a "SPECTRO ICP" system the layer composition was detected. The layer on the sample was dissolved with 2 ml of HCl acid; after the addition of up to 50 ml of the liquid, the solution was nebulized and then vaporized with an Ar plasma.

XRD

XRD methods exploit the fact that the spacing between atoms is comparable to the wavelength of the X-rays. This results in easily detected beams of high intensity emitted in certain directions when incident X-rays impinge at critical diffraction angles [90]. Under these conditions the well-known Bragg relation holds:

$$n_{\mathrm{i}}\lambda = 2a\sin\theta_{\mathrm{d}},$$

where λ is the wavelength, θ_{d} is the diffraction angle, a is the lattice parameter, and n_{i} is an integer value.

This technique is used to address all issues related to the crystal structure of bulk solids including lattice constants and crystallography, identification of unknown materials, orientation of single crystals and preferred orientation of polycrystals, defects, and stresses.

In bulk solids, large diffraction effects occur at many values of θ_{d}. In thin films, however, very few atoms are present to scatter X-ray into a diffracted beam when θ_{d} is large. For this reason, the intensities of the diffraction lines or spots will be unacceptably small unless the incident beam strikes the film surface at a near glancing angle. This, in effect, makes the film look thicker. Relative to bulk solids, thin films require long counting times to generate enough signal for suitable X-ray diffraction patterns.

The crystalline structure and texture of the coatings were analysed by *XRD* using a diffractometer with a Cu anode working at the power settings of 40 kV and 30 mA.

IBA

The projectile ions loose their energy through electronic excitation and ionization of target atoms. These electronic collisions are so numerous that the energy losses are considered to be continuous with depth. Sometimes the fast moving light ions (usually $^{4}\mathrm{He}^{+}$) penetrate the atomic electron cloud shield and undergo close impact collisions with the nuclei of the much heavier stationary target atoms [90]. The resulting scattering from the Coulomb repulsion is known as Rutherford scattering. Thus, it is classical two body elastic scattering. The collision is insensitive to the electronic configuration or chemical bonding of target atoms and depends solely on the masses and energies involved. A consequence of conserving energy is that

$$E_1 = \left\{ \frac{\sqrt{\left(M^2 - M_0^2\sin^2\theta\right)} + M_0\cos\theta_{\mathrm{s}}}{M_0 + M} \right\}^2 E_0,$$

where E_1 is the ion energy after collision, E_0 is the primary ion energy, M_0 is the ion mass, M is the atom mass, and θ_{s} is the scattering angle. As MeV *He* ions traverse the solid, they lose energy along their incident path at a rate dE/dx between 30 and 60 eV/ Å. The value of dE/dx can be used to obtain the composition depth profiles from the energy spectra of backscattered particles. In thin film analysis, the total energy loss ΔE into a depth t is approximately proportional to t:

$$\Delta E = \int^{t} \frac{dE}{dx} dx \cong \left. \frac{dE}{dx} \right|_{\text{in}} \cdot t,$$

where $dE/dx|_{\text{in}}$ is evaluated at some average energy between the incident energy E_0 and $E_0 - t(dE/dx)$. For each broad elemental peak detected in the case of a thin film on a substrate, therefore, the highest and lowest energies correspond to particles scattered at the surface of the film and near the interface film - substrate, respectively. Thus, by measuring the number and energy of backscattered ions, information on the nature of the elements present, their concentration, and their depth distribution can be simultaneously acquired without appreciable damage of the specimen.

The method of *IBA* was utilized on a "Tandetron HVEE" for investigations of the concentration depth profile of the coatings on the graphite substrate. The samples with a total thickness of 100 nm were analysed with 2 MeV $^4\text{He}^+$ ions at an angle of incidence of 0 °, exit angle of 15 ° and scattering angle of 165 °. Ions with an energy of 3.5 MeV to 5 MeV were used for analysing the coatings with different thicknesses but mostly of 1 μm. Depth profiles were extracted from the backscattered energy distribution using the simulation code SIMNRA 5.50 [91, 92]. This program gives a concentration depth profile in the units of atom / m^2. In order to obtain the depth in m, one has to divide the length scale by the local layer density (atom / m^3) [26]. The error of such a conversion is about 10% for thick layers, while for thin ones it is higher. Due to detector resolution features, using 2 MeV $^4\text{He}^+$ ions only isotopes with $\Delta M = 1$ can be separated for atomic masses below approximately 40. At values of $M \approx 200$ only atoms for which $\Delta M > 20$ can be resolved.

4 Results

4.1 Characterisation of deposited layers

4.1.1 EUROFER

The surface structure of the deposited layers and their cross-sections were investigated with a *SEM*. The sputtered coating had a good adhesion to the surface on all of the substrates. A *SEM* image of the sample with the magnetron deposited layer is shown in Fig. 4.1.

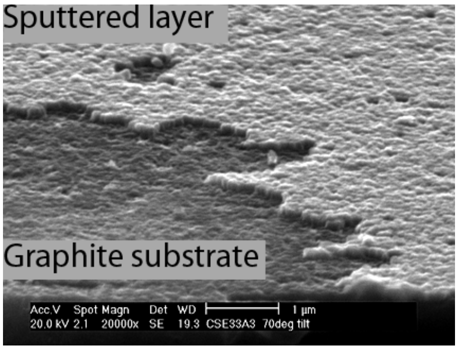

Figure 4.1: *SEM* image of sputtered EUROFER layer ($\sim$ 108 nm) on graphite substrate (CSE33A3)

The sputtered layer possesses a fine structure and homogeneously covers the substrate surface. Therefore substrate defects, such as pores or grooves due to polishing, are also visible on the samples coated by the magnetron sputtering. On the contrary, however, samples coated by plasma arc deposition reveal a coarse structure with drops and pores. The surface structure and a cross-section of the sample with a EUROFER layer of 30 μm are shown in Figs. 4.2a and 4.2b, correspondingly. The presence of pore on the arc deposited coatings is assumed to disappear during the hipping process that will be used to obtain a composite. The coatings deposited by both *PVD* techniques onto the SiC fibre (see Fig. 4.3) have a homogeneous thickness distribution around the fibre, which is important for the composite material.

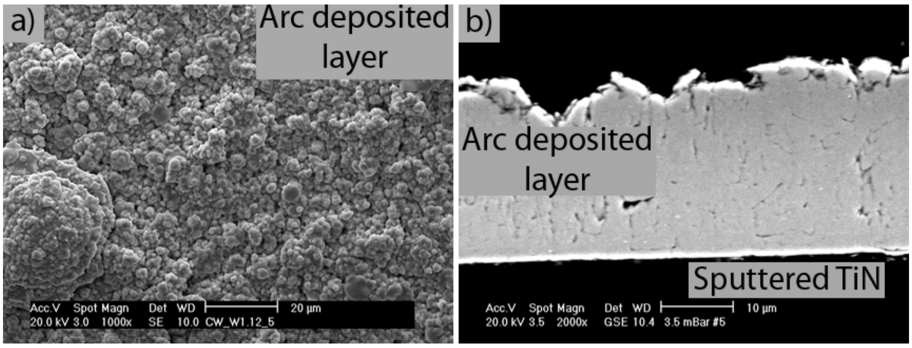

Figure 4.2: *SEM* images of samples with arc deposited EUROFER layer ($\sim$ 30 μm) a) the surface of the CW_W1A5 and b) a cross-section of the CS_TiN9A5

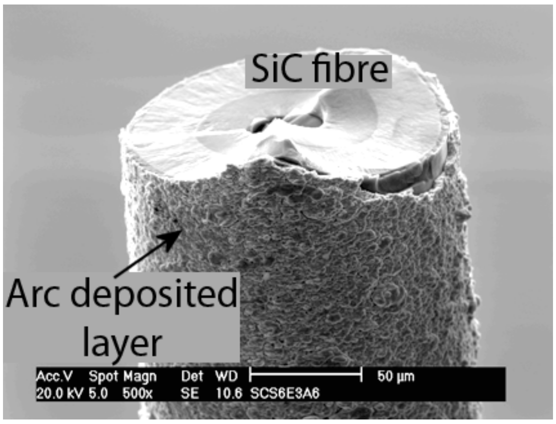

Figure 4.3: *SEM* image of SiC fibre coated with both magnetron (∼180 nm) and arc (∼6 μm) deposited EUROFER (SCS6E3A6)

Concerning the crystallographic analysis, EUROFER 97 was investigated by *XRD* as a reference powder (see Fig. 4.4). The sputtered coating yields different intensities to those of the powder and lacks some of the peaks due to the texture of the coating. Further texture measurements of the sputtered EUROFER film show that the surface is oriented in the (110) plane so that the layer exhibits a strong fibre texture around the surface normal. Stress measurements are not possible due to this high texture.

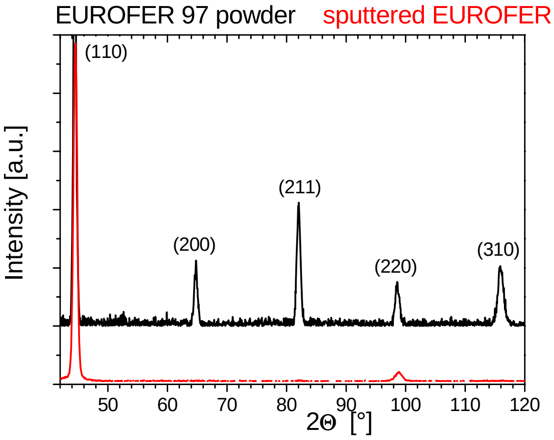

Figure 4.4: *XRD* spectrum of sputtered EUROFER layer in comparison with EUROFER 97 powder

To satisfy the demand for low impurity contamination in a coating, the magnetic configuration of the magnetron magnets of the sputter deposition facility has been improved. Before this change the maximum deposition rate was 0.5 nm min^{-1} obtained at 0.8 Pa of Ar pressure and 11.3 W cm^{-2} of applied power density. The thickest layer of 180 nm was deposited using these parameters within 6 h in a non-stop process. With the enhanced magnetron configuration, the maximum deposition rate is found to be 24.7 nm min^{-1} even at half the Ar pressure of 0.4 Pa and the lower applied power density of 4.5 W cm^{-2}. Such a significant improvement allows decreasing the O contamination in the layer from 8.8 at.% to less than 1.5 at.% (see Table 4.1).

The composition of the coatings was calculated from the results of two complementary analyses, namely *OES* and *IBA*. The data from these analyses is presented in Table 4.1 in comparison with the composition of the EUROFER 97 target [76]. The first two layers were deposited in the magnetron device employing the magnetron with the standard cathode unit and the enhanced one. The layer produced by plasma arc deposition was deposited before the facility had been optimised. Using an *OES* analysis the content of Fe, Cr, and Mn in $\mathrm{mg\,l^{-1}}$ was determined, whereas the relative concentration of C, O, W, and Fe+Cr+Mn was obtained by *IBA* (see Fig. 4.5).

	Target composition [76], [at.%]	Film deposition with standard magnetron cathode unit, [at.%]	Film deposition with enhanced magnetron cathode unit, [at.%]	Film produced by plasma arc deposition, [at.%]
Fe	89.2	74.0	85.9	87.2
Cr	9.5	8.8	10.1	11.6
Mn	0.4	0.4	0.4	0.8
W	0.3	0.3	0.3	0.4
O	0.6	8.8	1.8	$\ast$
C	0.005	7.7	1.5	$\ast$

Table 4.1: Composition of the target material EUROFER 97 and of the deposited layers in atomic percent, * below detector limit

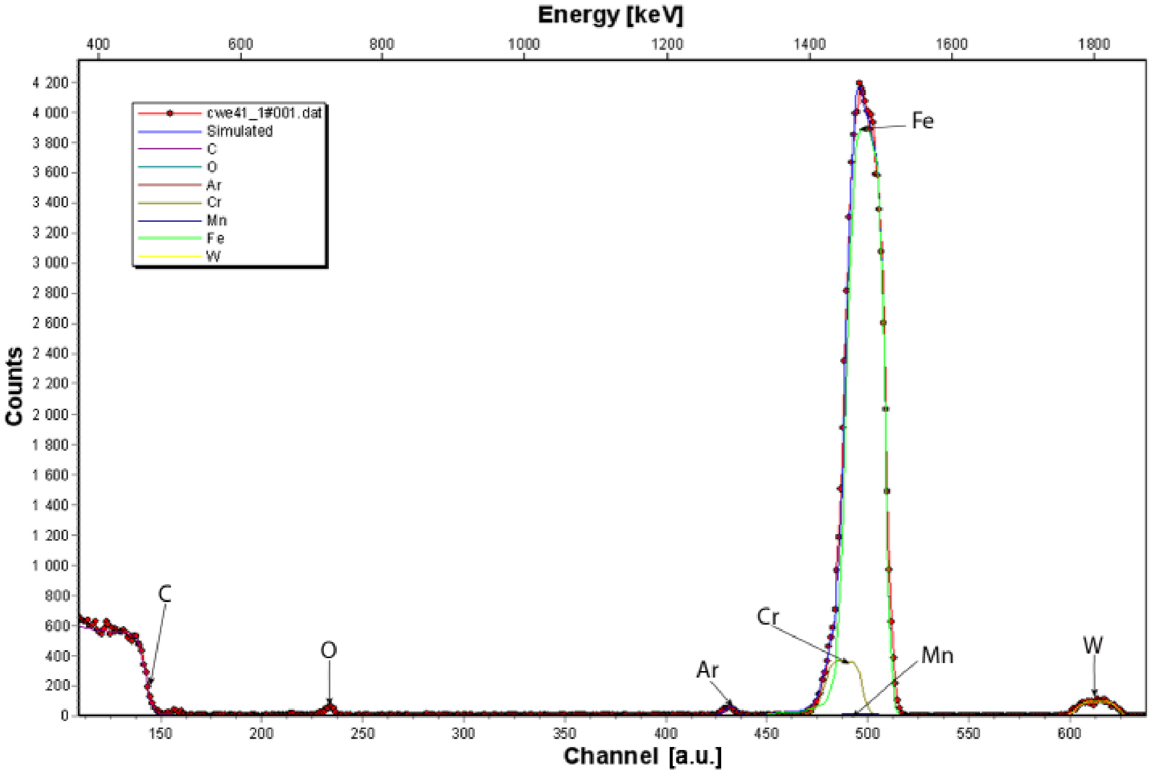

Figure 4.5: *IBA* spectrum from unheated EUROFER layer on graphite substrate (CWE41)

It is impossible to separately determine the Fe, Mn and Cr contents using *IBA* due to the detector's limited resolution. In spite of the fact that W has a very low content in the deposited layer, it can be evaluated with a good precision since the sensitivity of *IBA* increases with increasing atomic number. In the plasma arc deposited layer, the concentration of O and C contaminations were not determined due to the layer thickness and roughness.

Both types of layer, either sputtered with the enhanced cathode unit or arc deposited, show a composition of the main elements very close to that of the target material.

4.1.2 Ceramics

In ceramic coating deposition, the influence of different parameters such as applied power density q, partial pressure P, substrate bias V_{Bias} and substrate material were investigated. The quality of the film was found to depend significantly on these parameters.

TiC

The "TiC" coating was produced in two different ways: dual magnetron sputtering of Ti and C targets and standard *RF* magnetron sputtering of a TiC target.

The influence of the substrate on the layer structure is shown in Fig. 4.6. The sample CWTiC4 with the graphite substrate as well as the sample SiCTiC4 with the SiC substrate were coated at the same time. The images shown in Fig. 4.6a and b were taken from the sample CWTiC4, where the image Fig. 4.6b was made by tilting. On the graphite, the coating reveals cracking throughout the surface. The developed surface of the CWTiC4 has empty hillocks (see Fig. 4.6b).

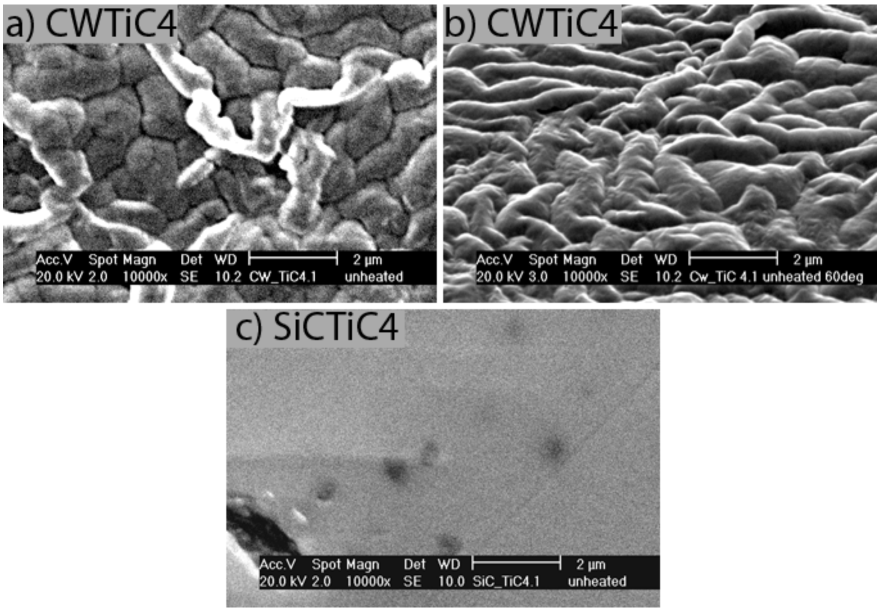

Figure 4.6: The influence of the substrate on the layer structure. *SEM* images of the "TiC4" layer (125 nm) deposited on a) graphite substrate, b) graphite substrate with tilting of the sample and c) SiC substrate

This surface structure could probably be formed due to high compressive stress in the layer during deposition, since the size of these formations (few μm) is much higher than the layer thickness (125 nm). In contrast to the CWTiC4, the SiCTiC4 reveals a fine structure. The defects, pores and grooves which are visible in Fig. 4.6c of the SiCTiC4, come from the substrate.

For comparison of the influence of the deposition parameters, such as applied power density and substrate bias, *SEM* images of coatings on a graphite substrate are shown in Fig. 4.7.

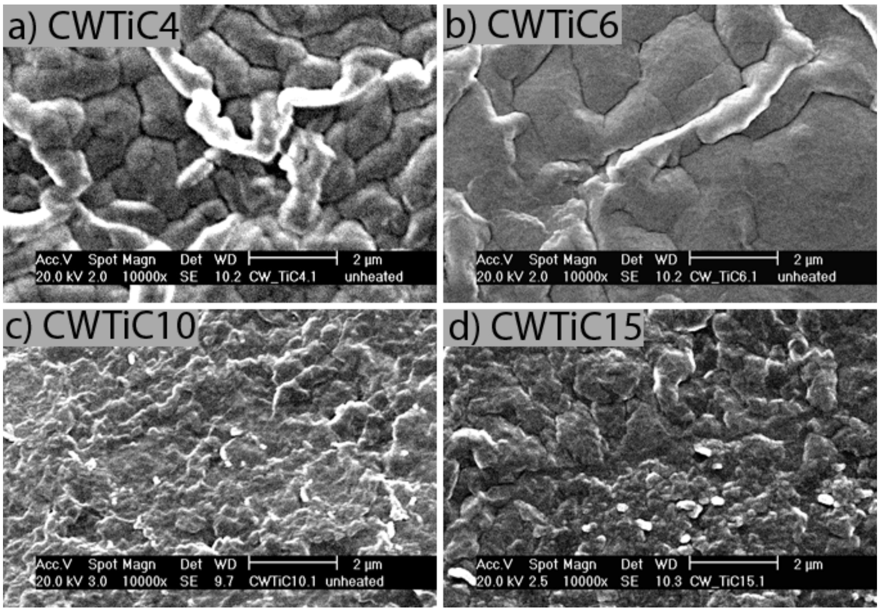

Figure 4.7: The influence of deposition parameters, such as applied power density to the C target q_{C}, standard and dual magnetron sputtering, and bias voltage V_{Bias} on the layer structure: a) $q_{\mathrm{C}} = 6.3\,\mathrm{W\,cm^{-2}}$, dual magnetron sputtering, $V_{\mathrm{Bias}} = 124\,\mathrm{V}$, the layer thickness $d = 125\,\mathrm{nm}$; b) $q_{\mathrm{C}} = 4.5\,\mathrm{W\,cm^{-2}}$, dual magnetron sputtering, $V_{\mathrm{Bias}} = 129\,\mathrm{V}$, $d = 110\,\mathrm{nm}$; c) $q_{\mathrm{TiC}} = 2.3\,\mathrm{W\,cm^{-2}}$, standard magnetron sputtering, $V_{\mathrm{Bias}} = 75\,\mathrm{V}$, $d = 45\,\mathrm{nm}$; d) $q_{\mathrm{C}} = 4.5\,\mathrm{W\,cm^{-2}}$, dual magnetron sputtering, changed every 5 min $V_{\mathrm{Bias}} = 176 - 54\,\mathrm{V}$, $d = 100\,\mathrm{nm}$

The variation of applied power density q_{C} to the C target and, at the same time, a constant applied power $q_{\mathrm{Ti}} = 1.4\,\mathrm{W\,cm^{-2}}$ to the Ti target, changes the composition of the layer. The composition of the layers investigated by *IBA* is presented in Table 4.2. With increasing q, the C concentration also increases. Thus, during deposition with $q_{\mathrm{C}} = 11.3\,\mathrm{W\,cm^{-2}}$ the layer is found to consist of 35 at.% of Ti and 64 at.% of C. While at $q_{\mathrm{C}} = 4.5\,\mathrm{W\,cm^{-2}}$ it contains 49 at.% of Ti and 47 at.% of C (CWTiC6). The same dependence of the coating stoichiometry on q was observed in [93].

The samples CWTiC4 and CWTiC6 deposited at the same parameters with the exception of q_{C} ($6.3\,\mathrm{W\,cm^{-2}}$ for CWTiC4 and $4.5\,\mathrm{W\,cm^{-2}}$ for CWTiC6) reveal not only composition changes but also different layer structures. Thus, the CWTiC6 (see Fig. 4.7b) has bigger and flatter hillocks than are observed for CWTiC4 (see Fig. 4.7a). A difference of 5 at.% is observed in C content in the CWTiC4 and CWTiC6 layers. The deposition by sputtering of

	q_{C} $[\mathrm{W\,cm^{-2}}]$	q_{TiC} $[\mathrm{W\,cm^{-2}}]$	Ti [at.%]	C [at.%]
CWTiC1	11.3	–	35	64
CWTiC4	6.3	–	45	52
CWTiC6	4.5	–	49	47
CWTiC10	–	2.3	42	54
CWTiC15	4.5	–	50	47

Table 4.2: Composition of the TiC layers deposited on graphite substrate in atomic percent

the TiC target (CWTiC10) results in a smoother layer (see Fig. 4.7c) in comparison to the CWTiC4 or CWTiC6 but also reveals a higher C content. In this case it is impossible to vary the C or Ti content by changing the applied power density. In all coatings produced by this method the C content is found to lie in the range from 53 to 57 at.%.

The applied substrate bias V_{Bias} has been found to affect the layer structure. The CWTiC6 and CWTiC15 were deposited at the same parameters with the exception of V_{Bias}: for CWTiC6 it was 119 – 129 V and for CWTiC15 it was switching between 176 V and 54 V every 5 min. By using this cyclically varied V_{Bias} it is possible to build a dense layer (sample CWTiC15 (see Fig. 4.7d)) which does not reveal such a developed layer structure with empty hillocks as was observed for CWTiC6. Therefore, the CWTiC15 is not subjected to high stress and, at the same time, the composition of the TiC layer remains the same.

The crystalline structure of the layers on both the glass and graphite substrates was investigated by *XRD* analysis. The spectra are presented in Fig. 4.8. Due to its amorphous structure and therefore absence of peaks from the substrate on a *XRD* pattern, the glass substrate used for the experiment allows more convenient investigation of the crystalline structure of the samples than other substrates. The coatings of glassTiC4 and glassTiC6 both possess a crystalline structure. The layers deposited by sputtering the TiC target reveal an amorphous structure. Therefore, it can be concluded based on the composition as well as the crystalline structure of the CWTiC10 sample coating, that sputtering of a single TiC target is an inappropriate way of producing a C diffusion barrier.

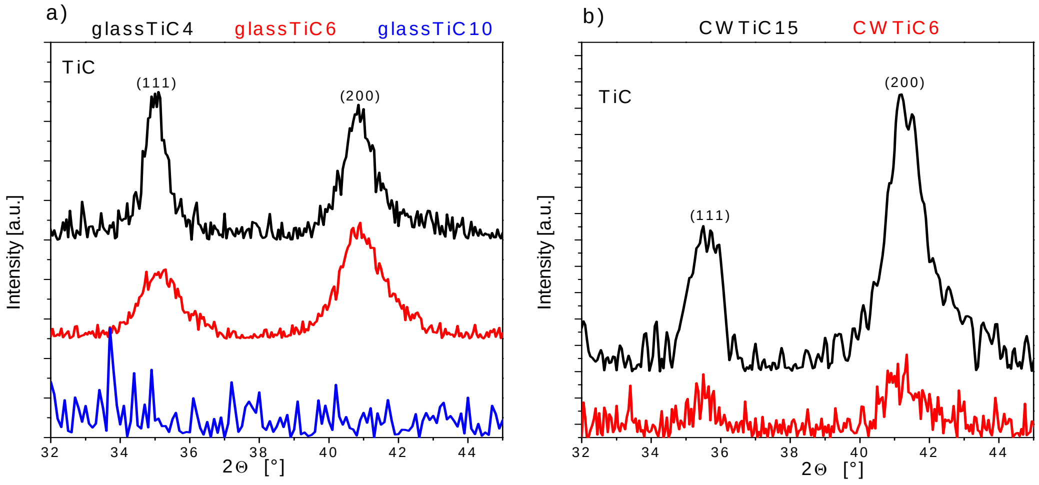

Figure 4.8: *XRD* spectra of TiC layers on a) glass and b) graphite substrates

In contrast to the sputtering of a TiC target, deposition by dual sputtering of Ti and C targets with cyclically varied V_{Bias} results in the right stoichiometry and a smooth layer with a crystalline structure of CWTiC15 (see 4.8).

For TiC layers on the CWE_TiC1 and SiCE_TiC1 samples the deposition parameters of CWTiC15 were used.

TiN

For the deposition of "TiN" coatings the reactive sputtering of a Ti target was utilized. Several parameters of the process influenced the layer properties: applied power density q, N_2 partial pressure P_{N_2}, the ratio R of the partial pressures of Ar and N_2 ($R = P_{\mathrm{Ar}}/P_{N_2}$) and substrate material.

The *SEM* images of graphite substrates coated with "TiN" layers are shown in Fig. 4.9. The influence of the variation of R on the layer structure is observed for the samples CWTiN1 (Fig. 4.9a), CWTiN6 (Fig. 4.9b), and CWTiN7 (Fig. 4.9c). The samples CWTiN1, CWTiN6, CWTiN7 and CWTiN8 were coated with the following R: 6, 3, 15, and 3, correspondingly. The CWTiN7 revealed a developed layer structure with empty hillocks, similar to the previously mentioned "TiC" coatings, possessing a high compressive stress. $R = 3$ seems to be the optimum for achieving a fine layer structure. In [94] the author paid special attention to the variation of R, where the best coating quality was obtained for $R = 9$.

The layers' composition investigated by *IBA* is presented in Table 4.3. All coatings have a composition close to stoichiometric TiN.

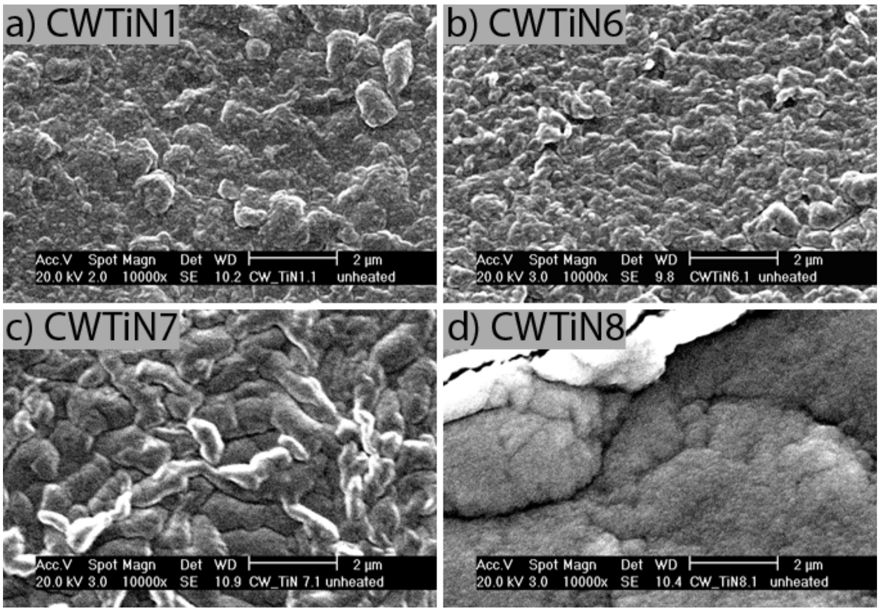

Figure 4.9: The influence of the ratio R of the partial pressures of Ar and N_2 and applied power density q on the layer structure: a) $q_{\mathrm{Ti}} = 2.3\,\mathrm{W\,cm^{-2}}$, $R = 6$, the layer thickness $d = 60\,\mathrm{nm}$, b) $q_{\mathrm{Ti}} = 2.3\,\mathrm{W\,cm^{-2}}$, $R = 3$, $d = 65\,\mathrm{nm}$, c) $q_{\mathrm{Ti}} = 2.3\,\mathrm{W\,cm^{-2}}$, $R = 15$, $d = 80\,\mathrm{nm}$, and d) $q_{\mathrm{Ti}} = 6.8\,\mathrm{W\,cm^{-2}}$, $R = 3$, $d = 350\,\mathrm{nm}$

	R	Ti [at.%]	N [at.%]
CWTiN1	6	47	50
CWTiN6	3	45	47
CWTiN7	15	47	48
CWTiN8	3	47	51

Table 4.3: Composition of the TiN layers deposited on a graphite substrate in atomic percent

The deposition rate of the coatings of CWTiN1, CWTiN6, and CWTiN7 was very low, $0.5\,\mathrm{nm\,min^{-1}}$. To increase this parameter, the applied power density q was increased. Another way to increase the deposition rate was to vary the gas flow. Thus, during deposition of Me layers raising the Ar gas flow and, as consequence, the partial pressure, leads to an increasing of the deposition rate. However, it is not quite the same for the reactive sputtering case (see subsection 3.2.1). In the "stoichiometric" deposition regime increasing of the reactive gas flow, in this case N_2, does not lead to a higher deposition rate. Therefore, it is only possible to vary q to obtain a higher deposition rate. q_{Ti} was increased from $2.3\,\mathrm{W\,cm^{-2}}$ for CWTiN6 to $6.8\,\mathrm{W\,cm^{-2}}$ for CWTiN8, which resulted in the higher deposition rate of $2.9\,\mathrm{nm\,min^{-1}}$ in contrast to the initial value of $0.5\,\mathrm{nm\,min^{-1}}$. All other settings remained the same. As distinct from the fine structure of the layer in the case of CWTiN6 (see Fig. 4.9b), the coating of CWTiN8 cracked during deposition (see Fig. 4.9d). Fig. 4.10a and b were taken from the same sample with and without sample tilting.

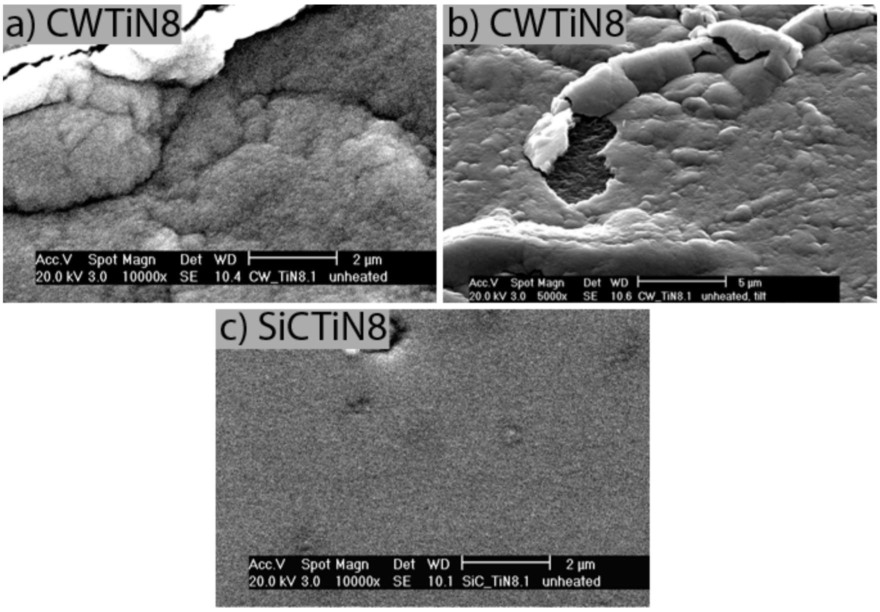

Figure 4.10: The influence of the substrate material on the layer structure (the layer thickness 350 nm): a) on graphite, b) on graphite, image with tilting applied, and c) on SiC

The layer is not only cracked but additionally some areas without any coating are observed. Hence, the increasing of q leads to a serious layer degradation because at a high deposition rate the surface energy is no longer the main driving force during the first stage of growth, the accumulation of compressive stresses becomes the dominant process [95].

The influence of the substrate material is shown for the case of graphite (CWTiN8) and SiC (SiCTiN8) substrates in Figs. 4.10a and c. These two samples were coated at the same time. In contrast to the CWTiN8, the SiCTiN8 (Fig. 4.10c) reveals a fine layer structure without any defects. The pores visible on the image are actually defects of the SiC substrate.

The crystalline structure of the coatings were examined by *XRD*. The results of the analysis are presented in Fig. 4.11. Both the layers of glassTiN1 and glassTiN6 demonstrate a crystalline layer structure.

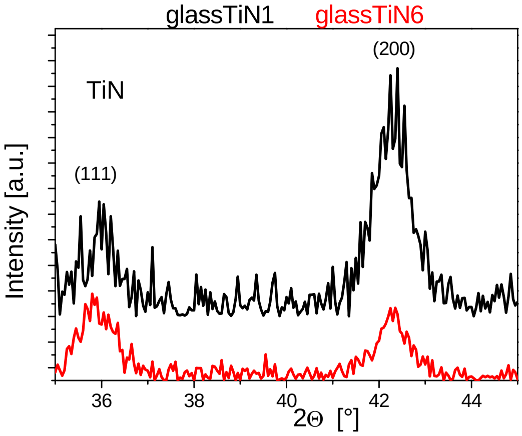

Figure 4.11: *XRD* spectra of TiN layers on glass substrates

Consequently, based on these results, the deposition parameters used for CWTiN6 were chosen for the deposition of a TiN interlayer and the ensuing annealing experiments.

ZrO_2

“ZrO_2” layers were formed by magnetron reactive sputtering similar to that used to produce “TiN”, where in that case the deposition of the layer was made by the sputtering of Zr target in reactive atmosphere of Ar and O_2.

In [96] the influence of different parameters on the quality of ZrO_2 layer was investigated. It was found that the coating had an amorphous structure before and after annealing at temperatures below 600 °C. As it was mentioned in subsection 3.2.1 devoted to a description of the magnetron technique, the sputter device “Discovery 18DC/RF Research Magnetron Sputter Deposition System” allows heating the samples to temperatures up to 600 °C. To obtain a crystalline ZrO_2 coating, the samples were therefore annealed after deposition. The duration of annealing was 30 min and the temperature 800 °C.

In Fig. 4.12 the *SEM* images of both SiC ($SiCZrO_25$) and graphite ($CWZrO_25$) substrates coated with a ZrO_2 layer (30 nm) before and after annealing are shown. The $SiCZrO_25$ are presented both with and without tilting (see Figs. 4.12a and c, and Figs. 4.12b and d). In the image made by tilting the $SiCZrO_25$ it is possible to observe the appearance of blisters. The reason for the appearance is not annealing, since they are visible on the unheated samples as well. The coating is about 40 nm in thickness, therefore the layer is too thin for the formation of blisters of such size.

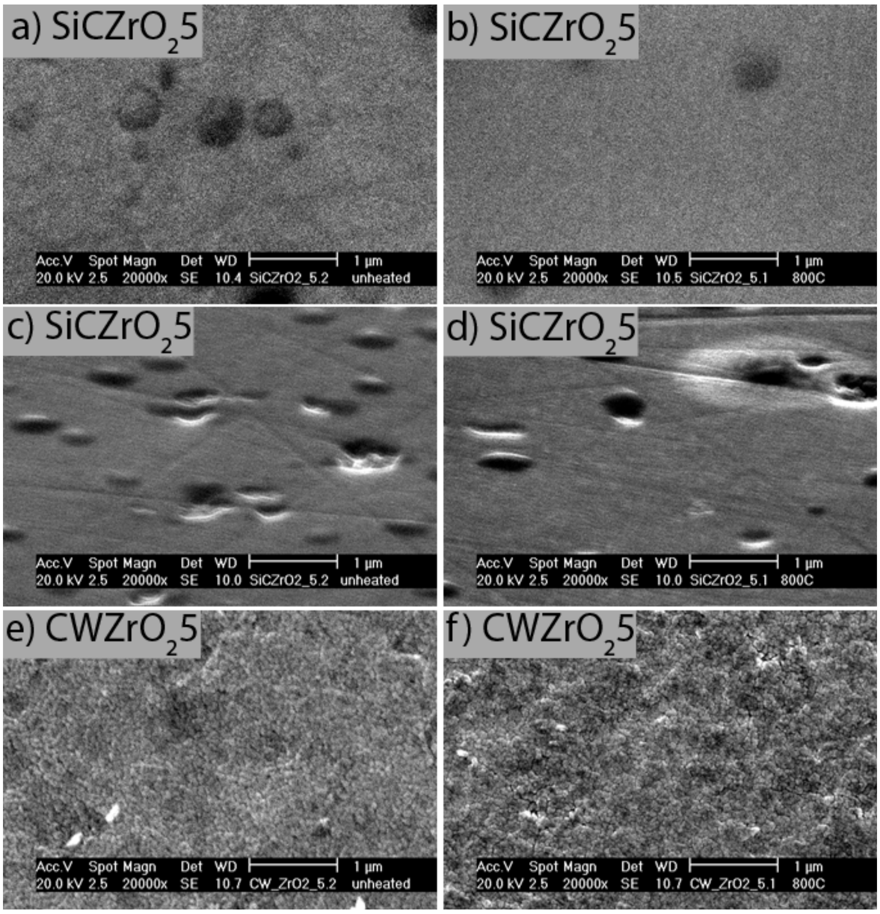

Figure 4.12: The influence of the substrate material and annealing on the layer structure. *SEM* images of samples coated with "ZrO_2" layer (30 nm) with and without annealing at 800 °C for 30 min: a) with SiC substrate, original , b) with SiC substrate, annealed, c) with SiC substrate, original, *SEM* image from tilted sample, d) with SiC substrate, annealed, *SEM* image from tilted sample, e) with graphite substrate, original, and f) with graphite substrate, annealed.

Besides, the increased concentration of Ar in the near-surface zone of the substrate was observed by means of *IBA*, as well as the rise of the roughness of the substrate surface. Consequently, the blisters appeared in the SiC substrate due to Ar ion implantation by applying of bias during deposition. The blister formation did not appear in the case of other as-deposited thin layers, since for *Me* layers the bias voltage was not applied to the substrate during deposition and for other ceramic layers the lower values of V_{Bias} were used. In turn, there is no blister formation on the CWZrO$_2$5 with graphite substrate observed. Annealing of the CWZrO$_2$5 does not affect the layer structure (Fig. 4.12f). The ZrO_2 layer reveals a fine structure in both cases of SiCZrO$_2$5 and CWZrO$_2$5.

The composition of "ZrO_2" layers was examined by *IBA*. Results of this analysis are presented in Table 4.4. All the layers before and after the annealing possess a composition close to stoichiometric ZrO_2.

For experiments applying ZrO_2 as a diffusion barrier the sample CWZrO$_2$6 with a layer

	Annealing	Zr [at.%]	O [at.%]
$CWZrO_25$	-	30	67
$CWZrO_25$	800 °C	31	66
$CWZrO_26$	-	29	67
$CWZrO_26$	800 °C	31	67

Table 4.4: Composition of the zirconia layers deposited on graphite substrate in atomic percent

thickness of 50 nm was produced but after annealing it revealed crack formation. Both samples with and without annealing are presented in Fig. 4.13. The images were made in *BSE* mode of *SEM* to provide a much less topological contrast to easily observe the crack formation. One can see that the increase of the layer thickness results in the formation of the cracks after annealing.

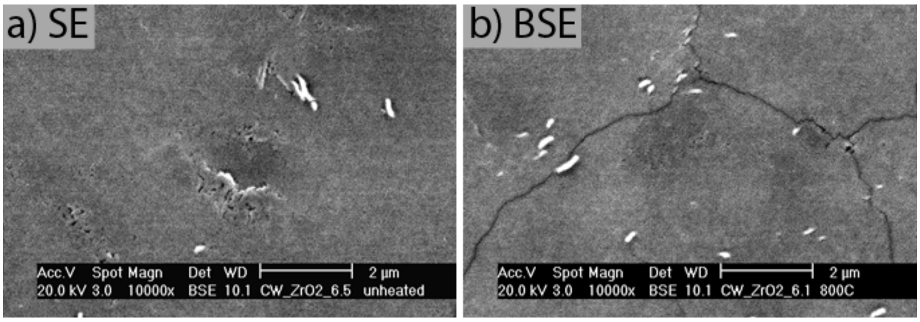

Figure 4.13: *SEM* images in *BSE* mode of graphite substrate coated with a "ZrO_2" layer with and without annealing at 800 °C for 30 min ($CWZrO_26$)

XRD analysis was made for the samples with and without annealing. The patterns reveal no peaks corresponding to ZrO_2, so crystalline ZrO_2 coatings have not been formed. As was mentioned in subsection 2.1, fast diffusion occurs within individual grain boundaries. Therefore, in the layer with small grains the diffusion flow is fast, since the majority of mass is transported through the grain boundaries. Due to this fact and the presence of cracks after annealing, the coating has not been investigated as a diffusion barrier.

Er_2O_3

For coating a graphite substrate with "Er_2O_3", two *PVD* techniques were used: the magnetron and filtered arc devices. In both cases the reactive sputtering of an Er target was used. For magnetron reactive sputtering, a mixture of Ar and O_2 was used to provide a higher deposition rate than would be produced in a pure O_2 atmosphere, i.e. without Ar. In the filtered arc device only O_2 was used. The principal difference between these two coating techniques was that the magnetron deposition was performed without heating while the arc deposition was done at a temperature of 600 °C.

In Fig. 4.14 the *SEM* images in *BSE* mode of graphite substrates coated with "Er_2O_3" layers before and after annealing are shown. The samples $CWEr_2O_32$ and $CWEr_2O_33$ were deposited by magnetron sputtering and then annealed at 800 °C with heating rate of $20\,K\,min^{-1}$.

The difference between these two samples is their thickness: the CWEr$_2$O$_3$2 (Figs. 4.14a and b) has a layer thickness of 160 nm, while the CWEr$_2$O$_3$3 (Figs. 4.14c and d) has a thicker layer of 460 nm. Crack formation after annealing is observed in both cases. In addition to cracks in the thick layer (CWEr$_2$O$_3$3) holes appear (Fig. 4.14d). To avoid crack formation, annealing parameters such as temperature and heating rate were varied. In spite of this, the crack propagation is also observed for the sample CWEr$_2$O$_3$2 annealed at the lower temperature of 650 °C and the slower heating rate of 2 K min^{-1}.

In Fig. 4.15 the *SEM* images in *BSE* mode of the sample coated by the filtered arc device are presented. The layer possesses a fine structure without any cracks. A defect on the surface in the form of a groove belongs to the under lying graphite substrate.

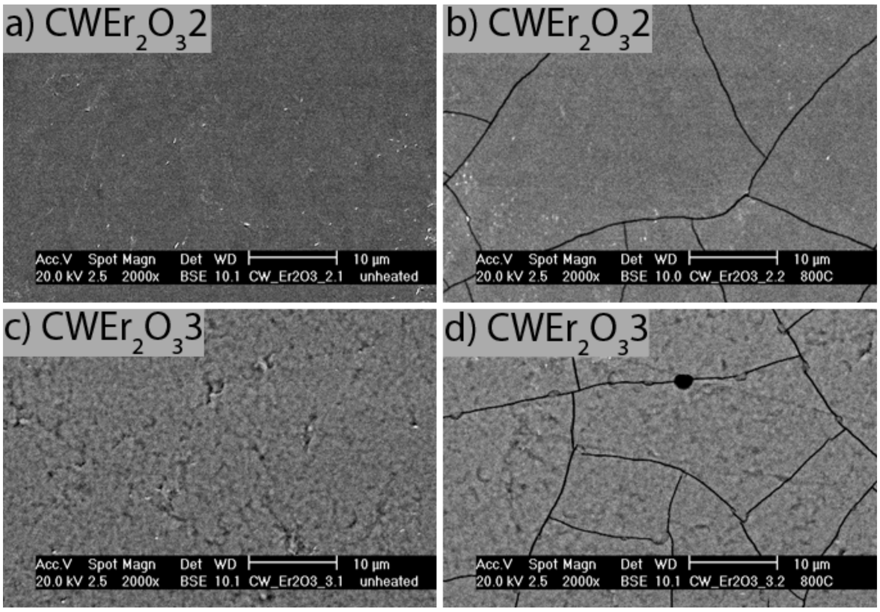

Figure 4.14: *SEM* images in *BSE* mode of graphite substrate with "Er$_2$O$_3$" layer coated by magnetron sputtering with and without annealing at 800 °C for 30 min: a) original sample (160 nm), b) annealed sample (160 nm), c) original sample (460 nm) and d) annealed sample (460 nm)

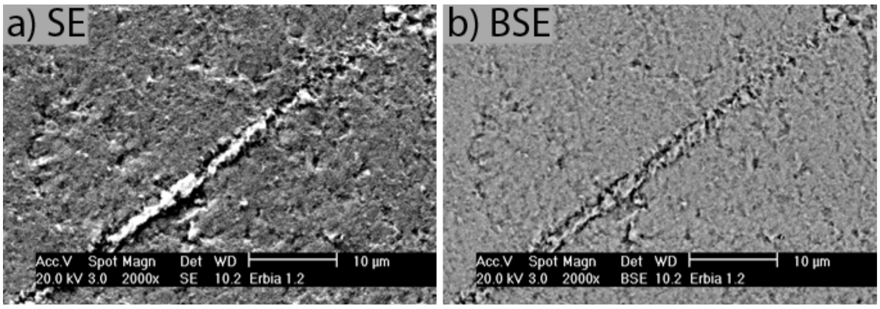

Figure 4.15: *SEM* images in *BSE* mode of graphite substrate with "Er$_2$O$_3$" layer (CWErbia1) coated by a filtered arc device at 600 °C

In Table 4.5 the composition of all the layers on graphite substrates with and without annealing is given. The layers deposited by magnetron sputtering have a higher O content before annealing than after.

	Annealing	Er [at.%]	O [at.%]
CWEr2O$_3$2	-	28	69
CWEr2O$_3$2	after deposition at 800 °C	36	61
CWEr2O$_3$3	-	28	71
CWEr2O$_3$3	after deposition at 800 °C	36	63
CWErbia1	during deposition at 600 °C	37	62

Table 4.5: Composition of the erbia layers deposited on graphite substrate in atomic percent

Perhaps, this redundant O has originally been incorporated in the layer defects and during annealing diffused to the sample surface. The annealed layers, as well as the layer produced by arc deposition, reveal a composition close to stoichiometric Er_2O_3.

The crystalline structure of the layers was examined by *XRD* (see Fig. 4.16). It was found that the as-deposited CWEr$_2$O$_3$2 possesses an amorphous structure, while after annealing the peaks that appeared are well fitted with a pattern corresponding to Er_2O_3 (Fig. 4.16a). In Fig. 4.16b an *XRD* pattern of the sample with two layers is given where Er_2O_3 serves as an interlayer and on top of the sample a EUROFER layer is deposited. As in the case of the annealed sputtered layer, the arc deposited layer reveals the same crystalline structure.

Finally, for the investigation of C diffusion in EUROFER through a Er_2O_3 layer, the sample CWErbia1 coated by arc deposition was chosen.

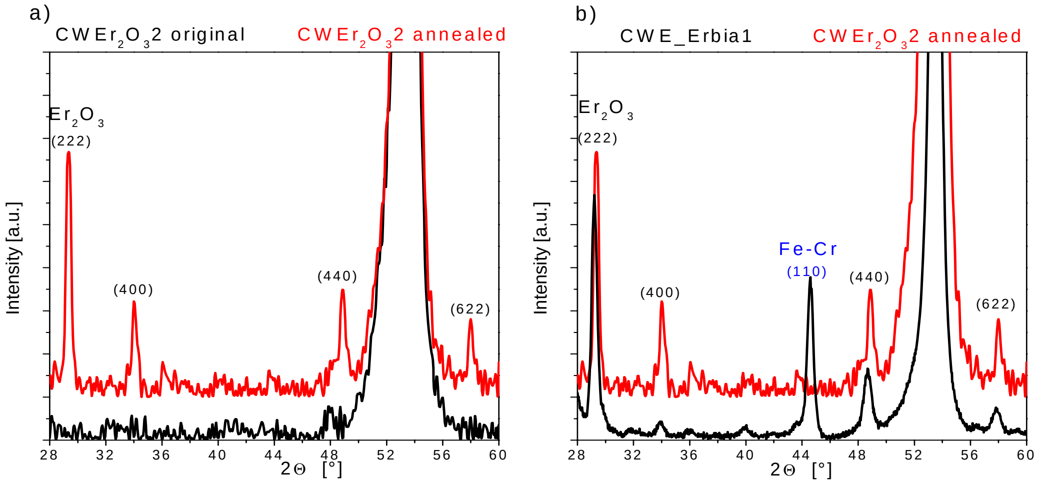

Figure 4.16: *XRD* spectra of Er_2O_3 layers on graphite substrates a) deposited by magnetron sputtering (the layer thickness 160 nm) with and without follow-up annealing at 800 °C for 30 min, b) Er_2O_3 layer deposited by the filtered arc device (the layer thickness 500 nm) at 600 °C in comparison with the Er_2O_3 layer (160 nm) deposited by magnetron sputtering and annealed at 800 °C for 30 min

4.2 Annealed samples

For the annealing experiments, EUROFER coatings deposited by magnetron sputtering with the enhanced magnetic configuration were used. Thick layers are described in more detail than thin ones because the former allow more analyses to be applied.

4.2.1 EUROFER layer

The SiC fibres were coated by both the magnetron and arc techniques. To simulate diffusion processes caused by heat loading during fabrication of the *MMC* and use at working temperatures, the fibres with 180 nm of magnetron and $\sim 6\,\mu$m of arc deposited coatings (SCS6E3A6) were annealed at temperatures of 600 and 800 °C for a duration of 2 h. *SEM* images of these specimens with and without annealing are shown in Fig. 4.17.

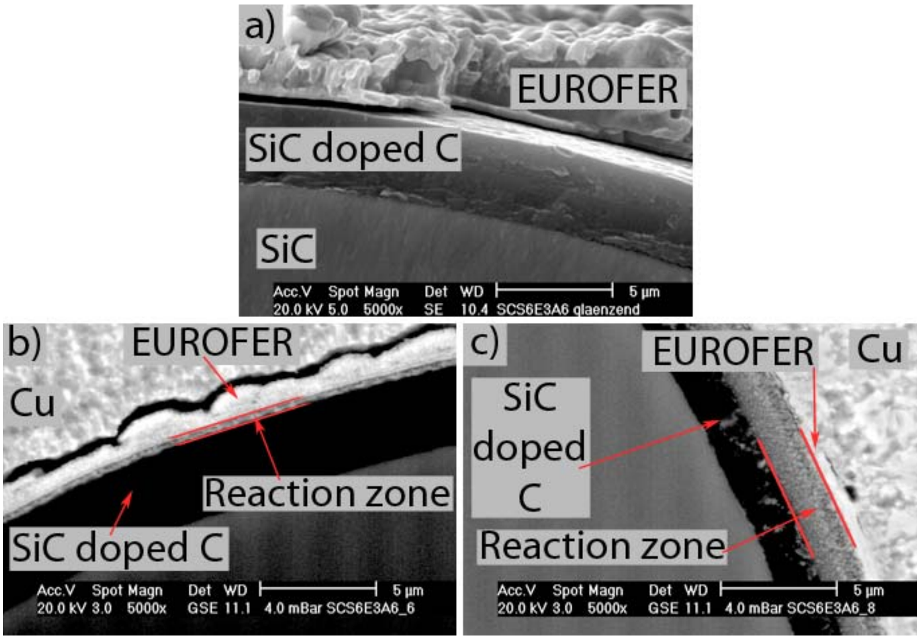

Figure 4.17: *SEM* images of SiC fibres coated by both the magnetron and arc techniques with and without annealing: a) original, b) annealed at 600 °C, and c) annealed at 800 °C (SCS6E3A6)

In Fig. 4.17a the fibre with both original layers is presented. The image was acquired from the pristine specimen without any preparation. The annealed fibres were additionally coated with Cu after annealing to protect layers from delamination during the following cross-section preparation and then were embedded in resin. The outer coating of the fibre, SiC doped C, reveals no difference in colour in the case of original sample, while for annealed coated fibres a zone with other colour appears marked with orange lines (see Figs. 4.17b and c). Let us refer this zone to as a reaction zone which is caused by the interdiffusion between the fibre and layers that can result in the formation of new compounds. As seen from Fig. 4.17c, the strong interdiffusion occurs between the elements of the EUROFER coating and the fibre even at a temperature of 800 °C. Consequently, after hipping at a temperature of 1000 °C part of the fibre will be dissolved in the steel matrix, which means a degradation of the composite properties. Obviously, more sophisticated analyses than *SEM* images are required to reveal processes which appear in the reaction zone, since the change of colour can be hardly visible or even mislead. But most of analyses are not applicable to fibres. Therefore, for a detailed picture of the reaction zone and the diffusion behaviour in the presence of interlayers, planar samples, pyrolytic graphite and SiC have been investigated.

Thin layer (50 nm of EUROFER)

Planar samples with a thin EUROFER layer of 50 nm in thickness were investigated by *SEM* with and without annealing in the temperature range of $400 - 1000$ °C for 2 h. The images of the samples with the SiC substrate (SiCE41) are given in Fig. 4.18 and those with graphite (CWE41) in Fig. 4.19. The as-deposited layer on both substrates reveals a fine structure (Figs. 4.18a and 4.19a). The defects, such as pores and grooves, in the case of the sample with SiC, belong to the substrate. The roughness of the graphite substrate is higher than that of the SiC one (60 nm for graphite and only 5 nm for SiC), therefore the EUROFER layer on graphite looks more rough than on SiC. The layer structure on both substrates does not change due to annealing at 400 °C in contrast to that at 600 °C. The hole formation is driven by surface diffusion and the beginning of crystal nucleation is observed for the SiCE41 sample after annealing at 600 °C (Fig. 4.18b). Higher temperatures of 750 and 1000 °C result in further crystal growth. In addition, coalescence of the holes leads to a labyrinth-like layer structure (Figs. 4.18c and d). *EDX* analysis of the crystal and the surrounding surface was done for the SiCE41 annealed at 1000 °C. The main elements of the crystal are found to be Fe and Cr, whereas the surrounding area contains only a small amount of Fe.

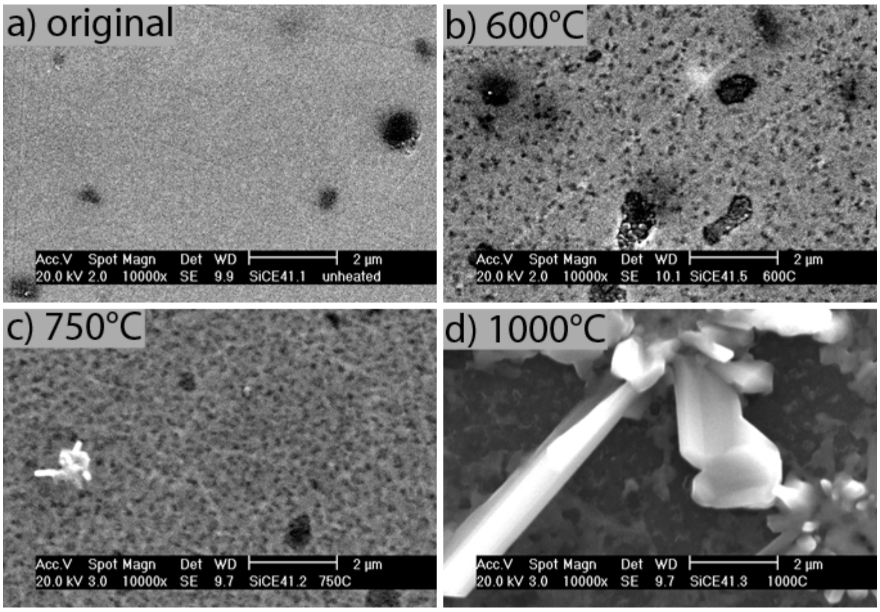

Figure 4.18: *SEM* images of samples with EUROFER layers on SiC with and without annealing in the temperature range of $400 - 1000$ °C for 2 h (SiCE41)

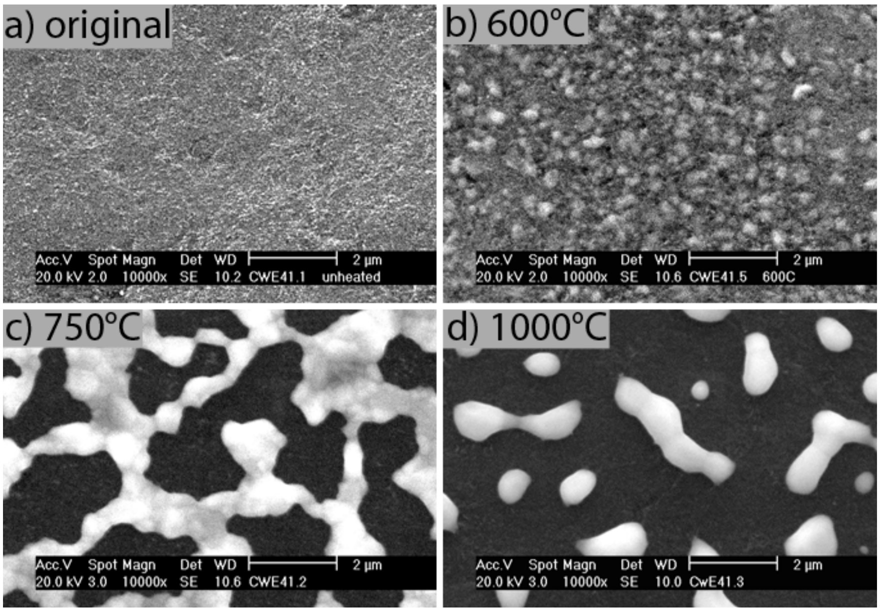

Figure 4.19: *SEM* images of samples with EUROFER layers on graphite with and without annealing in the temperature range of $400 - 1000\,^{\circ}\mathrm{C}$ for 2 h (CWE41)

The structure of the EUROFER layer of CWE41 begins to change in the temperature range 400 to 600 °C. The crystals formed at the surface of the sample after annealing at 600 °C consist of carbides (Fig. 4.19b). De-wetting of the formed carbide layer is observed in the temperature range 600 to 1000 °C revealing poor wetting on graphite. This mechanism was described in detail in [97, 98]. A labyrinth-like structure of the sample annealed at 750 °C (Fig. 4.19c) is an intermediate stage between holes and droplets formation. The holes appear due to surface diffusion at temperatures between 600 and 750 °C. The droplets' formation (Fig. 4.19d), i.e. the final stage, is observed for the sample annealed at 1000 °C.

The layer composition of the SiCE41 and CWE41 samples with and without annealing were investigated by *IBA*. In case of the sample with SiC substrate only the peaks of layer elements with atomic numbers higher than that of Si (14) are seen, since they do not overlap with the peak corresponding to Si. Therefore, in this case there is impossible to detect the C and O contents in the EUROFER layer because the atomic numbers of C and O are 6 and 8, respectively. The layer of SiCE41 reveals no difference in the layer composition to that of the sample as-deposited or annealed at 400 °C for 2 h. For the sample annealed at 600 °C there is no possibility to make a reliable estimation of the layer stoichiometry due to hole formation observed with *SEM*. The results of *IBA* of the samples with graphite substrate CWE41 with and without annealing are given in Fig. 4.20 and in Table 4.6. In Fig. 4.20a the concentration depth profile is related to the as-deposited sample, while in Fig. 4.20b the plot for the sample annealed at 600 °C is given. In spite of the fact that the layer structure does not change after annealing at 400 °C, the layer composition reveals an increase in the C content up to 7 at.%, in contrast to the as-deposited CWE41.

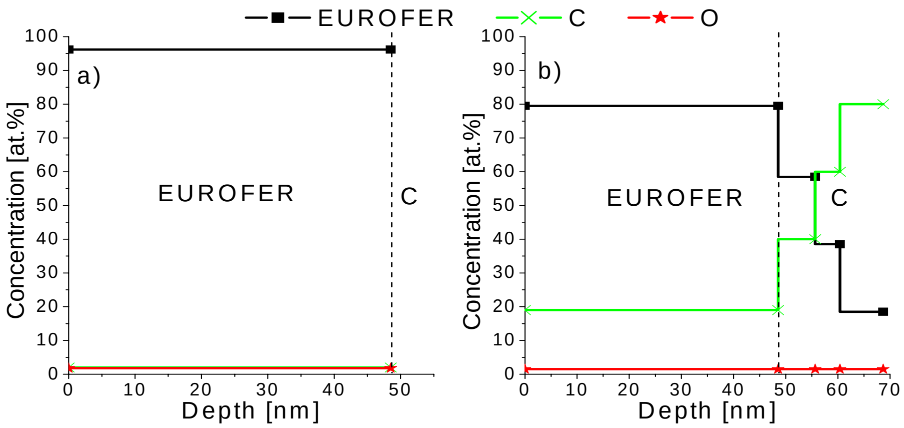

Figure 4.20: Concentration depth profiles of EUROFER layers on graphite substrate (CWE41) a) original and b) annealed at 600 °C for 2 h

Substrate	Graphite	
Layer	EUROFER	
Contamination	C [at.%]	O [at.%]
Original	2.0	2.0
Annealed at 400 °C	7.0	2.5
Annealed at 600 °C	19.0	1.5

Table 4.6: Mean contamination contents in the EUROFER layer with and without annealing for 2h, in atomic percent

Further increasing of the annealing temperature results in higher layer contamination with C. Thus, after heat treatment at 600 °C, 19 at.% of C is observed in the steel coating.

Thick layer (400 nm of EUROFER)

SEM images of the SiC and graphite substrates coated with 400 nm of EUROFER, with and without annealing at 750 °C for 2 h, are presented in Fig. 4.21. The as-deposited samples show a smooth surface. The sample with SiC substrate (SiCE43) reveals transformations after treatment similar to those on the SiCE41 (thin EUROFER layer of 50 nm on SiC). Hole formation in the EUROFER coating followed by agglomeration and growth of crystals are main features of the heated layer on the SiC substrate. In contrast to the SiCE43, after annealing the layer on graphite (CWE43) remains smooth however additionally crack propagation is observed.

In Fig. 4.22 results of *XRD* measurements are presented. The analysis was done only for the CWE43 sample, since in the case of the SiCE43, serious layer degradation was observed. The black line on the plot is related to the pattern of the as-deposited steel layer, while the red one characterises the annealed CWE43. A comparison of them brings to light the appearance of the cementite, i.e. Fe_3C phase, represented with a number of peaks.

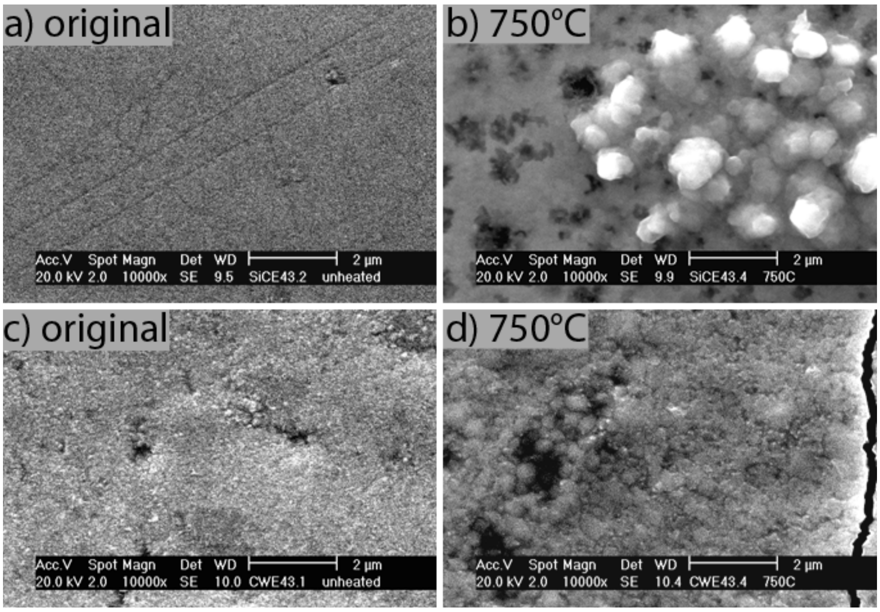

Figure 4.21: *SEM* images of samples EUROFER layers on SiC and graphite substrates with and without annealing at 750 °C for 2 h (SiCE43 and CWE43): a) and b) SiCE43, c) and d) CWE43

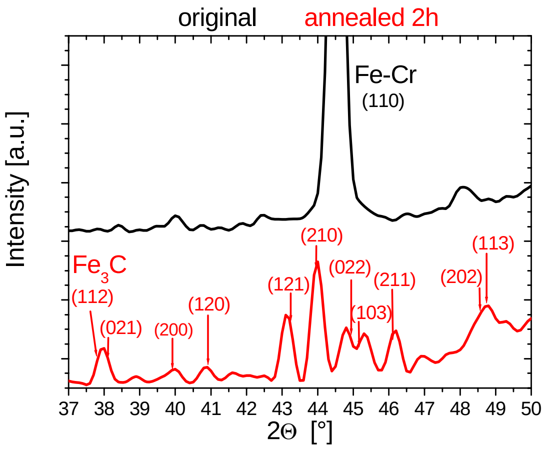

Figure 4.22: *XRD* spectra of samples with a EUROFER layer on graphite substrate with and without annealing at 750 °C for 2 h (CWE43)

A concentration depth profile in the reactive zone of the sample CWE43 is given in Fig. 4.23. As it was for the *XRD* spectra, the profiles of original and annealed samples are shown together for comparison. In Table 4.7 the mean contents of C and O in the EUROFER layer are presented. Heat treatment results in the interdiffusion of elements of both layer and substrate. Thus, the mean C concentration in the steel after annealing at 750 °C for 2 h is found to be of 27 at.% (7.2 wt.%). Data on the annealed CWE43 sample have been used for the calculation of the diffusion coefficient of C in EUROFER, which will be described in subsection 4.3.

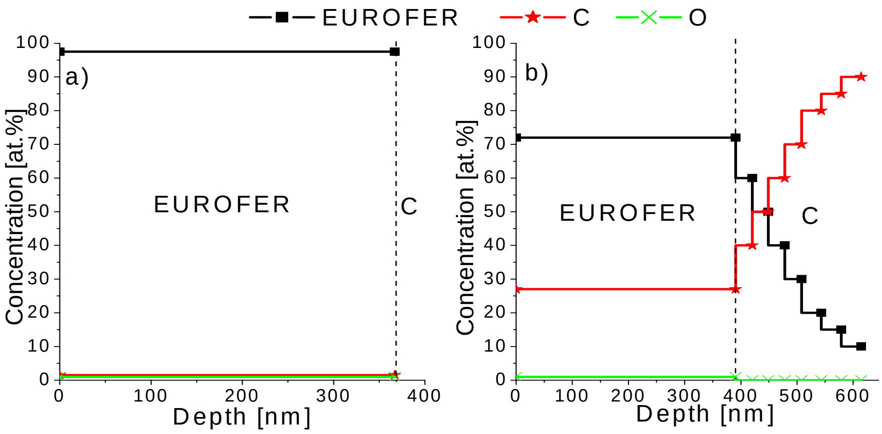

Figure 4.23: Concentration depth profiles of EUROFER layers on graphite substrate (CWE43) a) original and b) annealed at 750 °C for 2 h

Substrate	Graphite	
Layer	EUROFER	
Contamination	C [at.%]	O [at.%]
Original	1.5	1.0
Annealed at 750 °C	27.0	1.0

Table 4.7: Mean contamination contents in the EUROFER layer with and without annealing for 2h, in atomic percent

4.2.2 EUROFER layer with Me interlayer

Different metallic interlayers have been investigated as diffusion barriers to suppress C diffusion in EUROFER.

Ti

As a first attempt, a Ti interlayer was selected because the SiC fibres used in this work were originally specified for application with a Ti matrix.

Thin layers (40 nm of Ti / 50 nm of EUROFER)

The samples with thin Ti (40 nm) and thin EUROFER (50 nm) layers on both SiC (SiCE_Ti2) and graphite (CWE_Ti2) substrates were annealed in the temperature range 400 to 1000 °C for 2 h. *SEM* images of these samples are presented in Figs. 4.24 and 4.25. The layer surfaces remain smooth after annealing at 400 °C, while at 600 °C both samples appear to change. Hole formation is observed in the layers of the SiCE_Ti2 sample (Fig. 4.24b). An increase in the annealing temperature leads to layer agglomeration. The heterogeneous structure of the layer related to the SiCE_Ti2 heated to 1000 °C (Fig. 4.24d) has white formations that have been investigated further by *EDX*. They are found to consist mainly of Fe, whereas the grey areas have more Ti than Fe. The grains seen on the image belong to the SiC substrate.

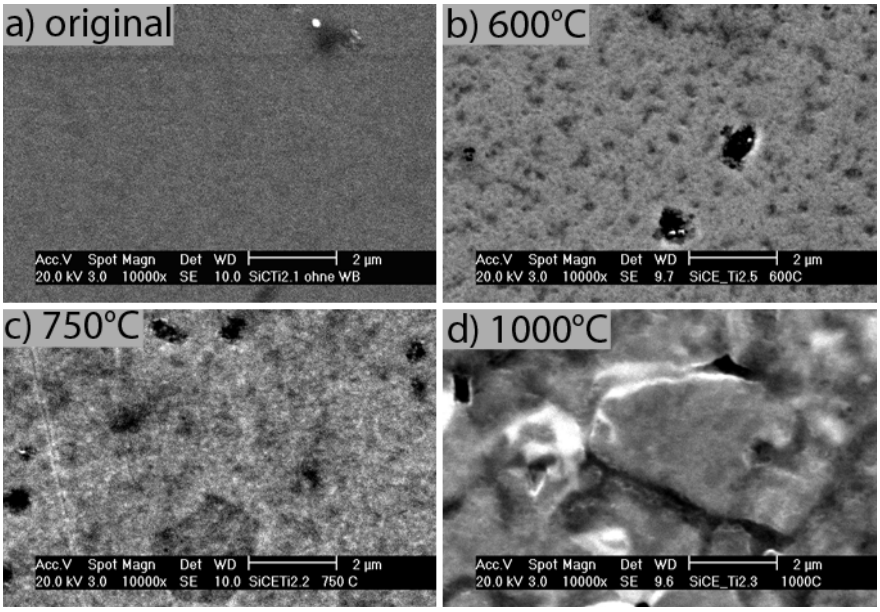

Figure 4.24: *SEM* images of samples with Ti / EUROFER layers on SiC with and without annealing in the temperature range of $400-1000\,^{\circ}\mathrm{C}$ for 2 h (SiCE_Ti2)

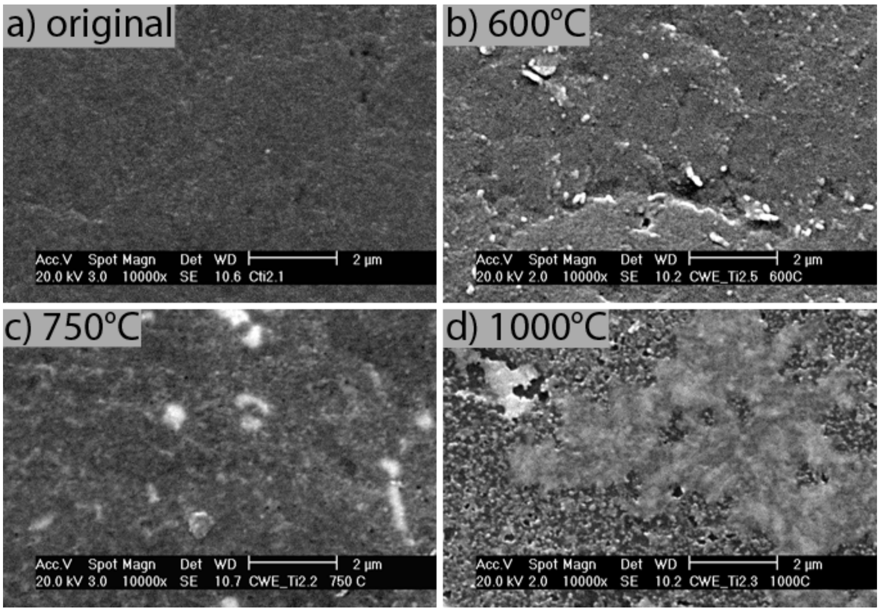

Figure 4.25: *SEM* images of samples with Ti / EUROFER layers on graphite with and without annealing in the temperature range of $400-1000\,^{\circ}\mathrm{C}$ for 2 h (CWE_Ti2)

In contrast to the SiCE_Ti2 sample, the CWE_Ti2 shows white particles that appear on the surface under annealing at 600 °C (Fig. 4.25b) and grow further with increased temperatures. The steel layer after annealing at 1000 °C (Fig. 4.25d) agglomerates at vertices formed by grains due to surface diffusion. The white particles consist of a higher Fe content than in the surrounding, as was observed for the SiCE_Ti2 sample. The rest of the layer shown in the *SEM* image in Fig. 4.25d has high Ti concentration and small amount of Fe.

In Fig. 4.26 and Table 4.8 the results of *IBA* for original and annealed samples are given. There is no difference found between the concentration depth profiles of the as-deposited and heated SiCE_Ti2 samples at 400 °C. *IBA* investigation of the samples with SiC substrate annealed at higher temperatures would be incorrect, since hole formation and layer agglomeration were observed (see Fig. 4.24b). In contrast to SiCE_Ti2, the Ti and Fe layers of the sample with graphite substrate CWE_Ti2 start to mix already at 400 °C. Additionally, C diffusion in the Ti layer results in 20 at.% of C in contrast to 9 at.% in the as-deposited layer. After annealing at the higher temperature of 600 °C, Ti diffuses through the steel layer and accumulates at the surface of the sample. Therefore, its concentration at the surface is found to be higher than in the EUROFER layer. High Fe and C contents are detected in "Ti" layer: 24.5 and 31.0 at.%, correspondingly.

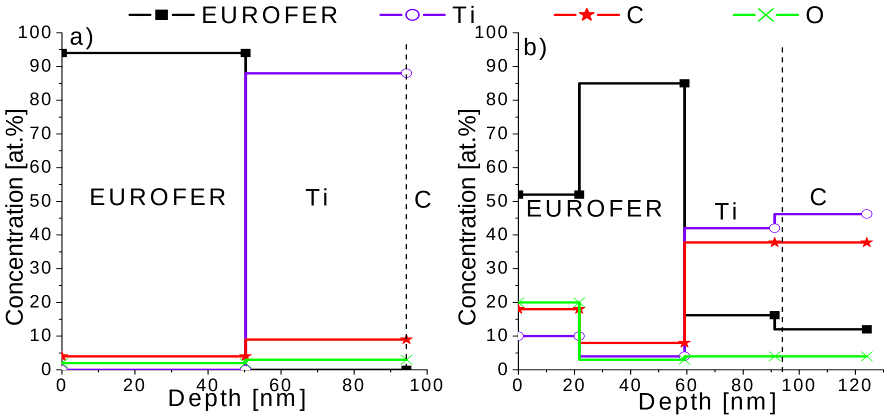

Figure 4.26: Concentration depth profiles of Ti / EUROFER layers on graphite substrate (CWE_Ti2) a) original and b) annealed at 600 °C for 2 h

Substrate	SiC	Graphite					
Layer	EUROFER	EUROFER			Ti		
Contamination	Ti [at.%]	C [at.%]	O [at.%]	Ti [at.%]	C [at.%]	O [at.%]	Fe [at.%]
Original	–	4.0	2.0	–	9.0	3.0	–
Annealed at 400 °C	–	3.0	3.0	1.0	20.0	5.0	2.0
Annealed at 600 °C		6.5	2.0	12.0	31.0	4.0	24.5

Table 4.8: Mean contamination contents in the EUROFER layer with thin Ti interlayer with and without annealing for 2h, in atomic percent

Thick layers (500 nm of Ti / 500 nm of EUROFER)

The samples with a 500 nm Ti layer and the same thickness of EUROFER on SiC (SiCE_Ti3) (Figs. 4.27a and b) and graphite (CWE_Ti3) (Figs. 4.27c and d) substrates were annealed at 750 °C for 2 h and further investigated by a number of techniques. The as-deposited layers of both the SiCE_Ti3 and CWE_Ti3 samples have a smooth surface (Figs. 4.27a and c).

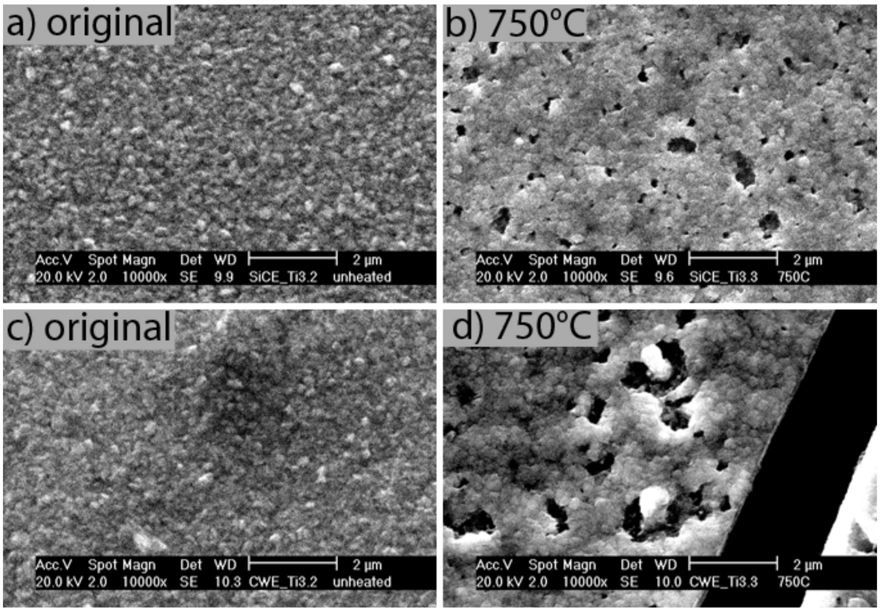

Figure 4.27: *SEM* images of samples with Ti / EUROFER layers on SiC and graphite substrates with and without annealing at 750 °C for 2 h: a) and b) SiCE_Ti3; c) and d) CWE_Ti3

In contrast, the annealed SiCE_Ti3 sample reveals not only crack propagation but also partial layer delamination. Only a small part of the layers of the CWE_Ti3 sample remains at the surface after annealing (Fig. 4.27d). Crack formation and partial layer delamination are observed in this part. Hole formation together with the appearance of particles are observed on both the SiCE_Ti3 and CWE_Ti3 samples.

The *IBA* and *XRD* investigations were not conducted due to the inappropriate surface conditions of these samples.

Cr

Cr has been chosen for suppression of C diffusion in EUROFER because of the low diffusivity of C in Cr. In addition, Fe has medium diffusivity in Cr which could help protect the layers from mixing and could also result in a good bonding due to interdiffusion.

Thin layers (50 nm of Cr / 50 nm of EUROFER)

The samples with a thin Cr (50 nm) and thin EUROFER (50 nm) layers on SiC (SiCE_Cr1) and graphite (CWE_Cr1) substrates were annealed in the temperature range 400 to 1000 °C. *SEM* images of these samples are shown in Figs. 4.28 and 4.29. The defects, pores, grooves from polishing, and cracks that appear in the images are related to the substrates. There is no difference observed between the original samples and those annealed at 400 °C on both substrates. The layers reveal a smooth structure in both the cases of SiCE_Cr1 and CWE_Cr1 as-deposited and annealed at temperatures up to 750 °C. Holes appear in the layer of SiCE_Cr1 at 600 °C due to surface diffusion (Fig. 4.28b).

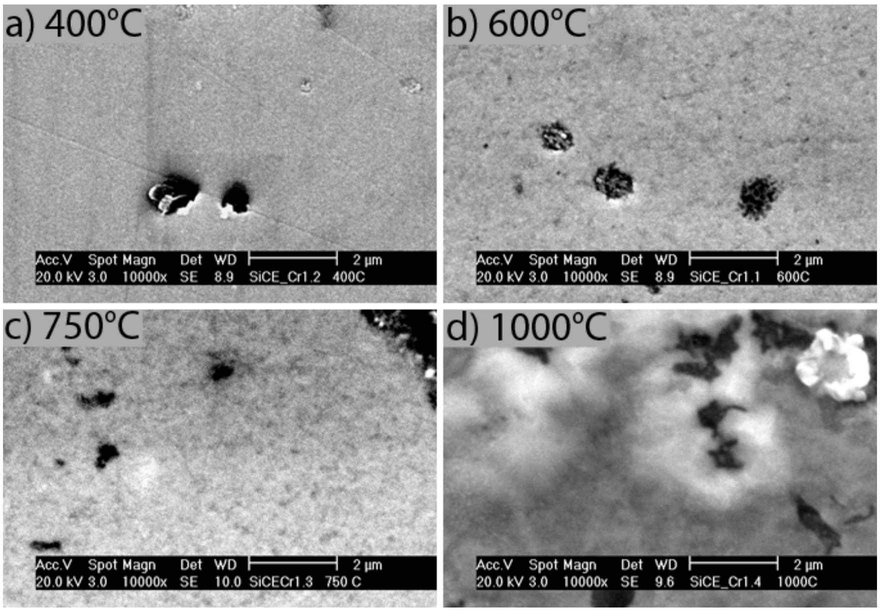

Figure 4.28: *SEM* images of samples with Cr / EUROFER layers on SiC annealed in the temperature range of 400 – 1000 °C for 2 h (SiCE_Cr1)

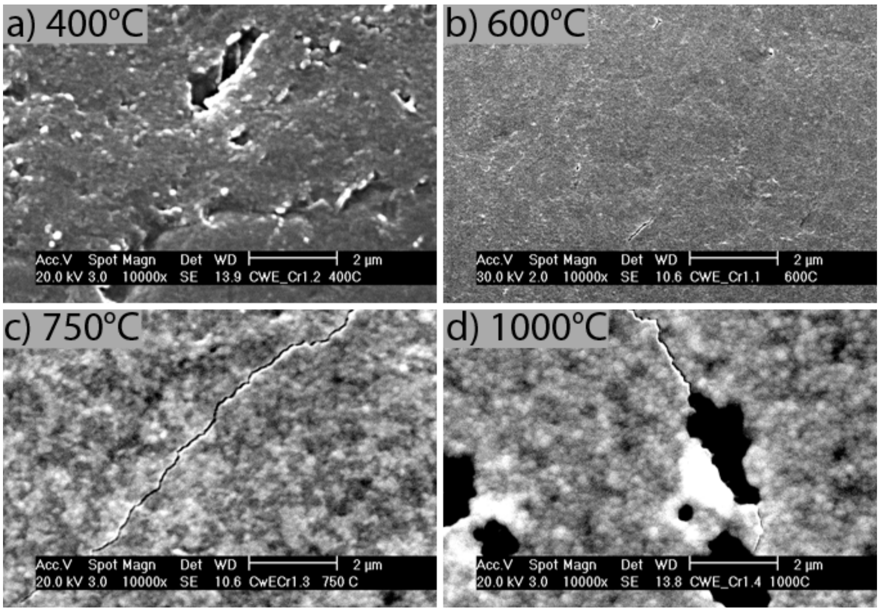

Figure 4.29: *SEM* images of samples with Cr / EUROFER layers on graphite annealed in the temperature range of 400 – 1000 °C for 2 h (CWE_Cr1)

Annealing at 750 °C intensifies this process and further growth of the holes is detected for the layers of SiCE_Cr1 (Fig. 4.28c). Small crystals are built on the surface during annealing at 1000 °C (Fig. 4.28d). The zones presented on the image as bright areas consist mainly of Fe and Cr, whilst grey areas have more Cr and only a small amount of Fe.

Crack initiation is observed on CWE_Cr1 caused by annealing at 600 °C with further propagation at higher temperature of 750 °C (Figs. 4.29b and c). In addition, the layer reveals the appearance of precipitates in the form of white specks at this temperature. Due to the small size of these formations it was impossible to carry out *EDX* analysis of the specks. The arrangement of the holes observed on the layers of CWE_Cr1 after annealing at 1000 °C (Fig. 4.29d) repeats grain boundaries of the underlying substrate.

Diffusion interaction between the layers and substrates caused by annealing was investigated by means of *IBA*. The samples annealed at temperatures above 600 °C were not examined, since at these temperatures the layers appeared to not cover the substrate completely. The results of the analysis are given in Figs. 4.30 and 4.31, and Table 4.9 for both substrates. In Table 4.9 the value of Cr diffused from the interlayer into EUROFER is written as the concentration of Cr (interlayer) in EUROFER. After annealing at 400 °C the Cr concentration in the steel for SiCE_Cr1 remained the same 10 at.% as in the original EUROFER layer within the error limits, whereas Fe diffused into the Cr interlayer and its concentration was 6 at.%. For CWE_Cr1 the content of Cr in EUROFER in the steel increased by 4 at.%, i.e. the total content of Cr in the EUROFER layer after annealing was 14 at.%.

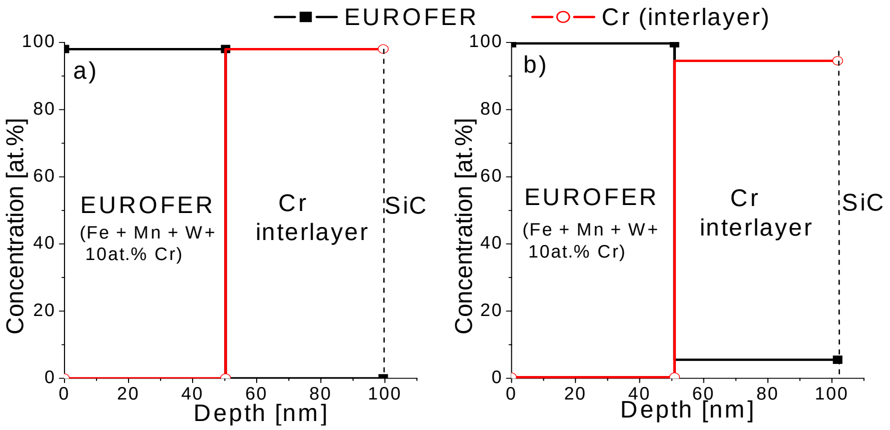

Figure 4.30: Concentration depth profiles of Cr (interlayer) / EUROFER layers on SiC substrate (SiCE_Cr1) a) original and b) annealed at 400 °C

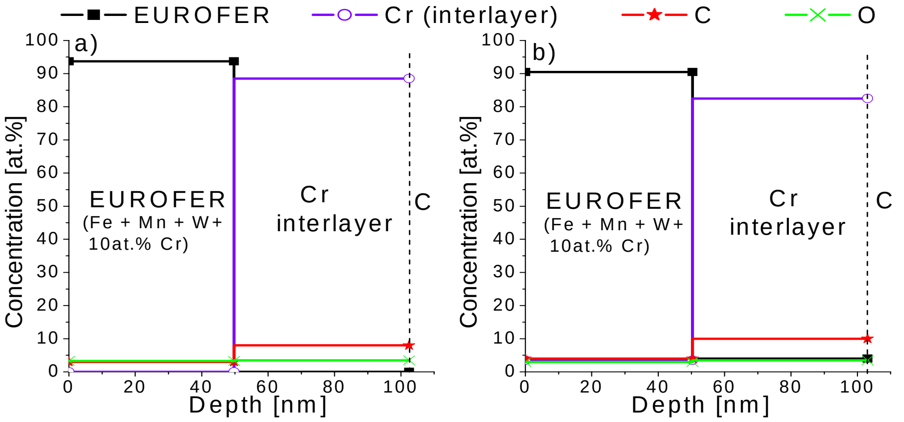

Figure 4.31: Concentration depth profiles of Cr (interlayer) / EUROFER layers on graphite substrate (CWE_Cr1) a) original and b) annealed at 400 °C

Furthermore, 4 at.% of Fe was observed in Cr due to interdiffusion between these two layers for the sample CWE_Cr1. Consequently, the Cr and EUROFER layers started to react at temperatures below 400 °C. Additionally, the C content in both the layers of CWE_Cr1 rose. After annealing at 600 °C the Cr and EUROFER layers appeared to be completely mixed for both SiCE_Cr1 and CWE_Cr1, i.e. the Cr content in EUROFER and the Fe content in Cr were so high that peaks in IBA spectra corresponded to Cr and Fe overlapped completely. Therefore, the word of “mixture” is given in the columns of Table 4.9 instead of the Cr and Fe concentration values. As for C, its content increased up to 31 at.% in “EUROFER” and to 36 at.% in “Cr” of CWE_Cr1.

Substrate	SiC	Graphite					
Layer	EUROFER	EUROFER			Cr		
Contamination	Cr (interlayer) [at.%]	C [at.%]	O [at.%]	Cr (interlayer) [at.%]	C [at.%]	O [at.%]	Fe [at.%]
Original	–	3.0	3.5	–	8.0	3.5	–
Annealed at 400 °C	–	4.0	3.5	4	10.0	3.5	4.0
Annealed at 600 °C	mixture	31.0	3.0	mixture	36.0	3.0	mixture

Table 4.9: Mean contamination contents in the EUROFER layer with thin Cr interlayer with and without annealing for 2h, in atomic percent

Thick layers (500 nm of Cr / 500 nm of EUROFER)

The samples consisting of 500 nm of Cr and 500 nm of EUROFER layers on SiC (SiCE_Cr4) and graphite (CWE_Cr4) substrates with and without annealing are presented in Fig. 4.32.

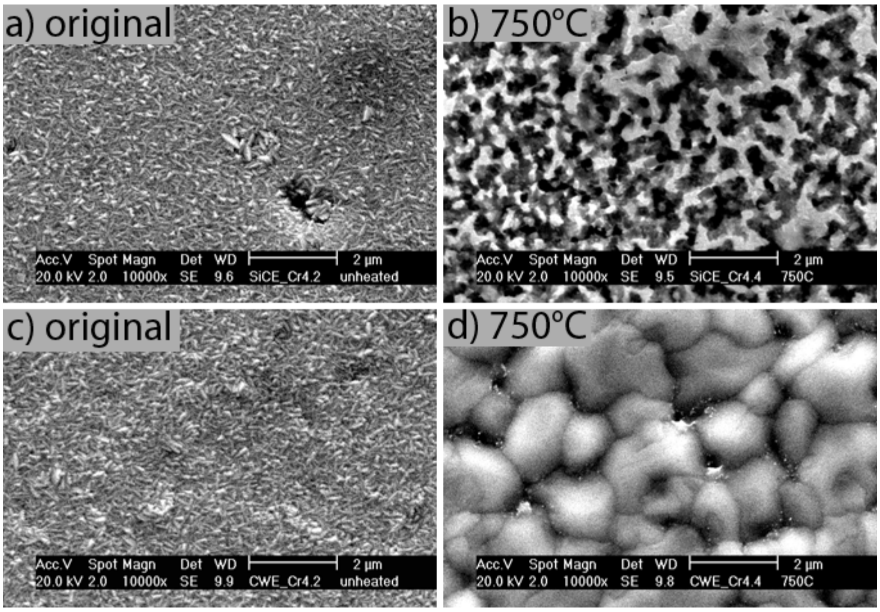

Figure 4.32: *SEM* images of samples with Cr / EUROFER layers on SiC and graphite substrates with and without annealing at 750 °C for 2 h (SiCE_Cr4 and CWE_Cr4): a) and b) SiCE_Cr4, c) and d) CWE_Cr4

The as-deposited layer reveals a smooth structure for both SiCE_Cr4 and CWE_Cr4 (Figs. 4.32a and c). Annealing of the SiC_Cr4 results in a sponge-like structure of the layer. On the *SEM* image (Fig. 4.32b) the bright areas are related to the rest of the layer, while the dark areas show the substrate located beneath. On graphite substrate the layers become cracked and form grains, differing from the grains of the substrate (Fig. 4.32d).

In Fig. 4.33 the results of *XRD* measurements are given. A comparison of the patterns of the original (black line) and annealed (red line) SiCE_Cr4 sample (see 4.33a) brings to light the appearance of new phases caused by mixing of the layers and decomposition of the substrate. Thus, peaks related to the new phases of Fe_3Si, $M_{23}C_6$, $(Fe, Cr)_{23}C_6$, and M_7C_3, $(Fe, Cr)_7C_3$, are found on the surface. For CWE_Cr4 the formation of new phases is also observed (see Fig. 4.33b), namely the peaks of cementite, Fe_3C, and Cr carbide, Cr_7C_3, are clearly seen on the signature of the annealed sample.

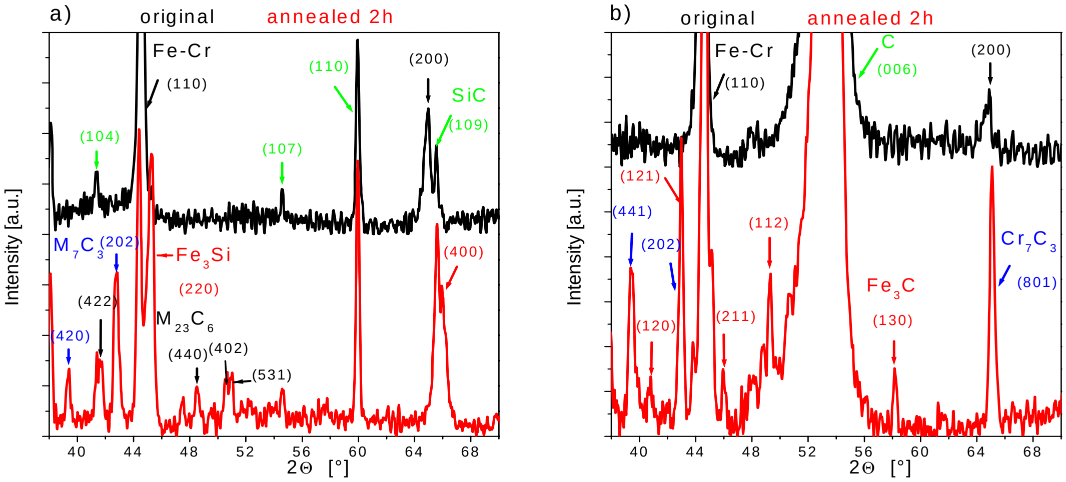

Figure 4.33: *XRD* spectra of samples with Cr / EUROFER layers a) on SiC and b) on graphite substrates with and without annealing at 750 °C for 2 h (SiCE_Cr4 and CWE_Cr4)

Due to the structure of the annealed SiCE_Cr4 it was not possible to carry out *IBA* investigations of the sample, therefore in Table 4.10 data of *IBA* analysis for CWE_Cr4 are only presented.

Substrate	Graphite		
Layer	EUROFER		
Contamination	C [at.%]	O [at.%]	Cr (interlayer) [at.%]
Original	1.0	2.0	–
Annealed at 750 °C	30.0	2.0	mixture

Table 4.10: Mean contamination contents in the EUROFER layer with thick Cr interlayer with and without annealing for 2h, in atomic percent

As was observed on thin layers of both SiCE_Cr4 and CWE_Cr1, annealing results in complete mixing of the layers of EUROFER and Cr. In addition to mixing, C has diffused through this newly formed layer and its concentration is 30 at.% near the sample's surface. Fe and Cr peaks overlap due to interdiffusion and it is impossible to detect their concentrations in the layers. Therefore, the concentration depth profile is not presented.

W

W has been chosen as a diffusion barrier for several reasons: low diffusion of C in W, low diffusion of Fe in W, and low self-diffusion of W. W forms carbides, therefore, during lengthy annealing C diffusion is assumed to be suppressed better than without annealing due to WC formation, since C diffusion is lower in WC than in pure W.

Thin layers (50 nm of W / 50 nm of EUROFER)

The samples with thin W (50 nm) and thin EUROFER (50 nm) layers on SiC (SiCE_W1) and graphite (CWE_W1) substrates were annealed in the temperature range from 400 to 1000 °C and *SEM* images of the samples are presented in Figs. 4.34 and 4.35. The layers on both substrates reveal a smooth surface before annealing (Figs. 4.34a and 4.35a). In the case of the SiCE_W1 sample not only are grooves from polishing observed but also pores of the substrate material become apparent on the layer surface. There are no visible changes seen in the layer structure of the original sample or the annealed one at temperatures below 600 °C (Fig. 4.34b). Layer mixing and agglomeration are observed for both SiCE_W1 and CWE_W1 annealed at 750 and 1000 °C (Figs. 4.34c and d, Figs. 4.35c and d). The precipitates that appeared at temperatures between 600 and 750 °C, start to join. These precipitates are clearly visible, especially in *BSE* mode, due to the difference in the atomic numbers of Fe (26) and W (74). In addition to precipitates, crack propagation is a distinctive feature for the CWE_W1 sample (Fig. 4.35c).

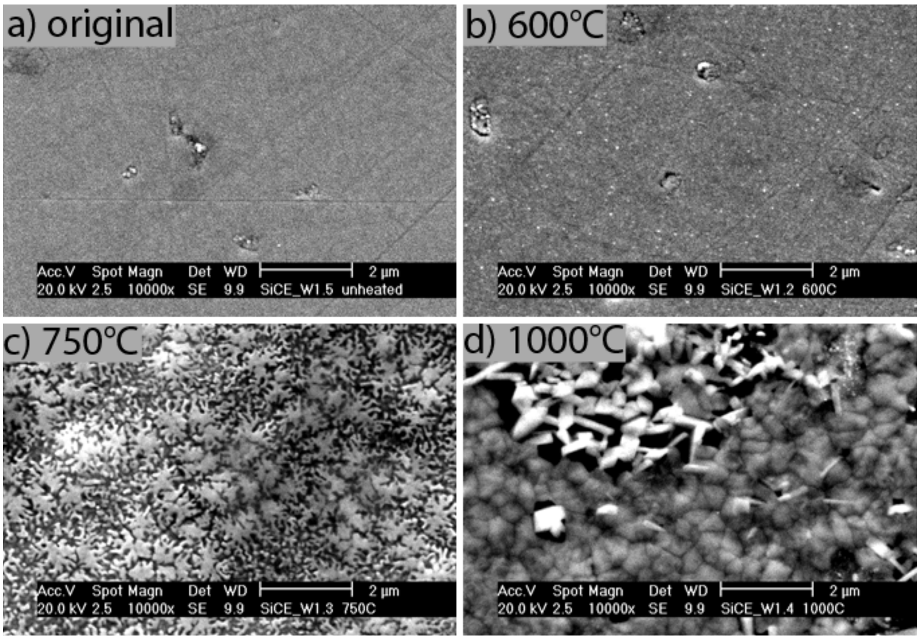

Figure 4.34: *SEM* images of samples with W / EUROFER layers on SiC with and without annealing in the temperature range of 400 – 1000 °C for 2 h (SiCE_W1)

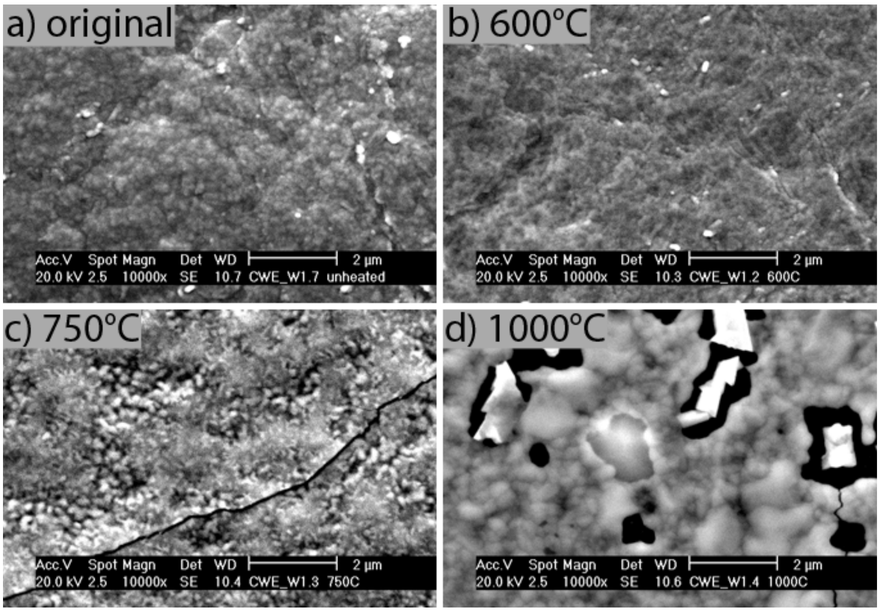

Figure 4.35: *SEM* images of samples with W / EUROFER layers on graphite with and without annealing in the temperature range of 400 – 1000 °C for 2 h (CWE_W1)

Upon annealing at 1000 °C crystals have been formed in both SiCE_W1 and CWE_W1. They are located directly on the substrate without any layer near their boundaries. The rest of the layer has a fine grain structure.

In Figs. 4.36 and 4.37 the results of *IBA* for original and annealed samples are shown. For clarity, the axis corresponded to the concentration of SiCE_W1 is made with a break. In Table 4.11 the contamination contents in the layers of SiCE_W1 and CWE_W1 are given. In the Table 4.11 the value for W diffused from the interlayer into EUROFER is given as the concentration of W (interlayer) in EUROFER.

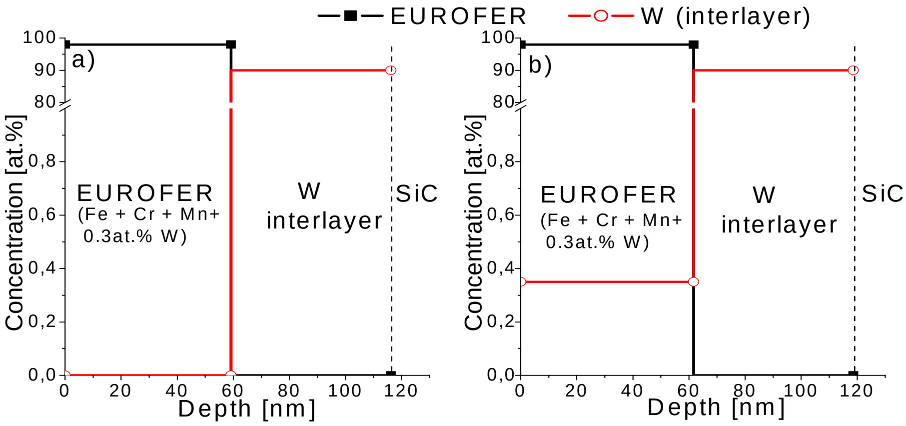

Figure 4.36: Concentration depth profiles of W (interlayer) / EUROFER layers on SiC substrate (SiCE_W1) a) original and b) annealed at 600 °C

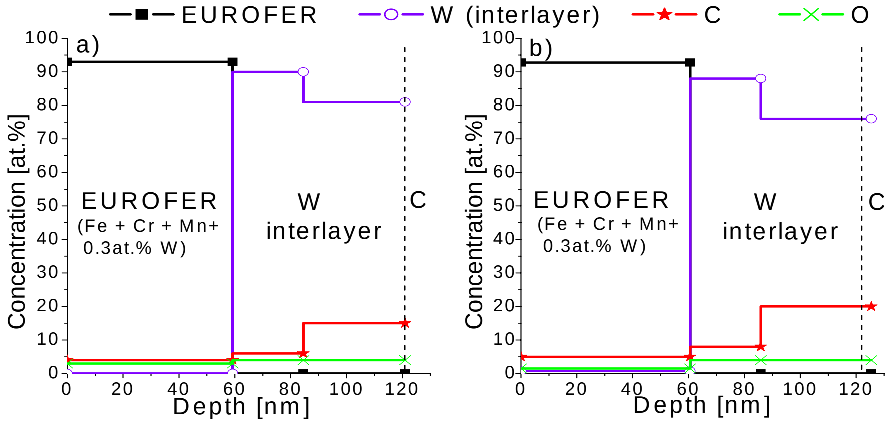

Figure 4.37: Concentration depth profiles of W (interlayer) / EUROFER layers on graphite substrate (CWE_W1) a) original and b) annealed at 600 °C

Substrate	SiC	Graphite				
Layer	EUROFER	EUROFER			W	
Contamination	W (interlayer) [at.%]	C [at.%]	O [at.%]	W (interlayer) [at.%]	C [at.%]	O [at.%]
Original	–	4.0	3.0	–	11.0	4
Annealed at 400 °C	–	4.0	4.5	–	13.0	6
Annealed at 600 °C	0.4	5.0	4.0	0.8	15.0	4

Table 4.11: Mean contamination contents in the EUROFER layer with thin W interlayer with and without annealing for 2h, in atomic percent

In the original W layer of CWE_W1 the C contamination of 6 at.% was observed, which increased to 15 at.% upon approaching the substrate. There are no changes found in the profiles of both SiCE_W1 and CWE_W1 after annealing at 400 °C, while annealing at 600 °C affects both C and W diffusion. For SiCE_W1, the W content of 0.4 at.% was higher than that in the original sample, i.e. the total content of W in the EUROFER layer after annealing was 0.7 at.%, since the content of W in the as-deposited EUROFER was 0.3 at.%. In the case of CWE_W1, C and additional W diffused from the W interlayer were observed in the EUROFER layer with the concentrations of 5 at.% and 0.8 at.%, respectively. The C concentration profile in the W interlayer had a step, thus near the steel only 8 at.% of C was detected, while near the substrate it was 20 at.%.

Thick layers (500 nm of W / 500 nm of EUROFER)

SEM images of the samples with 500 nm of W / 500 nm of EUROFER layers on SiC (SiCE_W2) and graphite (CWE_W2) substrates with and without annealing at 750 °C for 2 or 16 h are presented in Figs. 4.38 and 4.39, correspondingly. The original samples and those annealed for 2 h show a smooth layer structure (see Figs. 4.38a and b, and Figs. 4.39a and b). The annealed SiCE_W2 and CWE_W2 reveal a heterogeneous structure that appears as white specks on the images taken by means of *BSE*. An *EDX* analysis of them is impossible due to their small size. Annealing for a longer duration time results in infrequently disposed crystal growth for SiCE_W2 (as shown on the image with a low magnification, Fig. 4.38c). Crack formation and partial layer delamination were observed in the case of the sample with graphite substrate CWE_W2 (Fig. 4.39c).

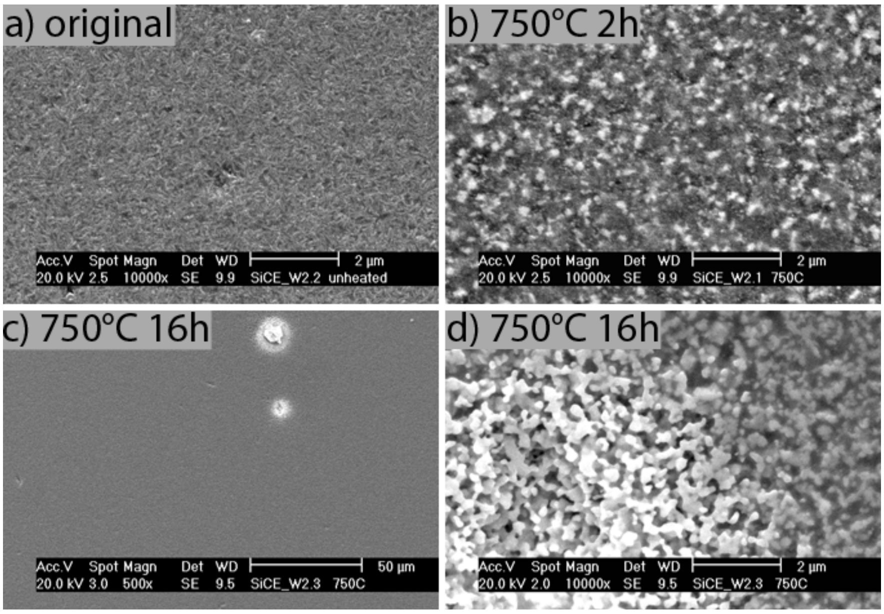

Figure 4.38: *SEM* images of samples with W / EUROFER layers on SiC with and without annealing at 750 °C for 2 and 16 h (SiCE_W2): a) magnification ×10000, b) magnification ×10000, c) magnification ×500 and d) magnification ×10000

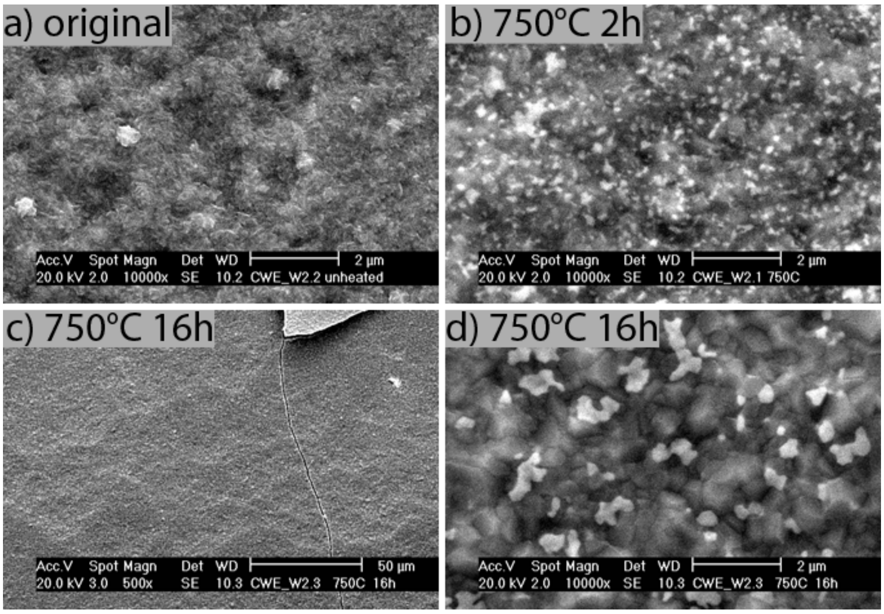

Figure 4.39: *SEM* images of samples with W / EUROFER layers on graphite with and without annealing at 750 °C for 2 and 16 h (CWE_W2): a) magnification ×10000, b) magnification ×10000, c) magnification ×500 and d) magnification ×10000

The *XRD* spectra of the original and annealed samples (see Fig. 4.40) demonstrate a big difference between the layers of SiCE_W2 and CWE_W2. In Fig. 4.40a three spectra are given belonging to the SiCE_W2: the original sample (black line); the sample annealed for 2 h (red line); and the sample annealed for 16 h (blue line). No new phases appear due to these heat treatment procedures, while peaks of new compounds are observed for the CWE_W2 due to C and W diffusion. Therefore, for the following calculation of the diffusion coefficient of W in EUROFER (described in subsection 4.3) the SiCE_W2 has been taken. In this case there are no compounds formed with substrate elements which can influence the rate of interdiffusion between layers.

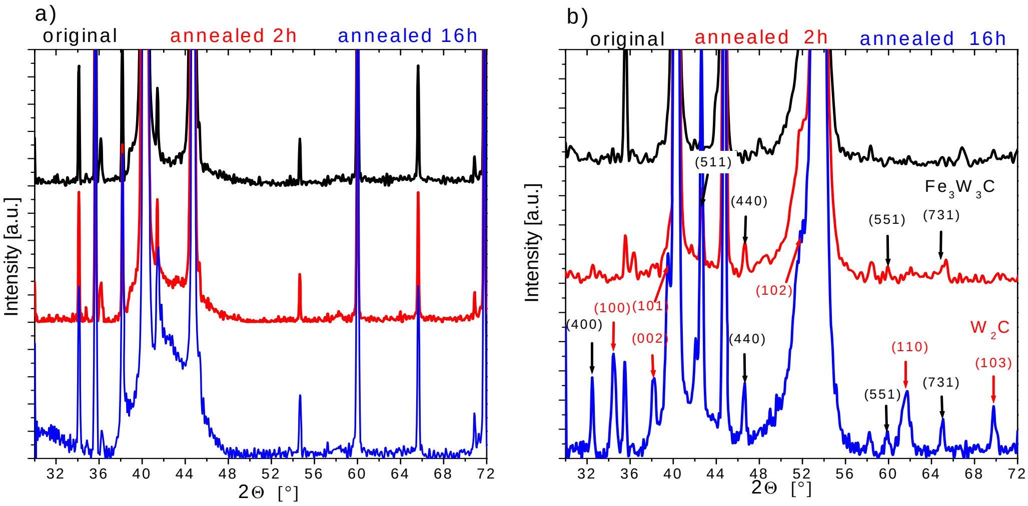

Figure 4.40: *XRD* spectra of samples with W / EUROFER layers a) on SiC and b) on graphite substrates with and without annealing at 750 °C for 2 and 16 h (SiCE_W2 and CWE_W2)

In Fig. 4.40b three spectra are given for the CWE_W2 in the same order as for the SiCE_W2: the original sample (black line); the sample annealed for 2 h (red line) with a Fe_3W_3C phase with peaks corresponded to the planes (511), (440), (551), and (731); and the sample annealed for 16 h (blue line) with the same Fe_3W_3C phase with addition of one more peak (400) and a new phase of W_2C with the peaks (100), (002), (101), (102), (110), and (103). The position of both the phases on the spectra are in a good agreement with *XRD* literature patterns.

The interdiffusion of EUROFER and W layers was investigated by analysing the *IBA* spectra of the SiCE_W2 sample with and without annealing. The concentration depth profiles are given in Fig. 4.41: a) spectrum of the original sample, b) spectrum of the sample annealed at 750 °C for 2 h, and c) spectrum of the sample annealed at 750 °C for 16 h. Additional W from the interlayer diffuses through EUROFER and its mean concentration in the steel layer after annealing for 2 h is 7.4 at.%, while after longer annealing of 16 h it rises up to 15.9 at.%. Therefore, the total W content in the EUROFER layer after annealing procedures is 7.7 at.% and 16.2 at.% for the samples annealed for 2 and 16 h, correspondingly.

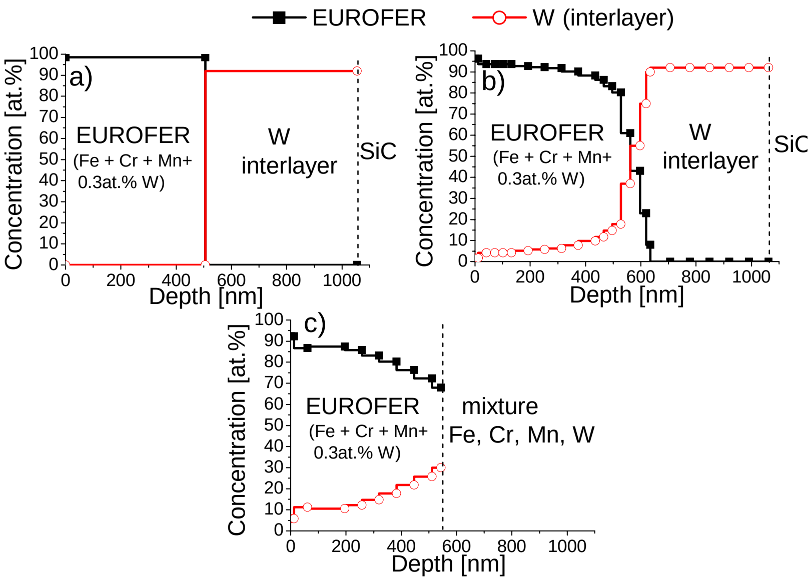

Figure 4.41: Concentration depth profiles of a) original, b) annealed at 750 °C for 2 h and c) annealed at 750 °C for 16 h samples with W (interlayer) / EUROFER layers on SiC (SiCE_W2)

In contrast to the spectrum in Fig. 4.41b, the spectrum in Fig. 4.41c contains only the concentration depth profile within the "EUROFER" layer. In this case it is impossible to detect the composition of the "W" layer due to intermixing of the EUROFER layer components and W because of the peaks overlapping. Values of the mean concentration of additional W diffused from W interlayer for all the samples are shown in Table 4.12.

Substrate	SiC	Graphite				
Layer	EUROFER	EUROFER			W	
Contamination	W (interlayer) [at.%]	C [at.%]	O [at.%]	W (interlayer) [at.%]	C [at.%]	O [at.%]
Original	–	2.0	2.0	–	3.0	2.0
Annealed for 2 h	7.4	3.0	2.0	5.5	8.0	2.5
Annealed for 16 h	15.9	7.0	2.0	6.9	15.5	2.5

Table 4.12: Mean contamination contents in the EUROFER layer with thick W interlayer with and without annelaing at 750C, in atomic percent

To investigate C and W diffusion into the EUROFER layer of the CWE_W2 sample, the concentration depth profiles were analysed. In Fig. 4.42 the profiles of the original sample annealed for 2 h and 16 h are plotted. For convenience, the same data is also given in Table 4.12. Only 3.0 at.% of the mean C content is found in the EUROFER layer after annealing for 2 h in comparison to 2.0 at.% of C in the original layer. The layers do not mix completely, while the mean W concentration in the steel is increased by 5.5 at.% for the CWE_W2 sample, i.e. the total content of W in the EUROFER layer after annealing is 5.8 at.%. Mixing of the W layer with EUROFER and C diffusion are more pronounced upon annealing over 16 h (see Fig. 4.42c).

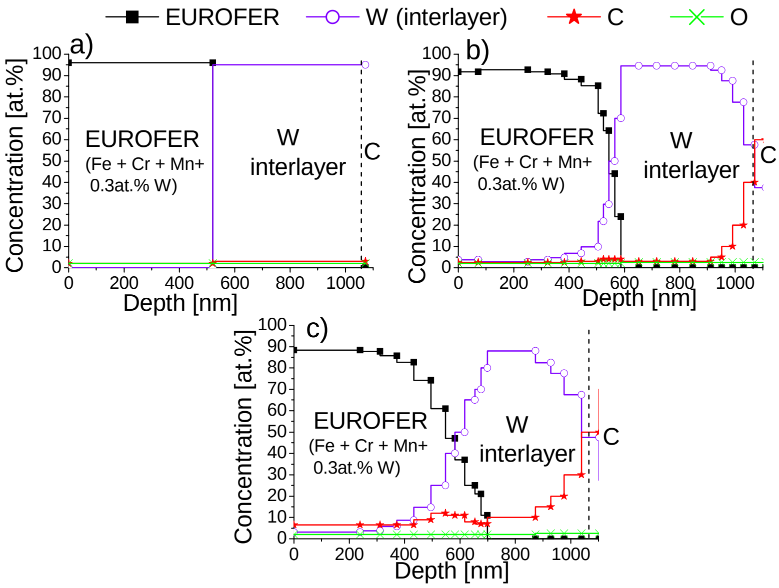

Figure 4.42: Concentration depth profiles of a) original, b) annealed at 750 °C for 2 h and c) annealed at 750 °C for 16 h samples with W (interlayer) / EUROFER layers on graphite (CWE_W2)

In this case, the mean concentrations of additional W diffused from the W interlayer and C detected in the steel are 6.9 at.% and 7.0 at.%, whereas in the W interlayer itself the C content is 15.5 at.%. A comparison of the mean concentration of additional W in the EUROFER layer after annealing the SiCE_W2 and CWE_W2 samples for 2 h and 16 h reveals a higher W content in case of the sample with the SiC substrate than that with graphite.

Re

Re was chosen for the suppression of C diffusion in the EUROFER layer due to the fact that it does not form carbides and C has a very low solubility in it (see more details in subsection 2.2.2). On the other hand, it forms compounds with Fe (described in subsection 2.2.3) which can serve as a good bonding between Re and EUROFER layers.

Thin layers (50 nm of Re / 50 nm of EUROFER)

The samples were investigated by means of *SEM* with and without annealing; the images of SiCE_Re1 and CWE_Re1 samples are shown in Figs. 4.43 and 4.44, respectively. The layers of SiCE_Re1 reveal a smooth surface structure both before and after annealing at 600 °C (Figs. 4.43a and b). The grooves seen in the images come from substrate polishing imperfections: due to its small thickness and fine coating structure produced by magnetron sputter deposition the layers just repeat the substrate's surface structure. The layers of CWE_Re1 reveal a rough surface because of the high roughness of the graphite substrate itself even after polishing. The layers of SiCE_Re1 react intensively in the temperature range of 600 – 750 °C (Figs. 4.43b and c), while for the CWE_Re1 it happens earlier at 600 °C (Fig. 4.44b).

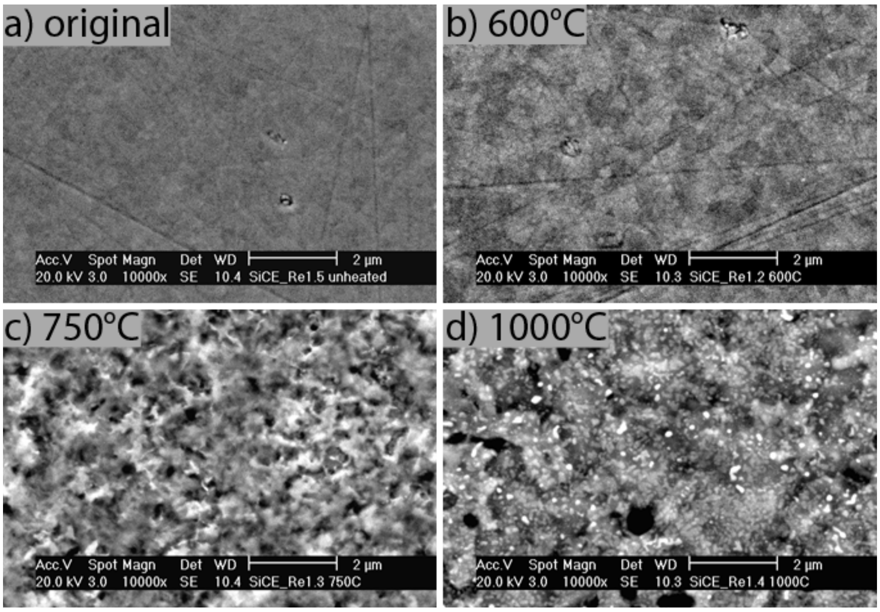

Figure 4.43: *SEM* images of samples with Re / EUROFER layers on SiC with and without annealing in the temperature range of $400 - 1000\,^{\circ}\mathrm{C}$ for 2 h (SiCE_Re1)

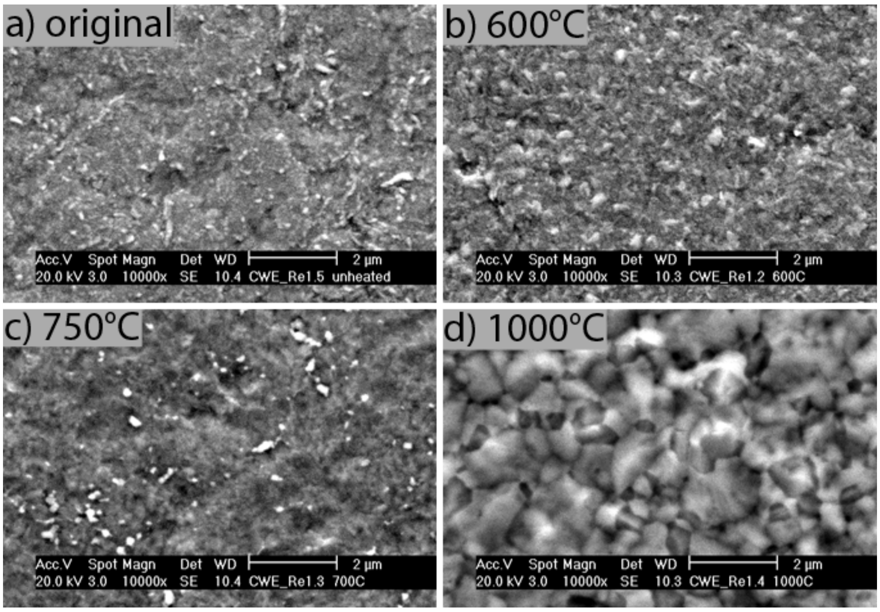

Figure 4.44: *SEM* images of samples with Re / EUROFER layers on graphite with and without annealing in the temperature range of $400 - 1000\,^{\circ}\mathrm{C}$ for 2 h (CWE_W1)

Small crystallites of carbide are formed (sample CWE_Re1 Fig. 4.44b) and they have a similar composition to that of the surrounding areas since the *SEM* images made in *BSE* mode do not show any locations on the surface with a different contrast. Seemingly, the white particles appear during annealing at 750 °C (Fig. 4.44c) because of the higher content of Re in the particles than in the rest of the layer. This is also confirmed by the *SEM* images made in *BSE* mode, since Re has higher atomic number than Fe (75 against 26). The arrangement of the particles follows the grain boundaries. At temperatures of 750 to 1000 °C the layers of both SiCE_Re1 and CWE_Re1 are mixed (Figs. 4.43c and d, and Figs. 4.44c and d). The *SEM* images in *BSE* mode of the layers annealed at 750 and 1000 °C show the presence of two different phases with a low and high content of Re. The white particles and precipitates are observed on the layer surface of the SiCE_Re1 annealed at 1000 °C (Fig. 4.43d). The dimensions of these formations are too small to make their detailed investigation by *EDX* possible. Based on the picture contrast, one can make the assumption that the precipitate consists mainly of Fe with additions of Re, while the white particles have much higher Re content.

Diffusion interaction between the layers caused by annealing was investigated utilizing *IBA* on the samples annealed at temperatures up to 600 °C, since at higher temperatures the layers were found to cover the substrate incompletely. The results are presented in Fig. 4.45 for SiCE_Re1 and in Fig. 4.46 for CWE_Re1 and Table 4.13. For clarity, the axis corresponding to the concentration of SiCE_Re1 is made with a break.

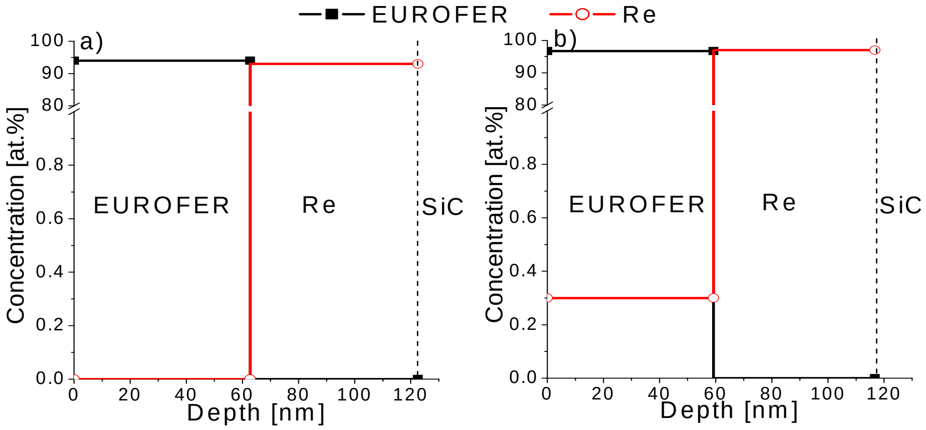

Figure 4.45: Concentration depth profiles of Re / EUROFER layers on SiC substrate (SiCE_Re1) a) original and b) annealed at 600 °C for 2 h

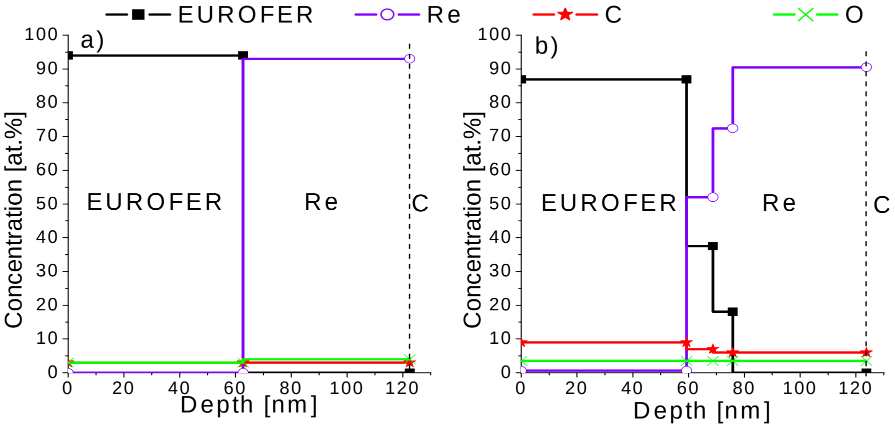

Figure 4.46: Concentration depth profiles of Re / EUROFER layers on graphite substrate (CWE_Re1) a) original and b) annealed at 600 °C for 2 h

Annealing at 400 °C does not change anything in terms of the layer composition of both SiCE_Re1 and CWE_Re1. At 600 °C Re diffuses into the EUROFER layer and its concentration is 0.3 at.% in the case of SiCE_Re1 and 0.6 at.% in the case of CWE_Re1. In addition to Re in the EUROFER layer of CWE_Re1, the C concentration is found to increase up to 9 at.%. A lower amount of C, about 6 at.%, is observed in the Re interlayer of CWE_Re1 (see Fig. 4.46b).

Substrate	SiC	Graphite				
Layer	EUROFER	EUROFER			Re	
Contamination	Re [at.%]	C [at.%]	O [at.%]	Re [at.%]	C [at.%]	O [at.%]
Original	–	3.0	3.0	–	3.0	4.0
Annealed at 400 °C	–	3.0	2.0	–	3.0	2.0
Annealed at 600 °C	0.3	9.0	3.5	0.6	6.0	3.5

Table 4.13: Mean contamination contents in the EUROFER layer with thin Re interlayer with and without annealing for 2h, in atomic percent

Thick layers (500 nm of Re / 500 nm of EUROFER)

The samples consisting of 500 nm of Re / 500 nm of EUROFER layers on SiC (SiCE_Re2) and graphite (CWE_Re2) substrates with and without annealing are presented in Fig. 4.47. Both the samples show a smooth surface before and after annealing. The only difference is that after annealing precipitate formation on the SiCE_Re2 looks like light specks (Fig. 4.47b), while on the surface of CWE_Re2 white particles are observed (Fig. 4.47d). These new uniformly distributed formations are also visible in the *BSE* mode of *SEM*, therefore they consist mainly of more heavy elements than the rest of the layer.

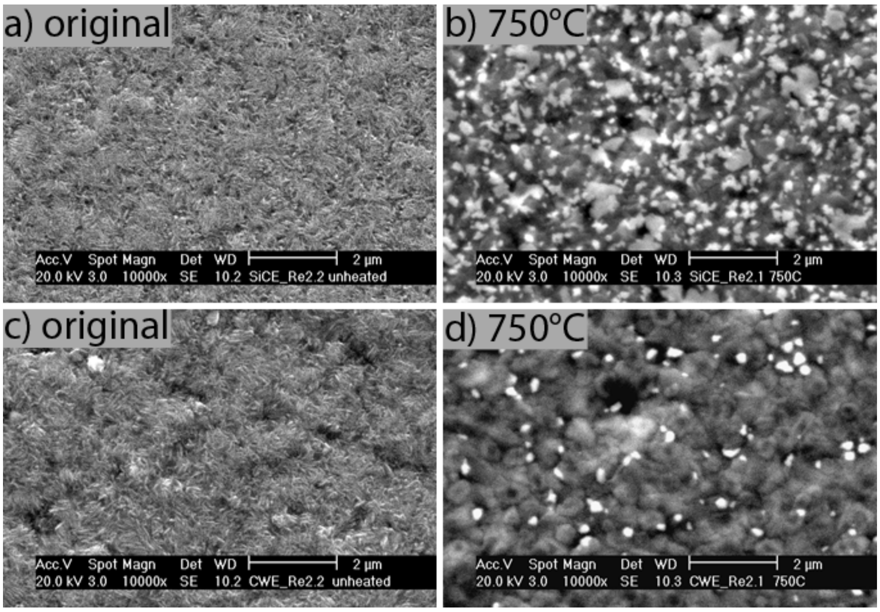

Figure 4.47: *SEM* images of samples with Re / EUROFER layers on SiC and graphite substrates with and without annealing at 750 °C for 2 h: a) and b) SiCE_Re2, c) and d) CWE_Re2

In both cases they are too small to allow the detection of composition by *EDX*.

In Fig. 4.48 the results of *XRD* measurements of SiCE_Re2 and CWE_Re2 are presented. Comparing patterns of the original and annealed samples of SiCE_Re2 shows the appearance of a new peak (211) corresponded to a Fe_2Re_3 phase. The same Fe_2Re_3 phase represented with two peaks (211) and (420) with the addition of a new compound of $Cr_{23}C_6$ with peaks (531) and (551) is observed in the pattern relating to CWE_Re2. New compounds between the layer elements and the elements of the substrate appear only for CWE_Re2. Because of this the sample with the SiC substrate (SiCE_Re2) has been taken for the following calculations of the diffusion coefficient of Re in EUROFER described below.

The concentration depth profiles in the reactive zone of the SiCE_Re2 and CWE_Re2 are presented in Figs. 4.49 and 4.50. For comparison, the spectra of the original samples are shown as well, where the layers are clearly separated in both cases.

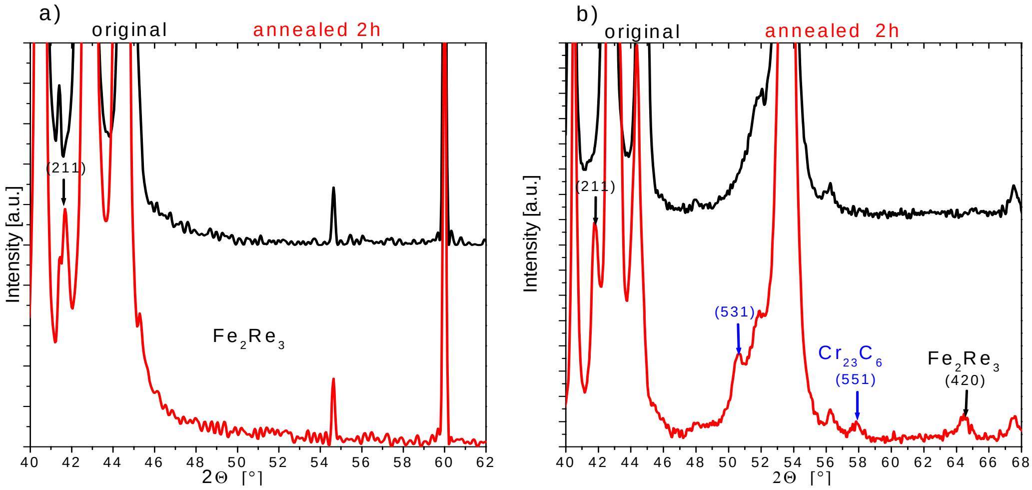

Figure 4.48: *XRD* spectra of samples with Re / EUROFER layers a) on SiC and b) on graphite substrates with and without annealing at 750 °C for 2 h (SiCE_Re2 and CWE_Re2)

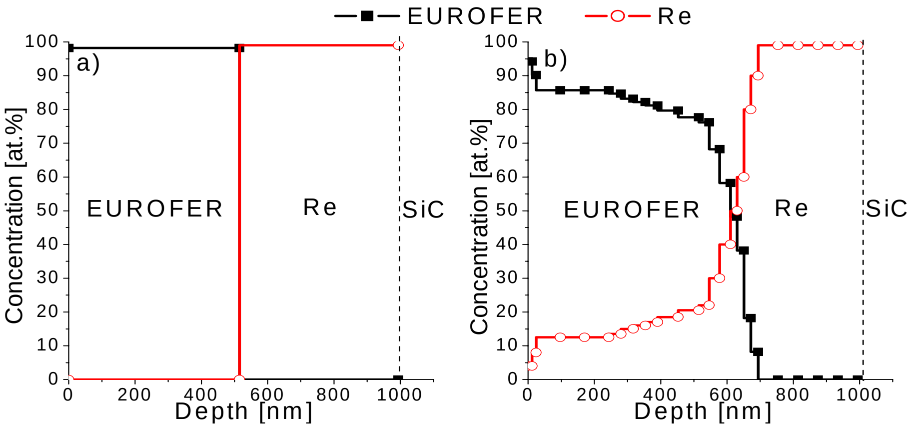

Figure 4.49: Concentration depth profiles of Re / EUROFER layers on SiC substrate (SiCE_Re2) a) original, b) annealed at 750 °C for 2 h

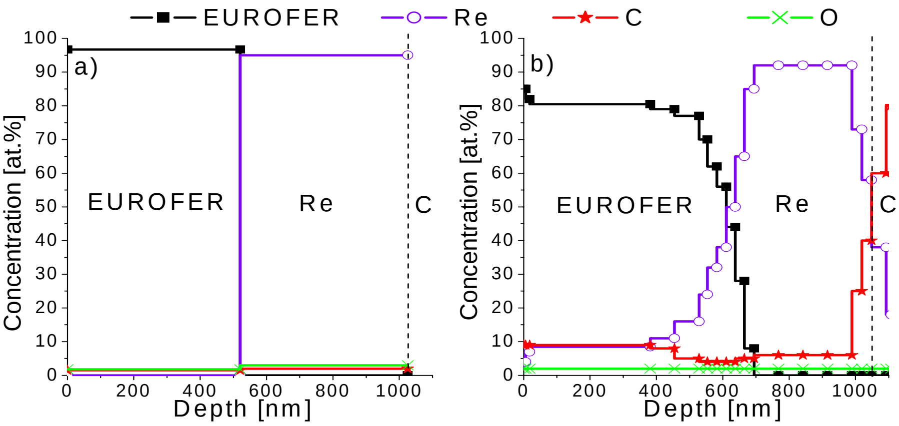

Figure 4.50: Concentration depth profiles of Re / EUROFER layers on graphite substrate (CWE_Re2) a) original, b) annealed at 750 °C for 2 h

Table 4.14 gives the mean contents of C and O in the Re layer and C, O and Re in the EUROFER layer for the CWE_Re2 sample, as well as the mean concentration of Re in the EUROFER layer of the SiC_Re2 sample. Due to annealing at 750 °C the layers partially mix in both cases. Interaction between the layers results in a mean Re content in the steel layer of 14.7 at.% for SiCE_Re2 and 10.0 at.% for CWE_Re2. In addition, C is found to diffuse through the Re layer into the EUROFER of the CWE_Re2 resulting in 8.0 at.% of Re in the steel layer. A lower C contamination of about 7.0 at.% is found in the Re layer.

Substrate	SiC	Graphite				
Layer	EUROFER	EUROFER			Re	
Contamination	Re [at.%]	C [at.%]	O [at.%]	Re [at.%]	C [at.%]	O [at.%]
Original	–	1.5	2.0	–	2.0	3.0
Annealed for 2 h	14.7	8.0	2.0	10.0	7.0	2.0

Table 4.14: Layers mean contamination contents in the EUROFER layer with thick Re interlayer with and without annealing at 750C, in atomic percent

Re / W

To improve C transport suppression by a diffusion barrier, a Re / W multilayer has been applied. In spite of the fact that the diffusion coefficient of C in W is very close to that of C in Re, the application of only a W or Re interlayer as a diffusion barrier seems not to be as optimal as the use of a Re / W multilayer for the following reasons. Firstly, W builds carbides and therefore a thick interface zone appears, which becomes brittle and could make a composite material worse. However, at the same time, the formation of W carbides would result in better protection of the EUROFER from C diffusion (see details in subsection 2.2.2). Secondly, Re does not form carbides but reacts intensively with Fe, which leads to deterioration of the suppression of C diffusion. The application of a Re / W multilayer could help solve these problems.

Two sets of samples were prepared on a graphite substrate, CWE_Re_W1 and CWE_Re_W2, with three interlayers of equal thicknesses (W / Re / W), and with four interlayers of equal thicknesses (Re / W / Re / W), correspondingly. The total thickness of each multilayer structure remained about 550 nm. Taking into account the fast mixing of Re and Fe, W was chosen as an adjoining layer to the steel.

Three layer structure (540 nm of (W / Re / W) / 500 nm of EUROFER)

The *SEM* images of the CWE_Re_W1 with 540 nm thick Re / W multilayer and 500 nm of EUROFER layer on the top with and without annealing are presented in Fig. 4.51. In this multilayer, each layer of Re and W has the same thickness of 180 nm. As in the case of the W interlayer, the samples reveal a smooth surface with and without annealing, and the same precipitates formation is observed, while cracks appear after a shorter annealing period (Fig. 4.51b). Partial layer delamination is observed after 16 h of annealing, as was with the W interlayer.

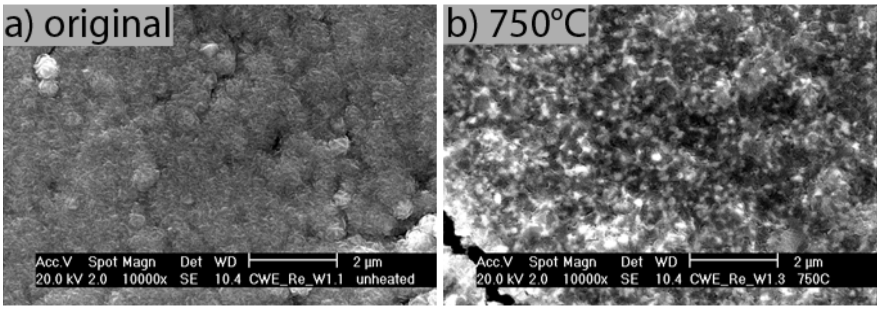

Figure 4.51: *SEM* images of samples with W / Re / W / EUROFER layers on graphite with and without annealing at 750 °C for 2 h (CWE_Re_W1)

An *XRD* analysis was performed for the both original and annealed (750 °C, 2 h) samples. The spectra of the CWE_Re_W1 are given in Fig. 4.52. The peaks appearing after annealing have a low intensity; therefore, it is not possible to clearly distinguish which phases have been formed. Additional difficulties with the phase determination come from the presence of several elements which have close peak positions. Thus, the peak corresponding to Fe_3W_3C (511) that appeared to be the most pronounced in the case of the W interlayer is not observed. Nevertheless, the position of small peaks coincide well with those of two phases observed in the spectra mentioned above, Fe_3W_3C and W_2C.

The original and annealed for 2 h samples were investigated by *IBA* and the results are presented in Fig. 4.53 and in Table 4.15. The original sample shows clear separation of the layers, as does the annealed one with only one exception: EUROFER and abutting W layers become partially mixed after annealing. Additional W diffuses from the W interlayer into the steel and its mean concentration in EUROFER is 5.4 at.%, i.e. the total W content in the steel layer is 5.7 at.% because the as-deposited EUROFER consists of 0.3 at.% of W. Two other interlayers, i.e. the second W and Re layers, are found to be separated from each other.

In the as-deposited layers the C content is higher in the Re / W interlayers (4 at.%) than in the EUROFER (2 at.%). After annealing, the mean concentration of C in all the layers is about the same. For the sample annealed over 16 h the analysis was not carried out due to strong layer degradation.

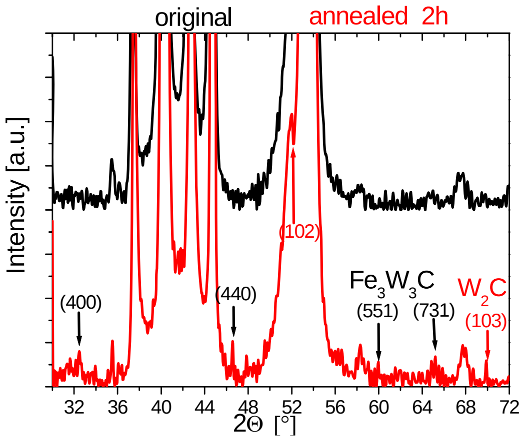

Figure 4.52: *XRD* spectra of samples with W / Re / W / EUROFER layers on graphite substrate with and without annealing at 750 °C for 2 h (CWE_Re_W1)

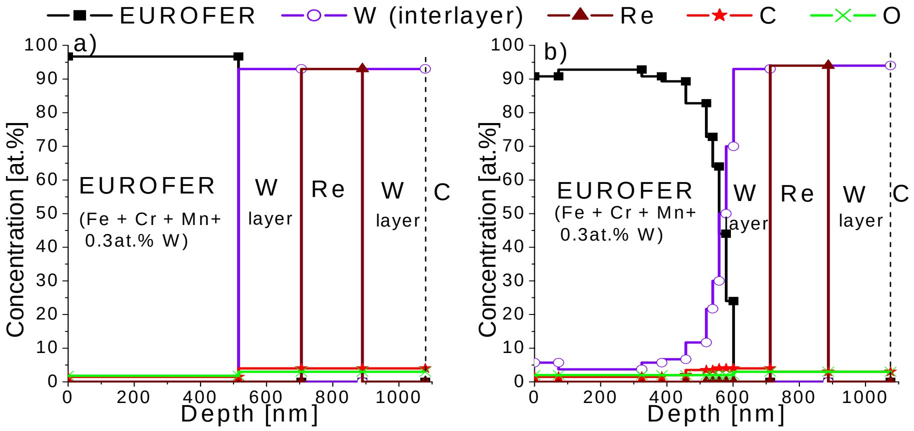

Figure 4.53: Concentration depth profiles of a) original, b) annealed at 750 °C for 2 h samples with W / Re / W / EUROFER layers on graphite (CWE_Re_W1)

Substrate	Graphite		
Layer	EUROFER		
Contamination	C [at.%]	O [at.%]	W (interlayer) [at.%]
Original	2.0	2.0	–
Annealed for 2 h	2.0	2.0	5.4

Table 4.15: Mean contamination contents in the EUROFER layer with W/ Re / W multilayer with and without annealing at 750C, in atomic percent

Four layer structure (560 nm of (Re / W / Re / W) / 500 nm of EUROFER)

The *SEM* images of CWE_Re_W2 with 560 nm thick Re / W / Re / W multilayer and 500 nm of EUROFER with and without annealing with different durations are presented in Fig. 4.54. In this multilayer each layer of Re and W has the same thickness of 140 nm. As in previous investigations, precipitate formation is observed (Figs. 4.54b and d). In contrast to the multilayer showed above, crack propagation appears only after longer annealing and does not reveal any layer delamination, as is seen in the low magnification image (Fig. 4.54c). Annealing over 16 h results in small grain formation with the presence of small white specks (Fig. 4.54d), which are smaller in size and number in comparison to the sample annealed for a shorter time.

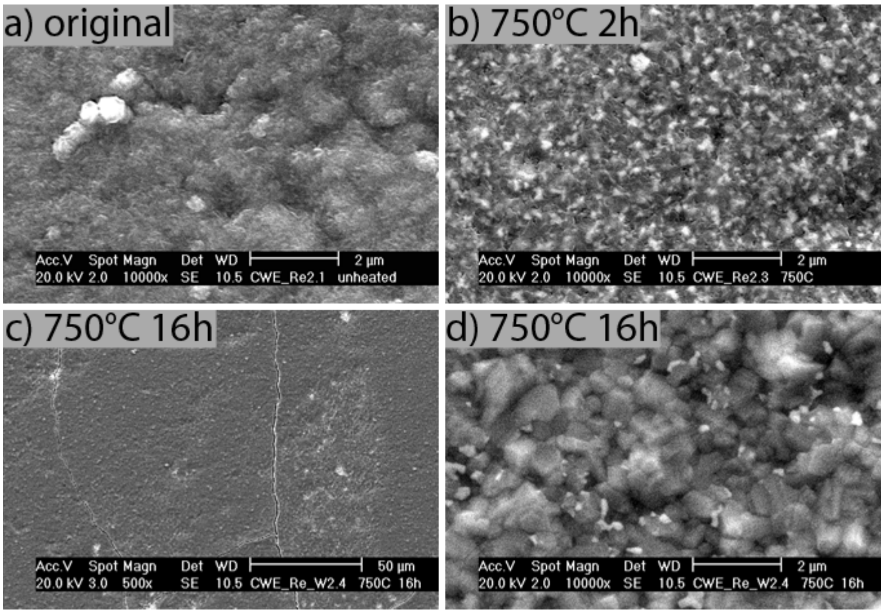

Figure 4.54: *SEM* images of samples with Re / W / Re / W / EUROFER layers on graphite with and without annealing at 750 °C for 2 and 16 h (CWE_Re_W2): a) magnification ×10000, b) magnification ×10000, c) magnification ×500 and d) magnification ×10000

In Fig. 4.55 the *XRD* patterns of the original (black line), annealed for 2 h (red line), and annealed for 16 h (blue line) samples are shown. As already observed, it is difficult to detect Fe_3W_3C in the patterns corresponded to the annealed samples because of the presence of the Re and W peaks coinciding with the most pronounced peak of Fe_3W_3C, namely (511). The subcarbide W_2C is clearly seen on the sample annealed for 16 h due to the appearance of the high intensity peak (100).

IBA was carried out for both the original and annealed samples (see Fig. 4.56 and Table 4.16). The as-deposited CWE_Re_W2 reveals four clearly separated interlayers and the EUROFER layer on top. After annealing for 2 h, the multilayer structure remains the same as it was before with only one exception: W from the W interlayer has partially diffused through the steel. The mean concentrations of additional W and C in the EUROFER layer are found to be 4.6 at.% and 2.5 at.%, correspondingly.

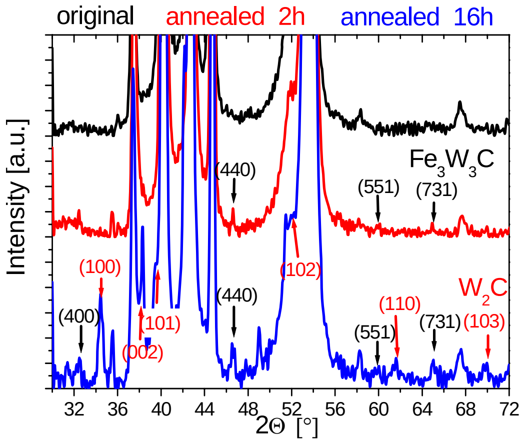

Figure 4.55: *XRD* spectra of samples with Re / W / Re / W / EUROFER layers on graphite substrate with and without annealing at 750 °C for 2 and 16 h (CWE_Re_W2)

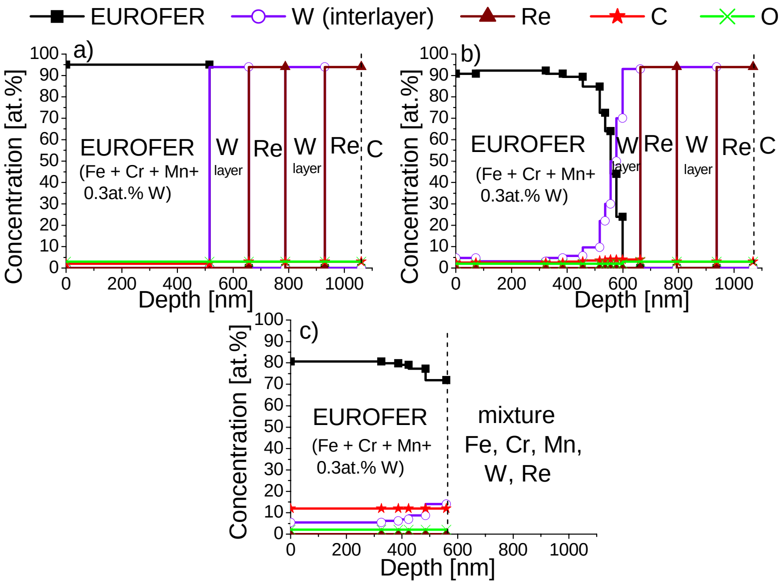

Figure 4.56: Concentration depth profiles of Re / W / Re / W / EUROFER layers on graphite substrate (CWE_Re_W2) a) original, b) annealed at 750 °C for 2 h and c) annealed at 750 °C for 16 h

Substrate	Graphite		
Layer	EUROFER		
Contamination	C [at.%]	O [at.%]	W (interlayer) [at.%]
Original	2.0	3.0	–
Annealed for 2 h	2.5	2.0	4.6
Annealed for 16 h	12.0	2.0	6.7

Table 4.16: Contamination contents in the EUROFER layer with Re / W / Re / W multilayer with and without annealing at 750C, in atomic percent

Therefore, after annealing the total W content in the steel is 4.9 at.%. The C content in all other layers remains approximately the same. In contrast to the sample annealed for 2 h, annealing for 16 h results in significant changes in the sample composition. As seen in Fig. 4.56c, the additional W and C contents in the steel rises to 6.7 at.% and 12 at.%, respectively. Importantly, the multilayer loses its structure because Re and W mix with the addition of some Fe: the deep part of the concentration depth profile (> 570 nm) is impossible to evaluate because of the peaks overlapping.

4.2.3 EUROFER layer with ceramic interlayer

Different ceramic layers, such as TiC, TiN and Er_2O_3, have been investigated as diffusion barriers because of the stability of these layers with respect to Fe at high temperatures.

TiC

The samples with a thin TiC (50 nm) and thin EUROFER (50 nm) layers on SiC (SiCE_TiC1) and graphite (CWE_TiC1) were annealed for 2 h at different temperatures ranging from 400 to 1000 °C. *SEM* images of the SiCE_TiC1 and CWE_TiC1 samples are presented in Figs. 4.57 and 4.58, correspondingly.

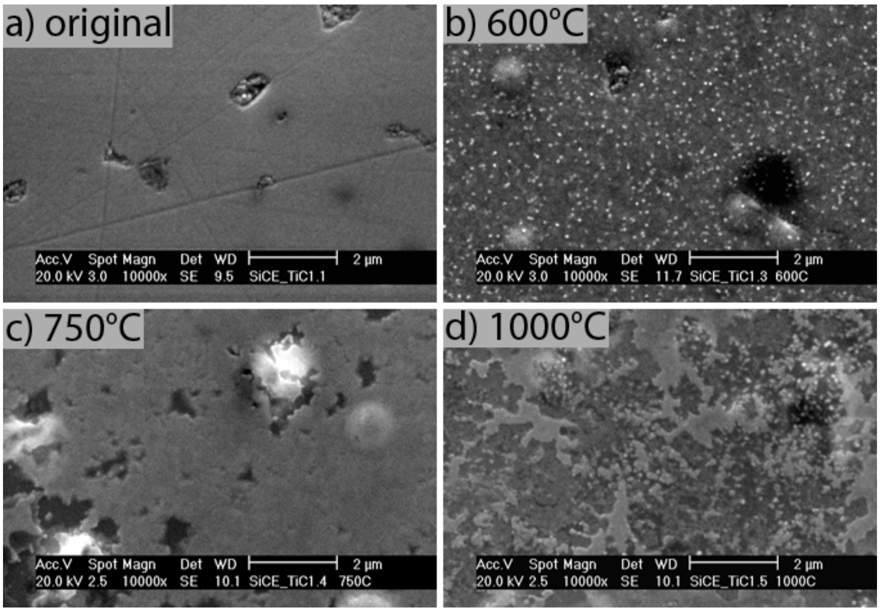

Figure 4.57: *SEM* images of samples with TiC / EUROFER layers on SiC substrate (SiCE_TiC1) with and without annealing in the temperature range of 400 − 1000 °C for 2 h

The as-deposited coatings on SiC and graphite show different layer structures due to the influence of the substrate material (see subsection 4.1.2). Thus, the SiCE_TiC1 possesses a smooth layer structure (see Fig. 4.57a), while the CWE_TiC1 (see Fig. 4.58a) reveals an undulating surface. After annealing at 400 °C the structure of the SiCE_TiC1 remains the same, whilst above 600 °C small white particles appear on the sample surface (see Fig. 4.57b). At the same time blisters form on the substrate. One possible reason for their formation is the incorporation of Ar into the SiC during the TiC deposition due to applying a bias voltage. At the higher temperatures of 750 and 1000 °C the blisters remain the same size (see Figs. 4.57c and d). Hole formation is observed in the layers of SiCE_TiC1 after annealing at 750 °C. An increase of temperature to 1000 °C results in further agglomeration of the layers.

There are no visible changes in the structure of the layers caused by annealing at 400 and 600 °C in comparison with the original CWE_TiC1 (see Figs. 4.58a and b). However, the EUROFER layer agglomerates due to annealing at 750 °C (see Fig. 4.58c) and, therefore, grey areas appear on the sample surface. In contrast to the steel, the TiC layer remains the same. One can see in the *SEM* image its undulating structure below the grey formations. At the highest temperature of 1000 °C TiC has also been destroyed. There are different areas on the surface (see Fig. 4.58d): grey formations consisting mainly of elements of the steel layer, dark grey areas which have more Ti and C, and black ones representing the substrate.

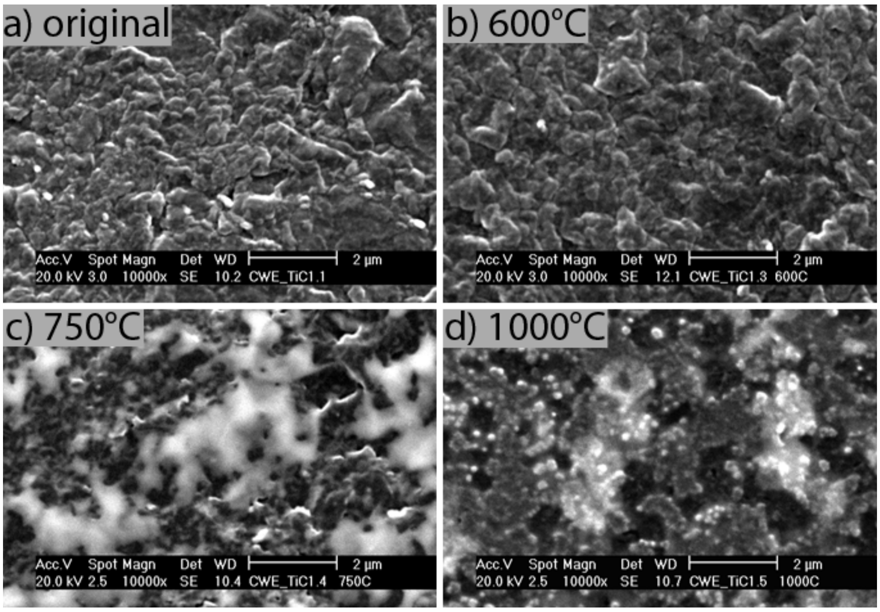

Figure 4.58: *SEM* images of samples with TiC / EUROFER layers on graphite substrate (CWE_TiC1) with and without annealing in the temperature range of 400 – 1000 °C for 2 h

Due to the small thickness of the layers it was impossible to carry out *XRD* investigations of the SICE_TiC1 and CWE_TiC1 samples.

In Fig. 4.59 the concentration depth profile of the as-deposited TiC and EUROFER layers is given. Mean contamination contents of the SiCE_TiC1 and CWE_TiC1 are presented in Table 4.17. For the sample with the SiC substrate there is only possibility to detect the Ti concentration in EUROFER, since the peaks from all elements with atomic numbers below 14 (Si) appear to overlap with the peak from Si. The content of Ti in the steel is found to rise to about 3 at.% due to annealing at 400 °C. An investigation of the SiCE_TiC1 annealed at higher temperatures is not appropriate due to the appearance of particles and layer agglomeration. The composition of the layers of the as-deposited sample and the heat treated one at 400 °C does not change in the case of the graphite substrate.

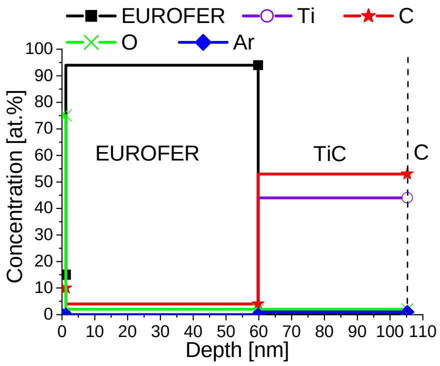

Figure 4.59: Concentration depth profile of the original sample with TiC / EUROFER layers on graphite (CWE_TiC1)

Substrate	SiC	Graphite		
Layer	EUROFER	EUROFER		
Contamination	Ti [at.%]	C [at.%]	O [at.%]	Ti [at.%]
Original	1	4	2	–
Annealed at 400 °C	3	4	2	–
Annealed at 600 °C		4	2	2

Table 4.17: Mean contamination contents in the EUROFER layer with TiC interlayer with and without annealing for 2h, in atomic percent

A small amount of Ar appears in the TiC layer owing to the applied substrate bias during ceramic deposition. Annealing at a temperature of 600 °C has resulted in a Ti contamination of 2 at.% in the steel. The C content remains the same for all the investigated samples.

TiN

The application of a TiN interlayer as a diffusion barrier was investigated for temperatures from 400 to 750 °C over 2 h. In Figs. 4.60 and 4.61, *SEM* images of the samples with a thin TiN (50 nm) and thin EUROFER (50 nm) layers on SiC (SiCE_TiN2) and graphite (CWE_TiN2) substrates are presented. As it was observed for the TiC layer, the structure of SiCE_TiN2 differs from that of the CWE_TiN2 due to the different substrate materials. The as-deposited SiCE_TiN2 reveals a fine, smooth structure that remains the same after annealing at temperatures up to 600 °C (see Figs. 4.60a and b). The heat treatment at higher temperatures of 750 °C initiates layer agglomeration. In contrast to the SiCE_TiN2, the CWE_TiN2 possesses a rough, developed layer structure. There are no visible changes found on it after annealing at temperatures up to 600 °C. Annealing at 750 °C causes agglomeration of the EUROFER layer that is presented in the image as grey areas (see Fig. 4.61c). As was observed for the CWE_TiC1 annealed at the same temperature, the ceramic interlayer remains stable. The layer located beneath those grey formations reveals the same structure to that it had before annealing.

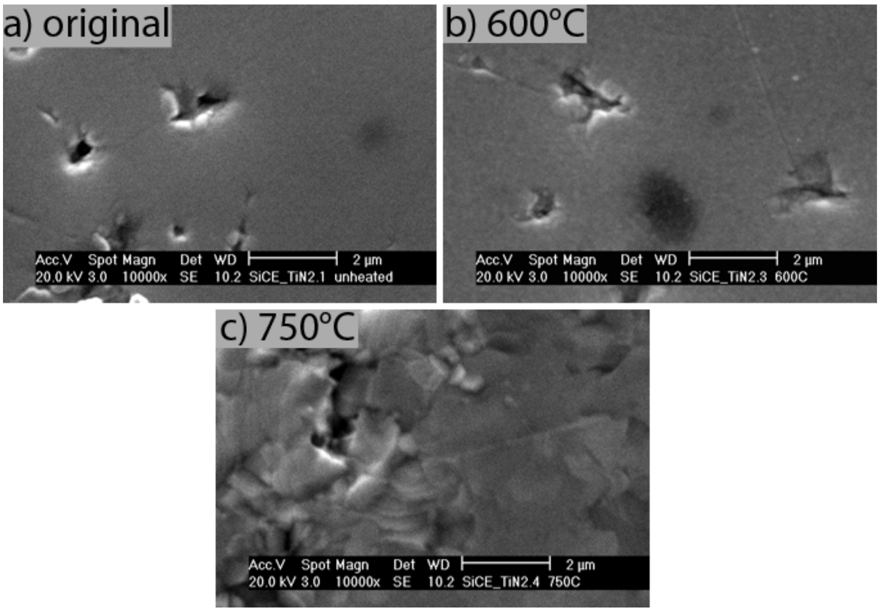

Figure 4.60: *SEM* images of samples with TiN / EUROFER layers on SiC substrate (SiCE_TiN2) with and without annealing in the temperature range of 400 − 750 °C for 2 h

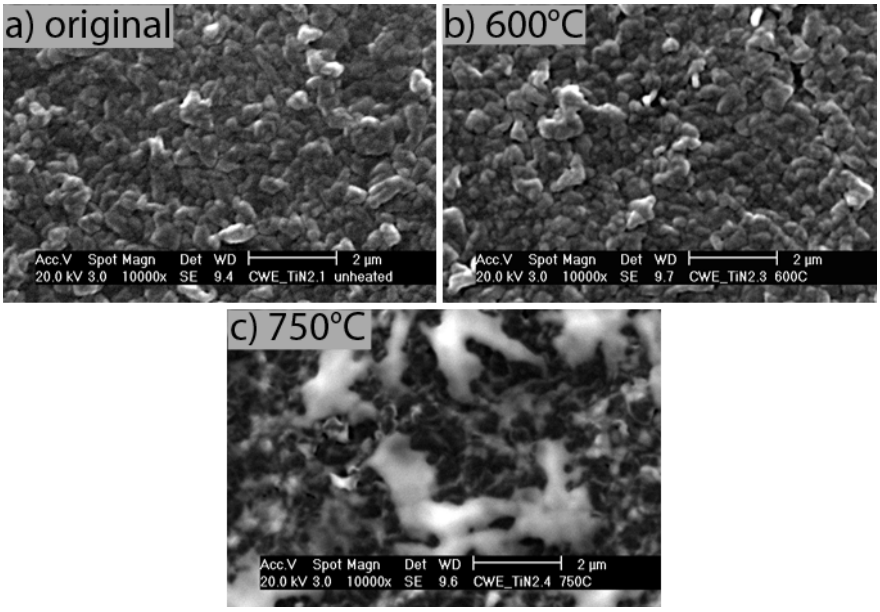

Figure 4.61: *SEM* images of samples with TiN / EUROFER layers on graphite substrate (CWE_TiN2) with and without annealing in the temperature range of 400 − 750 °C for 2 h

XRD analysis of the SiCE_TiN2 and the CWE_TiN2 was not performed due to the small thickness of the layers.

A concentration depth profile of the original CWE_TiN2 made by *IBA* is shown in Fig. 4.62. The detectable contents of contaminations in the EUROFER on SiC and graphite substrates are presented in Table 4.18. On SiC it is only possible to evaluate the amount of Ti in the steel due to peak overlapping. Thus, 1 at.% of Ti is found in the original EUROFER layer and in the annealed one at 400 °C. Ti content increases to 2 at.% upon annealing at 600 °C. In the CWE_TiN2 the same Ti concentration is observed and, in addition, 3 at.% of C and 4 at.% of N are found in the EUROFER layer with and without annealing. The O content decreases from 4 to 2 at.% after annealing.

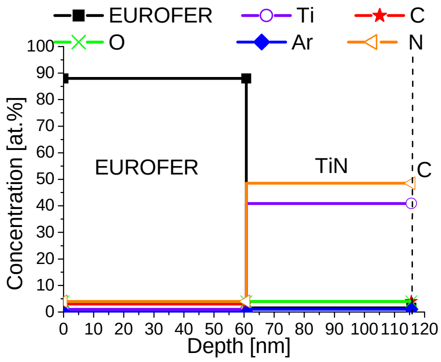

Figure 4.62: Concentration depth profile of the original sample with TiN / EUROFER layers on graphite (CWE_TiN2)

Substrate	SiC	Graphite			
Layer	EUROFER	EUROFER			
Contamination	Ti [at.%]	C [at.%]	O [at.%]	N [at.%]	Ti [at.%]
Original	1	3	4	4	–
Annealed at 400 °C	1	3	2	4	–
Annealed at 600 °C	2	3	2	4	2

Table 4.18: Mean contamination contents in the EUROFER layer with TiN interlayer with and without annealing for 2h, in atomic percent

Er_2O_3

A thick Er_2O_3 layer (500 nm) deposited by filtered arc facility was investigated as a diffusion barrier with respect to C. Only a graphite substrate was used in this investigation. The samples (CWE_Erbia1) with thick Er_2O_3 and thick EUROFER (500 nm) layers were analysed with and without annealing at 750 °C for 2 h.

In Fig. 4.63 the as-deposited and annealed CWE_Erbia1 samples are shown. The original sample has a fine structure. The roughness of the layer is governed by the roughness of the graphite substrate. After annealing the layer appears not to be cracked. Comparing the images of the original and annealed CWE_Erbia1 (Figs. 4.63a and b), the surface of the sample becomes more rough because of the growth of crystals of EUROFER on the surface.

The results of *XRD* analysis of the original and annealed samples are presented in Fig. 4.64. The black curve belongs to the original CWE_Erbia1, while the red one to the annealed CWE_Erbia1. They both show the same *XRD* pattern without any noticeable difference and reveal four peaks corresponding to Er_2O_3 phase (222), (400), (440), and (622); and one peak to EUROFER (110). In the pattern of the annealed sample, no new peaks are found.

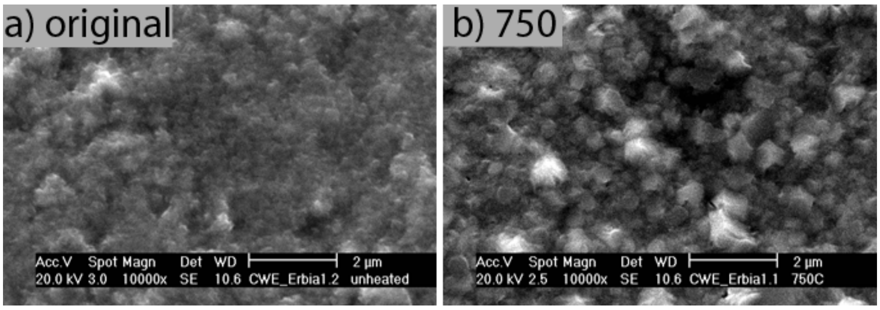

Figure 4.63: *SEM* images of samples with Er_2O_3 / EUROFER layers on graphite substrate with and without annealing at 750 °C for 2 h (CWE_Erbia1)

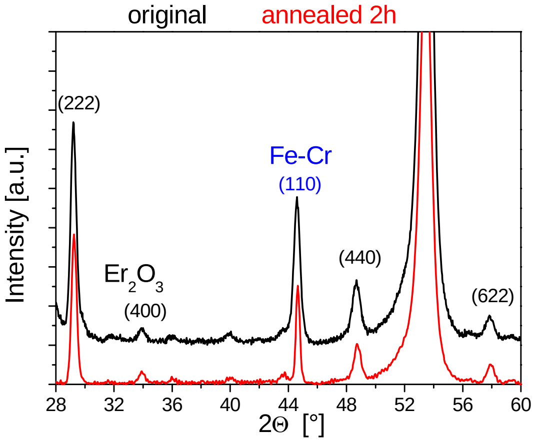

Figure 4.64: *XRD* spectra of samples with Er_2O_3 / EUROFER layers on graphite substrate with and without annealing at 750 °C for 2 h (CWE_Erbia1)

The composition of the layers was investigated by *IBA* and the results are presented in Fig. 4.65 and Table 4.19. The C and O content in both the layers of EUROFER and Er_2O_3 of the original sample are found to be about 2 at.%. The composition of the layers does not change upon annealing of the sample.

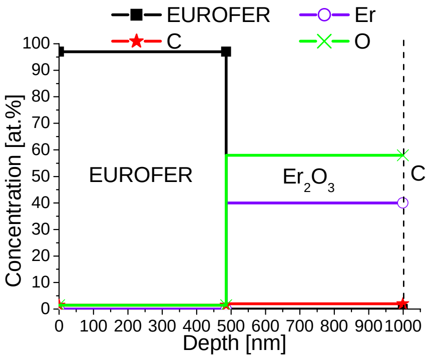

Figure 4.65: Concentration depth profile related to the both original and annealed samples with Er_2O_3 / EUROFER layers on graphite (CWE_Erbia1)

Substrate	Graphite		
Layer	EUROFER		Erbia
Contamination	C [at.%]	O [at.%]	C [at.%]
Original	1.5	1.5	2
Annealed for 2 h	1.5	1.5	2

Table 4.19: Mean contamination contents in the EUROFER layer with Erbia interlayer with and without annealing at 750C, in atomic percent

Therefore, the concentration depth profile given in Fig. 4.65 is also valid for the annealed sample. The roughness of the EUROFER layer after annealing is measured to be higher than before, in contrast to Er_2O_3 where the roughness remains the same.

4.3 Calculation of diffusion coefficients

When the concentration of diffusive species exceeds a certain value called the trace impurity level, the diffusion coefficient appears to depend on the concentration. To determine the concentration dependent diffusion coefficient, $D(C)$, an iterative scheme was used. In the experiment the depth profile of diffusing species was measured before and after annealing at a temperature of 750 °C. Using the diffusion code DIFFUSEDC diffusion was simulated taking into account the initial depth profile measured prior to annealing. The aim was to iteratively adjust $D(C)$ such that the simulation would reproduce the diffusion depth profile measured after annealing. Since DIFFUSEDC treats diffusion in binary systems, only two component diffusion couples could be investigated. The details on the concentration dependence of the diffusion coefficient and on the DIFFUSEDC code are explained in detail in Appendix B and reference [26]. This model was not suitable for the analysis of the interaction between ceramic and EUROFER layers, since the interlayer consisted of two components. The evaluation of the depth profiles of the annealed samples with thick deposited layers was much more precise than that of the thin ones due to the longer diffusion paths, therefore only thick layer samples were chosen for the calculations.

In Fig. 4.66 the concentration depth profiles of the sample CWE43 with a thick EUROFER layer (400 nm) on graphite with and without annealing at 750 °C for 2 h are shown. The black curve shows the original, i.e. as-deposited, C depth profile in the sample, while the blue one is the calculated depth profile of C in the steel after annealing, which fits the experimental profile of the annealed sample shown as a red line with open circles.

To calculate the diffusion coefficient of *Me* in EUROFER, the samples with W and Re layers were utilised. The samples with Ti and Cr interlayers were not analysed since their layers had mixed with EUROFER. For graphite substrates substantial C diffusion into the EUROFER layer took place where SiC proved to be stable within the applied temperature range. The varying C concentration in EUROFER had a significant impact on the diffusion of W and Re from the interlayer. For sample CWE_W2 with a graphite substrate annealed at 750 °C over 2 h the W concentration in the EUROFER layer was found to be 7 at.%, while for SiCE_W2 with a SiC substrate the W concentration was 16 at.%.

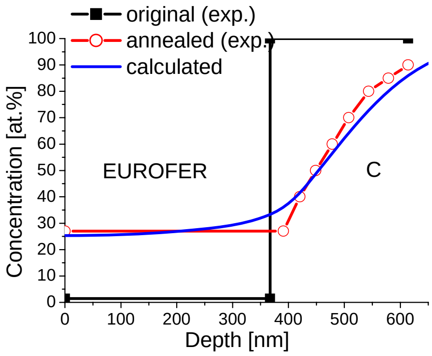

Figure 4.66: Concentration depth profiles of CWE43 with and without annealing at 750 °C for 2 h in comparison with the profile calculated by DIFFUSEDC

The reasons for this difference is discussed later in section 5. To avoid this influence of C, only the samples with SiC substrates were chosen for the calculations, since for both specimens SiC was found to be stable and did not react with the layers.

In Fig. 4.67 the depth profiles of the original and annealed samples with W and Re interlayers are presented together with the calculated ones. In Fig. 4.67a the results of the calculations for the SiCE_W2 with a W interlayer are shown. The black curve is the depth profile of W in the EUROFER layer prior to annealing. The experimental data for the samples annealed at 750 °C for 2 and 16 h are shown as a red line with open and filled circles respectively. By iteratively adjusting the diffusion coefficient of W in the steel, the blue and green curves have been fitted to the experimental data with the same parameters of fitting. Therefore, the diffusion coefficient $D(C)$ is not dependent on the annealing duration. The same fitting procedure has been done for SiCE_Re2 with the Re interlayer and the results of the simulation are given in Fig. 4.67b.

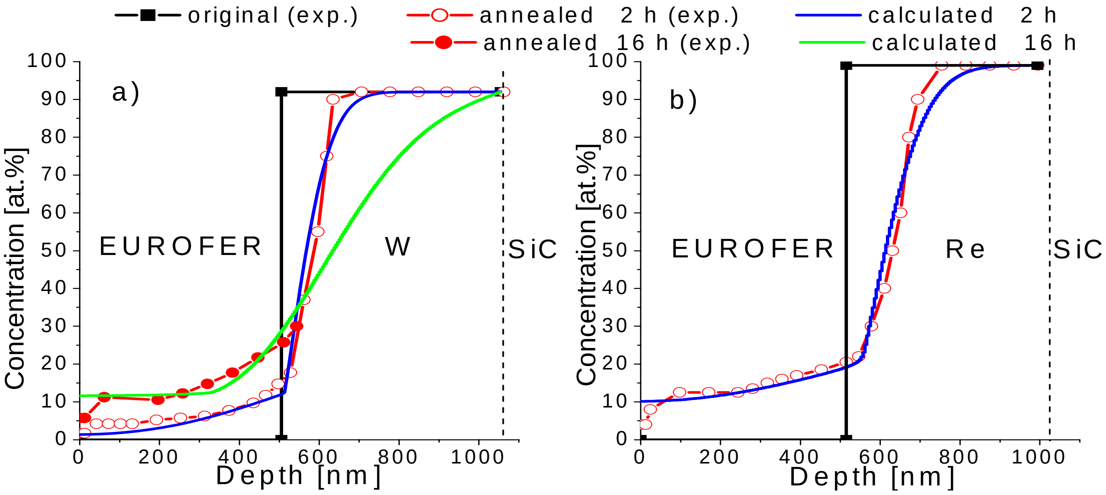

Figure 4.67: Concentration depth profiles of the samples with and without annealing at 750 °C for 2 and 16 h in comparison with the profiles calculated by DIFFUSEDC: a) SiCE_W2 with W interlayer, b) SiCE_Re2 with Re interlayer

The concentration dependent diffusivities are presented in Fig. 4.68. The black curve describes the diffusion coefficient of C in EUROFER, the blue and the red lines correspond to Re and W in EUROFER. All these profiles reveal similar shapes, i.e. they exhibit a sharp drop at a certain concentration of the diffusing species. The same feature of the $D(C)$ dependence for C diffusion in W was observed in [26]. As seen in Fig. 4.68, the curves consist of two plateaus, where the left upper ones correspond to species diffusion in the case of low concentrations and, therefore, no compounds are formed.

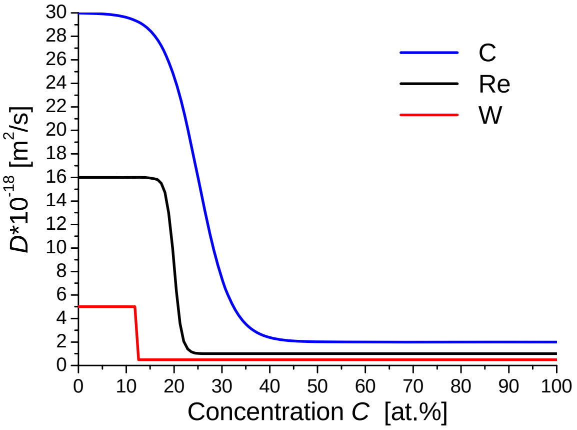

Figure 4.68: Dependence of diffusion coefficients D of C, Re and W in EUROFER on their concentration C obtained by the iterative fitting procedure

Here, high values of the diffusion coefficients are governed by the large gradients of the diffusing species concentrations. The transition stage between the two plateaus is explained by the formation of compounds which, in turn, affect the diffusivity because of changes in the chemical potential. Further, high concentrations lead to a lowering of the concentration gradient, and this process, together with the chemical potential change, results in significant decrease in the diffusion coefficient. The maximum diffusion coefficients of C, Re, and W in EUROFER are found to be $3 \cdot 10^{-17}\,\mathrm{m}^2\,\mathrm{s}^{-1}$, $1.6 \cdot 10^{-17}\,\mathrm{m}^2\,\mathrm{s}^{-1}$, and $5 \cdot 10^{-18}\,\mathrm{m}^2\,\mathrm{s}^{-1}$, respectively. It would not be correct to compare these values with tracer diffusion coefficients usually given in the literature due to the formation of compounds which influence the rate of diffusion. Therefore, according to [26], the estimated maximum values of diffusion coefficients are assumed to lie between the tracer diffusivities of species in pure EUROFER and the corresponding compounds.

5 Discussion

5.1 EUROFER

The EUROFER layer was deposited on SiC fibres as well as planar SiC and graphite substrates by magnetron and arc deposition techniques. Its stoichiometry and crystalline structure were found to be close to the target material. The annealing tests of the coated fibres conducted at temperatures of 600 and 800 °C for 2 h showed the necessity of a diffusion barrier to suppress the interdiffusion between the SiC fibres and the steel matrix. After annealing at 800 °C due to interaction between the fibre outer coating, namely SiC doped C, and EUROFER the reaction zone was found to consist of the part of the EUROFER layer and about half of the outer fibre coating. The appearance of this zone was shown in the corresponding *SEM* image (Fig. 4.17c in subsection 4.2.1). Estimation of the thickness of the C - EUROFER reaction zone was made by visual observation of the brightness of the *SEM* image caused by the difference in the atomic numbers: 26 for Fe and 6 for C. The contrast is sensitive to the concentration of Fe in C, and thus to the thickness of the reaction zone, which was found to be 2.2 μm. Unlike diffusion from EUROFER layer into the outer fibre coating the diffusion in the opposite direction could not be estimated by visual observation based on the *SEM* images. Furthermore, the contrast of the *SEM* image depends on the concentration and, therefore, it is not possible to detect the diffusion depth of Fe in the outer coating of the fibre due to low sensitivity of this method of analysis. Thus, calculation of the width of the reaction zone based on the known data for C - Fe, SiC - Fe and SiC - Fe - 20Cr diffusion couples (described in subsection 2.2) and using equation (2.2) gives significantly higher values than the measured width of the reaction zone. After annealing at 800 °C for 2 h the calculated thickness of the reaction zone would be:

$$\begin{array}{rll} \mathrm{C} \longrightarrow & \mathrm{Fe} & 2.6 \cdot 10^{3}\,\mu\mathrm{m} \\ \mathrm{SiC} \longleftrightarrow & \mathrm{Fe} & 156\,\mu\mathrm{m} \\ \mathrm{SiC} \longleftrightarrow & \mathrm{Fe\text{-}20Cr} & 4.5\,\mu\mathrm{m}. \end{array}$$

Even in case of the slowest diffusion process, i.e. interaction between SiC and Fe - 20Cr, the calculated thickness of the reaction zone is twice as thick as was actually observed through *SEM* analysis.

To evaluate the interdiffusion between the fibre and EUROFER components and to find an appropriate diffusion barrier, planar samples were investigated before and after annealing by different techniques: *SEM*, *XRD* and *IBA*. In [30, 31] it was found that SiC decomposed and formed Fe silicides at temperatures of 800 and 900 °C, respectively. In our experiments, in the case of the samples with SiC substrates, serious layer degradation was observed at annealing temperatures above 750 °C which made *XRD* and *IBA* investigations of the layer crystalline structure and composition impossible. The layer agglomerated and crystals formed on the surface of the SiCE41 (50 nm film thickness) and SiCE43 (400 nm film thickness) samples.

In contrast to SiC substrates, in the case of graphite substrates the C diffusion was observed even at the low temperature of 400 °C (CWE41 (50 nm film thickness)). The C content found in EUROFER for the CWE41 sample was 7 at.%. According to the binary phase diagram of Fe - C shown in Fig. C.5 (see Appendix C) this amount of C corresponds to mixture of pearlite and cementite phases. After annealing at 600 °C, where the C content in EUROFER was found to be 19 at.%, de-wetting of the deposited layers was observed (see Figs. 4.19c and d in subsection 4.2.1). This was likely caused by the formation of carbide which was suggested by the C concentration of 19 at.%, corresponding mainly to the cementite phase.

Detailed investigation of the graphite sample CWE43 with the EUROFER layer of 400 nm revealed cementite formation as well. In Fig. 5.1 a schematic sketch of the diffusion process and the following phase transformation is given.

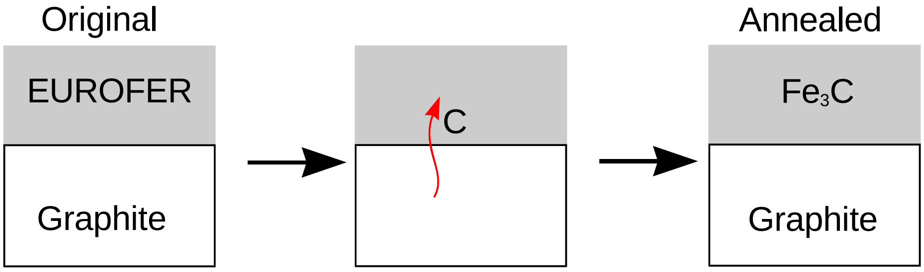

Figure 5.1: Schematic sketch of the phase transformation caused by diffusion of C in the CWE43 sample

The concentration depth profile of CWE43 annealed at 750 °C revealed a C content of 27 at.% in the EUROFER layer. This C content suggests the formation of a mixed cementite and graphite phases (Fe_3C + C), where 25 at.% of C are in a carbide state and the rest is in solution. The same conclusion can be drawn from the results of the *XRD* analysis. The *XRD* pattern (see Fig. 4.22 in subsection 4.2.1) of the annealed CWE43 shows peaks corresponded to Fe_3C. Therefore, as shown in Fig. 5.1, C diffusion caused by annealing results in the transformation of EUROFER into a cementite phase.

The tracer impurity diffusion coefficient of C in α-Fe for a temperature of 500 °C is $4.9 \cdot 10^{-12}\,\mathrm{m^2\,s^{-1}}$, according to [51]. Hence, using equation (2.2) for the diffusion depth described in subsection 2.1, only 0.01 s is necessary for C to diffuse through the pure Fe layer of 400 nm at this temperature. While EUROFER consists mainly of Fe, it has a marked amount of Cr and therefore the C diffusion coefficient in EUROFER should be lower than in pure Fe because the C diffusion in Cr is 2 orders of magnitude lower than in Fe. One can compare the tracer diffusion coefficient of C in pure Fe, Fe - 0.92Cr and pure Cr at 500 °C [52]:

$$\begin{array}{lll} \mathrm{C} \longrightarrow & \alpha\text{-Fe} & 4.9 \cdot 10^{-12}\,\mathrm{m^2\,s^{-1}} \\ \mathrm{C} \longrightarrow & \mathrm{Fe\ -\ 0.92Cr} & 5.2 \cdot 10^{-13}\,\mathrm{m^2\,s^{-1}} \\ \mathrm{C} \longrightarrow & \mathrm{Cr} & 2.8 \cdot 10^{-14}\,\mathrm{m^2\,s^{-1}}. \end{array}$$

It is seen that the addition of even around 1 wt.% of Cr in Fe decreases the diffusion coefficient of C by about one order of magnitude, which in turn, would result in a time of 0.08 s required to diffuse through the layer. This difference becomes negligible if one compares it with the annealing time of 7200 s (2 h) used during experiments with the EUROFER layer.

Since the C concentrations in the layer significantly exceeds the trace amounts for which the literature tracer diffusion coefficients are valid, the concentration dependence of the C diffusion coefficient has to be taken into account. The result of the $D(C)$ fitting procedure based on the experimental concentration depth profiles for the samples annealed at 750 °C for 2 h is given in Fig. 4.68 in subsection 4.3. The maximum value of the diffusion coefficient of C in EUROFER at 750 °C, appropriate to low C concentrations, is found to be $3 \cdot 10^{-17}\,\mathrm{m^2\,s^{-1}}$. This value is significantly lower than that published in the literature for the tracer impurity diffusion coefficient of C in pure Fe of $1.5 \cdot 10^{-10}\,\mathrm{m^2\,s^{-1}}$. The difference of seven orders of magnitude can be explained by a very fast initial diffusion of C in the steel and subsequent fast formation of carbides, mainly Fe_3C, since EUROFER consists of about 90 at.% of Fe. Therefore, for the majority of the annealing time this process should be considered as C diffusion in Fe_3C, which is formed due to C diffusion in EUROFER, rather than in original EUROFER. Besides, the diffusion coefficient of C in EUROFER is also lower than in pure Fe due to the presence of Cr in the steel. According to [39, 48], a similar effect has been observed for some carbides in comparison with pure metals.

5.2 EUROFER layer with Me interlayer

To suppress the fast C diffusion in EUROFER, different *Me* interlayers were investigated as a diffusion barrier.

5.2.1 Ti

In selecting an appropriate interlayer for the suppression of diffusion between the EUROFER matrix and SiC fibres, Ti was proposed first because the fibres were originally specified and produced for application with a Ti matrix. In [32, 33] the interaction between Ti and SiC was studied. It was found that at 900 °C they reacted and formed the following phases: $Ti_5Si_3C_X$ and TiC_X. However, there was no information at which temperature this interaction commenced.

The samples of SiCE_Ti2 with thin Ti (40 nm) and EUROFER (50 nm) layers on a SiC substrate were annealed at temperatures of 400 to 1000 °C. After annealing at 400 °C the structure and composition of the layers remained the same. Due to reactions between the layers and agglomeration, it was impossible to investigate the samples annealed at temperatures of 600 °C and higher. Annealing at 750 °C for 2 h of the sample SiCE_Ti3 with thick (500 nm) layers resulted in crack propagation and partial layer delamination. This can be explained by stresses in the layers caused by the transformation from α-Ti to β-Ti. The temperature for this transformation is 882 °C but with addition of 15 at.% of Fe it decreases to 595 °C as can be seen from the Fe - Ti phase diagram (see Fig. C.10 in Appendix C).

For the samples with graphite substrates the following diffusion processes should be taken into account: C diffusion in Ti, Ti in Fe and Fe in Ti. No data on the diffusion coefficient of Ti in Fe was found in the literature and so it was impossible to determine which diffusion process is faster: Fe in Ti or Ti in Fe. From [52] the tracer diffusion coefficient of Fe in β-Ti at 900 °C was estimated to be $3.05 \cdot 10^{-8}\,\mathrm{m}^2\,\mathrm{s}^{-1}$ while the diffusion coefficient of C in β-Ti at 950 °C was $1.34 \cdot 10^{-10}\,\mathrm{m}^2\,\mathrm{s}^{-1}$. Consequently, Fe diffuses quicker in β-Ti than C. Due to the diffusion of C and Fe in Ti caused by annealing at the temperatures of 400 to 1000 °C treated in this work, the following phases could be formed between Fe - Ti and C - Ti, according to the corresponding binary phase diagrams: TiFe, $\mathrm{TiFe_2}$ and TiC.

The schematic sketch of the diffusion processes occurring during annealing of the sample with Ti and EUROFER layers on graphite is presented in Fig. 5.2. By annealing the CWE_Ti2 samples with thin layers (50 nm) in the temperature range 400 to 1000 °C, the influence of the annealing temperature on the diffusion processes was investigated. After annealing at 600 °C for 2 h the Ti content in the EUROFER layer of CWE_Ti2 increased to 12 at.%, while the C concentration rose to 6.5 at.%. These diffusion processes of Ti and C into EUROFER are illustrated in Fig. 5.2. The C and Fe mean concentrations in the Ti interlayer were 31.0 and 24.5 at.%, respectively, indicating strong interdiffusion between the Ti and EUROFER layers at 600 °C. Moreover, at this temperature the diffusion rate of C in α-Ti was found to be about the same as the diffusion rate of Fe in α-Ti.

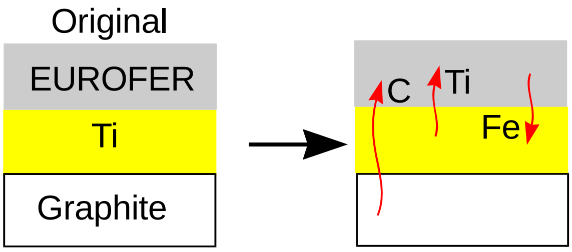

Figure 5.2: Schematic sketch of the diffusion processes of C, Ti and Fe in the CWE_Ti3 sample

After annealing at 750 °C the sample CWE_Ti3 with thick (500 nm) layers was destroyed: only small parts of the coatings remained on the sample surface which showed cracks and partial layer delamination. This is probably due to stresses in the film arising from the difference in the thermal expansion coefficients of the Fe - Ti and TiC compounds. Their formation was indicated by the *IBA* results which showed diffusion of C and Fe in Ti for the CWE_Ti2 sample with thin layers. Additionally, as mentioned above, the transformation from α-Ti to β-Ti occurs at lower temperatures in the presence of Fe, which can also lead to high stresses in the layers and to crack propagation.

5.2.2 Cr

As the next candidate, Cr was chosen due to the low diffusivities of C and Fe in Cr. In [34] reactions between SiC and Cr were investigated at 1000 °C. The following carbides and silicides were found to form: $\mathrm{Cr_5Si_3C}$, $\mathrm{Cr_7C_3}$, $\mathrm{Cr_3Si}$ and $\mathrm{Cr_{23}C_6}$. In [31] the interaction between SiC and Fe - 20Cr was studied and it was observed that after annealing at temperatures above 900 °C the reaction zone was composed of Fe_3Si, Cr_3Si, M_7C_3-type carbide (M = Cr, Fe) and graphitic C precipitates. Unfortunately, in both these articles the authors did not indicate the temperatures at which these reactions started. To analyse the diffusion processes taking place in the diffusion couple Cr - EUROFER one can compare their diffusion coefficients. The tracer diffusion coefficient of Fe in Cr at 1000 °C is $1.14 \cdot 10^{-18}\,\mathrm{m^2\,s^{-1}}$ [52], which is slightly lower than the value for Cr in γ-Fe at the same temperature, namely $4.01 \cdot 10^{-17}\,\mathrm{m^2\,s^{-1}}$ according to [52]. EUROFER consists of 9 wt.% of Cr, therefore, the self-diffusion of Cr can influence the Cr diffusion in EUROFER. One should compare the rate of Fe diffusion in Cr (Fe $\longrightarrow$ Cr) with the rate of Cr diffusion in the alloy of Fe and Cr (Cr $\longrightarrow$ Fe - Cr). The diffusion coefficient of Cr in Fe - 12.3 wt.% Cr at 1000 °C is $4.48 \cdot 10^{-14}\,\mathrm{m^2\,s^{-1}}$ [52], which is three orders of magnitude higher than for Cr in pure Fe and four orders of magnitude higher than for Fe in Cr. Consequently, the Cr diffusion in EUROFER proceeds much faster than Fe diffusion in Cr due to the significant contribution of the Cr self-diffusion.

In Fig. 5.3 the phase transformations of the EUROFER and Cr layers caused by the diffusion of Cr and decomposition of SiC are shown.

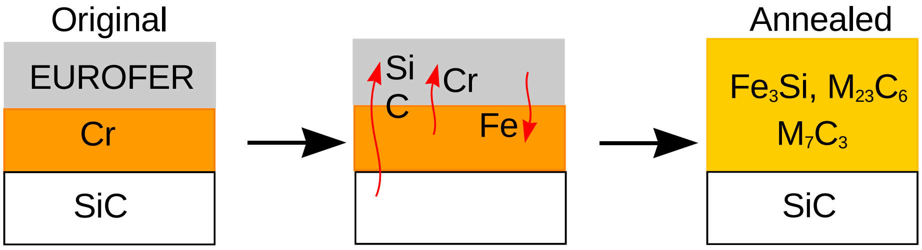

Figure 5.3: Schematic sketch of the phase transformations caused by diffusion of Si, C, Cr and Fe in the SiCE_Cr4 sample

The samples SiCE_Cr1 with thin (50 nm) layers were annealed at temperatures from 400 to 1000 °C for 2 h. This allowed an analysis of the interaction between Cr and EUROFER, and between Cr and SiC. After annealing at 400 °C the Cr concentration in the steel remained the same 10 at.% as in the original EUROFER layer, whereas Fe diffused into the Cr interlayer and its concentration was 6 at.%. After annealing at 600 °C the Cr and EUROFER layers were found to be completely mixed, i.e. the Cr content in EUROFER and the Fe content in Cr were so high that peaks in the *IBA* spectra corresponded to Cr and Fe were overlapped completely.

The sample SiCE_Cr4 with thick (500 nm) layers was investigated before and after annealing at 750 °C for 2 h. Due to the sponge-like structure of the layer (see Fig. 4.32b in subsection 4.2.2) it was impossible to perform the analysis of the layer composition by *IBA*. *XRD* analysis of the annealed SiCE_Cr4 brought to light the decomposition of SiC and the formation of new phases caused by the diffusion of Si and C into the intermixed layer. All these processes are indicated in Fig. 5.3. In the *XRD* pattern (see Fig. 4.33a in subsection 4.2.2) the peaks related to the following phases were observed: Fe_3Si, $M_{23}C_6$, that is $(Fe, Cr)_{23}C_6$, and M_7C_3, that is $(Fe, Cr)_7C_3$.

Consequently, already at the temperature of 600 °C the Cr and EUROFER layers are mixed and there is no more suppression of the interdiffusion between EUROFER and the substrate. Furthermore, in the presence of Cr it is sufficient to heat the SiC up to 750 °C to make it decomposed. This is unacceptable for the SiC / EUROFER composite material as it leads to the dissolving of the SiC fibres in the matrix at the assumed working temperature.

For the sample with a graphite substrate, one has to take into account, in addition to the interaction between Cr and EUROFER, also the C diffusion in Cr. The tracer diffusion coefficient of C in Cr at 1000 °C is $1.29 \cdot 10^{-11}\,\mathrm{m^2\,s^{-1}}$ [52]. Thus, the diffusion coefficients for the processes which can take place during annealing at 1000 °C of the sample with a graphite substrate coated by EUROFER and Cr layers, are [52]:

$$\begin{array}{ll}
\mathrm{Fe} \longrightarrow \mathrm{Cr} & 1.14 \cdot 10^{-18}\,\mathrm{m^2\,s^{-1}} \\
\mathrm{Cr} \longrightarrow \mathrm{Fe\ \text{-}\ 12.3\ wt.\%\ Cr} & 4.48 \cdot 10^{-14}\,\mathrm{m^2\,s^{-1}} \\
\mathrm{C} \longrightarrow \mathrm{Cr} & 1.29 \cdot 10^{-11}\,\mathrm{m^2\,s^{-1}}.
\end{array}$$

Instead of the diffusion coefficient of Cr in EUROFER, here the data for the diffusion of Cr in Fe - 12.3 wt.% Cr is given for comparison. Hence, the dominant process for a sample with a graphite substrate appears to be C diffusion which is much faster than Cr diffusion into EUROFER and Fe in Cr.

The schematic sketch of the diffusion processes occurring during annealing of the sample with Cr and EUROFER layers on graphite is presented in Fig. 5.4.

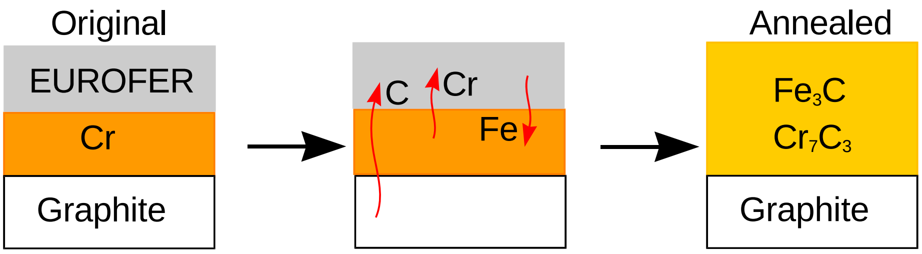

Figure 5.4: Schematic sketch of the phase transformations caused by diffusion of C, Cr and Fe in the CWE_Cr3 sample

As was done for samples with a SiC substrate, the samples CWE_Cr1 with thin (50 nm) layers on graphite were annealed at temperatures from 400 to 1000 °C for 2 h. Cr and EUROFER started to react at 400 °C. Thus, the Cr concentration in the steel was found to increase to 14 at.% (10 at.% of Cr in original EUROFER + 4 at.% of Cr diffused from the Cr interlayer), while 4 at.% of Fe was observed in the Cr interlayer. Additionally, C diffused through the Cr into the EUROFER layer and its content in the steel increased to 4 at.%, while in the Cr interlayer the C concentration rose to 10 at.%. Therefore, as it was assumed above, C diffusion in Cr is faster than other processes. Annealing at the higher temperature of 600 °C resulted in the complete intermixing of the Cr and EUROFER layers, in the same way as was observed for these layers on the SiC substrate (sample SiCE_Cr1). In addition, the C concentration strongly increased to 31 at.% in EUROFER layer. Similar changes in composition of the layers were observed for the CWE_Cr4 sample with thick (500 nm) layers annealed at 750 °C for 2 h. In this case it was impossible to distinguish the composition of intermixed layers except for the C concentration which increased to 30 at.%. After annealing at 750 °C the C content in the EUROFER layer with the application of a Cr interlayer was found to be even higher than in the EUROFER layer without any interlayers.

The structure of the layers also changed and new grains with a size of $1 - 2\,\mu$m were formed (see Fig. 4.32d in subsection 4.2.2). Additionally, the layers were found to be cracked. These changes are explained by the formation of new phases.

The results of *XRD* analysis (see Fig. 4.33b in subsection 4.2.2) are in good agreement with two previous investigations. The new phases have been formed due to C diffusion: Fe_3C and Cr_7C_3. This transformation can also affect the appearance of cracks in the layers.

Consequently, it is found that the Cr interlayer reacts intensively with EUROFER which leads to intermixing at 600 °C and causes decomposition of SiC at 750 °C. Therefore, it cannot be used as a diffusion barrier for the system of SiC / EUROFER.

5.2.3 W

W was chosen as a diffusion barrier due to its low self-diffusion, low C diffusion in W, low diffusion of Fe in W and medium diffusion of W in Fe.

The interaction between SiC and W was studied in [37] at temperatures of 600 to 1100 °C. It was found that the W film reacted with SiC only at temperatures higher than 950 °C. Therefore, in the experiments at 750 °C only Fe - W compounds were formed. At this temperature two Fe - W compounds exist according to the Fe - W binary phase diagram: stable FeW and metastable Fe_2W. To deduce the possible interactions between W and EUROFER, the diffusion coefficients of Fe in W and W in Fe should be compared. At 750 °C the tracer diffusion coefficient of W in α-Fe is $1.88 \cdot 10^{-16}\,\mathrm{m^2\,s^{-1}}$ [52] and there is no available data for the diffusion of Fe in W at that temperature. One can compare this value with the diffusion coefficient of Fe in W at higher temperatures. Thus, at 980 °C the tracer diffusion coefficient of Fe in W is $4.3 \cdot 10^{-18}\,\mathrm{m^2\,s^{-1}}$ [52], which is lower than for W in Fe at the lower temperature of 750 °C. Therefore, the diffusion of W in Fe is faster than Fe in W. Hence, it is expected that the reaction zone consists mainly of the EUROFER layer, while the majority of the W layer remains the same as before annealing.

A sketch of the phase transformation taking place in the layers on the SiC substrate is shown in Fig. 5.5. The samples SiCE_W1 with thin (50 nm) layers were annealed at temperatures from 400 to 1000 °C. This allowed an analysis of the interaction between W and Fe, and W with SiC. Investigation of the annealed sample revealed that the diffusion of additional W from the W interlayer in EUROFER is observed even at 600 °C. At this temperature the diffusion is slow, therefore only 0.4 at.% of additional W was detected in the EUROFER layer after annealing for 2 h, i.e. the total W content in EUROFER was 0.7 at.%.

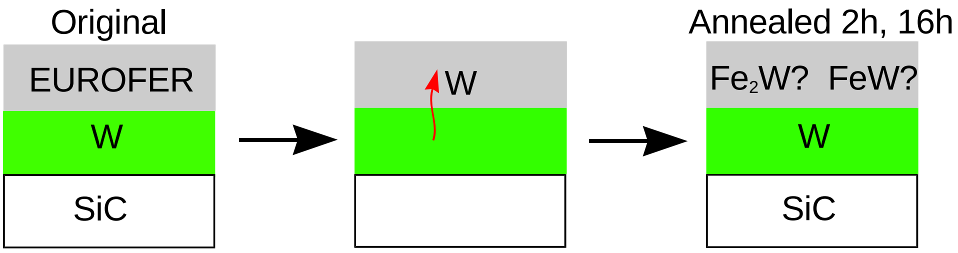

Figure 5.5: Schematic sketch of the phase transformation caused by diffusion of W in the SiCE_W2 sample with different annealing time

With increasing temperature the W concentration also increased. Due to degradation of the SiCE_W1 covered with thin layers, the influence of high annealing temperature of 750 °C on the W concentration in EUROFER was investigated for the samples SiCE_W2 coated with thick layers (500 nm). Annealing at 750 °C for 2 h of the SiCE_W2 sample resulted in a mean concentration of additional W diffused from the W interlayer of 7.4 at.% in the EUROFER layer, while the concentration in the main part of the W layer itself was found to remain the same as before annealing. After the longer duration of 16 h at the same temperature the W concentration in the steel, diffused from the W interlayer, increased to 15.9 at.%. Therefore, the total W content in EUROFER layer after annealing for 16 h was 16.2 at.%.

The presence of an increased W concentration in the EUROFER gave rise to the appearance of precipitate formation in the form of white specks visible in the images made in both *SE* and *BSE* modes of *SEM* (*SE* images shown in Fig. 4.38b and d in subsection 4.2.2).

The *XRD* patterns of the SiCE_W2 sample annealed at 750 °C for 2 and 16 h (see Fig. 4.40a in subsection 4.2.2) revealed similar peak positions to those observed for the original sample. No phase transformation was detected by this analysis, i.e. SiC did not decompose at 750 °C when in contact with W, what is in good agreement with the results given in [37]. On the other hand, no peaks corresponding to the formation of Fe - W compounds appeared on the patterns for the samples annealed at 750 °C for 2 and 16 h. Therefore, the Fe - W compound formation, in spite of the presence of precipitates in the *SEM* images and increased W concentration in EUROFER, is not confirmed by the results of *XRD* analysis. It is possible that the intensity of the peaks was too low to be detected due to the small amount of the formed compound or that the layer texture hindered the analysis.

Since SiC did not react with W at 750 °C and, consequently, had no influence on the diffusion of W in EUROFER, the concentration depth profiles of the original and annealed SiCE_W2 samples were used for the $D(C)$ fitting procedure. The results of the calculations are given in Figs. 4.67a and 4.68 in subsection 4.3. The fitting was performed for the depth profiles measured for samples annealed for 2 and 16 h. Since the same fitting parameters are valid for both the depth profile of the sample annealed for 2 h and for the sample annealed for 16 h, the annealing duration does not influence the dependence of the diffusion coefficient on concentration. The maximum $D(C)$ value of $5 \cdot 10^{-18}$ m^2 s^{-1} corresponds to the low W content in the steel. It is lower than the tracer diffusion coefficient of W in α-Fe, $1.88 \cdot 10^{-16}$ m^2 s^{-1}, at the same temperature. This difference is explained by the influence of other components of the EUROFER on the diffusion rate and also by the suppression of W diffusion caused by the possible formation of Fe - W compound.

To estimate the rates of the diffusion processes which can take place in the W interlayer due to annealing of the sample with a graphite substrate coated with W and EUROFER layers, the tracer diffusion coefficients of Fe in W and C in W should be compared. At a temperature of 980 °C, according to [52, 54], they are:

$$\begin{array}{ll} \mathrm{Fe} \longrightarrow \mathrm{W} & 4.3 \cdot 10^{-18}\,\mathrm{m^2\,s^{-1}} \\ \mathrm{C} \longrightarrow \mathrm{W} & 9.5 \cdot 10^{-15}\,\mathrm{m^2\,s^{-1}} \end{array}$$

Thus, the C diffusion is faster than Fe diffusion in W but it is close to the rate of the W diffusion in Fe even at the lower temperature of 750 °C.

In Fig. 5.6 the phase transformations of the EUROFER and W layers on the graphite substrate caused by diffusion of C and W are shown. To estimate the influence of annealing temperatures ranging from 400 to 1000 °C on the diffusion processes, the sample CWE_W1 with thin layers (50 nm) was investigated. After annealing at 600 °C for 2 h the W content in the EUROFER layer of the CWE_W1 increased by 0.8 at.%, i.e. the total W content in the steel was 1.1 at.%, while the C concentration increased by 1 at.% due to the diffusion of W and C into the EUROFER layer, as shown in Fig. 5.6. As it was observed for the same layers on SiC, W and EUROFER begin to react at 600 °C. To collect more data about transformations caused by annealing at 750 °C for 2 and 16 h, detailed investigations of the CWE_W2 sample with thick layers (500 nm) were carried out. The higher temperature of 750 °C resulted in faster C and W diffusion. The W content in the EUROFER of the CWE_W2 annealed for 2 h increased by 5.5 at.%, while the C content in the EUROFER was 3.0 at.%, as compared to 2.0 at.% in the as-deposited steel layer. C diffusion throughout the W also affected the C concentration in the W layer itself. Thus, the mean C concentration increased up to 8.0 at.%, in contrast to the original 3.0 at.%. In spite of the reaction of W with EUROFER, the major part of the W layer remained the same as before annealing, as was observed for the layers on the SiC substrate. W diffused from the W interlayer through the steel layer and the concentration of additional W at the sample surface was found to be 4 at.%, while no Fe was detected in the W layer. Consequently, W diffusion in EUROFER dominates over Fe diffusion in W what is in good agreement with the literature data presented above.

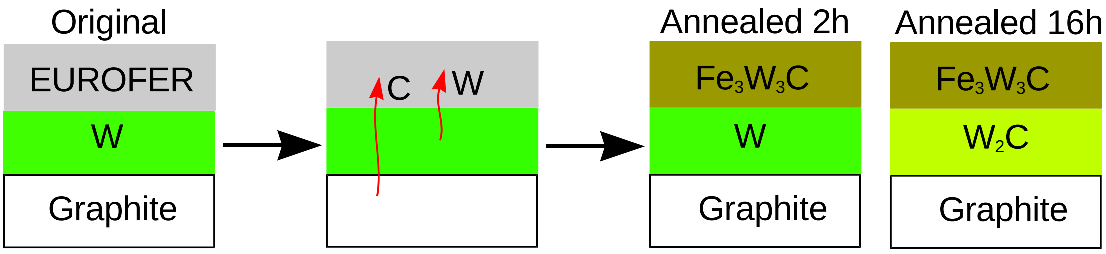

Figure 5.6: Schematic sketch of the phase transformations caused by diffusion of C and W in the CWE_W2 sample with different annealing time

A longer duration of 16 h at the same temperature of 750 °C gave rise to enlargement of the reaction zone between W and Fe and the mean W content was 6.9 at.%, while the concentration of W at the sample surface remained at the same value of 4 at.%. Therefore, the formed Fe - W - C compound suppresses further W diffusion in the steel. At the same time, the mean C concentration in the EUROFER layer increased to 7.0 at.%, which is significantly lower than that observed in the case of the Cr interlayer. With longer annealing, the mean C concentration in W increased to 15.5 at.%.

The presence of precipitates in the form of white specks on the *SEM* image is explained by the diffusion of W in the EUROFER followed by the formation of compounds involving Fe and W, as was described in subsections 2.2.3 and 2.2.4.

The results of the two previous analyses, *IBA* and *SEM*, correlate well with the results of *XRD* measurements (see Fig. 4.40b in subsection 4.2.2). The diffusion of C and W in EUROFER observed in the concentration depth profiles resulted in the formation of the compound Fe_3W_3C. Annealing for a longer time increased the amount of C and W in the EUROFER and, consequently, allowed further growth of Fe_3W_3C which led to an increasing of the intensity of the peaks corresponded to this phase. As for phase transformation in the W layer, the increase of the C content in the W led to the formation of W_2C that was detected on the sample annealed for 16 h (see Fig. 5.6). It was not observed on the sample annealed over 2 h due to the small amount of formed carbide, where carbide presence influences the intensity of peaks corresponding to this phase.

Partial delamination of the layers on graphite substrate was visible on the *SEM* images (see Fig. 4.39c in subsection 4.2.2) annealed for 16 h. This is the result of high tensile stress caused by heat treatment and the formation of W_2C which has a lower thermal expansion coefficient of $1.2 \cdot 10^{-6}\,\mathrm{K}^{-1}$ than that of W, $4.5 \cdot 10^{-6}\,\mathrm{K}^{-1}$. In the experiments, only α-W_2C could be formed since WC and β-, γ-W_2C, according to the W - C binary phase diagram, are formed at higher temperatures. On the other hand, the formation of subcarbide causes the reduction of C diffusion in EUROFER as the diffusion coefficient of C in W_2C is $8.1 \cdot 10^{-14}\,\mathrm{m}^2\,\mathrm{s}^{-1}$, in contrast to the diffusion coefficient of C in W of $2.8 \cdot 10^{-12}\,\mathrm{m}^2\,\mathrm{s}^{-1}$ [48].

The *BSE* image analysis of the surface of CWE_W2 annealed for 2 h gives 10% of the surface coverage by white specks. The mean concentration of W at the sample surface is 4 at.%. If one assumes that all W has reacted with Fe and C then the W concentration in the white specs should be about 40 at.%. This value is in a good agreement with data from [50] (see more details in subsection 2.2.4), where a W concentration in M_6C, that is $(Fe, W)_6C$ of $41 - 48$ at.% is reported.

As a consequence, in experiments with a W interlayer it is found that Fe and W begin to react at 600 °C. Due to C and W diffusion in the EUROFER of the CWE_W2, the steel layer has been changed due to the formation of a new phase Fe_3W_3C in it, while the W layer has partially converted to W_2C. Longer annealing results in further growth of a subcarbide phase and a stress increase with consequent crack propagation and partial layer delamination. The W concentration in EUROFER is found to be higher for the layer deposited on SiC than on graphite substrates. Since W has a high atomic number 74 and thus the precision of its detection by IBA is very high (error 0.05 at.%), it is impossible to explain the difference in concentrations through an error of spectra evaluation. Hence, the carbide Fe_3W_3C formed in the EUROFER layer significantly affects the further suppression of W diffusion.

5.2.4 Re

Re was proposed in the literature as an appropriate diffusion barrier material for C because it does not form carbides. Due to the absence of data on diffusion coefficients for the Re - Fe couple it was impossible to estimate the reaction rate between Fe and Re.

In Fig. 5.7 the phase transformation of the EUROFER layer caused by the diffusion of Re is shown. The samples SiCE_Re1 with thin (50 nm) layers were annealed at temperatures from 400 to 1000 °C for 2 h to analyse the interaction between Re and Fe as well as between Re and SiC. The concentration depth profile of SiCE_Re1 annealed at 600 °C obtained by IBA revealed the presence of 0.3 at.% of Re in the EUROFER and no Si and C in the Re.

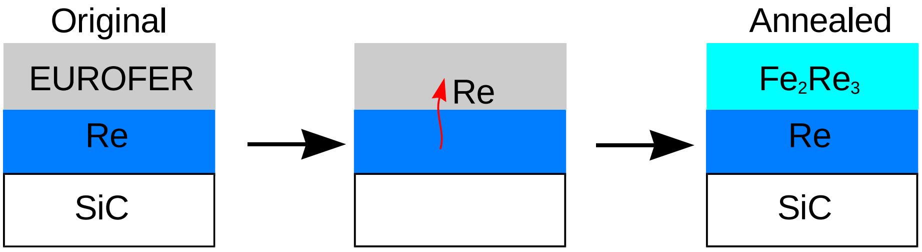

Figure 5.7: Schematic sketch of the phase transformation caused by diffusion of Re in the SiCE_Re2 sample

An investigation of the SiCE_Re1 annealed at higher temperatures by *IBA* was inappropriate due to the layer structure, as distinct from SiCE_Re2 with thick (500 nm) layers annealed at 750 °C for 2 h. At 750 °C it was found that SiC did not decompose and react with the Re and EUROFER layers. According to *IBA* results, the mean content of Re in the steel layer of the SiCE_Re2 was 14.7 at.% (see Table 4.14 in subsection 4.2.2). In the *XRD* pattern corresponding to SiCE_Re2 (see Fig. 4.48a in subsection 4.2.2) only a new phase of Fe_2Re_3 was observed. In that way, as a conclusion from these two analyses, no reaction between SiC and metals appeared. This conclusion is in good agreement with the observations mentioned in subsection 2.2.1 that no reaction was detected between Re and SiC at temperatures below 1100 °C [38]. The formation of a new phase between Fe and Re, namely Fe_2Re_3, can also explain the precipitate formation that was clearly seen on the *SEM* image (see Fig. 4.47b in subsection 4.2.2), because of the big difference in atomic numbers of Re (75) and Fe (26).

The concentration depth profiles of SiCE_Re2 before and after annealing at 750 °C were used for the fitting procedure of the diffusion coefficient depending on the concentration of Re in EUROFER. The maximum value of $1.6 \cdot 10^{-17}\,\mathrm{m^2\,s^{-1}}$ corresponds to the low Re content. It should be lower than the tracer impurity diffusion coefficient of Re in pure Fe due to the formation of a Fe_2Re_3 phase, which changes the chemical potential and, consequently, the value of the diffusion coefficient itself. Due to a lack of literature data, it is impossible to compare the calculated value of the diffusion coefficient with the tracer impurity diffusion coefficient of Re in Fe and estimate the influence of the Fe_2Re_3 compound formation on the rate of Re diffusion.

A schematic sketch of the phase transformations taking place in the layers on a graphite substrate CWE_Re2 is shown in Fig. 5.8. An analysis of the influence of annealing temperature on the interaction between Re and EUROFER and between Re and graphite of the CWE_W1 sample with thin layers (50 nm) was performed for the temperature range from 400 to 1000 °C for 2 h duration. Synchronous increase of the C and Re contents in the EUROFER layer due to diffusion (see Fig. 5.8) was observed after annealing at 600 °C. As a result, 9 at.% of C and 0.6 at.% of Re were found in the steel. For detailed investigation of the diffusion and phase formation, the CWE_Re2 sample with thick layers (500 nm) was analysed after annealing at 750 °C for 2 h. The C and Re concentrations of 8.0 and 10.0 at.%, respectively, were detected in the EUROFER layer.

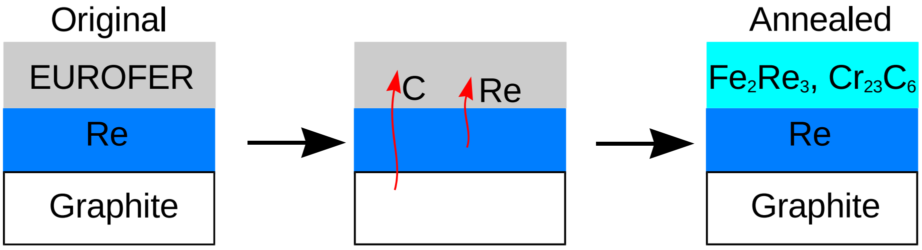

Figure 5.8: Schematic sketch of the phase transformations caused by diffusion of C and Re in the CWE_Re2 sample

The intermetallic compound Fe_2Re_3 was found to be formed in the annealed CWE_Re2, as it was for the sample with SiC substrate, SiCE_Re2, but in addition, $Cr_{23}C_6$ was formed because of C diffusion through the Re layer into the EUROFER. This conclusion is based on the results of *XRD* and *IBA* investigations. Thus, the appearance of both these phases was observed on the *XRD* patterns of the annealed CWE_Re2 (see Fig. 4.48b in subsection 4.2.2). Diffused C provides the formation of $Cr_{23}C_6$, while Re builds up the intermetallic compound. Re does not form a carbide (see more in subsection 2.2.2) and a ternary phase Re - Fe - C is absent, therefore free C forms carbides with Cr while diffusing into the steel that contains 9 at.% of Cr.

The presence of an Re - Fe compound has also been verified by observation of the precipitate formation in *SEM* images (see Fig. 4.47 in subsection 4.2.2). In contrast to Re - Fe, it is impossible to see $Cr_{23}C_6$ by *SEM*, since this carbide has a high Cr content and the atomic number of Cr is 24 which is very close to that of Fe, 26.

So, as a consequence, in experiments with a Re interlayer it was found that Re starts to react with Fe at 600 °C. In the EUROFER layer on SiC the formation of a new phase of Fe_2Re_3 has been observed after annealing, while on graphite two phases have appeared,

Fe_2Re_3 and $Cr_{23}C_6$. One can compare the Re concentration in EUROFER for SiCE_Re2 with the same value for CWE_Re2: in the former case, the Re content is 14.7 at.%, which is higher than for CWE_Re2 where only 10.0 at.% of Re has been detected. The same effect is observed for the W interlayer. Therefore, C diffusion and the following carbide formation influences the diffusion of Re species.

5.2.5 Re / W

Taking into account the experience of the application of W and Re as diffusion barriers for C, a Re / W multilayer was chosen. Since Re reacted intensively with Fe, W was selected as an adjoining interlayer to the steel. In [59, 60] the application of such a diffusion barrier was investigated. It was found that due to C diffusion one of the W layers was transferred into a WC compound, which in combination with the Re diminished the net C diffusion. This multilayer kept its structure at temperatures below 1600 °C, which is much higher than the maximum temperature in this work, 1000 °C.

For both multilayer samples, investigations by *XRD* and *IBA* were found to be much more difficult than those applied to single layer interlayers because of the peaks overlapping for W and Re.

In Fig. 5.9 a schematic sketch of the phase transformations caused by C and W diffusion in EUROFER is presented for the CWE_Re_W1 consisting of three layers with equal thicknesses of 180 nm: W / Re / W.

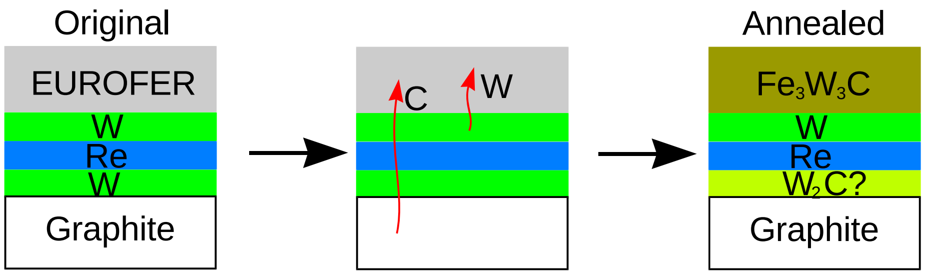

Figure 5.9: Schematic sketch of the phase transformations caused by diffusion of C and W in the CWE_Re_W1 sample

As it was observed earlier for the CWE_W2 with a *W* interlayer, the concentration depth profile of the CWE_Re_W1 annealed at 750 °C for 2 h reveals an increase of the mean W content by 5.4 at.%, therefore, the total W content in the steel is 5.7 at.%. At the same time, the mean C concentration remains the same 2.0 at.%. From the concentration depth profile given in Fig. 4.53 in subsection 4.2.2 it is seen that the C content rose to 4 at.% at the interface between the EUROFER and W layers. This can be explained by the formation of Fe_3W_3C compound at the reaction zone. In consequence, W partially diffused from the adjoining W interlayer through the EUROFER layer, while the major of the W layer itself remained the same. It confirms that the dominant process of Fe - W interaction is the W diffusion.

Regarding the multilayer structure, the Re and W interlayers did not mix or interdiffuse into each other after annealing at 750 °C for 2 h.

Due to the presence of Re and W peaks the most pronounced *XRD* peak of the Fe_3W_3C phase was hidden. However, all other peaks with lower intensities related to the compound were clearly observed, as well as the peaks corresponded to the W_2C phase. Hence, the Fe_3W_3C compound is formed in EUROFER as it is shown in Fig. 5.9. Taking into account the direction of C diffusion, one can assume that exactly the W layer adjoining the graphite is transferred to the W_2C rather than the W adjacent to the EUROFER.

The Fe_3W_3C compound in the form of precipitates in EUROFER was observed as white specks in the *SEM* image (see Fig. 4.51b in subsection 4.2.2). Additionally, the layers were found to be cracked due to annealing. It is explained by the formation of W_2C and the following increase of stress at the interface due to a mismatch in the thermal expansion coefficients of W_2C and W: $1.2 \cdot 10^{-6}\,K^{-1}$ and $4.5 \cdot 10^{-6}\,K^{-1}$ [48], respectively.

Because of crack formation and the absence of interdiffusion between Re and W at this temperature, the structure of the multilayer was modified to a system with four-interlayers, namely Re / W / Re / W, with one W interlayer directly adjacent to the EUROFER layer. This multilayer had a total thickness of 560 nm, and the interlayers possessed equal thicknesses of 140 nm each.

The diffusion processes and following phase transformations are shown in the schematic sketch for the CWE_Re_W2 sample in Fig. 5.10.

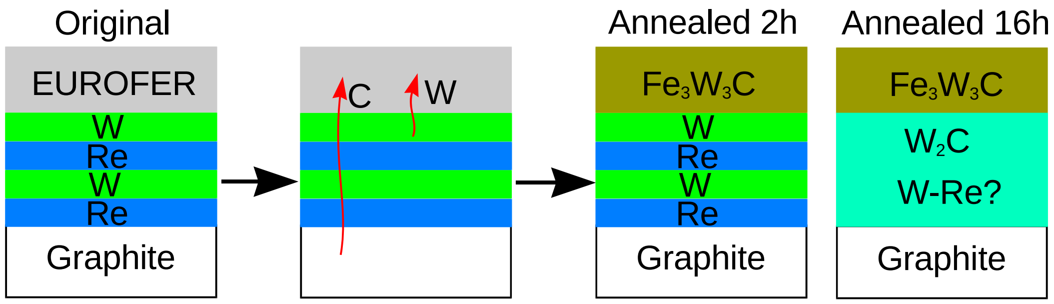

Figure 5.10: Schematic sketch of the phase transformations caused by diffusion of C and W in the CWE_Re_W1 sample with different annealing time

After annealing at 750 °C for 2 h the mean content of additional W diffused in EUROFER from the adjacent interlayer rose to 4.6 at.%, i.e. the total W content in EUROFER was 4.9 at.%. The mean C concentration was 2.5 at.% and its concentration also increased slightly at the interface zone between EUROFER and W because of C diffusion (see Fig. 5.10), as was observed in the previous case of the CWE_Re_W1 sample. In the CWE_Re_W2 sample each interlayer was thinner than in the CWE_Re_W1, therefore the part of the W layer adjacent to the steel which did not react with EUROFER was also thinner. It was found that the interlayers composing the multilayer did not react between each other after annealing for 2 h. After annealing for 16 h the interdiffusion between Re and W interlayers took place.

Due to an overlapping of the peaks relating to Re and W it was impossible to separate them and detect the composition of each interlayer by *IBA*. As regards the EUROFER layer, its composition changed due to a simultaneous increase of the mean concentrations of C and additional W (from interlayer) to 12.0 and 6.7 at.%, correspondingly. This strong rise of the C content could also be a consequence of the interaction between W, Re and Fe.

Precipitate formation in the form of white specks was observed in the *SEM* images related to the samples annealed for 2 and 16 h. One significant difference between these two samples was the absence of crack formation in case of the sample annealed for only 2 h, in contrast to that annealed for 16 h. Unlike the W interlayer, the multilayer did not delaminate after long annealing for 16 h because of the lower stress in the layer due to the formation of the thinner W_2C layer at the interface.

A Fe - W compound was formed due to W diffusion into the EUROFER and the presence of precipitates. This was confirmed by the results of *XRD* analysis since very small peaks in the *XRD* patterns belonging to Fe_3W_3C were observed. Additionally to the Fe_3W_3C phase, W_2C was detected for the sample annealed for 16 h. Due to the presence of numerous peaks from Re and W in the *XRD* pattern the peaks related to the W - Re phase, which could have been formed in the CWE_Re_W2 annealed for 16 h, were hidden.

In conclusion, the longer duration of 16 h at 750 °C leads to the mixing of Re and W and loss of the diffusion barrier properties. The observed discrepancies in the temperatures of layer intermixing compared to [59,60] can be explained by two important differences. The first one is the thickness of the interlayers. In this work each layer was 140 nm in thickness, while in [59,60] the thickness of the interlayers varied from 2 to 10 μm. Thus, in the latter case each layer was significantly thicker than in case of the CWE_Re_W2. The second fact is that the composition of these interlayers in [59,60] was measured by applying energy dispersion X-ray spectroscopy and an electron probe micro analyzer to the sample cross-section in the middle of each layer. The precision of both those techniques is much lower than that of the *IBA* used in this work. Furthermore, the authors did not investigate the composition of the interface between Re and W. In these experiments, the concentration depth profile, and therefore the composition of the layer at every point, was investigated by *IBA* which is very sensitive to the content of W and Re.

5.3 EUROFER layer with ceramic interlayer

Three different ceramic interlayers, TiC, TiN and Er_2O_3, were selected as a diffusion barrier for C due to their stability at high temperatures with respect to Fe.

5.3.1 TiC

Before application of the TiC interlayer as a diffusion barrier, investigations of the influence of such deposition parameters as applied power density, bias voltage and sputtering of TiC or Ti and C targets on the layer structure and its composition were performed. Since an increase of the deposited coating's thickness led to its degradation, only samples with a 50 nm thick TiC layer working as a diffusion barrier were used in the annealing experiments.

The samples with TiC and EUROFER layers on SiC (SiCE_TiC1) and graphite (CWE_TiC1) substrates were annealed at temperatures from 400 to 1000 °C for 2 h. Annealing of the SiCE_TiC1 at temperatures higher than 400 °C resulted in blister formation in the SiC substrate. These blisters are obviously formed in an Ar enriched surface zone of the SiC substrate. The enrichment is due to the implantation of energetic Ar ions at the beginning of the deposition process. This conclusion was made basing on observation by *IBA* of an increased Ar content near the surface zone of the substrate due to application of the bias during deposition. Additionally, in the similar case of blistering in the SiC sample with a ZrO_2 layer, the roughness of the substrate increased. Such phenomena can be explained in the following way. According to [99], blisters are plastic dome-shaped bulgings of the surface layer of mostly circular circumferences. The blistering appears due to a critical gas concentration in the target caused by gas ion implantation. Such effects were observed for ions of different gases, including Ar^+, with different substrate materials. If the gas is introduced into the solid by implantation, strong nonequilibrium states of the gas-substrate system may be obtained [99]. Due to sufficiently low temperatures, the diffusion of the implanted gas is negligible. No blistering was observed for the samples being as-deposited and annealed at 400 °C. Since the Ar atoms diffuse via the vacancy mechanism, this process proceeds very slowly at such temperatures. An increase of the temperature accelerates the Ar diffusion. The Ar atoms can accumulate in the pores located near the surface of the SiC. Due to stress caused by the excess of pressure in the cavities (pores) the blisters start to grow. At temperatures of 750 °C and higher, holes in the cover of the bulgings were observed. In addition to the blistering, the layers were agglomerated at temperatures of $750 - 1000$ °C.

To find the reason for the blistering, one should compare the deposition parameters of TiC, TiN and ZrO_2. In contrast to TiC and ZrO_2, TiN did not reveal any blistering of the samples before and after annealing. In both depositions a V_{Bias} was applied to the substrates. For TiN the values of the applied V_{Bias} varied from 65 to 80 V, whereas for TiC and ZrO_2 it was changing every 5 min between 55 and 180 V. Since the mean projectile range depends on the ion energy, Ar is implanted deeper into the substrate in the case of a higher electric potential. Therefore, the blistering was observed for the samples with TiC and ZrO_2 as distinct from TiN. Consequently, the possible solution of the problem for SiC substrate could be the use of a low V_{Bias}. However, the samples with graphite and SiC substrates could not be deposited simultaneously because low values of V_{Bias} are not suitable for the graphite in terms of coating quality. As it was observed for samples with a graphite substrate deposited at a low V_{Bias}, the structure of the TiC layer possessed empty hillocks. This layer structure at the interface zone leads to degradation of the composite properties due to fibre debonding.

As for the CWE_TiC1, the structure and composition of the layers did not change upon annealing at temperatures up to 600 °C. According to the *SEM* image of the sample annealed at 750 °C (see Fig. 4.58c in subsection 4.2.3), an assumption can be made that the TiC layer was stable, since its hilly structure was observed below the agglomerated EUROFER observed in the form of grey formations. It was impossible to carry out *IBA*, *XRD* investigations of the layer composition and phase formations due to inappropriate surface conditions of the sample. After annealing at 1000 °C both layers were destroyed.

One can estimate the effectiveness of the application of a TiC interlayer by comparison with a pure Ti interlayer. The C concentration in the EUROFER with a Ti barrier after annealing at 600 °C for 2 h increased by 2 at.%, while with the TiC barrier it remained the same as for the as-deposited sample. Concerning interaction between the layers, the Ti and EUROFER layers were partly intermixed after annealing, since 25 at.% of Fe was found in the Ti and 12 at.% of Ti in the EUROFER. As to TiC, only 2 at.% of Fe was found in the interface zone between TiC and EUROFER. Therefore, in addition to the suppression of C diffusion at 600 °C, TiC was found to be stable with respect to reactions with EUROFER.

5.3.2 TiN

Prior to applying the TiN layer as a diffusion barrier the influence of different parameters, such as applied power density, partial pressure of N_2 and substrate bias, on composition, surface structure and crystalline structure of TiN was studied. The samples with a thin (50 nm) TiN interlayer on SiC (SiCE_TiN2) and graphite substrates (CWE_TiN2) were annealed at temperatures from 400 to 750 °C. Since the deposition rate of TiN was $0.5\,\mathrm{nm\,s^{-1}}$, it was impossible to produce layers with 500 nm thickness used in the other investigations.

The surface structure of the as-deposited coatings was different for SiCE_TiN2 and CWE_TiN2 due to the influence of the substrate material on layer growth. After annealing at temperatures below 750 °C for 2 h, both TiN and EUROFER homogeneously covered the surface of the SiCE_TiN2 and CWE_TiN2 samples. In accordance with *IBA* spectra, the TiN and EUROFER layers started to react at 600 °C since the Ti content in the EUROFER increased to 2 at.% after annealing. In addition, C diffused into the TiN and its concentration was 12 at.% after annealing at 600 °C. At the same time, the C concentration in the EUROFER remained the same as for the original sample. At 750 °C the surface roughness of the SiCE_TiN2 sample increased due to the growth of small crystals (see Fig. 4.60c in subsection 4.2.3). As regards to CWE_TiN2, the EUROFER layer began to agglomerate at this temperature, while TiN remained stable according to the *SEM* images and *EDX* analysis (see Fig. 4.61c in subsection 4.2.3).

In [44] it was found that a TiN layer on steel substrate could withstand temperatures up to 950 °C before starting to form titanium carbonitride. In the experiments reported here, the TiN layer appeared to be stable at temperatures up to 750 °C and did not react with EUROFER at all. The content level of Ti in the EUROFER of 2 at.% after annealing at 600 °C can be explained by the presence of some free Ti in the TiN layer which had not formed a compound during deposition. This assumption also correlates with the fact that the TiN layer remained the same after annealing at 750 °C, while the EUROFER agglomerated. If the layers reacted then the layer structure of the TiN would have changed.

5.3.3 Er_2O_3

In [88] Er_2O_3 was investigated as a H diffusion barrier. Since both H and C diffuse via interstitials, one can suggest that Er_2O_3 can also be applied as the C diffusion barrier basing on the good experience with H described in [88]. Furthermore, Er_2O_3 does not reveal any phase transformation at temperatures up to 2200 °C, and because of its stability this material is currently investigated as an insulating coating to prevent contact with liquid Li in future fusion reactors [100].

Er_2O_3, in contrast to all the other layers, was deposited by a filtered arc technique since it was impossible to produce a coating possessing a crystalline structure by magnetron deposition. Additionally, only this layer was deposited at the elevated temperature of 600 °C. The data on Er_2O_3 is limited and therefore it was hard to predict the interaction processes which could occur between EUROFER and Er_2O_3.

The sample CWE_Erbia1 with a thick (500 nm) erbia coating on a graphite substrate was annealed at 750 °C for 2 h. After annealing the crystals of EUROFER were grown on the sample surface which resulted in an increase of the layer roughness observed during processing of the IBA spectra. In spite of the crystals growth, the surface of the sample was homogeneously covered without any open areas. Neither a new phase formation appeared, nor any interaction between the Er_2O_3 and EUROFER was observed, according to *SEM*, *IBA* and *XRD*. Er has the high atomic number of 68, therefore even a small amount of this element diffused into EUROFER, after decomposition, can be detected by *IBA* with high precision and phase formation would be seen by the appearance of white specks (because of the high atomic number) on the *SEM* image. Furthermore, the C concentration in both Er_2O_3 and EUROFER layers remained at the same level of 2 and 1.5 at.%, correspondingly, as before annealing. Since the interlayer was deposited at 600 °C, thermal stress caused by the temperature rise should be lower than that for all other interlayers. This can significantly influence the layer resistance to crack propagation and delamination.

5.4 Comparison of investigated interlayers

To make a detailed comparison of the investigated samples with and without an interlayer, the mean concentrations of C and interlayer components are presented as diagrams in Fig. 5.11 and Fig. 5.12. In Fig. 5.11 data for the samples with thin (50 nm) layers annealed at 600 °C for 2 h are given, while in Fig. 5.12 data for thick (500 nm) layers annealed at 750 °C for 2 h are presented. To estimate the effectiveness of application of each interlayer, results for the sample without any interlayer, i.e. possessing only a EUROFER layer, are also given in the figures.

As seen, the worst case is related to the application of a Cr interlayer. The samples annealed at 600 °C with all investigated interlayers, except Cr, did not mix completely with the EUROFER layer and the C concentration in EUROFER remained below 10 at.%.

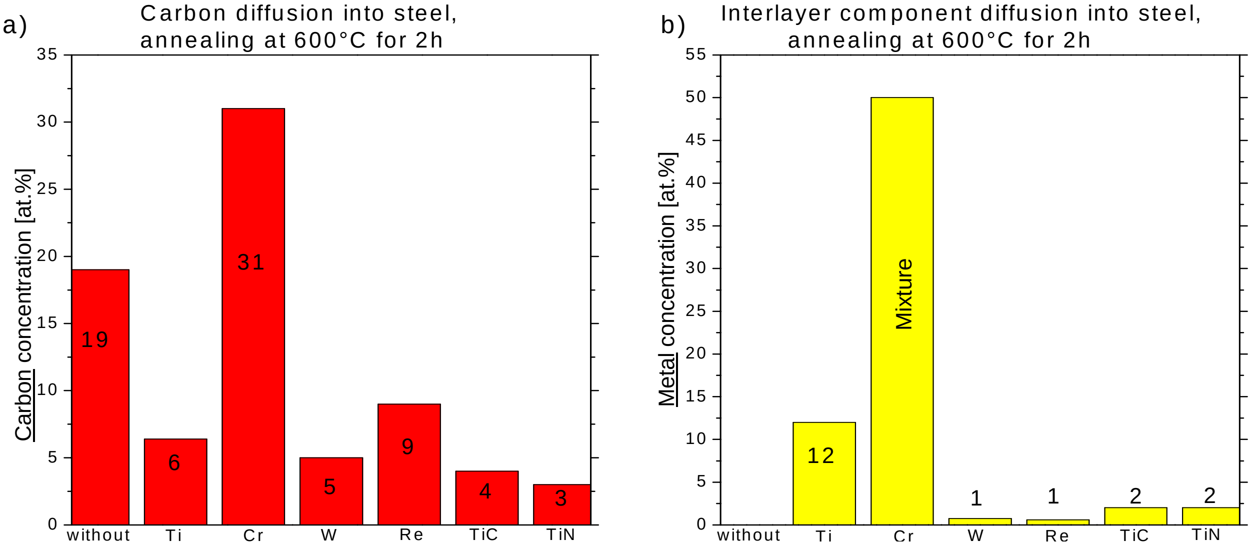

Figure 5.11: Mean C and interlayer component concentration in EUROFER layer for "thin" samples (each layer 50 nm) after annealing at 600 °C for 2 h: a) mean C concentration and b) mean concentration of interlayer component

Accordingly, these interlayers suppressed C diffusion, since the C concentration in EUROFER without any interlayer was at the higher level of 19 at.%. In contrast, after annealing of the sample with a Cr interlayer both Cr and EUROFER were found to be mixed and, moreover, the C concentration in the "EUROFER" (which was actually not EUROFER any more in terms of its content) was even higher than that without any interlayer. The situation was a little better with the Ti and Re layers. The application of Ti as a diffusion barrier decreased the C concentration in the EUROFER down to 6 at.%, while with Re only to 9 at.%, but the mean Ti concentration in the steel of 12 at.% was significantly higher than in the case of Re, 1 at.%. The best results were observed with the W and TiN layers. TiN suppressed C diffusion better than W but the Ti content in the EUROFER appeared to be higher than the W content. If the assumption about the presence of free Ti in TiN is correct, then over an extended period the W concentration in the EUROFER would rise in comparison to Ti, since TiN is stable even at higher temperatures. TiC is not considered in the group of the successful layers due to blistering, the reason for which is only suggested and is not confirmed experimentally.

In histograms of Fig. 5.12 the results of *IBA* analysis for samples annealed at 750 °C for 2 h are shown. For Ti the C and interlayer component concentrations in EUROFER are not given since both layers have mostly delaminated from the graphite substrate and partly delaminated from the SiC. Because of the low deposition rate of TiC and TiN they have not been investigated with a thickness of 500 nm and, consequently, they are not presented in these figures either. The opposite problem has arisen during deposition of Er_2O_3: owing to a very high deposition rate (compared to the other interlayers) this interlayer has been investigated only with a thickness of 500 nm. Additionally, the results for both multilayers are presented here.

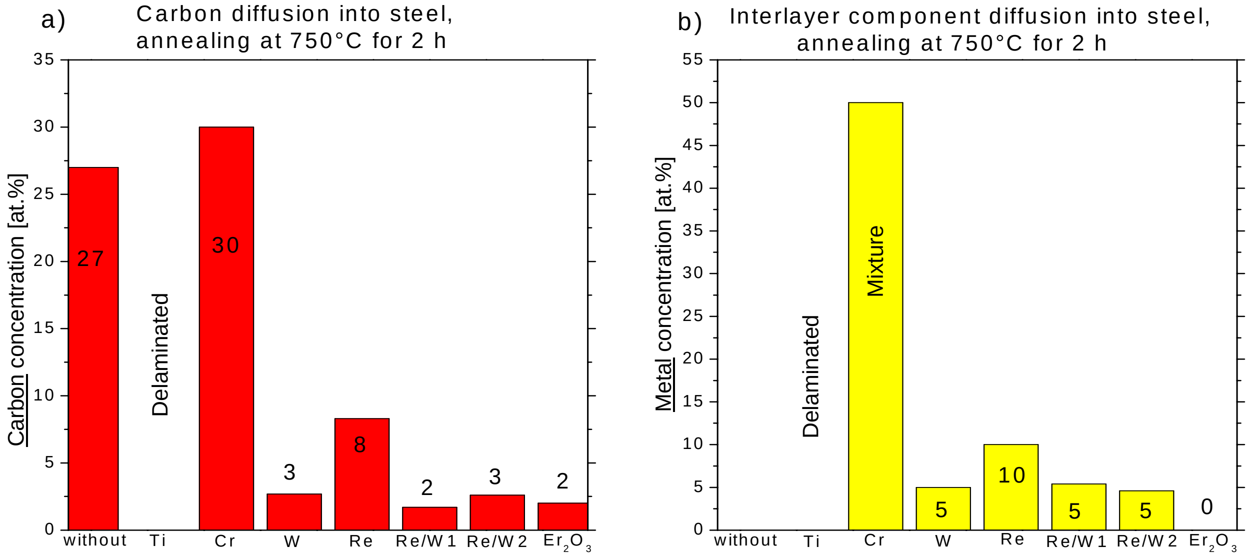

Figure 5.12: Mean C and interlayer component concentration in EUROFER layer for "thick" samples (each layer 500 nm) after annealing at 750 °C for 2 h: a) mean C concentration and b) mean concentration of interlayer component

Among the thick layers, the application of a Cr interlayer results in the highest concentrations of C and interlayer components in the EUROFER. The same situation appears for thin layers. In addition, only for a Cr interlayer has the decomposition of SiC, and thus the diffusion of Si and C, been detected. As for the thin layers, with the application of a Re interlayer both C and interlayer component concentrations are relatively high, which makes the use of Re as the barrier ineffective. Other metallic interlayers show quite similar results with the exception of the Re / W1 multilayer where crack propagation after annealing is observed. The best layer serving as a diffusion barrier is Er_2O_3 as the C concentration in the EUROFER has not increased upon annealing and no interlayer component diffusion into the steel has been detected.

In conclusion, the best candidates for further investigations as a diffusion barrier with fibres seem to be W, Re / W2, TiN and Er_2O_3.

5.5 Annealing of SiC fibres with W interlayer

The W interlayer was chosen for the first annealing experiments with SiC fibres because of the simplicity of its deposition. To investigate the applicability of the results gathered with coatings on planar graphite substrates to the coatings on SiC fibres, a set of fibres (SCS6E_W3) was prepared with a coating similar to that of the planar sample CWE_W2. The fibres were coated with EUROFER and a W interlayer using magnetron sputtering thereby applying the same deposition parameters that had been used for CWE_W2. The layers had a uniform thickness distribution in the radial direction, i.e. around the fibre, while in the axial direction, along the fibre, the thickness varied due to the construction of the fibre holder. Due to the inhomogeneous distribution of the layer along the fibre the thickness of the layers was significantly lower than for the planar samples: the total thickness of the layers deposited on the planar substrate was 1 μm, while the coatings on the fibre were thinner (the total thickness $\sim$ 700 nm, see Fig. 5.14b).

The same annealing procedure (750 °C for 2 h) as for planar samples was applied to the coated SiC fibres.The surface of the annealed planar sample (see Fig. 5.13a) looked similar to the surface of the annealed fibre (see Fig. 5.13c). The W and EUROFER layers were found to react in both cases, leading to the appearance of a precipitate formation visible on the *SEM* image of Figs. 5.13a and c as white specks caused by the difference in the atomic numbers for Fe (26) and for W (74). Formation of holes on the surface of the coated fibres, which was not observed on the surface of the planar sample, can be explained by the difference in the layer thickness. No cracks on the annealed coated fibre were found, according to the *SEM* image made at low magnification (Fig. 5.13b). Consequently, the results obtained for the planar graphite samples show the same reaction behaviour as the SiC fibres.

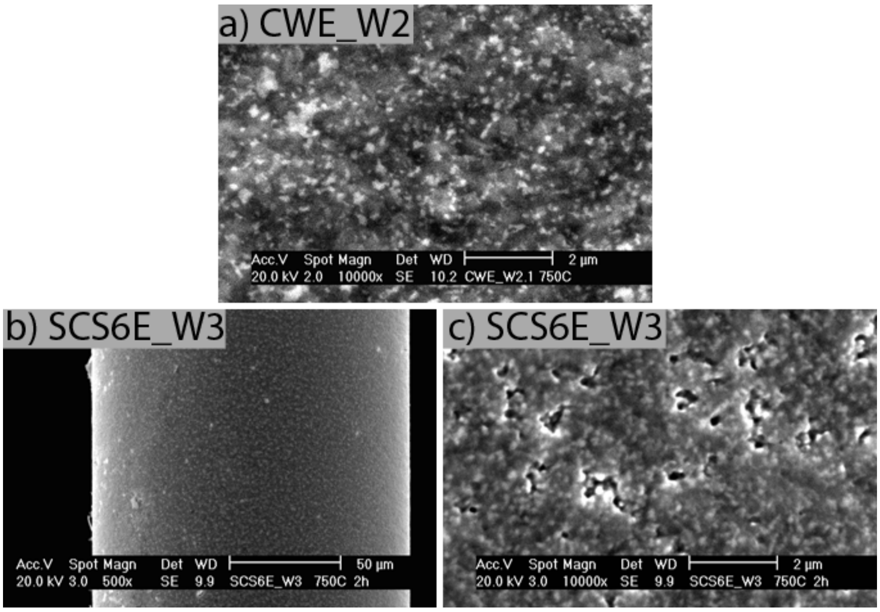

Figure 5.13: Comparison of the *SEM* surface images of the samples coated with both W and EUROFER layers annealed at 750 °C for 2 h: a) image of sample with planar graphite substrate with magnification of ×10000, b) image of the SiC fibre with magnification of ×500 and c) image of the SiC fibre with magnification of ×10000

To show the effectiveness of application of the W interlayer as a diffusion barrier, cross-sections of the SiC fibres with and without interlayer are presented in Fig. 5.14. In Fig. 5.14a the cross-section of the fibre coated with a EUROFER layer (SCS6E3A6) by both magnetron and arc processes (no barrier layer) after annealing is shown. To protect the annealed fibres from the delamination of the coating during preparation of the cross-section they were additionally coated with Cu and then embedded in resin. At the beginning of subsection 4.2.1 this sample, SCS6E3A6, was shown after annealing at temperatures of 600 and 800 °C for 2 h (see Fig. 4.17).

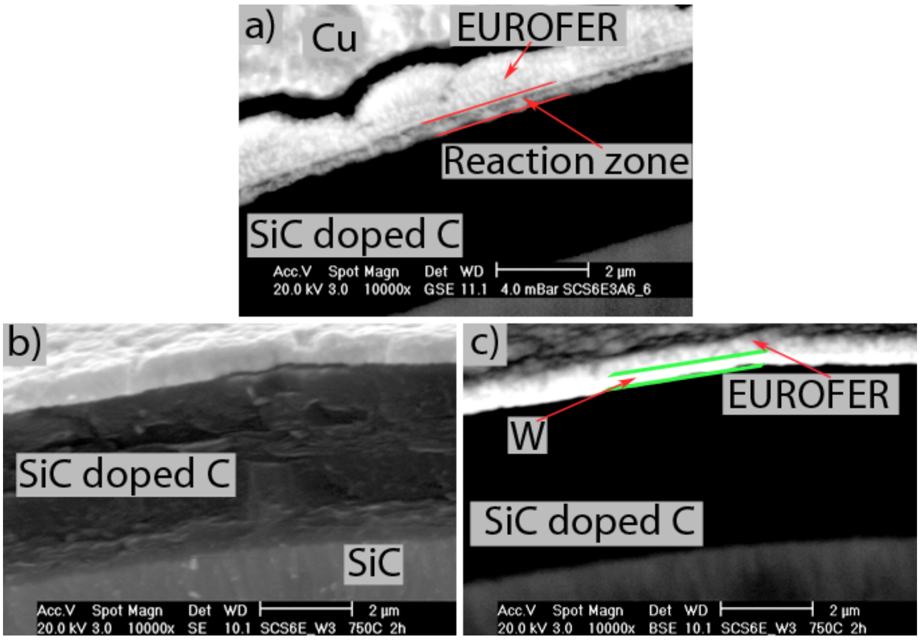

Figure 5.14: *SEM* images of SiC fibres a) SiC fibre coated with EUROFER layer by both magnetron and arc techniques annealed at 600 °C (SCS6E3A6), b) SiC fibre coated with W and EUROFER layers by magnetron technique annealed at 750 °C for 2 h, image made in *SE* mode, and c) SiC fibre coated with W and EUROFER layers by magnetron technique annealed at 750 °C for 2 h, image made in *BSE* mode

Here the cross-section of the SCS6E3A6 after annealing only at 600 °C is presented in Fig. 5.14a with the higher magnification of ×10000. The region limited by red lines is the reaction zone which appeared due to the interdiffusion between the fibre and coating caused by annealing. The cross-section of the SiC fibre coated with the W and EUROFER layers (SCS6E_W3) described above is shown in Figs. 5.14b and c. These images were made from the same location in *SE* and *BSE* modes. A white stripe visible in Fig. 5.14c corresponds to the W interlayer. Since the atomic numbers of Fe (26) and C (6) are much lower than of W (74), the EUROFER layer and outer fibre coating are visible as grey and black areas, respectively. If W had interacted with the fibre, the reaction zone would have appeared on the *BSE* image between the white and black stripes. One can conclude from the *SEM* images taken after annealing the SCS6E_W3 at an even higher temperature of 750 °C than applied to the SCS6E3A6 shown here, that no reaction zone has formed. Therefore, the W interlayer has effectively suppressed the interdiffusion between the SiC fibre and the EUROFER layer at 750 °C.

6 Summary and Conclusion

To increase the operating temperature of the first wall of future fusion reactor, a new composite material, EUROFER (a 9%Cr steel) reinforced by SiC fibres, has been proposed. The main tasks of the work presented here are investigation of the interfacial behaviour between SiC fibre and EUROFER 97 matrix elements and possible ways of controlling the diffusion interfacial reactions by applying an additional interlayer. The following materials have been investigated as diffusion barriers:

- Metals: Ti, Cr, W, Re and Re / W
- Ceramics: TiC, TiN and Er_2O_3.

Two directions of the work are described, namely coating deposition procedures and a study of the influence of annealing on interface diffusion and reaction processes.

Deposition

In this work, problems associated with the deposition of EUROFER due its ferromagnetic properties arose. To make the deposition of EUROFER 97 feasible, the magnetron sputter and plasma arc facilities were improved. This allowed an increase in the deposition rate by the magnetron facility from an original $0.5\,\mathrm{nm\,min^{-1}}$ to about $25\,\mathrm{nm\,min^{-1}}$, which resulted in a significant decrease of O and C contents in the EUROFER layer. As for the plasma arc facility, the longer non-stop deposition process for over 2 h became possible by a modification, in contrast to the 20 min with the original configuration. The composition and crystalline structure of the coatings made by both magnetron and arc depositions are close to those of bulk EUROFER 97.

Magnetron sputter process was utilised for the deposition of *Me* interlayers: Ti, Cr, W and Re. All of them were deposited in *DC* mode without any modification of the deposition technique. The layers revealed crystalline structure and low content of O and C.

For the deposition of ceramic coatings, the task was to achieve the composition and crystalline structure of the stoichiometric TiC, TiN, ZrO_2 and Er_2O_3 compounds. In addition, the ceramic coatings were to possess a smooth layer structure without cracks or blistering.

For the deposition of TiC the influence of the variation of such factors as the dual sputtering of Ti and C targets, substrate material, bias voltage, and applied power density on the composition and layer structure has been investigated. It was found that the layer possesses a crystalline structure and composition close to stoichiometric TiC only in the case of dual magnetron deposition. The substrate material influences the structure of the deposited layer. By applying a cyclically varied bias voltage, a smooth layer structure was formed on the graphite substrate instead of an undulating layer structure as deposited at low values of the bias voltage. In the case of a SiC substrate Ar ion implantation was assumed to be the reason for the blister formation, where blisters appeared after annealing at temperatures above 400 °C.

For the deposition of TiN, reactive sputtering was utilised. The influence of the applied power density, substrate material, and the ratio of the partial pressures of Ar and N_2 on the layer composition and structure were investigated. The application of a high power density to the Ti target was found to cause serious layer degradation. As was observed for TiC, the structure of the TiN coating depends on the substrate material. It was found that the ratio of the partial pressures of Ar and N_2 gases equal 3 was the optimum for achieving a fine layer structure with composition close to the stoichiometric TiN.

For the deposition of ZrO_2, reactive sputtering was used. In contrast to the two previous ceramic coatings, in this case the substrate material did not affect the layer structure. In spite of the fact that the layer was smooth and its composition close to that of stoichiometric ZrO_2, it was not investigated as a diffusion barrier for the following reasons: 1) the layer structure remained amorphous both before and after annealing at 800 °C; 2) crack propagation was observed in the layer deposited on a graphite substrate; 3) blister formation was found on the SiC substrate with and without annealing.

Er_2O_3 deposition was carried out with both the magnetron sputter and filtered plasma arc processes. The layer revealed a smooth fine structure when deposited on both graphite and SiC substrates. After annealing at 800 °C, the coating produced by the magnetron deposition revealed a crystalline structure and a composition corresponding to stoichiometric Er_2O_3, albeit cracked. To overcome this problem, a filtered plasma arc facility was utilised for the deposition of Er_2O_3 at 600 °C. The layer produced in this way showed the required stoichiometry and crystallinity, with a smooth structure. In addition, the achieved deposition rate of $100\,\mathrm{nm\,min^{-1}}$ was almost 20 times higher than that by the magnetron deposition technique.

Annealing experiments

The SiC fibres coated with EUROFER by both the magnetron and plasma arc processes were investigated at temperatures up to 800 °C to simulate the temperature loads of the future composite material during production and operating conditions. These annealing tests showed the necessity of a diffusion barrier for the suppression of the interdiffusion between the fibre and matrix elements. Investigations of the planar samples confirmed this conclusion.

Since the outer coating of used SiC fibres consists mainly of C, the diffusion of C into EUROFER has been thoroughly studied. The cementite Fe_3C formed during annealing was found to strongly decrease the rate of C diffusion. A dependence of the diffusion coefficient, D, of C on its concentration in EUROFER has been calculated for the temperature of 750 °C. The maximum value of D corresponded to low C concentrations and was estimated to be $3 \cdot 10^{-17}\,\mathrm{m^2\,s^{-1}}$. This value appears to be lower than the tracer diffusion coefficient of C in pure Fe at the same temperature and as assumed to be due to the following factors:

- For most of the annealing time the process should be considered as C diffusion in Fe_3C, rather than in pure Fe, since cementite decelerates C transport and, therefore, decreases the diffusion coefficient of C

- The presence of Cr in the EUROFER composition: C diffusion is slower in Fe - Cr alloy than in pure Fe.

Diffusion processes in the presence of different interlayers have been studied.

With a Ti barrier, the intermixing of Ti and EUROFER layers was observed upon annealing at temperatures higher than 400 °C. This intermixing is assumed to be the reason for the crack appearance and their further propagation and, for the layers deposited on the graphite substrate, an almost complete delamination caused by the transformation of α-Ti to β-Ti at lower temperatures.

With a Cr barrier, the complete intermixing of Cr and EUROFER was detected at 600 °C. Only in the case of a Cr interlayer the decomposition of SiC at 750 °C was observed that resulted in the phase formations Fe_3Si, $(Fe, Cr)_{23}C_6$ and $(Fe, Cr)_7C_3$. The intermixing makes the suppression of C diffusion by the application of Cr essentially worse since C diffusion leads to the formation of Fe_3C and Cr_7C_3. Furthermore, C concentration in this layer appears to be even higher than in EUROFER annealed at the same temperature but without application of any interlayer.

As regards to a W diffusion barrier, the interaction of W and EUROFER starts at 600 °C. The diffusion coefficient of W in EUROFER at the temperature of 750 °C was found to be independent of the annealing time. The maximum value of D corresponded to low W concentrations and was estimated to be $5 \cdot 10^{-18}\,\mathrm{m^2\,s^{-1}}$. In addition to EUROFER, some new phases were formed due to annealing, namely Fe_3W_3C and α-W_2C. The application of a W barrier seems to be useful since the C concentration in EUROFER is kept well below that without an interlayer. This interlayer has also been tested with SiC fibres because of good experience with planar substrates and the simplicity of its deposition. In contrast to SiC fibres coated only with EUROFER, no interaction between the layers and the fibre is observed after annealing at 750 °C for 2 h.

Similar to W, the interaction between a Re interlayer and EUROFER becomes evident at 600 °C. The diffusion of Re in EUROFER is faster than W in EUROFER, which results in a higher concentration of Re in the steel, and, as a consequence, a higher value of the diffusion coefficient of Re in EUROFER, $1.6 \cdot 10^{-17}\,\mathrm{m^2\,s^{-1}}$, for low concentrations. Owing to Re diffusion, the Fe_2Re_3 compound is formed. In addition to Fe_2Re_3, for the sample on a graphite substrate, $Cr_{23}C_6$ is built due to C diffusion. The interaction of Re with EUROFER makes the suppression of C diffusion by an Re interlayer worse.

Utilising a Re / W multilayer, the W diffusion from an adjoining layer in combination with simultaneous C diffusion into the EUROFER is found to form Fe_3W_3C. Longer annealing transforms the intermediate W interlayer into W_2C. In combination, these processes lead to the formation of an effective barrier with very promising results on the suppression of C diffusion observed using a four-layer coating.

A TiC interlayer seems to be more effective for the suppression of C diffusion than pure Ti. It was found that TiC remains stable up to 750 °C.

A TiN interlayer appears to be also stable up to temperatures around 750 °C. Furthermore, it effectively suppresses C diffusion in the EUROFER at these temperatures.

Regarding ceramic barrier layers, the best results were achieved with the application of an Er_2O_3 interlayer. In this case, no diffusion of C as well as no interaction between the Er_2O_3 and EUROFER was observed after annealing at 750 °C.

Finally, according to a comparison of the effectiveness of each interlayer, the following interlayers can be proposed for use as a diffusion barrier in the system of SiC fibre - EUROFER 97 matrix: W, Re / W multilayer, TiN and Er_2O_3.

References

[1] R.L. Klueh, D.R. Harries: *High-Chromium Ferritic and Martensitic Steels for Nuclear Applications.* American Society for Testing and Materials, 2001.

[2] W.M. Stacey: *Fusion: an introduction to the physics and technology of magnetic confinement fusion.* John Wiley & Sons (1984).

[3] J. Wesson: *Tokamaks.* Second Edition. Clarendon Press, Oxford (1997).

[4] D. Maisonnier, I. Cook, P. Sardain, R. Andreani, L. Di Pace, R. Forrest, L. Giancarli, S. Hermsmeyer, P. Norajitra, N. Taylor, D. Ward: *A Conceptual Study of Commercial Fusion Power Plants.* FINAL REPORT OF THE EUROPEAN POWER PLANT CONCEPTUAL STUDY. EFDA-RP-RE-5.0 (2004).

[5] K. Ehrlich, M. Gasparotto, L. Giancarli, G. Le Marois, S. Malang, B. van der Schaaf: European Material Assessment Meeting. Karlsruhe (2001).

[6] H. Bolt, V. Barabash, W. Krauss, J. Linke, R. Neu, S. Suzuki, N. Yoshida, ASDEX Upgrade Team: *Materials for the plasma-facing components of fusion reactors.* Journal of Nuclear Materials, 329–333 (2004) 66.

[7] R. Andreani, E. Diegele, R. Laesser, B. van der Schaaf: *The European integrated materials and technology programme in fusion.* Journal of Nuclear Materials, 329–333 (2004) 20.

[8] S.J. Zinkle, N.M. Ghoniem: *Operating temperature windows for fusion reactor structural materials.* Fusion Engineering and Design, 51-52 (2000) 55.

[9] E.E. Bloom: *Structural materials for fusion reactors.* Nuclear Fusion, 30 9 (1990) 1879.

[10] K. Ehrlich: *Materials research towards a fusion reactor.* Fusion Engineering and Design, 56-57 (2001) 71.

[11] T. Muroga, M. Gasparotto, S.J. Zinkle: *Overview of materials research for fusion reactors.* Fusion Engineering and Design, 61-62 (2002) 13.

[12] S.N. Rosenwasser, P. Miller, J.A. Dalessandro, J.M. Rawls, W.E. Toffolo, W. Chen: *The application of martensitic stainless steels in long lifetime fusion first wall/blankets.* Journal of Nuclear Materials, 85-86 (1979) 177.

[13] A.-A.F. Tavassoli, A. Alamo, L. Bedel, L. Forest, J.-M. Gentzbittel, J.-W. Rensman, E. Diegele, R. Lindau, M. Schirra, R. Schmitt, H.C. Schneider, C. Petersen, A.-M. Lancha, P. Fernandez, G. Filacchioni, M.F. Maday, K. Mergia, N. Boukos, Baluc, P. Spätig, E. Alves, E. Lucon: *Materials design data for reduced activation martensitic steel type EUROFER.* Journal of Nuclear Materials, 329-333 (2004) 257.

[14] R. Lindau, A. Möslang, M. Schirra: *Thermal and mechanical behaviour of the reduced-activation-ferritic-martensitic steel EUROFER.* Fusion Engineering and Design, 61-62 (2002) 659.

[15] S.H. Avner: *Introduction to physical metallurgy.* McGraw-Hill, Inc., 1974.

[16] P. Fernández, A.M. Lancha, J. Lapeña, M. Hernández-Mayoral: *Metallurgical characterization of the reduced activation ferritic/martensitic steel Eurofer'97 on as-received condition.* Fusion Engineering and Design, 58–59 (2001) 787.

[17] P. Fernández, M. García-Mazarío, A.M. Lancha, J. Lapeña: *Grain boundary microchemistry and metallurgical characterization of Eurofer'97 after simulated service conditions.* Journal of Nuclear Materials, 329–333 (2004) 273.

[18] R. Lindau, A. Möslang, M. Schirra, P. Schlossmacher, M. Klimenkov: *Mechanical and microstructural properties of a hipped RAFM ODS-steel.* Journal of Nuclear Materials, 307–311 (2002) 769.

[19] R. Schaeublin, T. Leguey, P. Spätig, N. Baluc, M. Victoria: *Microstructure and mechanical properties of two ODS ferritic/martensitic steels.* Journal of Nuclear Materials, 307–311 (2002) 778.

[20] M. Klimiankou, R. Lindau, A. Möslang: *TEM characterization of structure and composition of nanosized ODS particles in reduced activation ferritic–martensitic steels.* Journal of Nuclear Materials, 329–333 (2004) 347.

[21] J.H. You, H. Bolt: *Overall mechanical properties of fiber-reinforced metal matrix composites for fusion applications.* Journal of Nuclear Materials, 305 (2002) 14.

[22] J.-K. Kim, Y.-W. Mai: *Engineered interfaces in fibre reinforced composites.* Elsevier (1998).

[23] M.F. Ashby, D.R.H. Jones: *Engineering Materials 1. An Introduction to their Properties and Applications.* Second Edition. Elsevier (1996).

[24] M. Ohring: *Materials science of thin films: deposition and structure.* Academic Press (2002).

[25] J. Cranck: *The mathematics of diffusion.* Second edition. Clarendon Press. Oxford (1975).

[26] K. Schmid, J. Roth: *Concentration dependent diffusion of carbon in tungsten.* Journal of Nuclear Materials, 302 (2002) 96.

[27] K. Schmid, J. Roth, W. Eckstein: *Influence of diffusion on W sputtering by carbon.* Journal of Nuclear Materials, 290-293 (2001) 148.

[28] P.G. Shewmon: *Diffusion in solids.* McGraw-Hill Book Company (1963).

[29] J.S. Park, K. Landary, J.H. Perepezko: *Kinetic control of silicon carbide / metal reactions.* Materials Science & Engineering, Part A259 (1999) 279.

[30] W.M. Tang, Z.X. Zheng, H.F. Ding, Z.H. Jin: *A study of the solid state reaction between silicon carbide and iron.* Materials Chemistry and Physics, 74 (2002) 258.

[31] W.M. Tang, Z.X. Zheng, H.F. Ding, Z.H. Jin: *Control of the interface reaction between silicon carbide and iron.* Materials Chemistry and Physics, 80 (2003) 360.

[32] S. Goorse, Y. Le Petitcorps: *A new approach in the understanding of the SiC / Ti reaction zone composition and morphology.* Composites, Part A29 (1998) 1221.

[33] W.J.J. Wakelkamp, F.J.J. van Loo, R. Metselaar: *Phase relations in the Ti-Si-C system.* Journal of the European Ceramic Society, 8 (1991) 135.

[34] K. Bhanumurthy, R. Schmid-Fetzer: *Interface reactions between silicon carbide and metals (Ni, Cr, Pd, Zr).* Composites, Part A32 (2001) 569.

[35] K. Bhanumurthy, R. Schmid-Fetzer: *Solid state phase equilibria and reactive diffusion in the Cr-Si-C system.* Zeitschrift fuer Metallkunde, 87 (1996) 61.

[36] L.B. Lundberg: *Silicon carbide - tungsten heat pipes for heat - temperature service.* I&EC Production Research and Development, 19 (1980) 241.

[37] L. Baud, C. Jaussaud, R. Madar, C. Bernard, J.S. Chen, M.A. Nicolet: *Interfacial reactions of W thin film on single-crystal (001) β-SiC.* Materials Science and Engineering, B29 (1995) 126.

[38] J.S. Chen, E. Kolawa, M.A. Nicolet, L. Baud, C. Jaussaud, R. Madar, C. Bernard: *Stability of rhenium thin films on single crystal (001) β-SiC.* Journal of Applied Physics, 75 (2) (1994) 897.

[39] C. Arvieu, J.P. Manaud, J.M. Quenisset: *Interaction between titanium and carbon at moderate temperatures.* Journal of Alloys and Compounds, 368 (2004) 116.

[40] Q.H. Fan, A. Fernandes, J. Gracio: *Diamond coating on steel with a titanium interlayer.* Diamond and Related Materials, 7 (1998) 603.

[41] F.J.G. Silva, A.P.M. Baptista, E. Pereira, V. Teixeira, Q.H. Fan, A.J.S. Fernandes, F.M. Costa: *Microwave plasma chemical vapour deposition diamond nucleation on ferrous substrates with Ti and Cr interlayers.* Diamond and Related Materials, 11 (2002) 1617.

[42] Ch. Linsmeier, J. Luthin, P. Goldstraß: *Mixed material formation and erosion.* Journal of Nuclear Materials, 290-293 (2001) 25.

[43] V.G. Ralchenko, A.A. Smolin, V.G. Pereverzev, E.D. Obraztsova, K.G. Korotoushenko, V.I. Konov, Yu.V. Lakhotkin, E.N. Loubnin: *Diamond deposition on steel with CVD tungsten intermediate layer.* Diamond and Related Materials, 4 (1995) 754.

[44] H.P. Lorenz: *Investigation of TiN as an interlayer for diamond deposition on steel.* Diamond and Related Materials, 4 (1995) 1088.

[45] S.V. Nagender Naidu, P. Rama Rao: *Phase diagrams of binary tungsten alloys.* Indian Institute of Metals, Calcutta (1991) 232.

[46] W.J. Arnoult, R.B. McLellan: *The solubility of carbon in rhodium, ruthenium, iridium and rhenium.* Scripta Metallurgica, 6 (10) (1972) 1013.

[47] Y. Isobe, Y. Yazawa, P. Son, M. Miyake: *Chemically vapor-deposited Mo/Re double layer coating on graphite at elevated temperatures.* Journal of the Less-Common Metals, 152 (1989), 239.

[48] E. Lassner, W.-D. Schubert: *Tungsten: properties, chemistry, technology of the element, alloys, and chemical compounds.* Kluwer Academic / Plenum Publishers, New York (1999) 49.

[49] H. Okamoto: *Phase diagrams of binary iron alloys,* (1993).

[50] D.V. Shtansky, G. Inden: *Phase transformation in Fe-Mo-C and Fe-W-C steel -1. The structural evolution during tempering at 700* °C. Acta Metallurgica, 45 (7) (1997) 2861.

[51] H. Mehrer: *Numerical data and functional relationships in science and technology.* Group III: Crystal and solid state physics. Springer, Volume 26 (1990).

[52] J. Askill: *Tracer diffusion data for metals, alloys, and simple oxides.* IFI (1970).

[53] R.C. Weast: *Handbook of chemistry and physics.* CRC (1977 - 1978).

[54] V.Ya. Shchelkonogov: *Diffuzionnoe vzaimodeistvie ugleroda s wolframom.* Elekronnie Svoistva Tverdih Tel. Fazovie Prevrashcheniya. 621.039.391 (1978) 115.

[55] *Materials Science and Metallurgy*, 4th ed. Pollack, Prentice-Hall (1988).

[56] W.D. Callister: *Materials science and engineering. An introduction.* John Wiley & Sons, Inc. (2003).

[57] T.B. Massalski, Binary Alloy Phase Diagrams, Volume 1. ASM (1986).

[58] A.M. Khar'kova, T.Ya. Velikanova: Porosh. Metall., 12 (1987) 52 in Russian; TR: Sov. Powder Metall., 26(12), (1987) 994.

[59] K. Tokunaga, T. Matsubara, Y. Miyamoto, Y. Takao, N. Yoshida, N. Noda, Y. Kubota, T. Sogabe, T. Kato, L. Plöchl: *Changes of composition and microstructure of joint interface of tungsten coated carbon by high heat flux.* Journal of Nuclear Materials, 283-287 (2000) 1121.

[60] S. Tamura, X. Liu, K. Tokunaga, Y. Tsunekawa, M. Okumiya, N. Noda, N. Yoshida: *High-temperature properties of joint interface of VPS-tungsten coated CFC.* Journal of Nuclear Materials, 329-333 (2004) 711.

[61] M. Ghosh, K. Bhanumurthy, G.B. Kale, J. Krishnan, S. Chatterjee: *Diffusion bonding of titanium to 304 stainless steel.* Journal of Nuclear Materials 322 (2003) 235.

[62] P.R. Smith, M.L. Gambone, D.S. Williams, D.I. Garner: *Heat treatment effects on SiC fiber.* Journal of Materials Science, 33 (1998) 5855.

[63] K.K. Chawla: *Composite Materials. Science and Engineering.* Second Edition. Springer (2001).

[64] Speciality Materials, Inc.: Manufactures of Boron and SCS silicon carbide Fibres. www.specmaterials.com

[65] M.E. de Juan Pardo: *Characterisation and Mitigation of Chemical Erosion of Doped Carbon Materials.* Max-Planck Institut für Plasmaphysik Ph.D. thesis (2004).

[66] Catalog Section H-8785, Union Carbide (1969).

[67] B.T. Kelly: *Physics of graphite.* APPLIED SCIENCE PUBLISHERS LTD, London (1981).

[68] Wacker-Chemie GmbH: Specification of SiC.

[69] K.K. Chawla: *Ceramic matrix composites.* Chapman & Hall, London (1993).

[70] C.J. Smithells: *Metals, Reference book.* Volume III. Butterworths, London (1967).

[71] Y.S. Touloukian: *Thermophysical Properties of High Temperature Solid Materials. Volume 4: Oxides and Their Solutions and Mixtures.* Thermophysical Properties Research Center, Purgue University (1967).

[72] Y.S. Touloukian: *Thermophysical Properties of High Temperature Solid Materials. Volume 5: Nonoxides and Their Solutions and Mixtures, Including Miscellaneous Ceramic Materials.* Thermophysical Properties Research Center, Purgue University (1967).

[73] M.F. Ashby, D.R.H. Jones: *Engineering Materials 2. An Introduction to Microstructures, Processing and Design.* Second Edition. Butterworth-Heinemann (1998).

[74] J.B. Wachtman: *Mechanical properties of ceramics.* John Willy & Sons, Inc. (1996).

[75] FRIATEC AG: Comparative physical data. Zirconium oxide, partially stabilized. www.friatec.de

[76] BÖHLER EDELSTAHL, Inspection-Certifivate-No.: 029060 (1991).

[77] M. Konuma: *Film deposition by plasma techniques.* Springer-Verlang (1992).

[78] S. Inouea, T. Saekia, H. Uchidaa, K. Koterazawaa, M. Iwasa: *Effects of ion flux on the properties of dc magnetron-sputtered stainless steel films.* Vacuum, 66 (2002) 257.

[79] K. Leinartas, M. Samulevičienė, A. Bagdonas, R. Juškenas, E. Juzeliūnas: *Structural and anticorrosive properties of magnetron-sputtered Fe–Cr–Ni and Fe–Cr–Ni–Ta alloy films.* Surface and Coatings Technology, 168 (2003) 70.

[80] G. Terwagnea, J. Colaux, G.A. Collins, F. Bodart: *Structural and quantitative analysis of nitrided stainless steel coatings deposited by dc-magnetron sputtering.* Thin Solid Films, 377-378 (2000) 441.

[81] J. Koskinen, P. Torri, J.-P. Hirvonen, A. Mahiout, A. Stanishevsky: Arc discharge deposition of stainless steel coatings at different nitrogen pressures. Surface and Coatings Technology, 80 (1996) 57.

[82] S. Berg, T. Nyberg: *Fundamental understanding and modeling of reactive sputtering processes.* Thin Solid Films 476 (2005) 215.

[83] S.M. Rossnagel, J.J. Cuomo, W.D. Westwood: *Handbook of plasma processing technology. Fundamentals, Etching, Deposition, and Surface Interactions.* Noyes Publications, New Jersey USA (1990).

[84] D.A. Karpov, I.F. Kislov,A.I. Ryabchikov, A.A. Ganenko: *Experiments on thick coatings deposited by means of arc technology.* Surface and Coatings Technology 89 (1997) 58.

[85] D. Karpov: *Arc sources of metallic plasma for coatings in vacuum and for high speed vacuum pumping.* Vacuum 46 (1995) 825.

[86] D.A. Karpov: *Cathodic arc sources and macroparticle filtering.* Surface and Coatings Technology 96 (1997) 22.

[87] H. Bolt, F. Koch, J.L. Rodet, D. Karpov, S. Menzel: *Al_2O_3 coatings deposited by filtered vacuum arc - characterization of high temperature properties.* Surface and Coatings Technology 116–119 (1999) 956.

[88] F. Koch, R. Brill, H. Maier, D. Levchuk, A. Suzuki, T. Muroga, H. Bolt: *Crystallization behavior of arc-deposited ceramic barrier coatings.* Journal of Nuclear Materials 329–333 (2004) 1403.

[89] P.F. Kane, G.B. Larrabee: *Characterization of Solid Surfaces.* Plenum Press, New York (1976).

[90] L.C. Feldman: *Fundamentals of surface and thin film analysis.* Elsevier Science Publishing Co., Inc. (1986).

[91] M. Mayer: *SIMNRA user's guide.* Technical Report IPP 9/113, Max-Planck-Institut für Plasmaphysik, Garching (1997).

[92] M. Mayer: *Ion beam analysis of rough thin films.* Nuclear Instruments and Methods in Physics Research B, 194 (2002) 177.

[93] S. Inoue, Y. Wada, K. Koterazawa: *Deposition of TiC films by dual source dc magnetron sputtering.* Vacuum 59 (2000) 735.

[94] R. Hubler: *Transition metal nitrides thin films deposition using a dynamically controlled magnetron sputtering apparatus.* Surface and Coatings Technology 158–159 (2002) 680.

[95] F. Vaz, P. Machado, L. Rebouta , J.A. Mendes , S. Lanceros-Méndez , L.Cunha , S.M.C. Nascimento, Ph. Goudeau , J.P. Rivière , E. Alves , A. Sidor: *Physical and morphological characterization of reactively magnetron sputtered TiN films.* Thin Solid Films 420 –421 (2002) 421.

[96] S.H. Jeong, I.S. Bae, Y.S. Shin, S.-B. Lee, H.-T. Kwak, J.-H. Boo: *Physical and electrical properties of ZrO_2 and YSZ high-k gate dielectric thin films grown by RF magnetron sputtering.* Thin Solid Films 475 (2005) 354.

[97] C. Schrank , C. Eisenmenger-Sittner, E. Neubauer, H. Bangert , A. Bergauer: *Solid state de-wetting observed for vapor deposited copper films on carbon substrates.* Thin Solid Films 459 (2004) 276.

[98] C. Eisenmenger-Sittner, E. Neubauer, C. Schrank , J. Brenner, C. Tomastik: *Solid state de-wetting of vapor deposited films on planar and fiber-shaped carbon substrates.* Surface and Coatings Technology 180 -181 (2004) 413.

[99] R. Behrisch (editor) *Sputtering by Particle Bombardment II. Sputtering of Alloys and Compounds, Electron and Neutron Sputtering, Surface Topography.* Springer-Verlag Berlin Heidelberg (1983).

[100] B.A. Pint, P.F. Tortorelli, A. Jankowski, J. Hayes, T. Muroga, A. Suzuki, O.I. Yeliseyeva, V.M. Chernov: *Recent progress in the development of electrically insulating coatings for a liquid lithium blanket.* Journal of Nuclear Materials 329–333 (2004) 119.

Appendices

A Introduction to Fusion

Fusion has the potential of providing an essentially inexhaustible source of energy for the future [2]. For two nuclei to fuse, they need sufficient energy to overcome the repulsive Coulomb force acting between them. Due to the presence of this Coulomb barrier the cross-sections of the nuclear reactions between charged particles reaches reasonable values only at high incident energies of the colliding particles. This condition leads to the selection of elements with low atomic numbers as the reacting fuel elements. Therefore, the most promising fusion reaction is the D-T reaction which occurs between the hydrogen isotopes deuterium and tritium:

$$^{2}\mathrm{D}_1 +\ ^{3}\mathrm{T}_1 \longrightarrow\ ^{4}\mathrm{He}_2\,(3.5\,\mathrm{MeV}) +\ ^{1}\mathrm{n}_0\,(14.1\,\mathrm{MeV})\,.$$

The reaction is induced in collisions between particles and the cross-section for this reaction, shown in Fig. A.1, is therefore of fundamental importance. The cross-section corresponding to the D-T reaction is much greater than that for other potential fusion reactions at low energies ($E < 200$ k eV), which is the reason why this reaction is the most favourable.

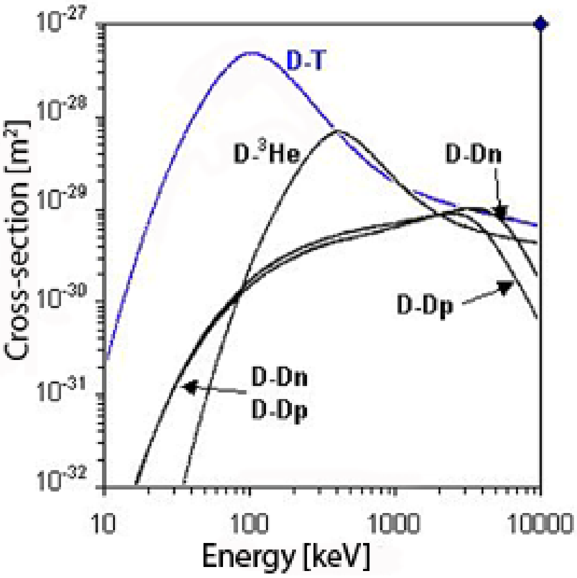

Figure A.1: Cross-sections for the reactions D-T, D-D and D-^{3}He [3].

The fusion of 1 g of T together with 2/3 g of D produces 576 GJ of thermal energy [2]. The D fuel is abundant and can be extracted from seawater where it exists as 0.0153 at.%. T does not occur naturally but sufficient quantities to fuel a fusion reactor may be bred from Li in a so-called blanket surrounding the vacuum vessel via the following reactions [3]:

$$^{6}\mathrm{Li}_3 +\ ^{1}\mathrm{n}_0 \longrightarrow\ ^{3}\mathrm{T}_1 +\ ^{4}\mathrm{He}_2 + 4.8\,\mathrm{MeV}$$

$$^{7}\mathrm{Li}_3 +\ ^{1}\mathrm{n}_0 \longrightarrow\ ^{3}\mathrm{T}_1 +\ ^{4}\mathrm{He}_2 +\ ^{1}\mathrm{n}_0 - 2.5\,\mathrm{MeV}.$$

It is suggested therefore to place the Li breeding blanket around the fusion chamber, where the fusion neutrons can produce T.

To overcome the repulsive Coulomb force, the D and T particles should have an energy of about 10 keV. At these energies the hydrogen atoms are ionized and form a plasma, i.e. macroscopically neutral collection of ions and electrons. This plasma can be magnetically confined if it is placed in a strong magnetic field. In this configuration, the charged particles describe helical paths around the field lines. If the field lines are oriented parallel to the reactor walls then the escape of the particles from the reaction zone is hindered and the thermal flux is decreased. For these conditions the transport of particles across the magnetic field takes place mainly by collisions between the particles. The thermal flux across the magnetic field is significantly decreased if the Larmor radius is much less than the mean free path between the particles collisions. For a D-T plasma this condition is satisfied with a magnetic field of 100 G for a plasma with temperature $\sim$ 10 keV and density $10^{21}\,\mathrm{m}^{-3}$. The quality of the magnetic cofinement is characterised by a different criteria, namely the Lawson criterion:

$$n\tau_{\mathrm{E}}T \geq f(T),$$

where n is the plasma density, T is the plasma temperature and τ_{E} is the energy confinement time, which characterises the heat insulation. For fusion reactors working on the D-T reaction the criterion for the optimal energy conditions relates to the minimum of the curve $n\tau_{\mathrm{E}}(E)$, which corresponds to following parameters: $n\tau_{\mathrm{E}} \geq 0.5 \cdot 10^{20}\,\mathrm{m}^{-3}\,\mathrm{s}$ and $T = 17$ keV.

In the simplest plasma confinement systems, the magnetic field lines remain within a toroidal chamber. However, in a simple toroidal system with a purely toroidal magnetic field the magnetic field curvature and gradient results in a vertical drift which is in opposite directions for the ions and electrons and therefore leads to charge separation and the creation of a radial electric field. To avoid this, the addition of a twist of the magnetic field lines is necessary. A poloidal magnetic field must be applied additionally to the toroidal one to compensate this charge separation. The resulting helical magnetic field is entirely contained within the toroidal confinement chamber. The manner of producing this poloidal field differs in the two main reactor concepts: the tokamak and stellarator. In the tokamak concept the poloidal field is produced by a toroidal current flowing in the plasma (see Fig. A.2a), while in stellarator by external coils (see Fig. A.2b).

The tokamak concept was proposed by Tamm and Sakharov and realised by Artsimovich in 1952. The toroidal magnetic field is produced by a set of toroidal coils which encircle the plasma. An electric current in the plasma gives rise to the poloidal component of the magnetic field and, therefore, the twist is produced by the plasma itself. The current also serves for part of the plasma heating.

The stellarator concept was proposed by Spitzer in 1951. In a stellarator the twist of the magnetic field lines is produced by external coils placed around the plasma torus. These external coils have the advantage that the current can be controlled from the outside.

Tokamaks have proved to be very successful in fusion experiments and exactly this concept has been proposed for the experimental fusion reactor *ITER*. In contrast to tokamaks, stellarators are very difficult to build from the engineering point of view. Nevertheless, the worlds most advanced stellarator, W-7X, is currently being built in Greifswald in Northern Germany.

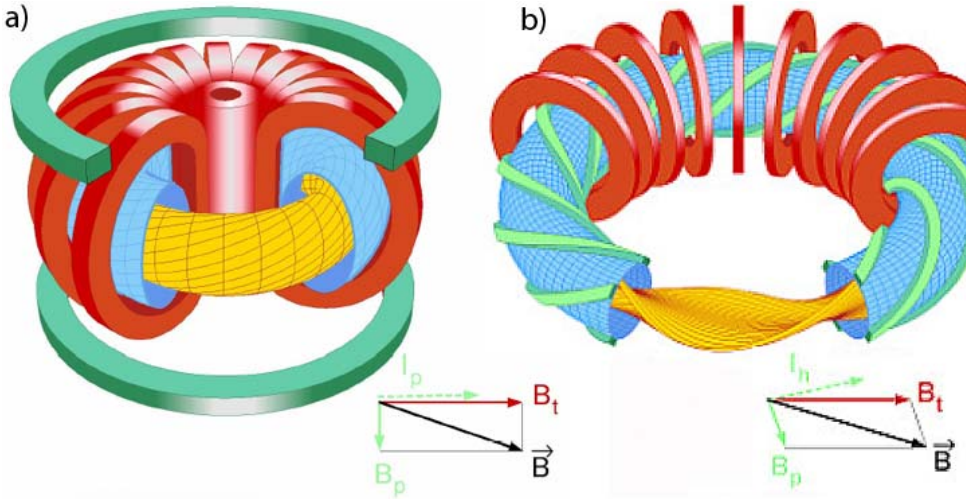

Figure A.2: Schematic view of two magnetic confinement concepts: a) tokamak and b) stellarator

DEMO, which is planned to be the first electricity producing reactor, is based on the tokamak concept as shown in Fig. A.3. There are currently four plant models of it, denoted by the letters A - D. Each of these models supposes a life time of 25 full power years. These models differ principally in the concepts used for the divertor cooling [4] (red area in Fig. A.3).

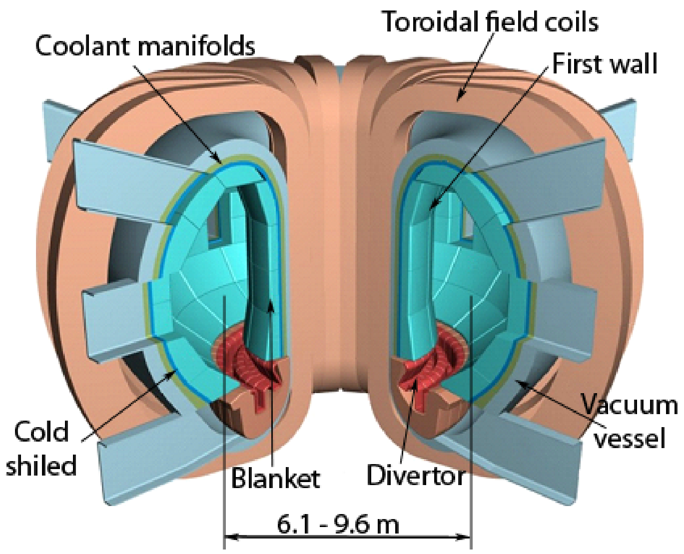

Figure A.3: Schematic view of *DEMO*. The major radius is different for all plant models: model A 9.55 m, model B 8.6 m, model C 7.5 m and model D 6.1 m

The main parameters of these models are shown in Table A.1, where the plant efficiency is the ratio between the net electric power output and the fusion power and aspect ratio is the ratio between major radius and minor radius.

Parameter	Model A	Model B	Model C	Model D
Fusion power [GW]	5.00	3.60	3.41	2.53
Plant efficiency	0.31	0.36	0.42	0.60
Aspect ratio	3.0	3.0	3.0	3.0
Major radius [m]	9.55	8.6	7.5	6.1
Plasma current [MA]	30.5	28.0	20.1	14.1
Average temperature [keV]	22	20	16	12
Average neutron wall load [$\mathrm{MW/m^2}$]	2.2	2.0	2.2	2.4
Divertor peak load [$\mathrm{MW/m^2}$]	15	10	10	5

Table A.1: The main parameters of the four plant models of DEMO

In model A based on a liquid lithium-lead blanket with water cooling, the structural material is EUROFER 97. In model B based on a blanket of alternate layers of lithium ortho-silicate and beryllium pebbles, helium is used as the coolant. The structural materials are EUROFER 97 and 316 stainless steel. In model C the heat is removed by circulation of the lithium-lead itself and helium coolant passing through channels in the structure. A combination of *ODS RAFM* steel and EUROFER 97 is planned to be used in this case. Model D has a lithium-lead blanket in which the LiPb itself is circulated as the primary coolant. The structure material is a SiC / SiC composite. A helium-cooled divertor requires the development of a W alloy as a structural material due to the high operating temperature of the coolant ($600-700\,^\circ\mathrm{C}$), which is incompatible with the maximum operation temperature of EUROFER 97 [4]. It is from such considerations that the problem of the limitation of the operating temperature of EUROFER 97 first appeared. This problem can be solved by the method proposed in this work which suggests the use of SiC fibres as a reinforcing material for EUROFER 97.

B Computation of Diffusion Coefficients

As mentioned in subsection 2.1, to determine the diffusion coefficient taking into account its concentration dependence, Fick's second law has to be solved:

$$\frac{\partial C(x,t)}{\partial t} = \frac{\partial C(x,t)}{\partial x}\frac{\partial D(x,t)}{\partial x} + D(x,t)\frac{\partial^2 C(x,t)}{\partial x^2}, \text{ with } D(x,t) \equiv D(C(x,t)). \tag{B.1}$$

Equation (B.1) can not be solved analytically for arbitrary boundary conditions and $D(C)$ dependences. Therefore, a numerical scheme based on finite differences was adopted.

The program DIFFUSEDC [26, 27] uses the explicit finite difference method. The depth range of x is divided into intervals Δx and the time into intervals Δt. By using a Taylor's series expansion and neglecting higher orders in the expansion of x, keeping time t constant, the first and second directional derivatives of the concentration can be written as:

$$\begin{aligned}\frac{dC(x,t)}{dx} &= \frac{C(x+\Delta x,t) - C(x-\Delta x,t)}{2\Delta x},\\ \frac{d^2C(x,t)}{dx^2} &= \frac{C(x+\Delta x,t) - 2C(x,t) + C(x-\Delta x,t)}{\Delta x^2}.\end{aligned}$$

Similarly, for the time derivative of the concentration one can write the following forward difference expression keeping x constant:

$$\frac{dC(x,t)}{dt} = \frac{C(x,t+\Delta t) - C(x,t)}{\Delta t}.$$

Thus, the diffusion equation (B.1) can be transformed into the equation:

$$\begin{aligned}\frac{C(x,t+\Delta t) - C(x,t)}{\Delta t} &= [D(x+\Delta x,t) - D(x-\Delta x,t)]\frac{C(x+\Delta x,t) - C(x-\Delta x,t)}{2\Delta x} + \\ &\quad + D(x,t)\frac{C(x+\Delta x,t) - 2C(x,t) + C(x-\Delta x,t)}{\Delta x^2}.\end{aligned} \tag{B.2}$$

The program DIFFUSEDC solves the equation (B.2) with the following boundary condition:

$$\left.\frac{dC(x,t)}{dx}\right|_{\text{boundary}} = 0,$$

which corresponds to an infinite diffusion barrier on the surface, i.e. no out-diffusion. The depth profile calculated in this way can be fitted to an experimental depth profile by variation of the concentration dependence of the diffusion coefficient [26, 27]. As shown in [25] the value 0.5 is critical for $D\Delta t/\Delta x^2$. The depth profile, which is used for the DUFFUSEDC calculation has to be specified such that

$$\frac{D\Delta t}{\Delta x^2} \ll 0.5, \tag{B.3}$$

since otherwise the solution becomes unstable. The choice of the $\Delta t/\Delta x^2$ ratio is based on a trade off between calculation time and accuracy. A small value of Δx results in high accuracy but long calculation times due to the requirement (B.3).

The program DIFFUSEDC allows simulations with both a constant and concentration dependent diffusion coefficient. The function for $D(C)$ can be specified either by a set of data points or by a Boltzmann function with four parameters A_0, A_1, X_0 and dX as shown in Fig. B.1.

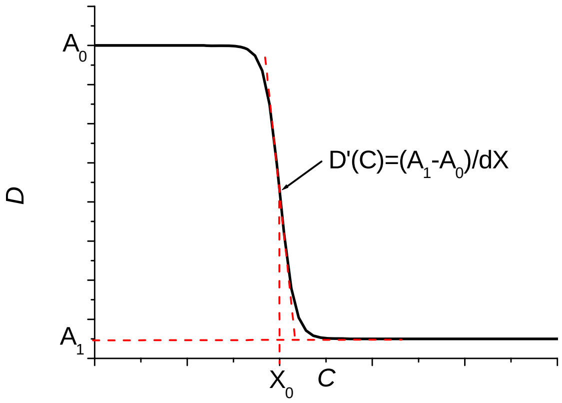

Figure B.1: Variable parameters for specification of the shape of $D(C)$

After deciding on the proper Δt and Δx step widths the measured diffusion depth profile is fitted by iteratively varying the four parameters of the Boltzmann function. A user-friendly interface makes the fitting very straight forward and allows the profiles to be viewed together in the same window (see Fig. B.2).

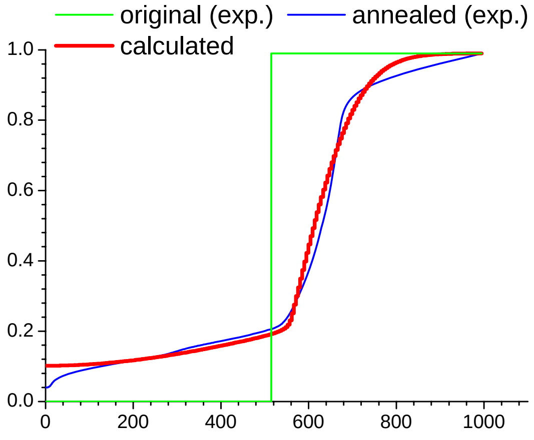

Figure B.2: Diffusion depth profiles

All data used in the fitting as well as the calculated depth profile can be stored for later use.

C Binary and Ternary Phase Diagrams

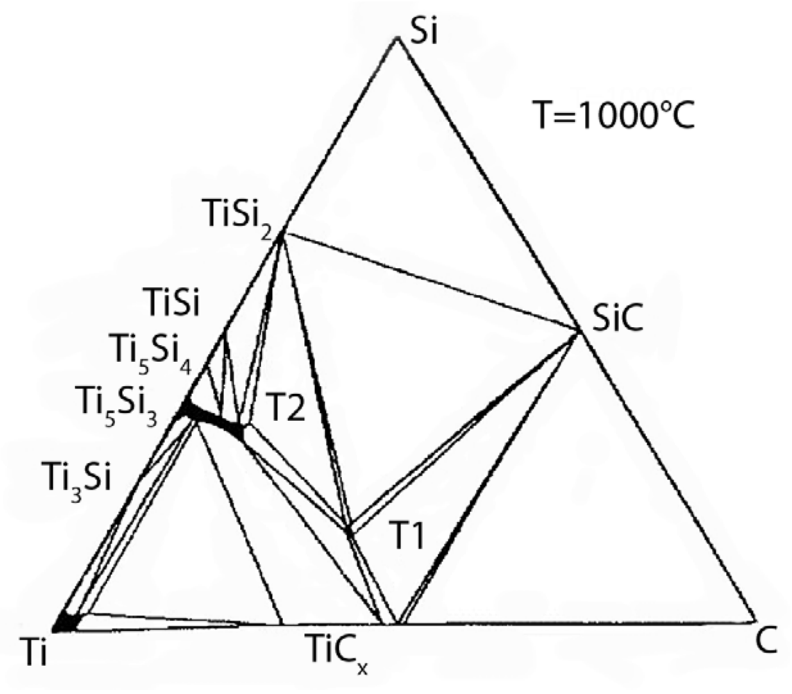

Figure C.1: Isothermal section of the Ti–Si-C ternary phase diagram at 1000 °C (T1 = Ti_3SiC_2 and T2 = $Ti_5Si_3C_x$) [33]

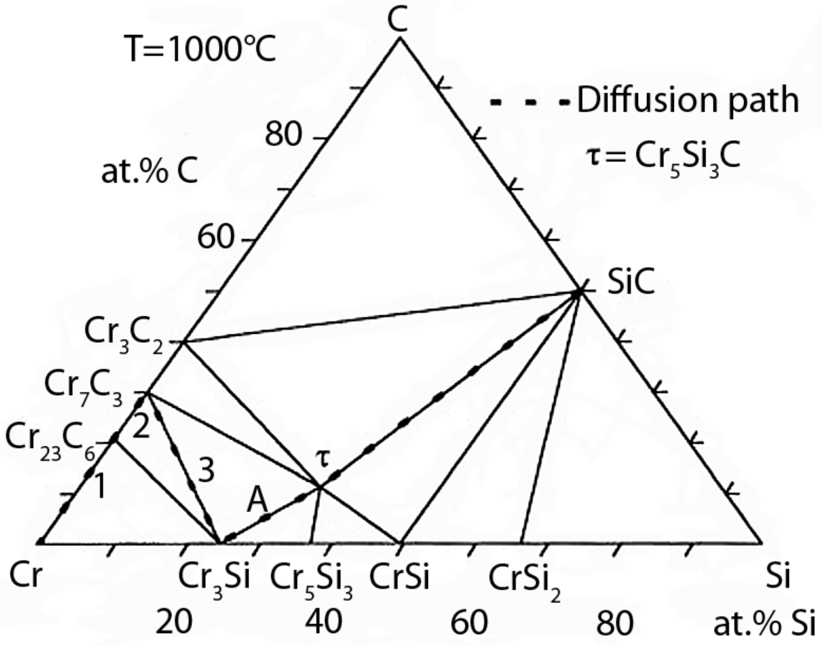

Figure C.2: Isothermal section of the Cr–Si-C ternary phase diagram at 1000 °C [35]

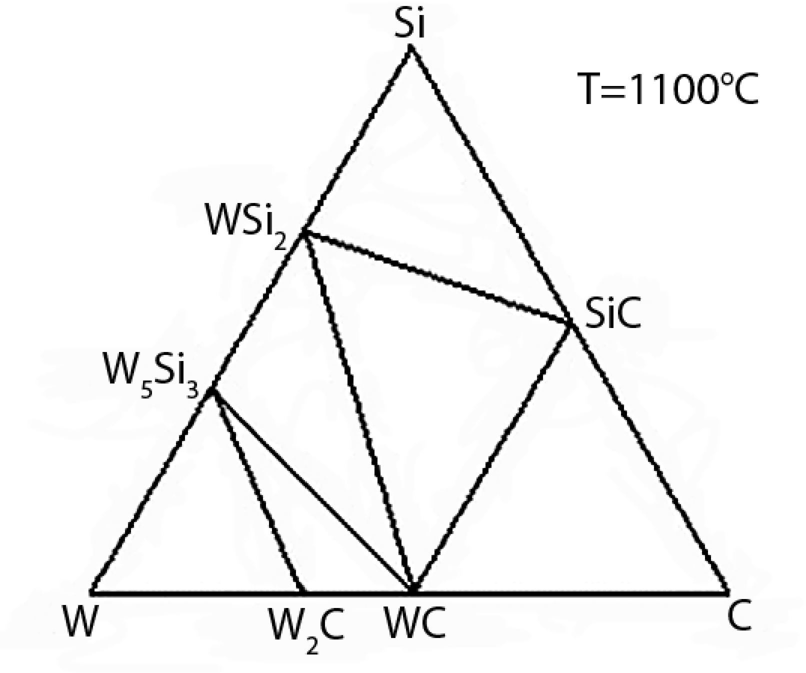

Figure C.3: Isothermal section of the W–Si-C ternary phase diagram at 1100 °C [37]

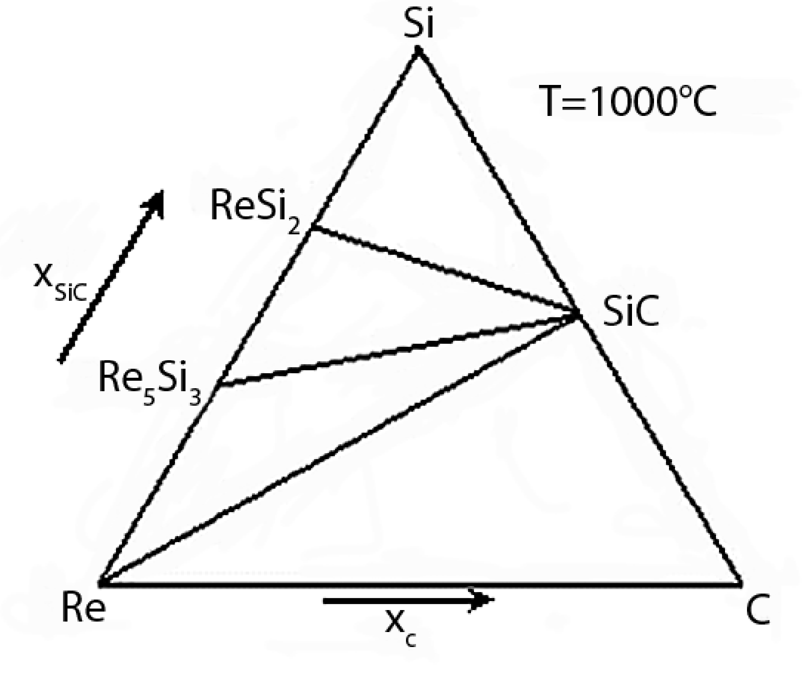

Figure C.4: Isothermal section of the Re–Si-C ternary phase diagram at 1100 °C [38]

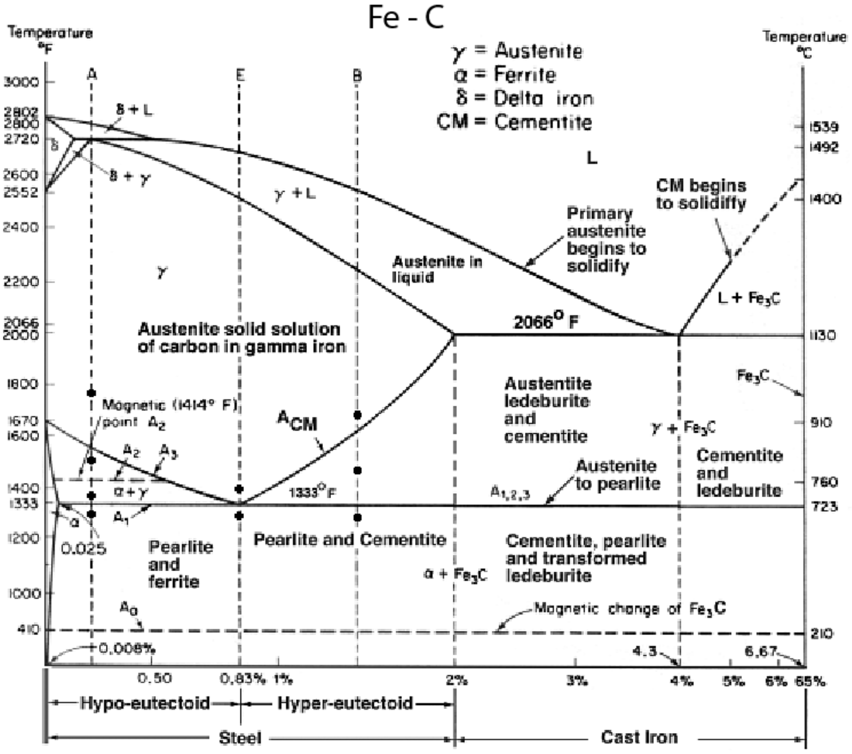

Figure C.5: Fe-C binary phase diagram [55]

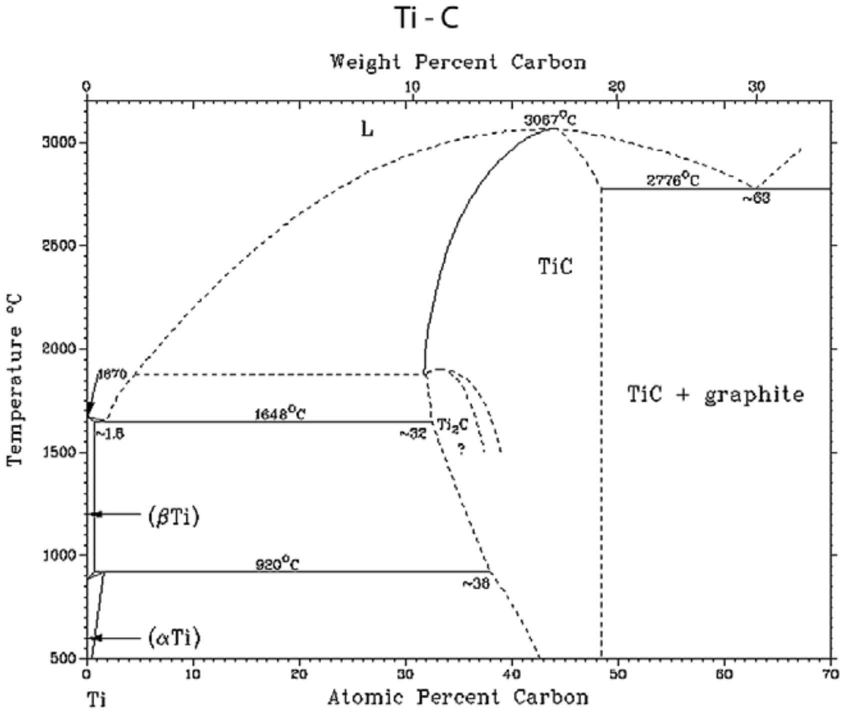

Figure C.6: Ti-C binary phase diagram [57]

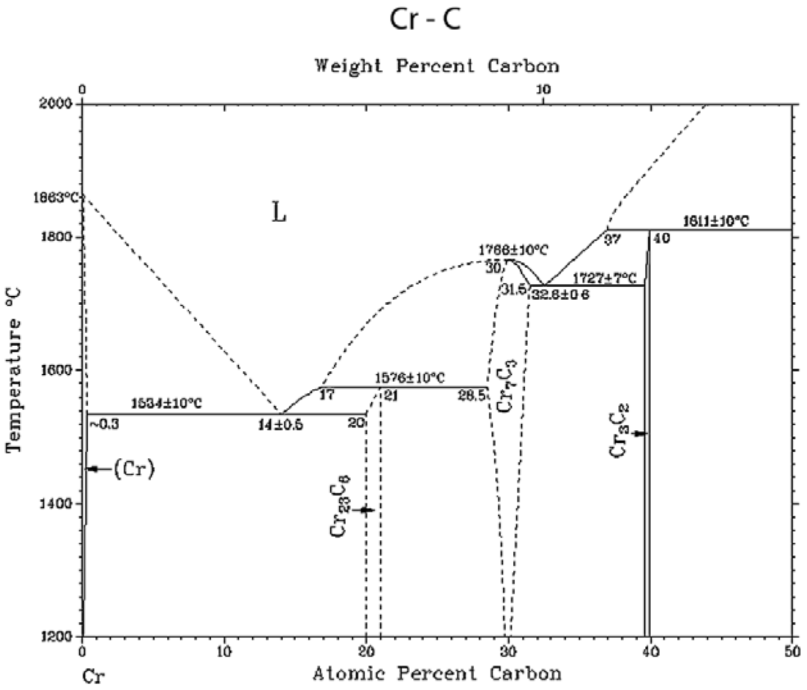

Figure C.7: Cr-C binary phase diagram [57]

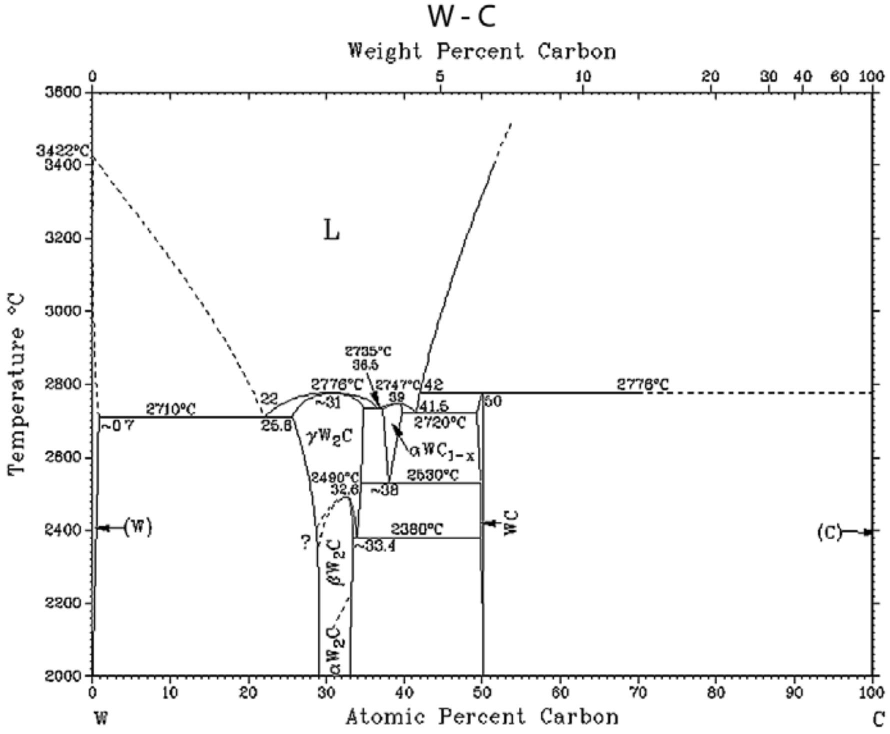

Figure C.8: W-C binary phase diagram [45]

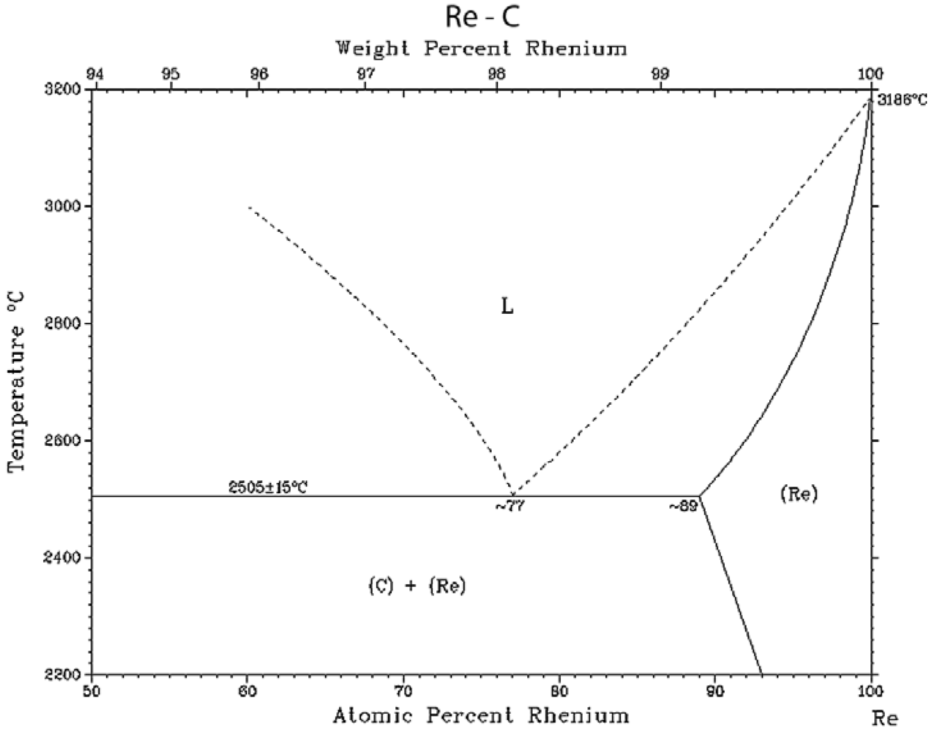

Figure C.9: Re-C binary phase diagram [58]

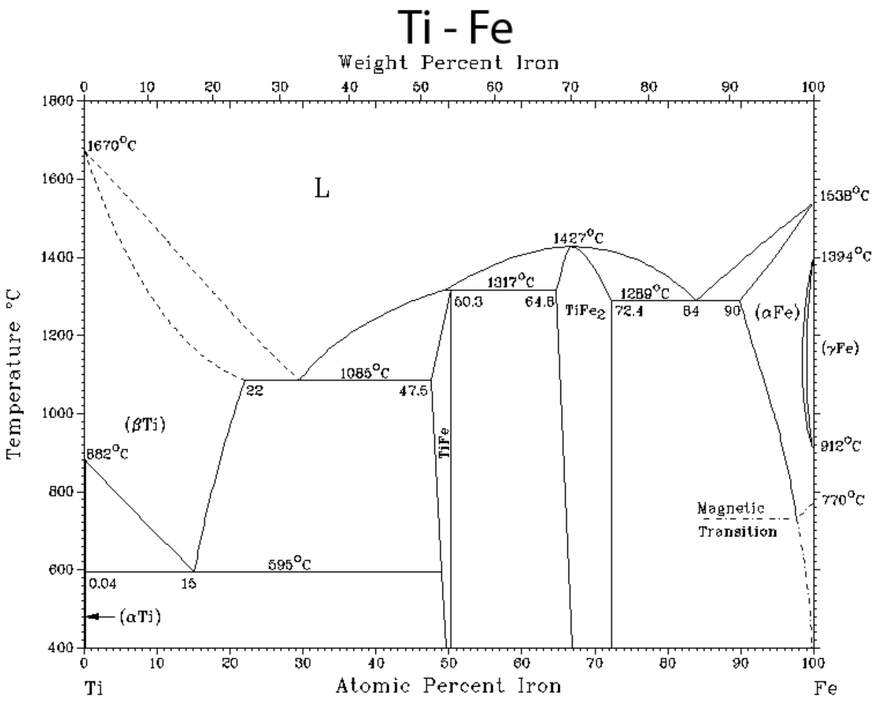

Figure C.10: Ti-Fe binary phase diagram [57]

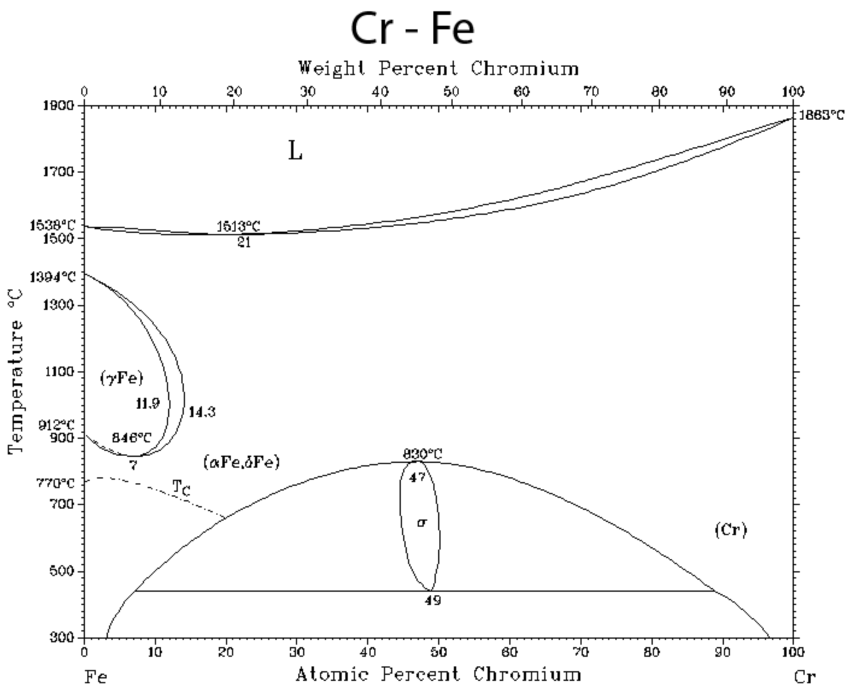

Figure C.11: Cr-Fe binary phase diagram [57]

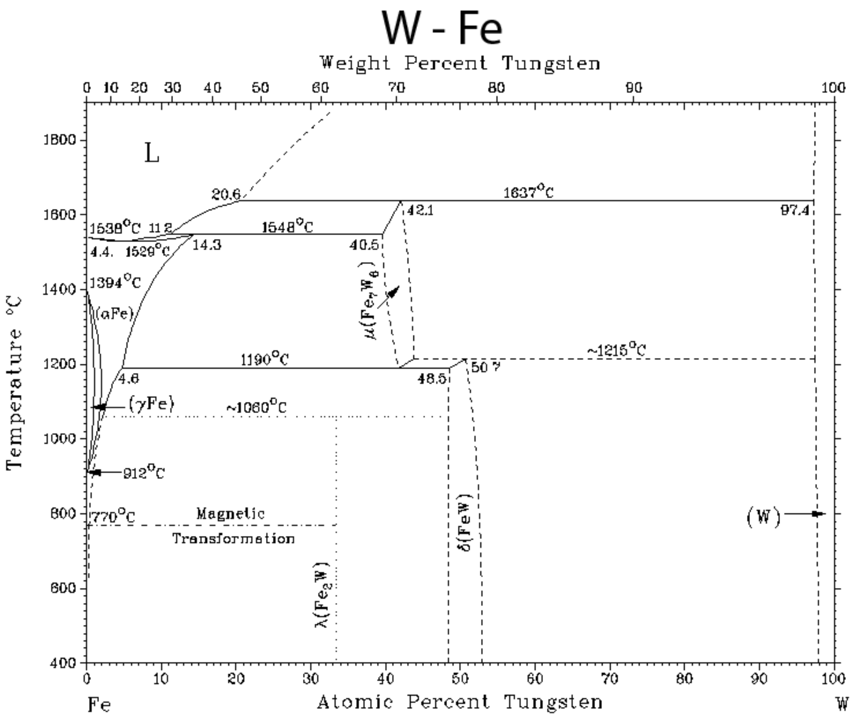

Figure C.12: W-Fe binary phase diagram [48]

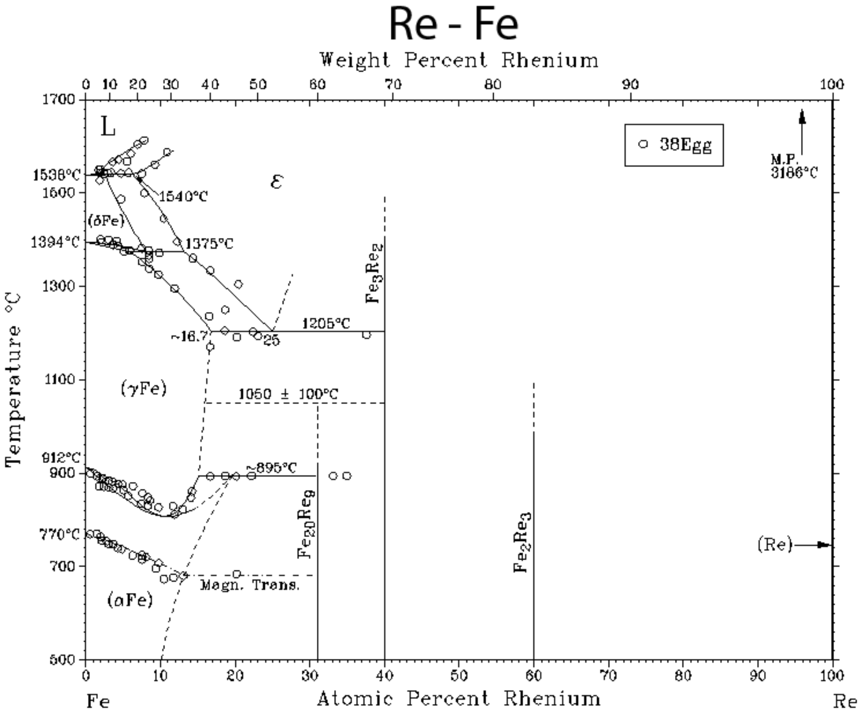

Figure C.13: Re-Fe binary phase diagram [49]

Acknowledgments

Now, at the end of my work I would like to thank all people who helped, supported and taught me during these last three years. It has been a very interesting period of my life and I feel very honoured to have been able to study for my PhD at the Max-Planck-Institut für Plasmaphysik.

Above all, Prof. Dr.-Ing. Dr.-Eng. Hans-Harald Bolt for obtaining a scholarship from the Max-Planck Society and providing me with a very interesting topic for my PhD work at the Materials Research Division. He was an exceptional supervisor who provided me not only with helpful advice on all aspects of my work but also, perhaps even more importantly, valuable critical comments and remarks.

Prof. Dr. mont. habil. Ewald Werner, who provided me with the opportunity to take my degree at the Technical University of Munich and for his reviewing of this thesis.

Dr. Annegret Brendel, who helped me a lot at the very beginning of my work as my tutor and for her corrections of my reports, articles and this thesis.

Dr. Hans Maier and Dr. Jeong-Ha You, who were always open and accessible for my questions. They are experts in their fields and I always found their advices to be very useful.

Dr. Klaus Schmid, who was very kind to me. I used his program (DIFFUSEDC) extensively for calculations of diffusion. Furthermore, I would like to thank him for discussions of the results of calculation and for reading some parts of this PhD work.

Dr. Martin Balden and Stefan Lindig, who taught me a lot of things concerning analysis techniques and helped me whenever I asked.

Freimut Koch, who taught me a lot of things concerning deposition techniques and was very helpful in spite of being a very busy person.

Till Höschen, who carried out all the annealing experiments on his high vacuum annealing set-up and was always very friendly.

Gabriele Matern, who carried out a important part of the samples' preparation. She polished about 500 graphite samples!

Joachim Dorner and Michael Fusseder, who took care of the TANDEM accelerator during the IBA measurements.

Dr. Christian Linsmeier, whose seminar for PhD students was very helpful. He was always open for different questions.

Dr. Simon Pinches who significantly improved this PhD work from the English point of view.

All PhD students within the Materials Research Division for a very pleasant climate during my PhD study.

All members of the Materials Research Division.

Finally, I would like to thank the most important person for me, my husband Dr. Denis Levchuk, I aim to become similar to him, who is my ideal. I would like to thank him not only for support and advices, but also for his understanding.